General Motors Corporation
Legal Staff

Facsimile
(810) 986-3173

Telephone
(810) 947-9212

FEB 16 2001

L. Robert Shelton,
Executive Director
NATIONAL HIGHWAY TRAFFIC
SAFETY ADMINISTRATION
400 Seventh Street, S.W., Room 5220
Washington, DC 20590

Dear Mr. Shelton:

Re: **Settlement Agreement**
**Section B. Fire Safety Research**

Enclosed is a final report prepared by Jeffrey Santrock of General Motors Corporation, entitled, "Evaluation of Motor Vehicle Fire Initiation and Propagation Part 4: Propagation of an Underbody Gasoline Pool Fire in a 1996 Passenger Van."

This final report relates to Project B.3 (Fire Initiation and Propagation Tests).

Yours truly,

D. K. Nowak-Vanderhoef

Deborah K. Nowak-Vanderhoef
Attorney

Enclosure

Mail Code: 480-106-304
Research Engineering Building 30500 Mound Road Warren, Michigan 48090-9055

# Evaluation of Motor Vehicle Fire Initiation and Propagation Part 4: Propagation of an Underbody Gasoline Pool Fire in a 1996 Passenger Van

Jeffrey Santrock
General Motors Corporation

## ABSTRACT

This report describes a vehicle fire propagation test conducted pursuant to an agreement between General Motors and the United States Department of Transportation. This fire test was conducted on November 15, 1996. The test vehicle was a crash-tested 1996 Plymouth Voyager obtained from the National Highway Traffic Safety Administration. In the crash test, the test vehicle was stationary and struck in the rear by a moving barrier. No leaks were detected in the fuel system of the test vehicle during the crash test or the subsequent roll test performed after the crash test. No fire was observed during the crash test, nor was there evidence of fire present in the test vehicle after the crash test. To create a gasoline pool under the test vehicle for the fire test, approximately 10 gallons of gasoline were added to the fuel tank and allowed to flow out of a hole drilled in the filler tube. The estimated flow rate of gasoline from the drilled hole was 243 mL/min. A hand-held propane torch was used to ignite the gasoline. The fire was allowed to burn until flames spread into the passenger compartment and along the headlining panel to the front of the passenger compartment. Flames entered the passenger compartment through the left rear vent window and through the open spot-weld seam at the rear of the left rear wheelhouse. The carpet, the left rear quarter trim panel, the molding on the D-pillar, the interior trim panel on the lift gate, and the lower surface of the cushion in the second bench seat were burning 150 seconds after the gasoline pool was ignited. Flames spread forward along the lower surface of the headlining panel approximately 175 seconds after ignition. Manual fire suppression using a water spray and a dry powder fire suppressant started approximately 210 seconds after ignition.

## Table of Contents

## List of Figures

## List of Tables

## 1 Introduction and Test Summary

This report describes a full-scale vehicle fire test conducted on November 15, 1996. This test was conducted by General Motors (GM) pursuant to an agreement between GM and the U.S. Department of Transportation. As part of this agreement, General Motors and the National Highway Traffic Safety Administration (NHTSA) jointly have developed 13 separate vehicle fire safety research projects. One of these projects, entitled "Fire Initiation and Propagation Tests", involves conducting vehicle crash tests to investigate potential ignition events that occur in vehicle crashes, and subsequent vehicle fire tests to characterize fire propagation in these crash-tested vehicles. The vehicle models to be tested, and the crash- and fire-test methods to be used for Project B.3 are described in another report [1]. The objectives of these fire tests are:

- To determine the principal fire paths and time-lines for flame propagation into the passenger compartment under the test conditions;
- To identify which components burn and to measure the thermal environments around those components associated with their ignition under the test conditions; and
- To measure air temperatures, heat fluxes, and combustion gas concentrations in the passenger compartment under the test conditions.

The vehicle used in this test was a 1996 Plymouth Voyager (VIN: 2P4FP25B2TR549233) with the following options: 2.4 liter 4-cylinder engine, a 3-speed automatic transmission, anti-skid brakes, air conditioning, and a rear window defogger. This vehicle was obtained from the National Highway Transportation Safety Administration after being crash tested by Transportation Research Corporation in East Liberty, Ohio on March 22, 1996 [2]. In the crash test, this vehicle was stationary and struck in the left rear by a vehicle impactor. The impactor had a deformable aluminum honeycomb face as described in FMVSS214 [3]. The alignment of the impactor to the vehicle was set so that the face of the impactor overlapped 70% of the rear of the vehicle. The impact angle was 180° with respect to the low track centerline of the vehicle. The mass of the vehicle was 1946 kg (4,290 lbs.). The mass of the impactor was 1342 kg (2959 lbs.). The impact speed was 81.5 km/h (50.6 mph). The fuel system did not leak fluid during the crash test or during the subsequent static roll test performed as specified in FMVSS301 [4].

Figure 1 shows photograph of the rear of the test vehicle as it was received from the Transportation Research Corporation. The static crush of the left rear of the vehicle was 435 mm. The rear hatch window was broken. The left rear vent window was pinned open by the deformed left quarter panel.


Figure 1. Fire Test F961116. View of the rear of the test vehicle after shipment from Transportation Research Corporation.

Inspection of the test vehicle revealed that spot weld seams around the left rear wheelhouse seperated during the crash test. These included a horizontal weld seam between the wheelhouse panel and the floor pan panel, a vertical weld seam between the rear of the wheelhouse panel and the left quarter panel, and a horizontal between the inner- and outer- wheelhouse panels. The seam openings around the left rear wheelhouse are shown in Figure 2.

This vehicle was used to study propagation of a gasoline pool fire located under the rear portion of the vehicle. As the fuel system of the test vehicle was not ruptured and did not leak gasoline during the crash test or during the subsequent static roll test, an artificial means of creating a gasoline pool under the test vehicle was used in this test. A hole was drilled in the filler tube close to where it entered the fuel tank. Liquid gasoline flowed from the hole and pooled under the test vehicle. Gasoline vapor above the liquid pool was ignited with a propane torch.


Figure 2. Fire Test F961116. Interior view of the left rear wheelhouse, floor pan, and lift gate of the test vehicle. The torn spot weld seams between the wheelhouse and the floor pan and the inner and outer wheelhouse panels are shown here. The second bench seat and interior trim were removed for this photograph.

Flames from the burning gasoline pool entered the left rear wheelhouse and ignited the filler shield. The filler shield melted and sagged onto the tire as it burned. Flames spread into the passenger compartment through the open spot weld seam at the rear of the left rear wheelhouse and the left rear vent window. The carpet, the left rear quarter trim panel, the molding on the D-pillar, the interior trim panel on the lift gate, and the lower surface of the cushion in the second bench seat were burning within 150 seconds after the gasoline pool was ignited. Flames started to spread across the headlining panel approximately 175 sec after ignition.

Manual fire suppression began approximately 215 sec after ignition. A water spray and a dry powder fire suppression agent were used to extinguish the fire. Table 1 contains an approximate time-line summarizing the fire development during this test.

Table 1

Summary of Fire Development during in Fire Test F961116

| Time[1] (sec) | Event |
|---|---|
| -32 | Plug removed from hole in filler neck and gasoline begins to accumulate in a pool under the test vehicle |
| 0 | Gasoline pool was ignited by a propane torch |
| 5 - 10 | Flames from the burning gasoline pool entered the left rear wheel house |
| 10 - 15 | Heated gases started to enter the vehicle through the split spot weld seam between the left rear wheelhouse and the floor pan |
| 60 - 90 | The filler shield sagged onto the left rear tire |
| 90 - 110 | Flames entered the passenger compartment through the split spot weld seam and ignite the left rear quarter trim panel |
| 100 - 105 | Flames from the wheel house sporadically reached the bottom of the left rear vent window |
| 110 - 115 | Flames emerging from the left rear wheel house sporadically reached the top of the left rear vent window |
| 120 - 130 | The lower surface of the foam pad in the second bench seat cushion started to burn |
| 135 | Flames began to enter the passenger compartment through the left rear vent window |
| 150 | Flames in the left rear corner of the passenger compartment sporadically reached the headlining panel |
| 170 | The headlining panel ignited and flames spread laterally across the rear of the passenger compartment and forward toward the middle bench seat |
| 183 | The upper surfaces of the middle bench seat back ignited |
| 215 | Fire suppression began |

[1]Time after ignition of the gasoline pool.

## 2 Vehicle Condition and Test Protocols

The fire test described in this report was conducted at the Factory Mutual Test Center in West Glocester, Rhode Island. The crash-tested vehicle was prepared for the fire tests at the General Motors Research and Development Center (GM R&D Center) in Warren, Michigan, and shipped to the Factory Mutual Test Center. The test vehicle was returned to the GM R&D Center after the fire test, where it was systematically disassembled to permit closer inspection of the fire damage and identification of fire spread paths that were not obvious during the tests.

A detailed record of this test was obtained by video cameras located both inside and outside the test vehicle (**APPENDIX A**). Thermal radiation signatures from the burning vehicle were measured using infrared imaging systems (IR cameras), also located inside and outside the test vehicle (**APPENDIX B**). Flame spread in areas not visible to the video or infrared cameras, such as in the instrument panel, was tracked by thermocouples and heat flux transducers installed in the test vehicle before the fire test (**APPENDICIES C** and **E**). The air temperature in the passenger compartment was measured using an aspirated thermocouple probe assembly containing six shielded thermocouples (**APPENDIX D**). Pressure measurements were made to determine the pressure gradient across the dash panel and airflow through the driver's window during this test (**APPENDIX F**). Heat transfer to six locations in the passenger compartment was measured using differential flame thermometers (**APPENDIX G**). The heat release rate of the fire was measured using the Fire Products Collector (FPC) at the test facility (**APPENDIX H**). The gaseous combustion products in the passenger compartment were measured by FTIR gas analysis of gas sampled continuously from the passenger compartment during the test (**APPENDIX I**) and by GC/MS analysis of grab-samples acquired from the passenger compartment during the test (**APPENDIX J**).

The test vehicle was placed in a fluid containment pan[1] and centered under the fire products collector. Figure 3 is a photograph of the test vehicle in place on the fluid containment pan before the test. The test vehicle was placed in the center of the pan. All doors were closed. The left rear vent window was wedged open and could not be closed. The rear hatch window was broken in the crash test and was not replaced. All other windows were intact and raised to their fully closed

[1] The fluid containment pan was a rectangular steel pan (length = 25 ft. (7.6 m) width = 15 ft. (4.6 m), height = 4 in. (0.10 m)) to prevent spilled and leaking automotive fluids from spreading in the test facility. This fluid containment pan was fabricated from two sheets of carbon steel. Angle-braces were welded to the underside of the pan to keep it from flexing under the weight of the vehicle. The bottom of the fluid containment pan was lined with concrete landscaping paving blocks on a level bed of sand. The joints between the paving blocks were filled with sand. The purpose of this treatment was to place the test vehicle on a non-metal, semi-porous surface with absorptive properties similar to an asphalt or concrete road surface.

positions. No attempt was made to heat the engine or exhaust system. All components in the vehicle were at ambient temperature at the start of the fire test.

Figure 3. Fire Test F961116. Photograph of the test vehicle in position in the fluid containment pan before the fire test.

A 3 mm diameter hole was drilled in the base of the filler neck near where it connected to the fuel tank. A short piece of nylon rod was inserted into the hole. Approximately 10 gallons of regular gasoline was added to the fuel tank, and the filler cap was replaced. The temperature of the gasoline had been equilibrated to approximately 22°C before filling the fuel tank of the test vehicle. The plug was removed from the hole and not reinserted into the hole at any time during this fire test. Gasoline was allowed to flow from the hole drilled in the filler tube onto the ground. Gasoline vapor above the gasoline pool was ignited artificially with a propane torch approximately 32 seconds after removing the plug (see **SECTION 3**).

To synchronize the different data acquisition systems, an air horn was sounded to signal three events during this test: removal of the plug from the hole drilled in the filler tube, artificial ignition of the gasoline, and the end of each test. The air horn was audible on the videotapes, except for the tape in camera 3, which had a malfunctioning microphone. In this case, an object moving in its field of view signaled the start of the test. One channel of the data acquisition system for vehicle

instrumentation monitored a normally open switch, which was depressed at the start of the test. The real-time clock in the FTIR data system was synchronized to the real-time clock in the vehicle instrumentation data system.

Five criteria were established before the test to guide the decision to stop the tests and extinguish the fire. The intent of these criteria was to allow flames to spread into the passenger compartment sufficiently so that the principle fire paths could be determined while preserving physical evidence of fire paths that were not readily visible during the test or in any of the videos of the test. This physical evidence would be lost if the test vehicle were allowed to burn completely. The criteria used were:

- When the air temperature in the passenger compartment measured between the front seats at the height of an adult occupant exceeded 200°C and was increasing rapidly, or
- When the concentration of carbon monoxide in the passenger compartment exceeded 1% and was rising rapidly, or
- When flames visibly impinged on one or both front seats, or
- When the head-lining covering the forward section of the roof was in flames, or
- When flashover in the passenger compartment was evident.

After ignition, an attempt was made to evaluate these criteria continuously. As flames spread into the passenger compartment, conditions changed rapidly allowing insufficient time for objective evaluation of each of these criteria. The test was stopped after observing that flames had spread along the entire lower surface of the headlining panel.

## 3 Ignition

Figures 4 and 5 show views of the ignition from the rear and left side of the test vehicle, respectively. (Refer to Fig. A1 for a diagram showing the locations of the video cameras during this test.)

Figure 4. Fire Test F961116. Video still from Camera 1 showing ignition of the gasoline pool from the rear of the test vehicle.

The flow rate of gasoline from the hole drilled in the filler tube prior to ignition was estimated from the rate of increase in the pool diameter. Figure 6 shows a plot of the diameter of the gasoline pool for the first 35 seconds of the test. The flow rate was estimated from the increase in the diameter of the pool under the test vehicle. This estimate yielded a value of 243 mL/min for the flow rate of gasoline from the hole drilled in the filler tube.[2]

[2] This estimate of flow rate assumed that the gasoline pool had a depth of 1 mm [5].

Figure 5. Fire Test F961116. Video still from Camera 2 showing ignition of the gasoline pool from the left side of the test vehicle. The structure in the foreground is the support for a fire suppression system located above the test floor.

A series of separate laboratory experiments was performed to confirm this estimate. In four replicate experiments, heptane[3] was pumped through tubing onto the surface of a reinforced cement construction board similar to the material used to line the bottom of the fluid containment pane during this fire test. The tubing had an exit diameter of 3 mm, and the exit was located 20 cm above the surface of the concrete board. The flow rate of heptane was 250 ± 5 mL/min. The duration of flow was 30 seconds. The mean pool diameter at 30 seconds was 40 ± 2 cm, which is similar to the diameter of the gasoline pool at 30 seconds estimated from the video tapes (Fig. 6). The agreement of these estimates indicates that the flow rate of gasoline from the hole drilled in the filler tube before ignition was approximately 243 mL/min.

[3] The spreading characteristics of heptane on a concrete surface have been determined to be similar to those of gasoline [5].

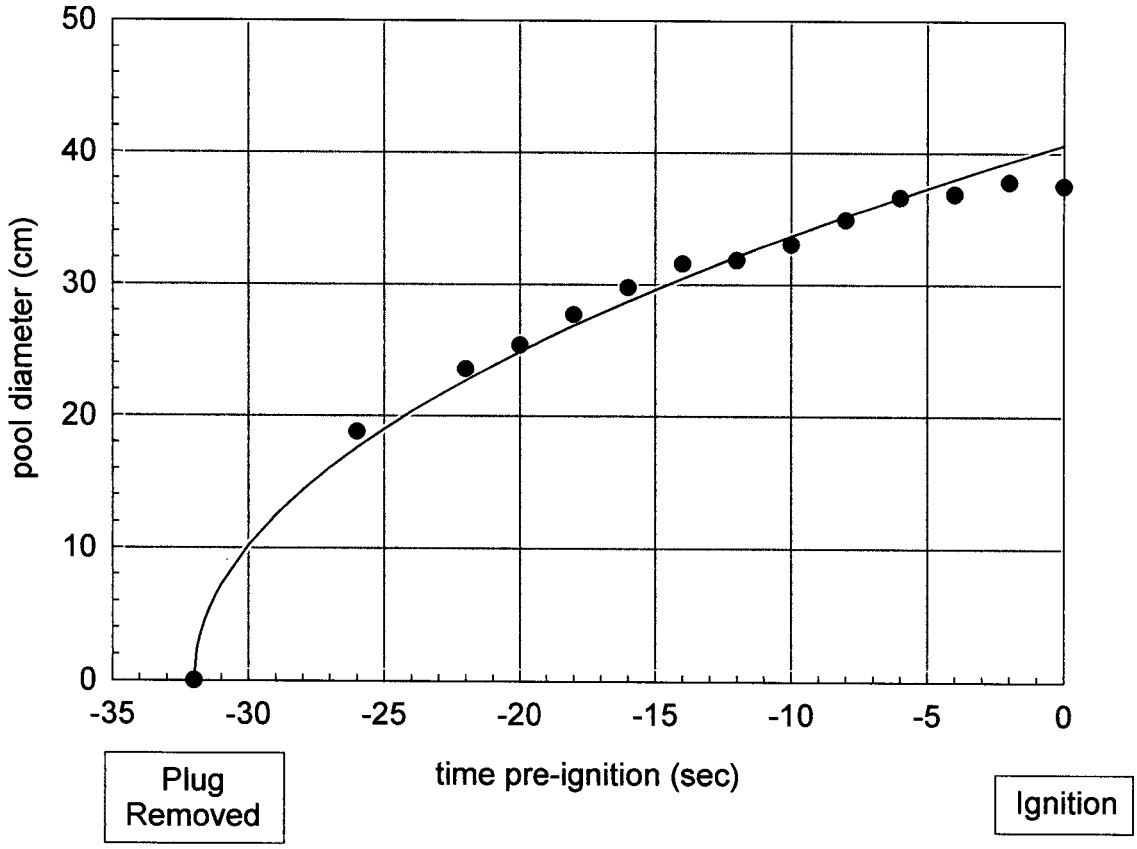


Figure 6. Fire Test F961116. Plot of gasoline pool diameter versus time ($\lambda$) determined by analysis of the video from Camera 3 from the start of gasoline flow to ignition. The uncertainty in determining pool diameter was estimated to be $\pm$ 1 cm. Also shown in this figure is the pool diameter expected for a flow rate of 243 mL/min given a pool depth of 1 mm (—).

## 4 Behavior of the Underbody Gasoline Pool Fire in this Test

Figure 7 shows two plots of the estimated diameter of the pool from the start of gasoline flow to the end of the test. These estimates were determined by analysis of the videos from Cameras 1 and 4. These estimates differ slightly because the pool was not circular and these cameras viewed the pool from different angles. (Refer to Figure A.1 for a diagram of the video camera layout for this test.) These plots show that the diameter of the pool increased uniformly before ignition. After the gasoline was ignited, the diameter remained approximately constant for about 90 seconds, indicating steady-state burning conditions in which the rate of fuel consumption approximately equaled the mass-flow rate of gasoline from the hole in the filler neck. The diameter of the burning pool increased from approximately 40 to 80 cm between 80 and 200 seconds post-ignition (Fig. 7), indicating that the rate of fuel input had increased. For example, Figure 8 shows the burning pool at 80 and 200 seconds post-ignition from right side of the vehicle. The pool diameter approximately doubled during this time interval.

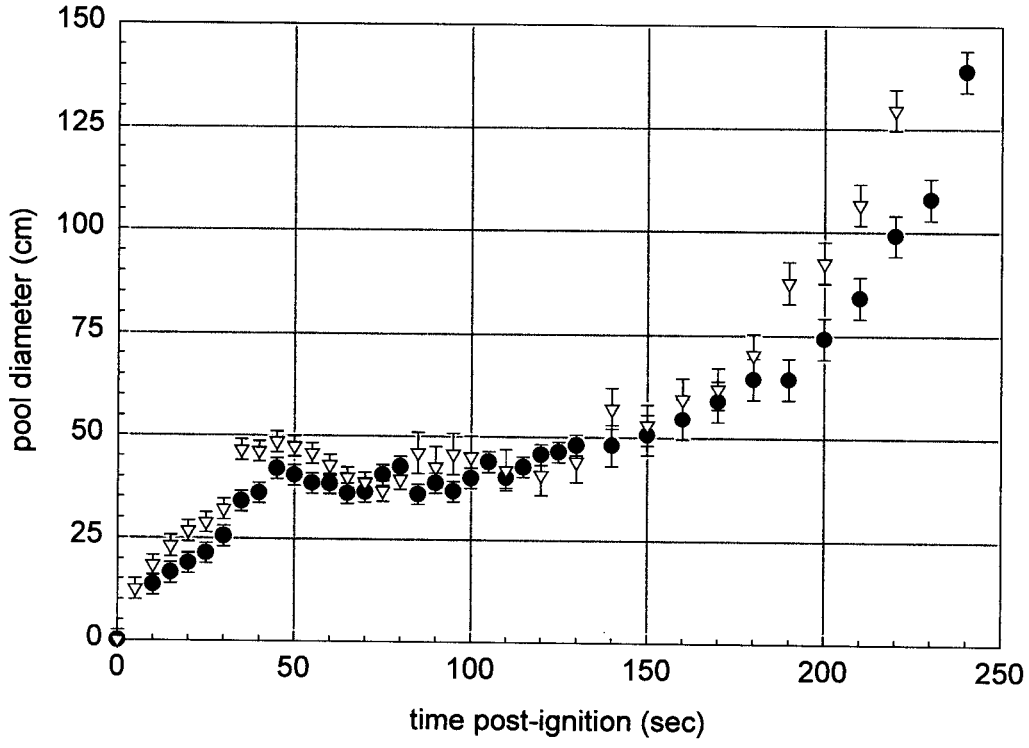


Figure 7. Fire Test F961116. Plot of pool diameter versus time determined by analysis of the video from Cameras 1 (λ) and 4 (▽) from the start of gasoline flow to the end of the test.

Figure 8. Fire Test F961116. Video stills from Camera 4 showing the right side of the test vehicle at 80 (upper panel) and 200 (lower panel) post-ignition. The diameter of the burning fuel under the vehicle was approximately 40 cm at 80 seconds post-ignition and approximately 80 cm at 200 seconds post-ignition.

Under steady-state burning conditions, a 40 cm-diameter gasoline pool fire would be expected to produce a flame about 1 m high [5]. However, the fuel tank and floor pan of the test vehicle were 15 to 30 cm above the burning pool and obstructed the upward movement of the fire plume. Flames spread radially along the lower surface of the gasoline tank and upward around its sides onto the floor pan.

During the period when the diameter of the burning pool was approximately constant (e.g., 40 to 120 seconds post-ignition), the fire plume appeared to have been localized to the areas directly under the fuel tank and floor pan to the left of the fuel tank (Fig. 9).[4]

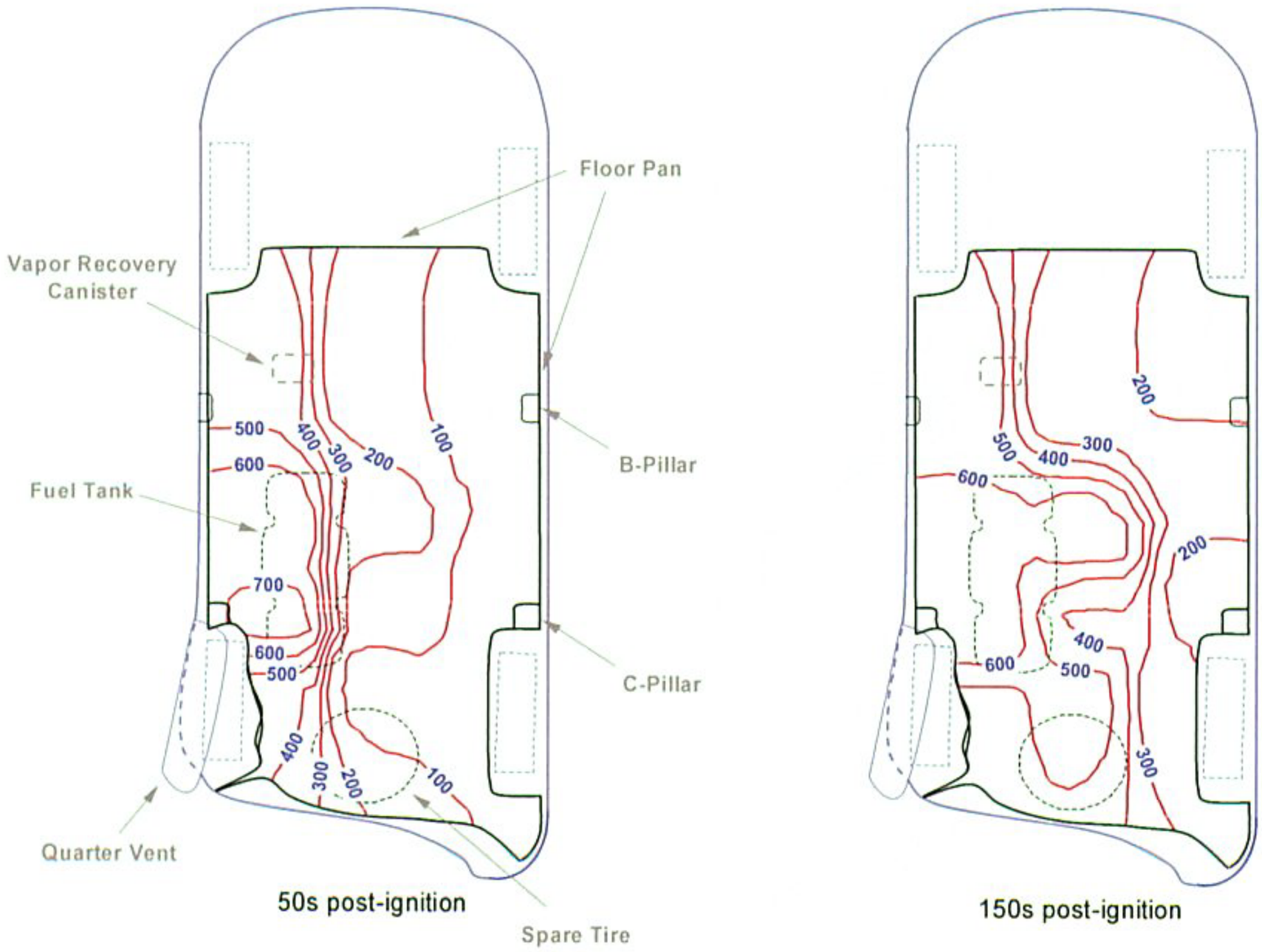


Figure 9. Fire Test F961116. Isothermal contour plots showing temperatures profiles estimated from the responses of the C-thermocouples located below the floor pan. The unit of temperature in these plots is degrees Celsius.

---

[4]Isothermal contours of the temperature below the second bench seat cushion were estimated from the temperature data recorded from the C-Thermocouples using a three-dimensional interpolation command available in SigmaPlot® 4.0 for Windows® [**6**]. This command used an inverse distance method to generate\ temperature values for points on a uniformly spaced Cartesian grid from the [x,y,t] triple data from these thermocouples. Refer to Figure A7 in **APPENDIX A** for the approximate locations of the C-thermocouples on the Floor pan. Refer to **APPENDIX B** for the data from the C-Thermocouples.

As the diameter of the burning pool began to increase, the fire plume appeared to contact the floor pan to the right of the fuel tank (Fig. 9).

The thermocouple junctions of the C-thermocouples were located approximately 1 cm below the lower surface of the floor pan. Thus, temperatures recorded from these thermocouples were an indication of the intensity of the flames near the thermocouple junction. Using a threshold value of 600°C to indicate continuous direct flame contact with the thermocouple junction, these isothermal contour plots indicate the approximate area of flame contact with the lower exposed surfaces of the test vehicle.

Figure 10 shows the locations of thermocouples on the lower surface of the fuel tank and a heat flux transducer in the floor pan above the filler neck.

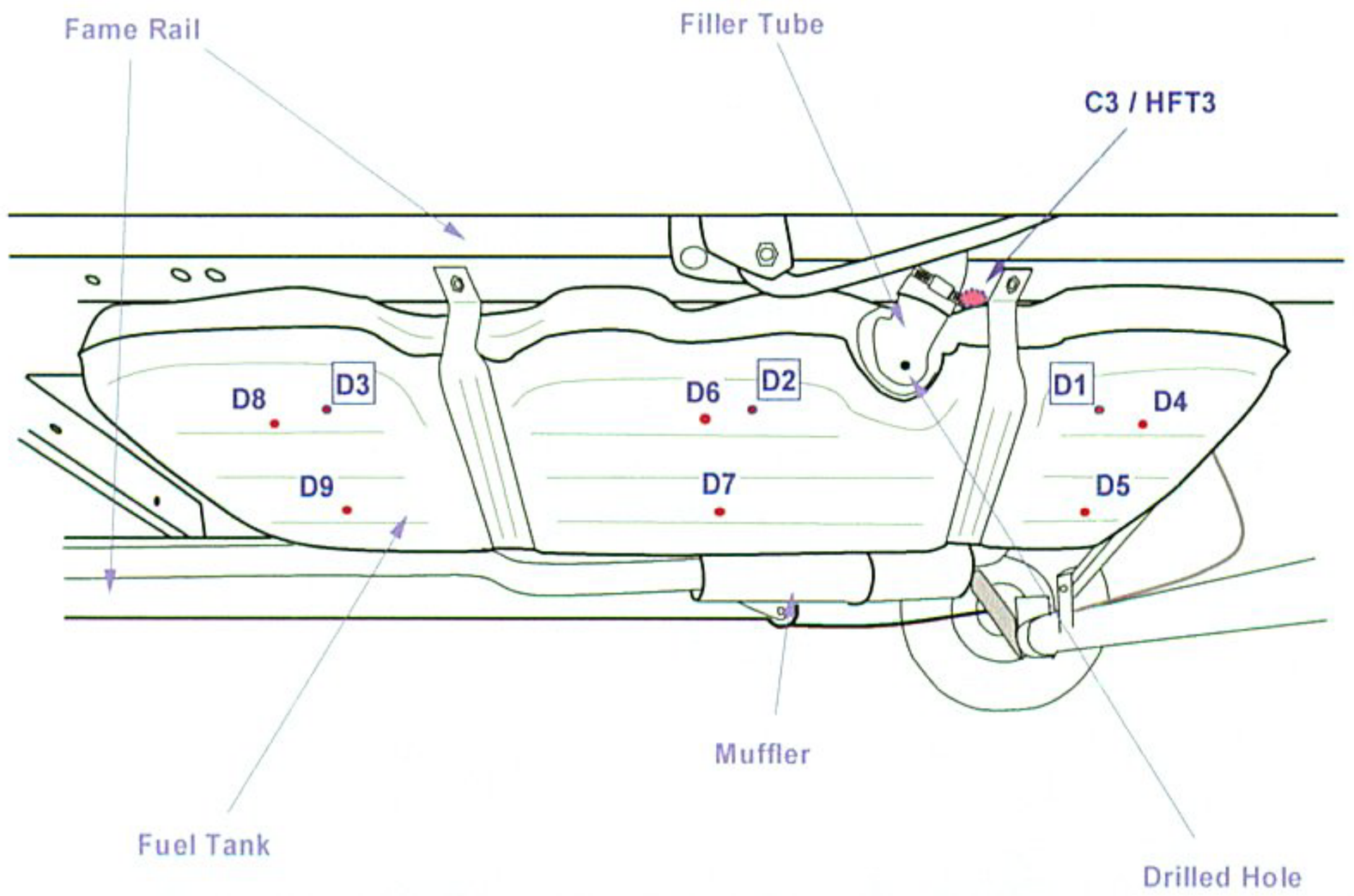


Figure 10. Fire Test F961116. View of the underbody of the test vehicle showing the locations of thermocouples on the fuel tank and a heat-flux transducer/radiometer assembly in the floor pan. Thermocouples D1 through D3 were located in the liquid gasoline. Thermocouples D4 through D8 were located on the lower surface of the fuel tank. Thermocouple C3 extended approximately 1 cm below the lower surface of the floor pan. The face of Heat Flux Transducer 3 was flush with the lower surface of the floor pan. The approximate location of the hole drilled in the filler tube is shown for reference.

The heat flux to the area of the floor pan that was just above the filler, the approximate center of the gasoline pool, was approximately 75 $kW/m^2$ for the first 100 seconds of the test (Fig. 11). The heat flux to the fuel tank was not measured, but the temperatures recorded from thermocouples on its lower surface indicated that the heat flux was greatest in the center and the left rear corner of the fuel tank (Fig's 12 and 13).

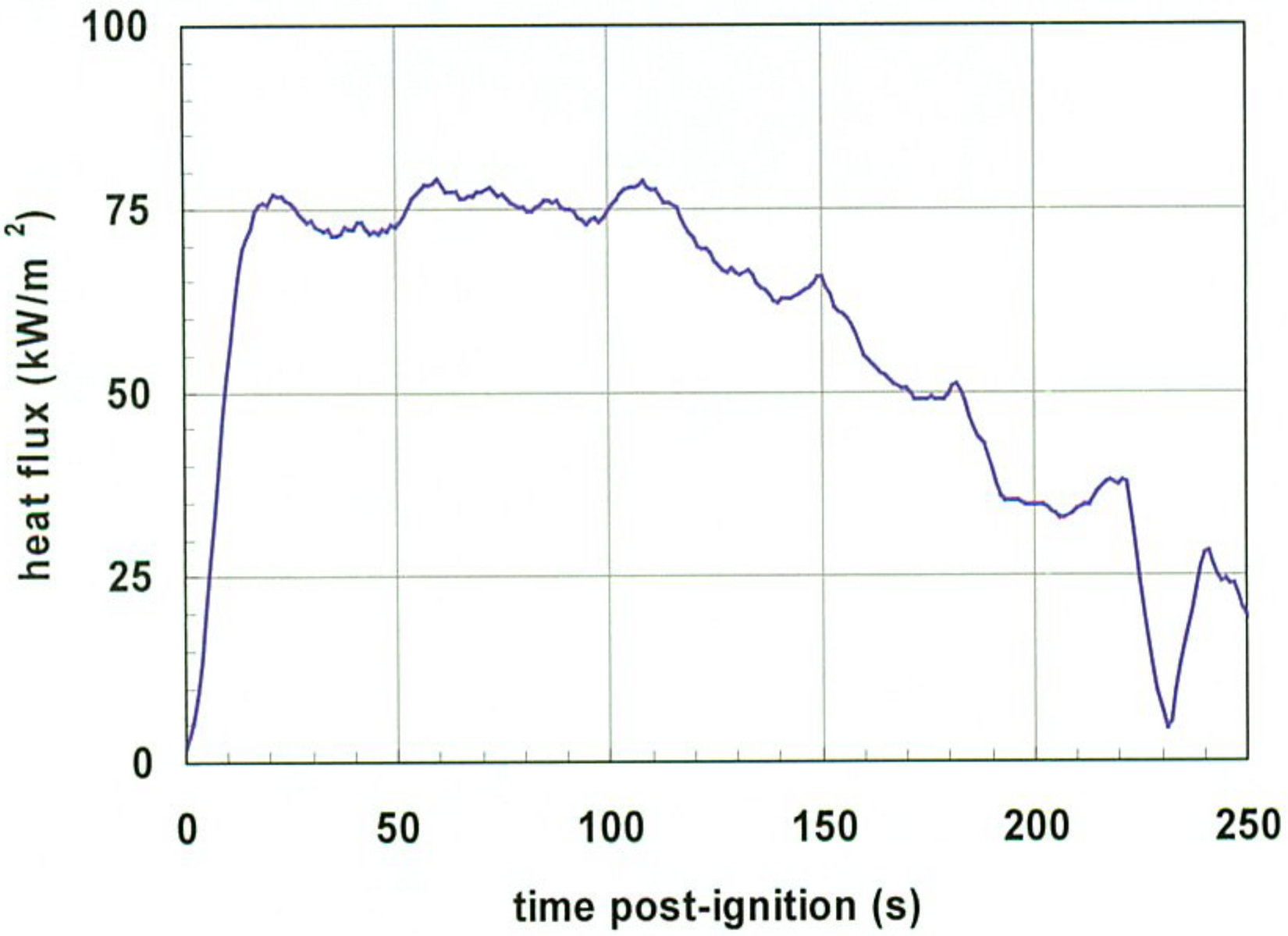


Figure 11. Fire Test F961116. Plot of heat flux to Heat Flux Transducer 3 located in area of the floor pan above the filler tube.

Heat transfer through the bottom of the fuel tank also heated the liquid gasoline inside the tank (Fig. 14). This does not appear to have caused an increase in the pressure in the fuel system, nor a concomitant increase in the flow rate of gasoline from the hole in the filler tube. Data recorded from thermocouples immersed in the gasoline indicates the temperature of the liquid increased from approximately 10°C before ignition to 42°C at 200 seconds post-ignition (Fig. 14)., which would have caused an increase in its equilibrium vapor pressure from about 4 to 11 psi.[5] A pressure gauge (instrumentation added for this test) in the fuel system recorded no detectable pressure increase in the fuel system at any time during this test. Gasoline vapor produced by volatilization of the liquid gasoline in the fuel tank apparently vented to atmosphere through the vent on the vapor recovery canister, thus preventing a pressure built-up in the fuel tank.

---

[5] The true vapor pressure of a 9 Reid vapor pressure gasoline was estimated using the following equation:

$$\ln(P) = 10 + \left(\frac{\ln(RVP) - 0.6983}{0.995}\right) - \left(\frac{5149.9}{459 + t}\right)$$

where p is the true vapor pressure, RVP is Reid Vapor Pressure, and t is temperature in F.

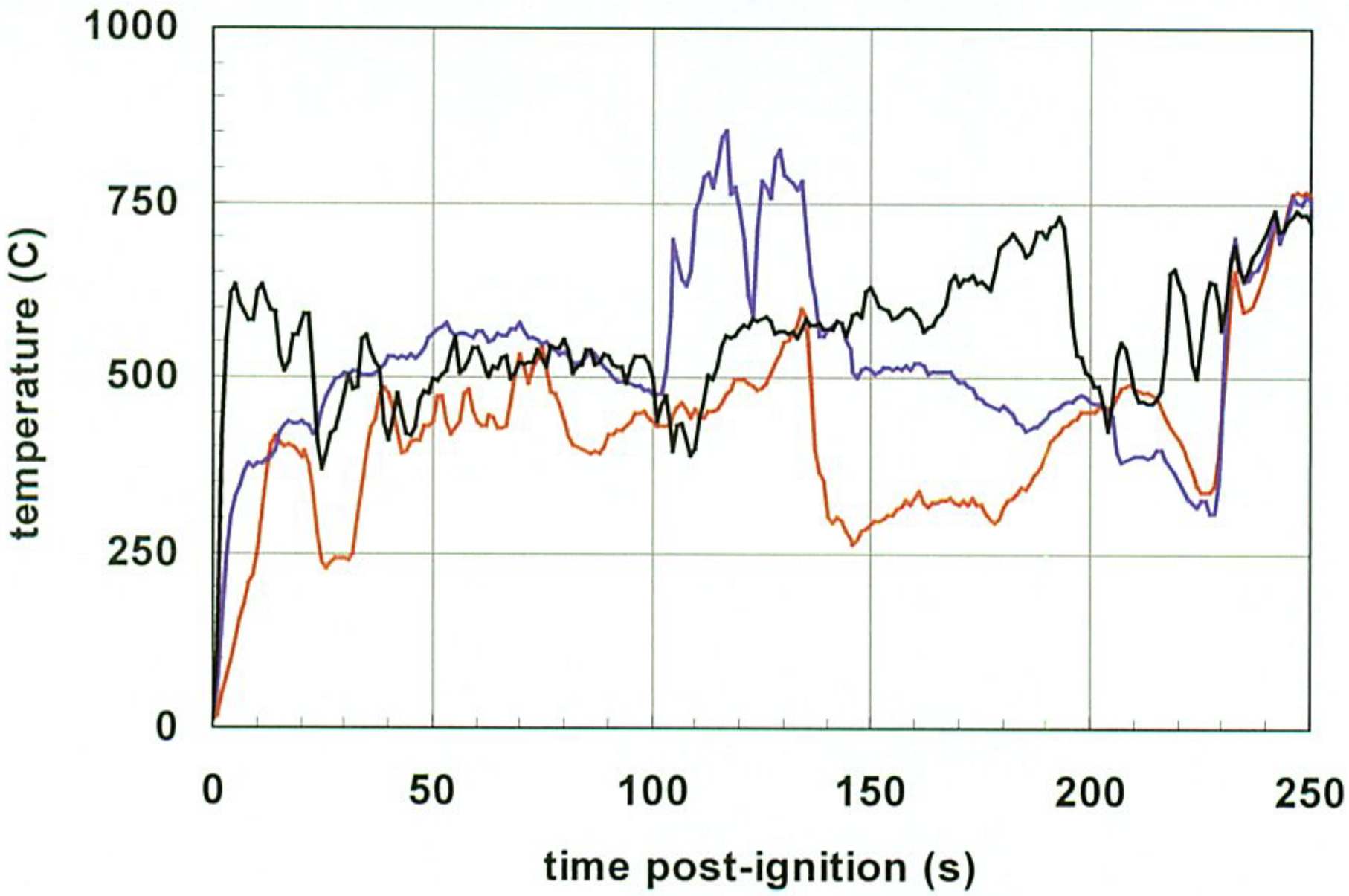


Figure 12. Fire Test F961116. Plots of temperatures recorded from Thermocouples D4 (—), D6 (—), and D7 (—) located on the bottom surface of the fuel tank.

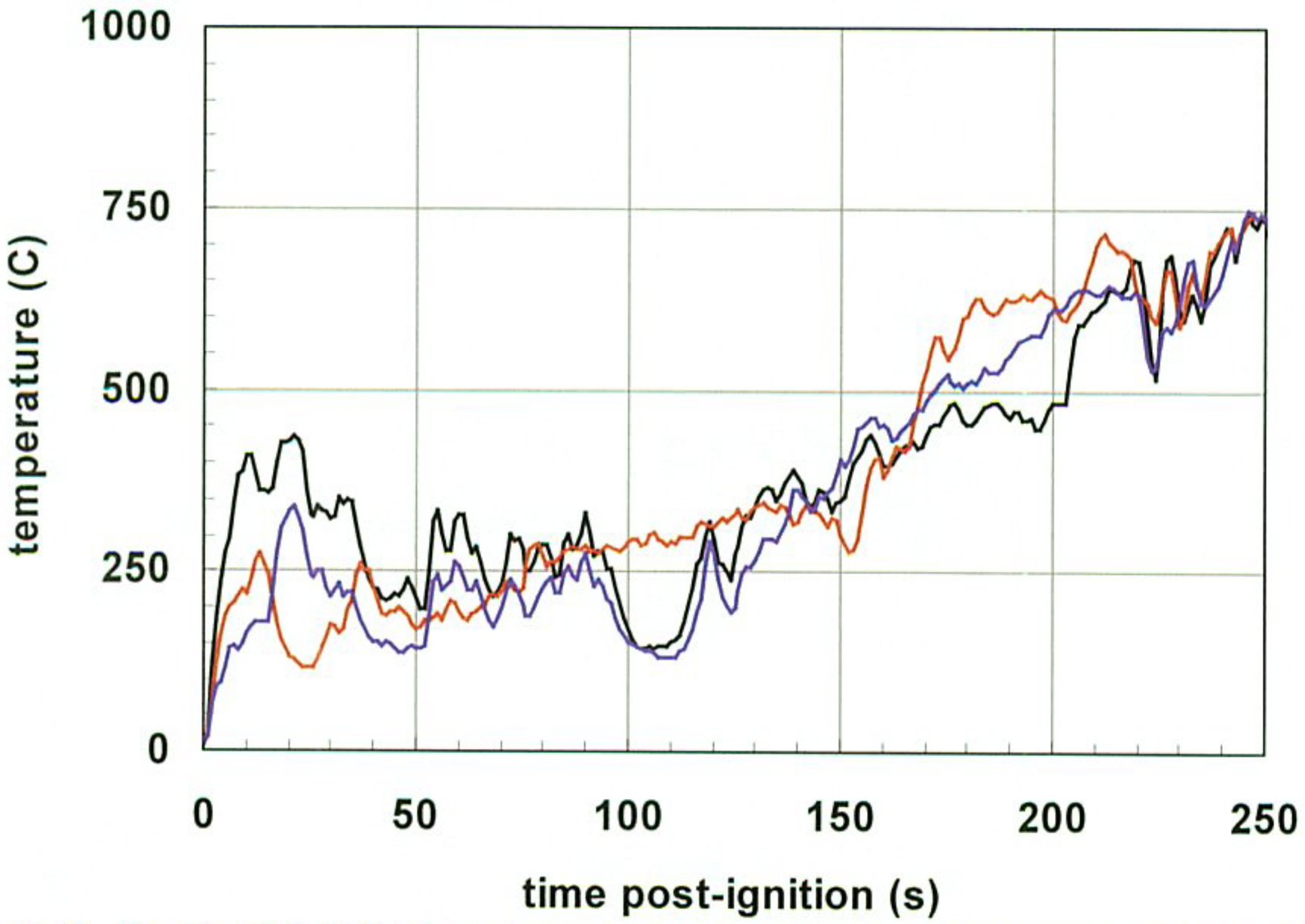


Figure 13. Fire Test F961116. Plots of temperatures recorded from Thermocouples D5 (—), D8 (—), and D9 (—) located on the bottom surface of the fuel tank.

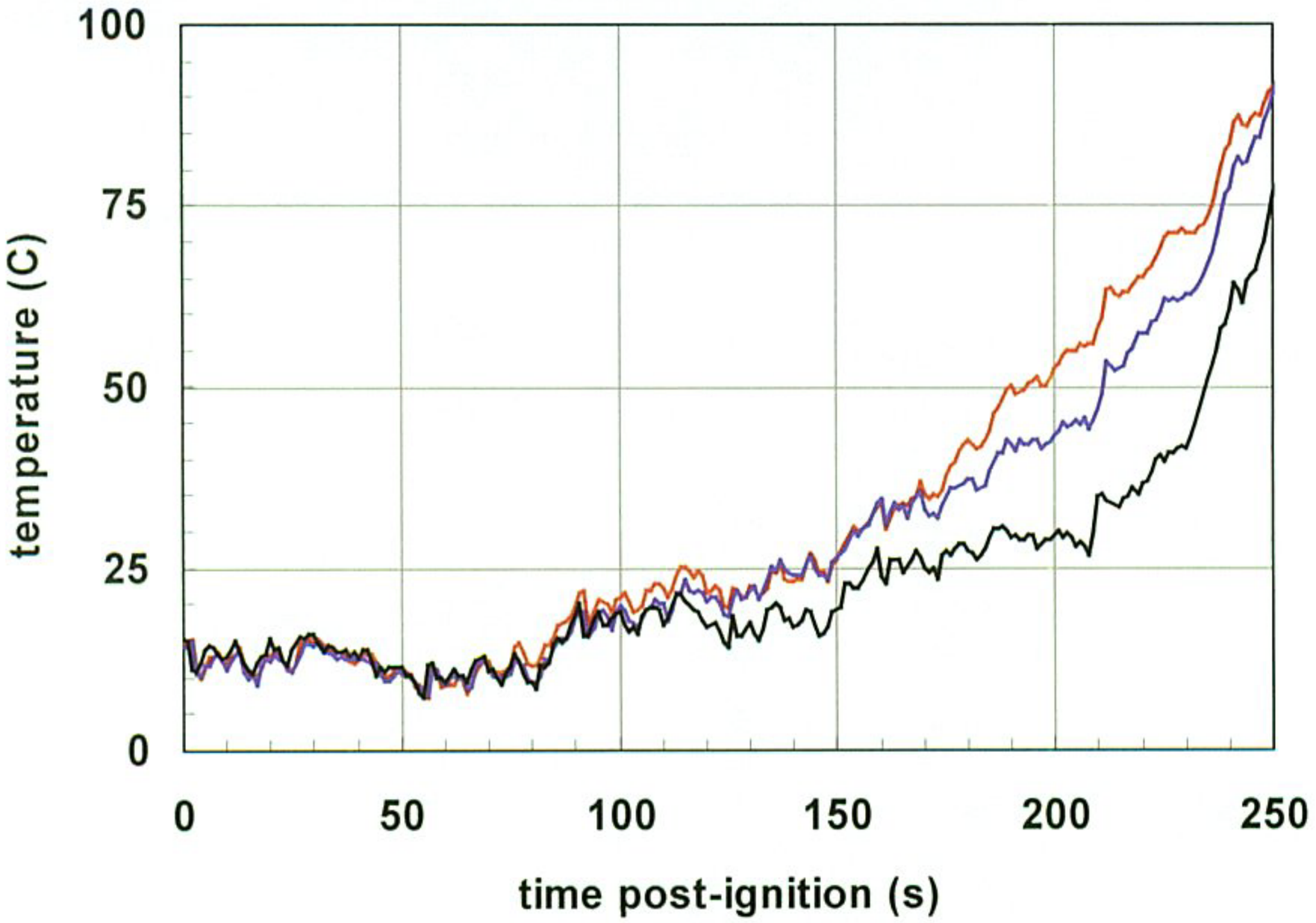


Figure 14. Fire Test F961116. Plots of temperatures recorded from Thermocouples D1 (—), D2 (—), and D3 (—) immersed in the liquid gasoline in the fuel tank.

The source of additional fuel that caused the size of the burning pool under the test vehicle to increase appears to have been molten plastic dripping from components on the vehicle heated by flames, primarily poly(ethylene) dripping from the fuel tank. The liquid gasoline in the fuel tank acted as a heat sink, absorbing heat from the wall and preventing a rapid loss of the bottom and sides of the tank. Temperatures recorded from thermocouples on the bottom of the fuel tank were greater than the melting point of the poly(ethylene) used to fabricate the tank (Fig.'s 12 and 13).[6] In some areas, the temperature exceeded the thermal decomposition temperature of poly(ethylene).

In two separate tests conducted at the Building and Fire Research Laboratory of the National Institute of Standards and Technology, gasoline tanks for 1996 Chrysler minivans were exposed to flames continuously from a small propane burner [7]. In both of these tests flaming drops of melted polyethylene started dripping from the tank within 60 seconds after the tank was first exposed to flames. In one test where the fuel tank was empty, the entire tank melted, creating a

[6] The melting point of the poly(ethylene) resin used in the fuel tank of the test vehicle was 128°C. The major thermal decomposition of the this material occurred at 387°C [8].

pool of molten polyethylene burning on the surface beneath the original location of the tank. Most of the polyethylene was eventually consumed by fire. In the other test. water was added to the tank as a heat-sink. In this test, the walls of the tank were not consumed by the fire, but the presence of water in the tank did not prevent the poly(ethylene) resin at the exterior surface of the tank from melting and dripping onto the ground.

These results suggest that a similar process occurred during the vehicle fire test described in this report. The diameter of the fire plume under the test vehicle started to increase about 120 seconds post-ignition. Loss of material from the outside of the fuel tank would not have increased the diameter of the hole in the filler neck, which would have resulted in an increase in the flow rate of gasoline from the hole. It would, however, have added combustible material to the burning pool below the vehicle. Polyethylene dripping from the bottom and sides of the fuel tank may have been the additional fuel that caused the increase in pool diameter between 120 and 200 seconds post-ignition (Fig. 7).

An increase in flame volume in the area between the spare tire and floor pan was observed between 200 and 205 seconds post-ignition (Fig. 15). The diameter of the pool fire below the vehicle did not appear to increase at this time (Fig. 7). Analysis of the temperature data recorded from thermocouples below the floor pan also indicated that the area of the floor pan exposed to flames also increased during this period (Fig. 17). The size and intensity of the fire plume below the vehicle did not change appreciably between 180 and 200 seconds post-ignition. Starting at about 200 seconds post-ignition, an area with temperatures greater than 700°C appeared to the right of the fuel tank and spread forward and rearward along the longitudinal center-line of the floor pan over the next 10 seconds (Fig. 16).

The fuel tank contained approximately 38.5 L (10 gallons) of gasoline at the start of the test. By 200 seconds post-ignition, the fuel tank had lost an estimated 833 mL of gasoline[7], which was slightly more than 2% of the gasoline in the tank at the start of the test and would not have resulted in a significant reduction in the liquid level in the fuel tank. The tests conducted at the National Institutes of Standards and Technology indicate that this residual liquid gasoline would have acted as a heat-sink, preventing the inner surface of the lower portion of the fuel tank from melting even when the outer surface was exposed directly to flames.

[7] The estimate of the total volume of gasoline lost from the tank assumes that the hole drilled in the filler tube was the only source of liquid gasoline and that the flow rate of gasoline through this opening was constant at about 243 mL/min through 200 seconds post-ignition.

Figure 15. Fire Test F961116. Video stills from Camera 1 at 200 (upper) and 202 (lower) seconds post-ignition.

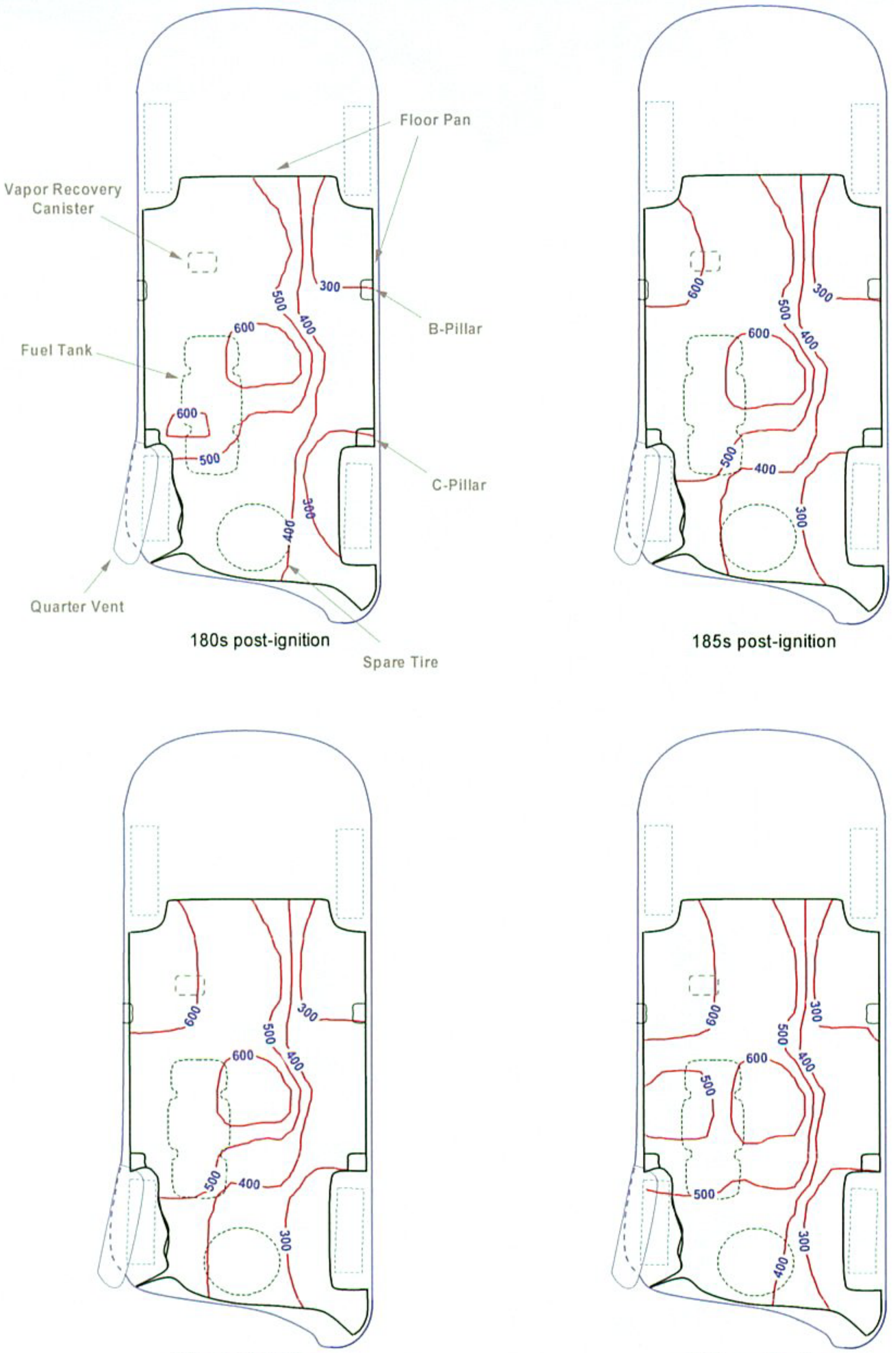


Figure 16. Fire Test F961116. Isothermal contour plots showing temperature profiles estimated from the responses of the C-thermocouples.

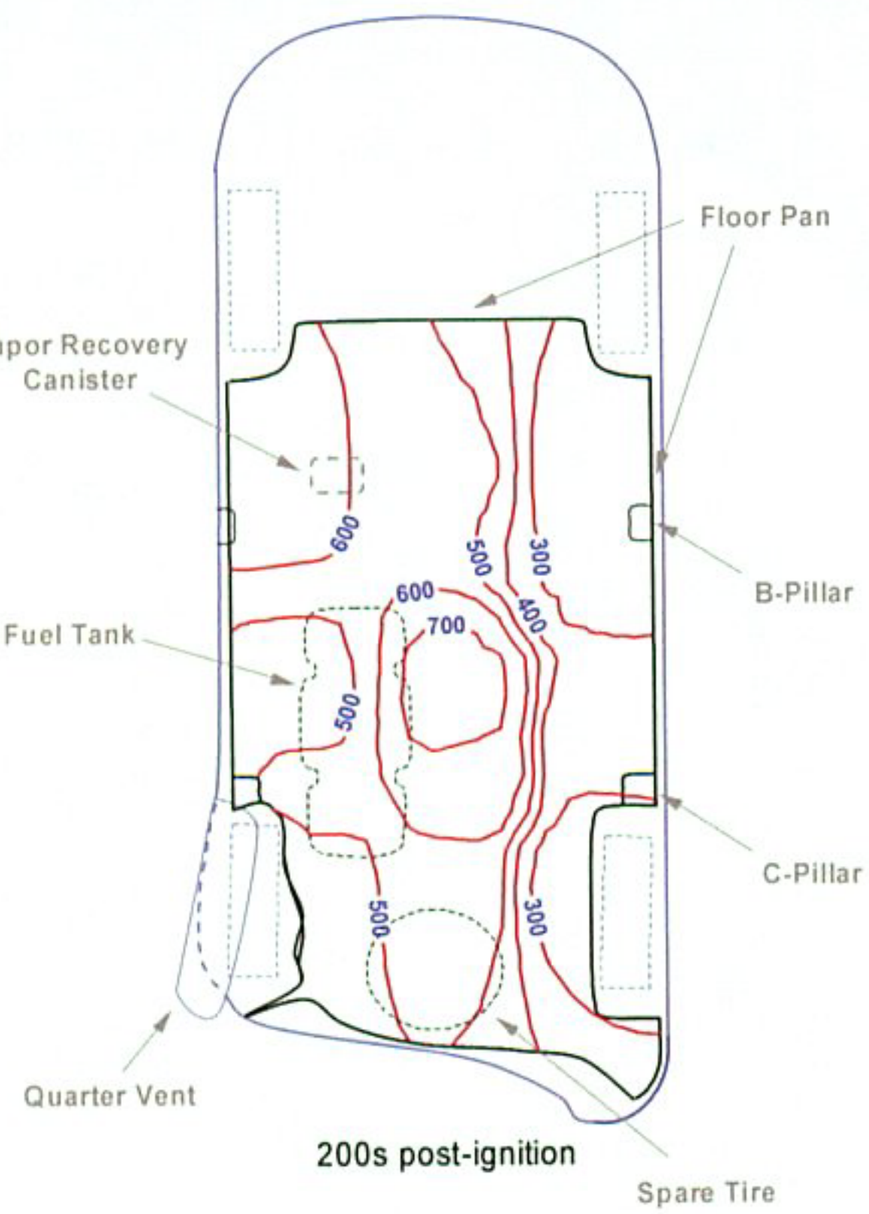


200s post-ignition

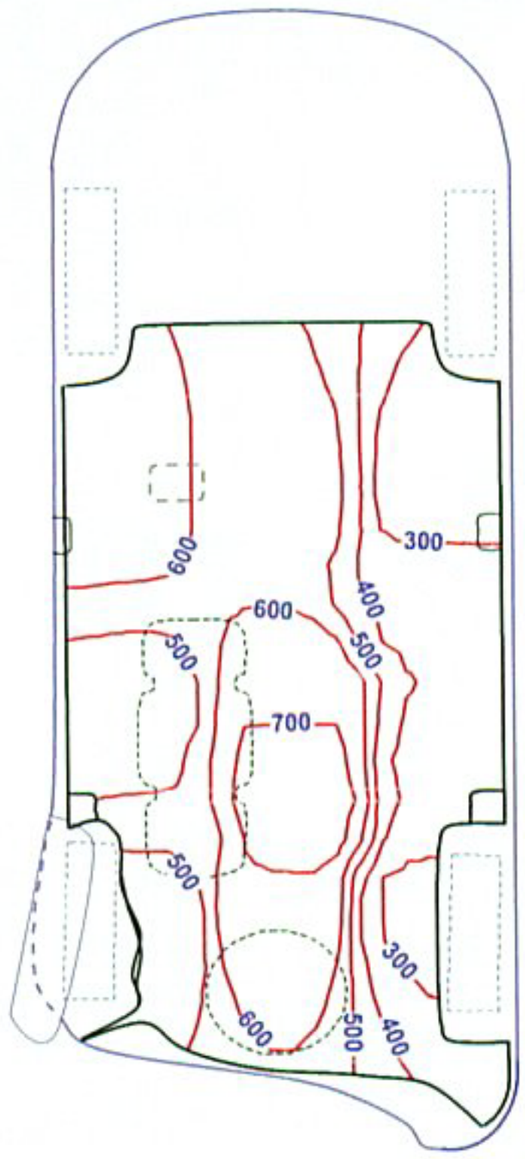


205s post-ignition

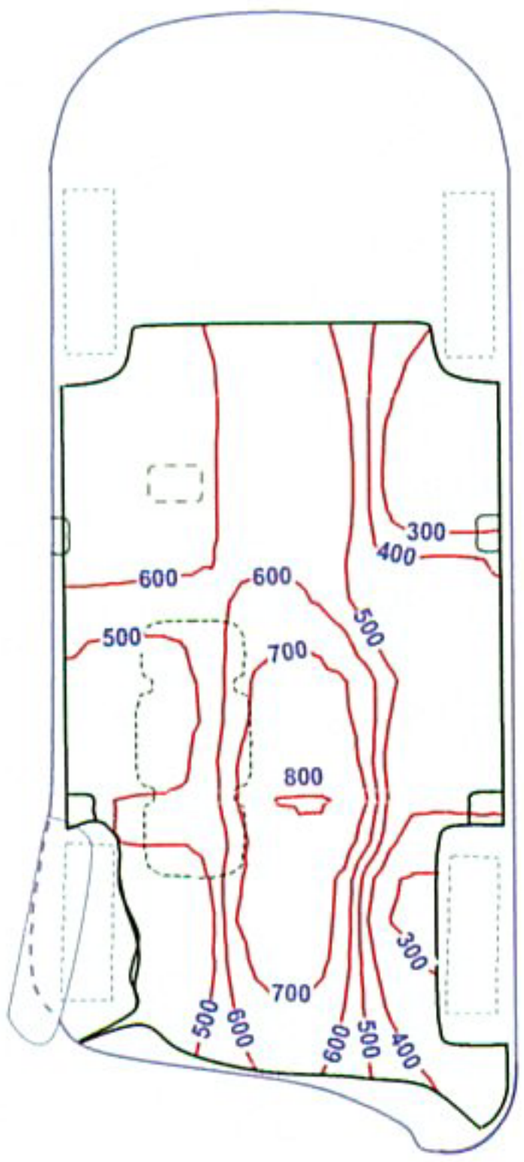


210s post-ignition

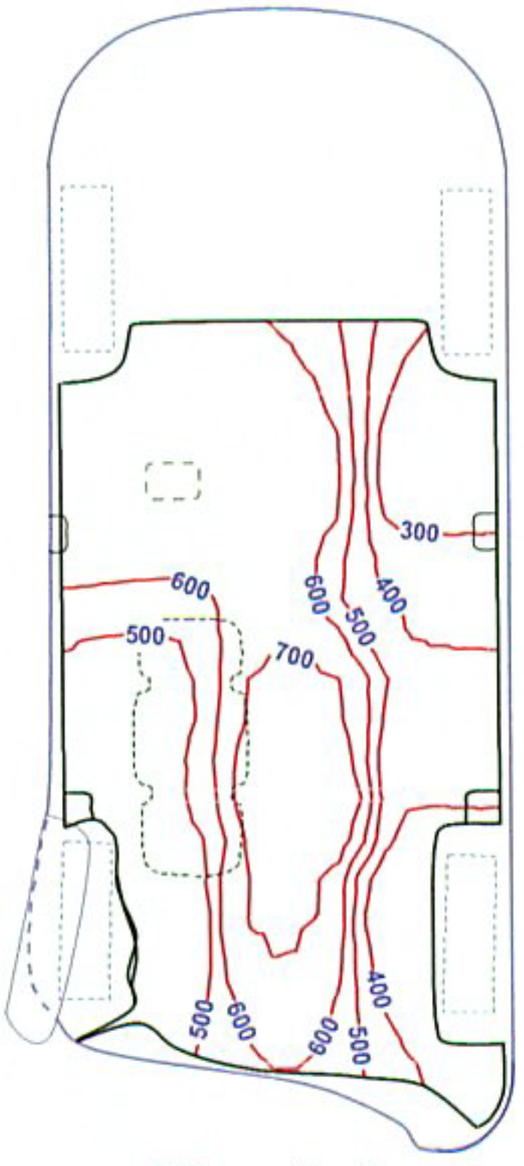


215s post-ignition

Figure 16, continued. Fire Test F961116. Isothermal contour plots showing temperature profiles estimated from the responses of the C-thermocouples.

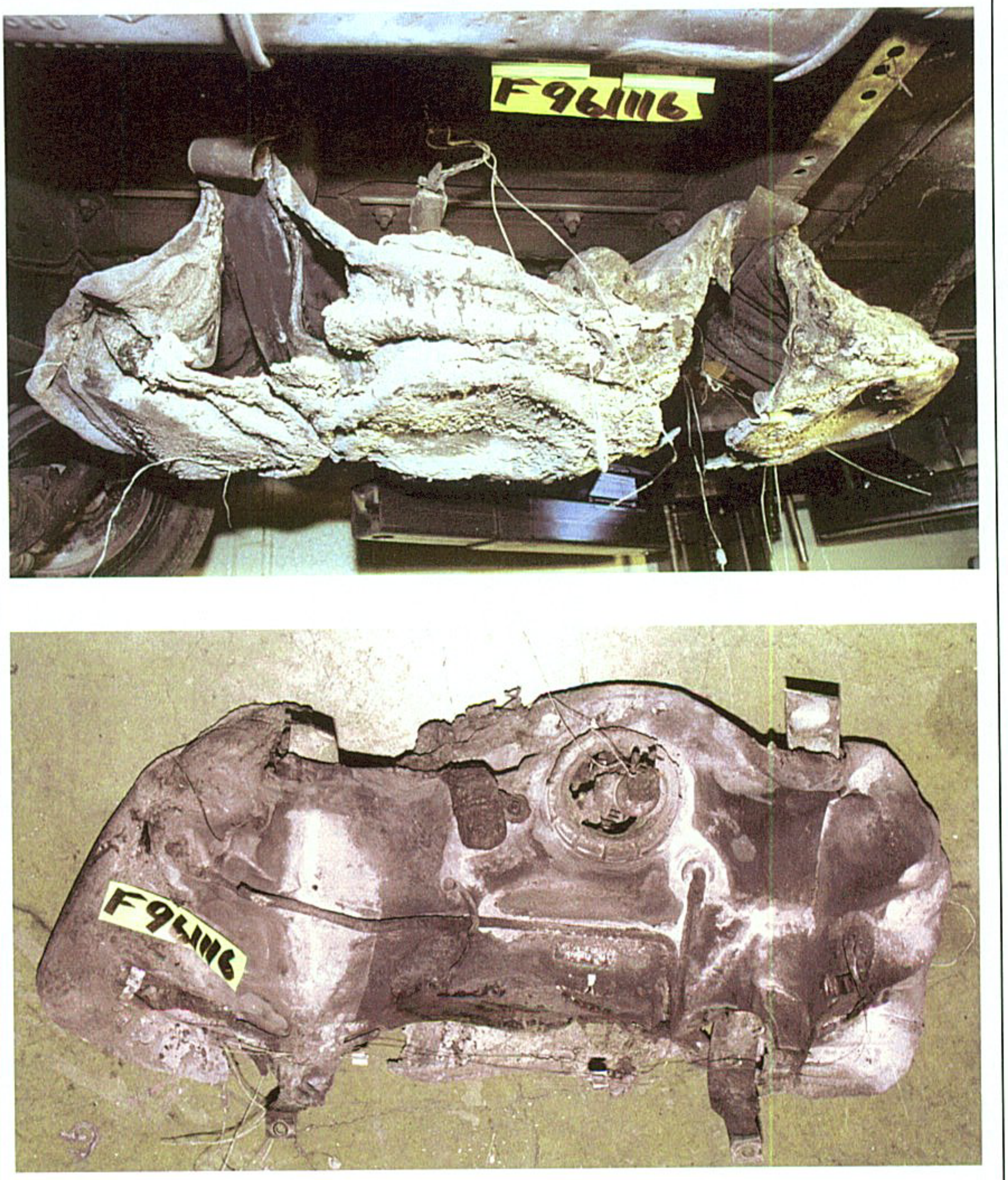


Figure 17. Fire Test F961116. Photographs of the fuel tank after the fire test: an inboard side-view of the fuel tank in place on the test vehicle (upper) and a top-view of the fuel tank removed from the test vehicle (lower).

With no liquid contacting the upper portion of the fuel tank, the poly(ethylene) resin would have eventually softened and melted when exposed to heat from the flames.

Inspection of the fuel tank after this test revealed that the exterior surface of the bottom of the tank was melted and charred, but the interior surface was not melted or charred. Two sections were missing from the bottom of the tank, where the fuel tank straps appeared to have contracted when sprayed with water after the test and tore the softened plastic (Fig. 17). The top of the fuel tank also was charred, with some areas showing signs of having melted and flowed. Holes were observed in the fuel pump flange where it had been consumed by fire (Fig. 17). A single hole was observed in the side of the upper panel of the fuel tank just below and forward the fuel pump flange (Fig. 17). The holes in the fuel pump flange and the side of the fuel tank were above the level of the liquid gasoline in the fuel tank at the start of the test, and were at the apparent origin of the flame jet observed between 200 and 205 seconds post-ignition. These results suggest that gasoline vapor issuing from one or more holes that developed in the fuel tank above the liquid level caused the increase in flame volume and intensity under the test vehicle observed between 200 and 205 seconds post-ignition

An increase in the size of the fire immediately to the left of the test vehicle occurred at approximately 213 seconds post-ignition (Fig. 18). This cause of this appears to have been combustible solid material, that was already burning, falling from the left side of the vehicle. Possible sources of this material could have been the rocker molding or the molding on the left quarter panel.

It was difficult to determine when the fire damage occurred to many of the melted or charred components on the exterior of the test vehicle because the fire was not extinguished immediately after the signal to end this test was given. At first, a fine water mist was used to extinguish the fire in the interior of the vehicle. The residual gasoline in the fuel tank, estimated to have been about 9½ gallons at the end of the test, appeared to have spilled shortly after the commencement of fire suppression. Approximately 60 pounds of dry chemical was expended in an unsuccessful attempt to extinguish the burning gasoline confined to the area around the test vehicle by the fluid containment pan. The gasoline pool re-ignited several times after the fire was extinguished with the dry chemical. The fire was finally extinguished with water from a large fire hose (diameter = 3 in.), which cooled hot metal on the under-side of the vehicle and prevented re-ignition of the gasoline vapor.

Figure 18. Fire Test F961116. Video stills from Camera 1 at 210 (upper) and 213 (lower) seconds post-ignition.

## 5 Flame-Spread into the Passenger Compartment

Flames and hot gas flowed across the bottom and up around the sides of the fuel tank. Because of a slight upward tilt of the vehicle toward its left rear corner, the fire plume was channeled rearward between the left frame rail and the left rocker, into the left rear wheel house (Fig. 19). Flames began to emerge in the wheelhouse between 10 and 15 seconds post-ignition, impinging directly upon the wheelhouse splash shield.[8] Material was observed dripping from the splash shield approximately 60 seconds post-ignition.

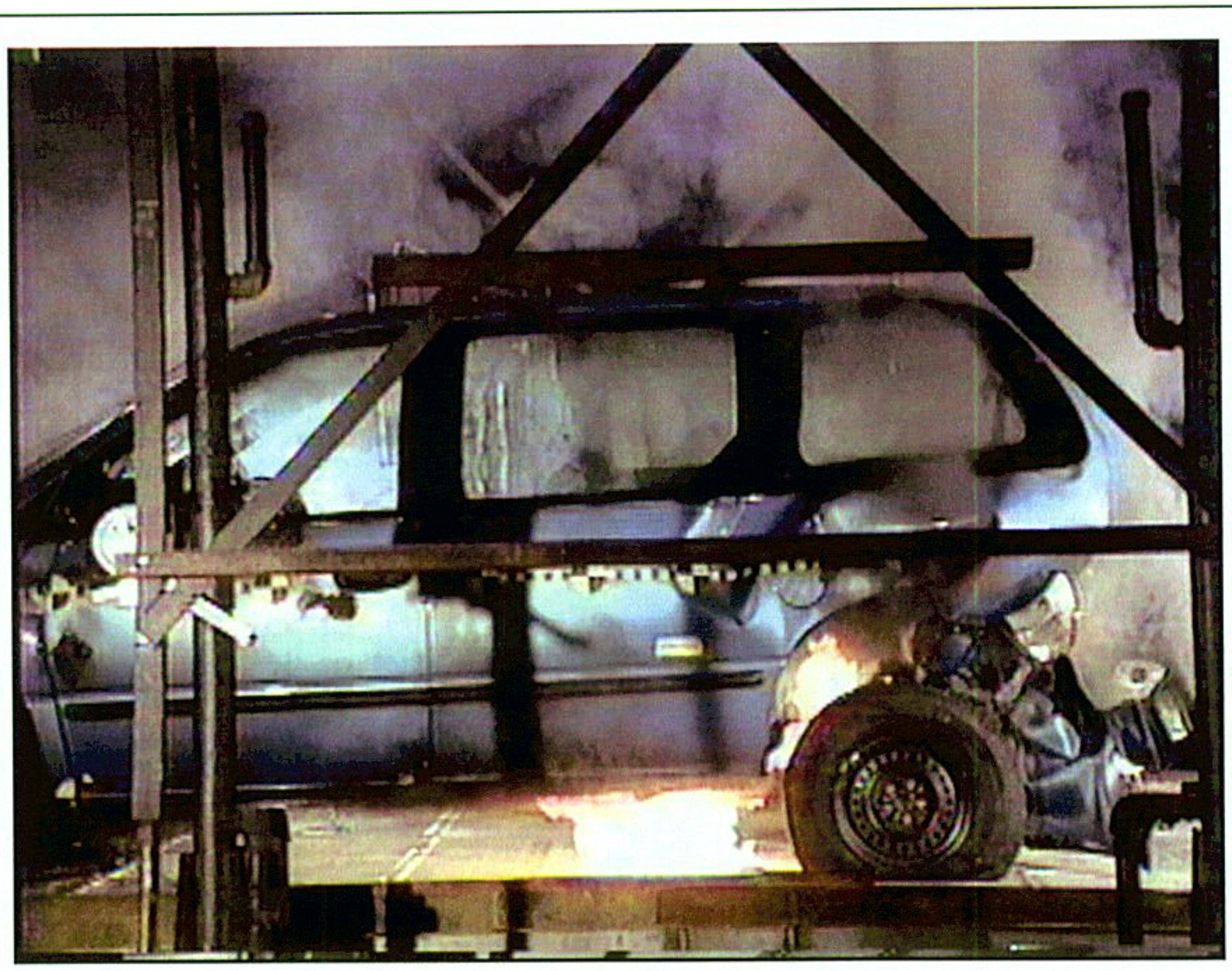

Figure 19. Fire Test F961116. Video still from Camera 2 at 30 seconds post-ignition showing flames spreading radially along the lower surface of the fuel tank, and channeled into the left rear wheelhouse.

[8] The wheelhouse splash shield in the test vehicle was poly(propylene) with approximately 2% inorganic filler. This material had a melting point of 166°C. The major thermal decomposition of this material occurred at 310°C, and the secondary thermal decomposition temperature occurred at 368°C [8]. The splash shield was about 2 mm thick and covered approximately the front half of the wheel house.

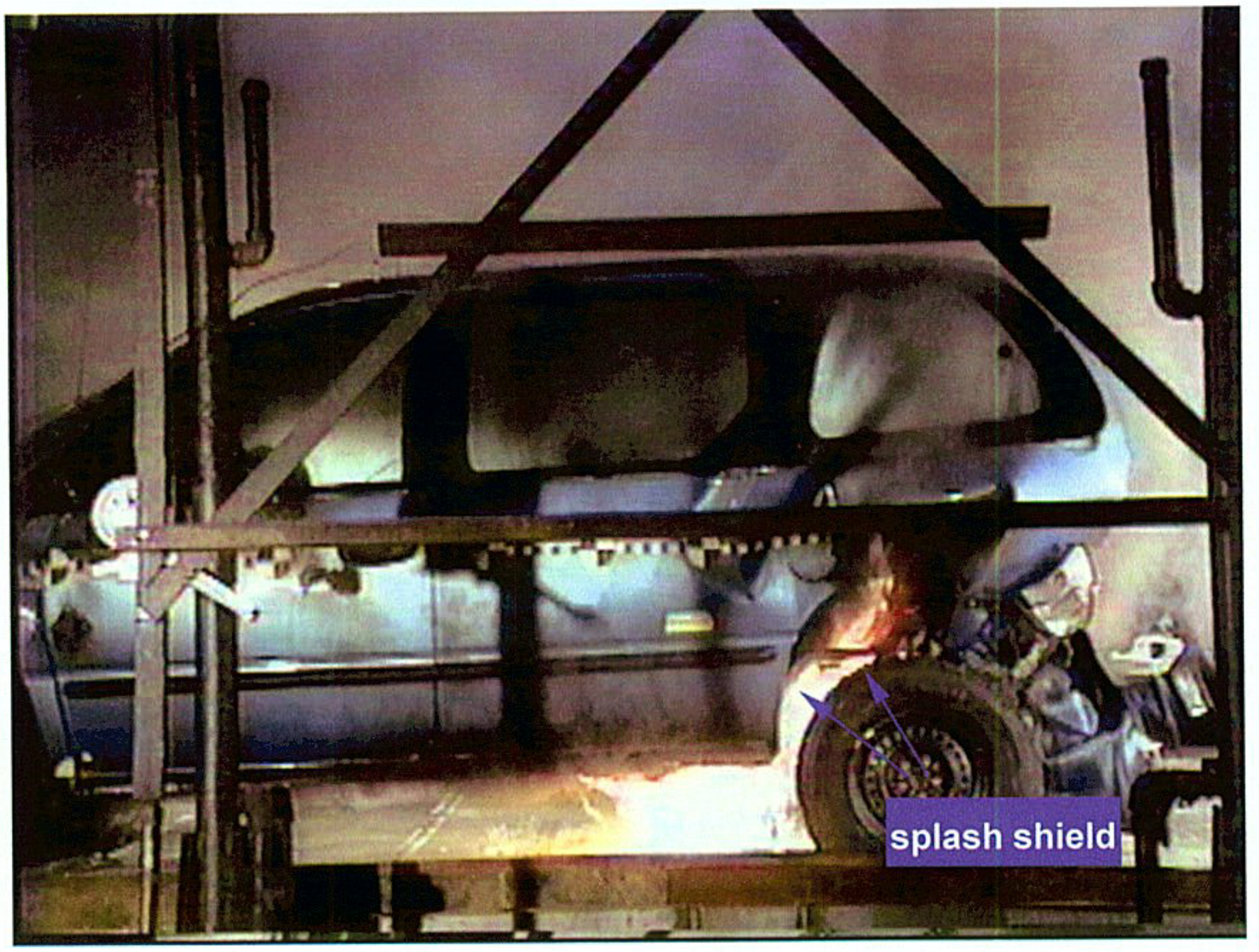


Figure 20. Fire Test F961116. Video still from Camera 2 at 75 seconds post-ignition showing wheelhouse splash shield melting and sagging onto the left rear tire (arrows).

The splash shield sagged onto the left rear tire between 60 and 90 seconds post-ignition (Fig. 20). The upper surface of the left rear tire appeared to ignite between 120 and 140 seconds post-ignition. Early involvement of the wheelhouse splash shield and left rear tire in the fire concentrated flames in the left rear wheelhouse. Flames entered the passenger compartment through the split weld-seams around the left rear wheelhouse and through the left quarter vent.

### 5.1 Flame-Spread through the Split Weld-Seams Around the Rear Left Wheelhouse

Figures 21 through 25 show a series of video stills from Cameras 2 and 6 at -10, 15, 50, 100, and 150 seconds post-ignition. Smoke and flames obscured the left rear wheelhouse shortly after the gasoline pool was ignited. Objects in the exterior and interior of the test vehicle are discernable in Figure 21, which shows video stills from Cameras 2 and 6 before ignition of the gasoline pool.

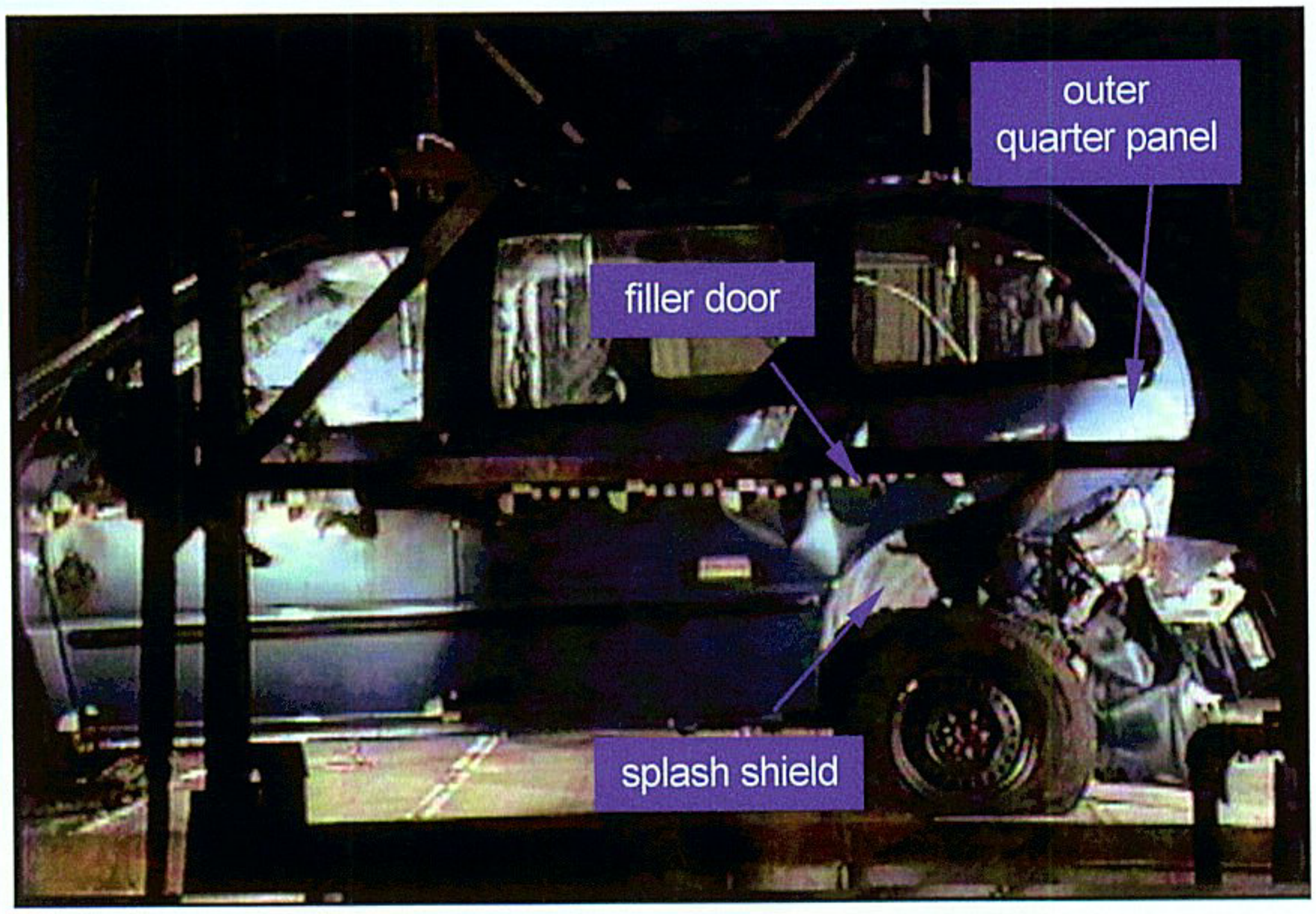


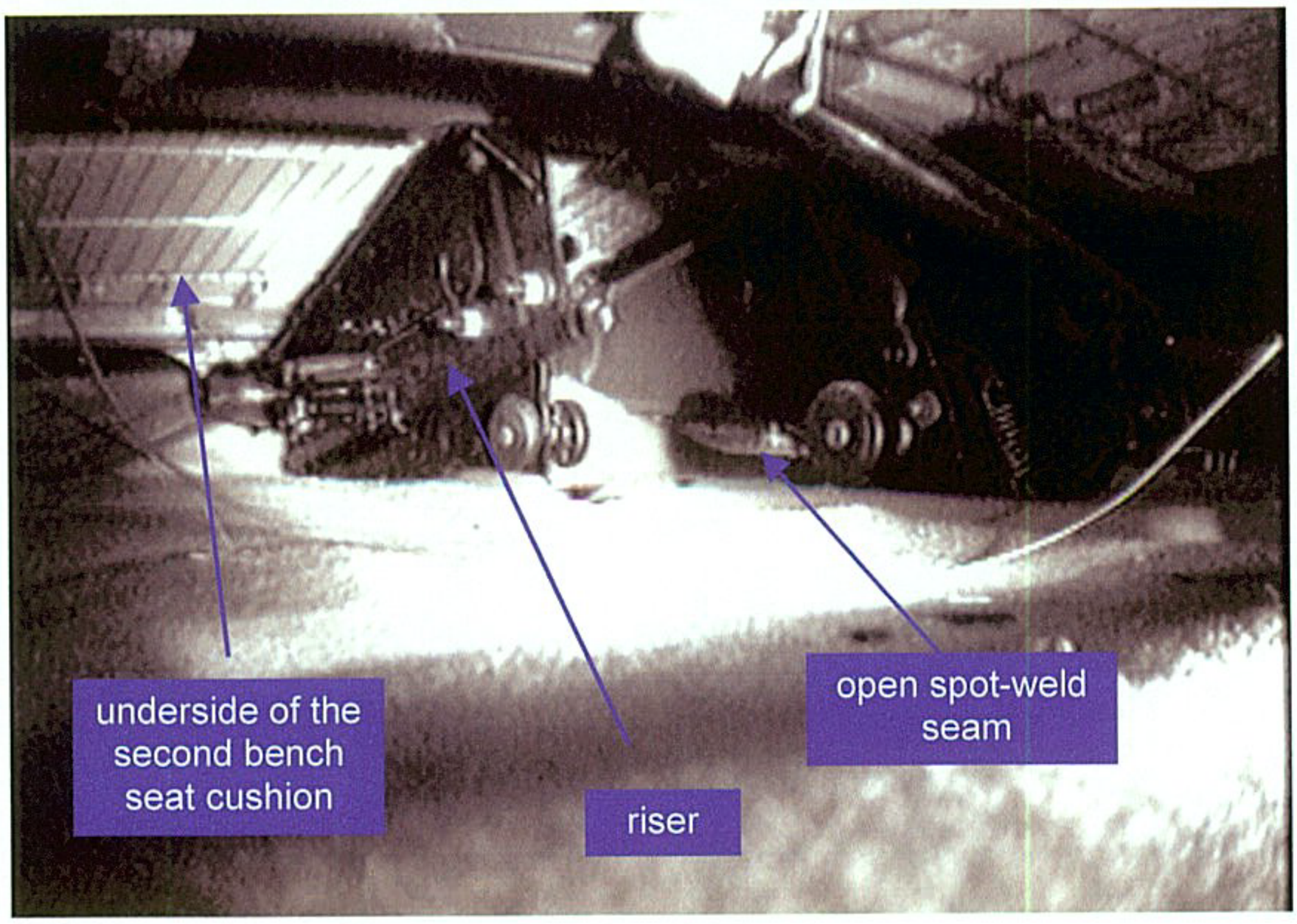


Figure 21. Fire Test F961116. Video stills from Camera 2 (upper) and Camera 6 (lower) 10 seconds before the gasoline pool was ignited.

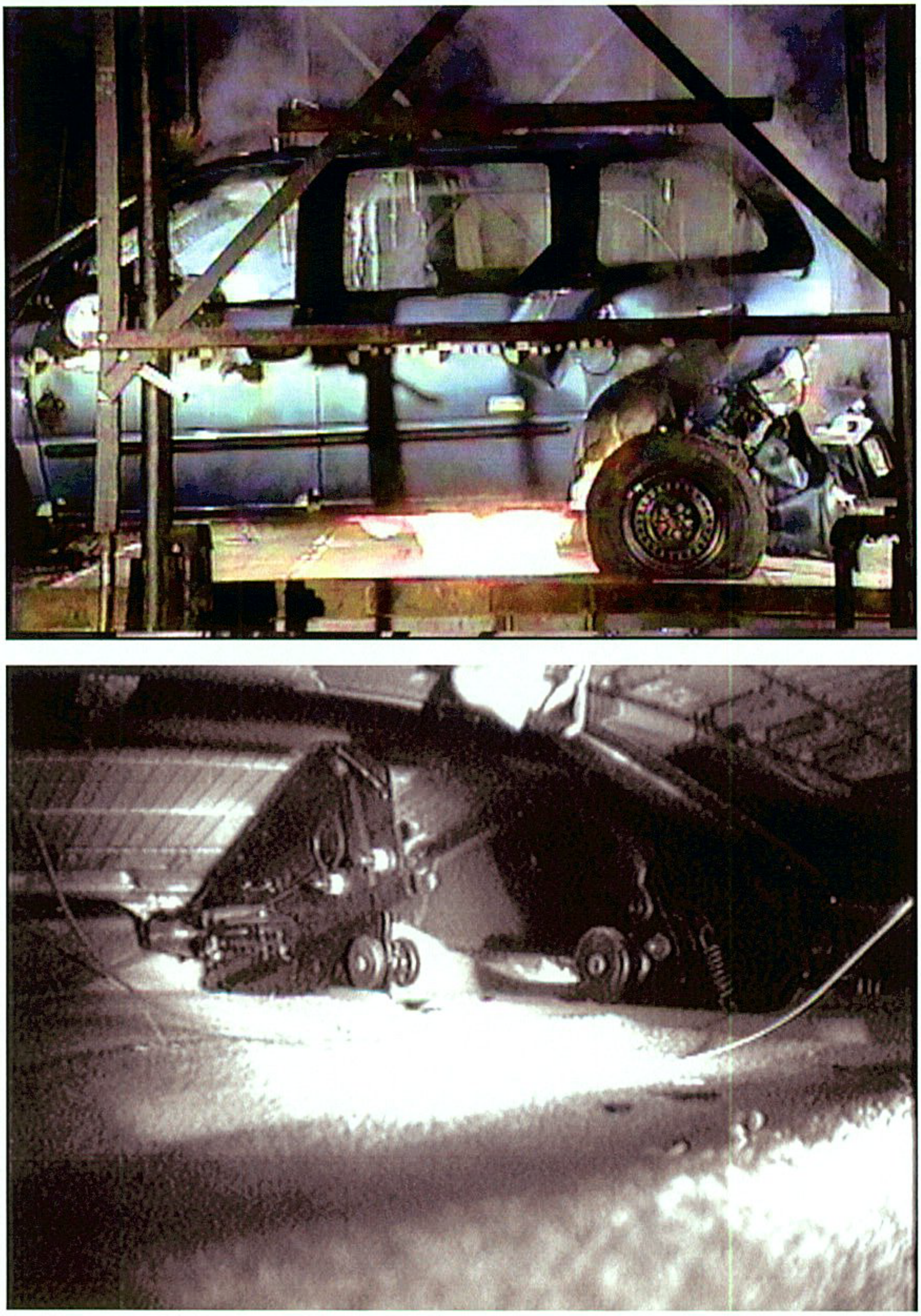

Figure 22. Fire Test F961116. Video stills from Camera 2 (upper) and Camera 6 (lower) at 10 seconds post-ignition.

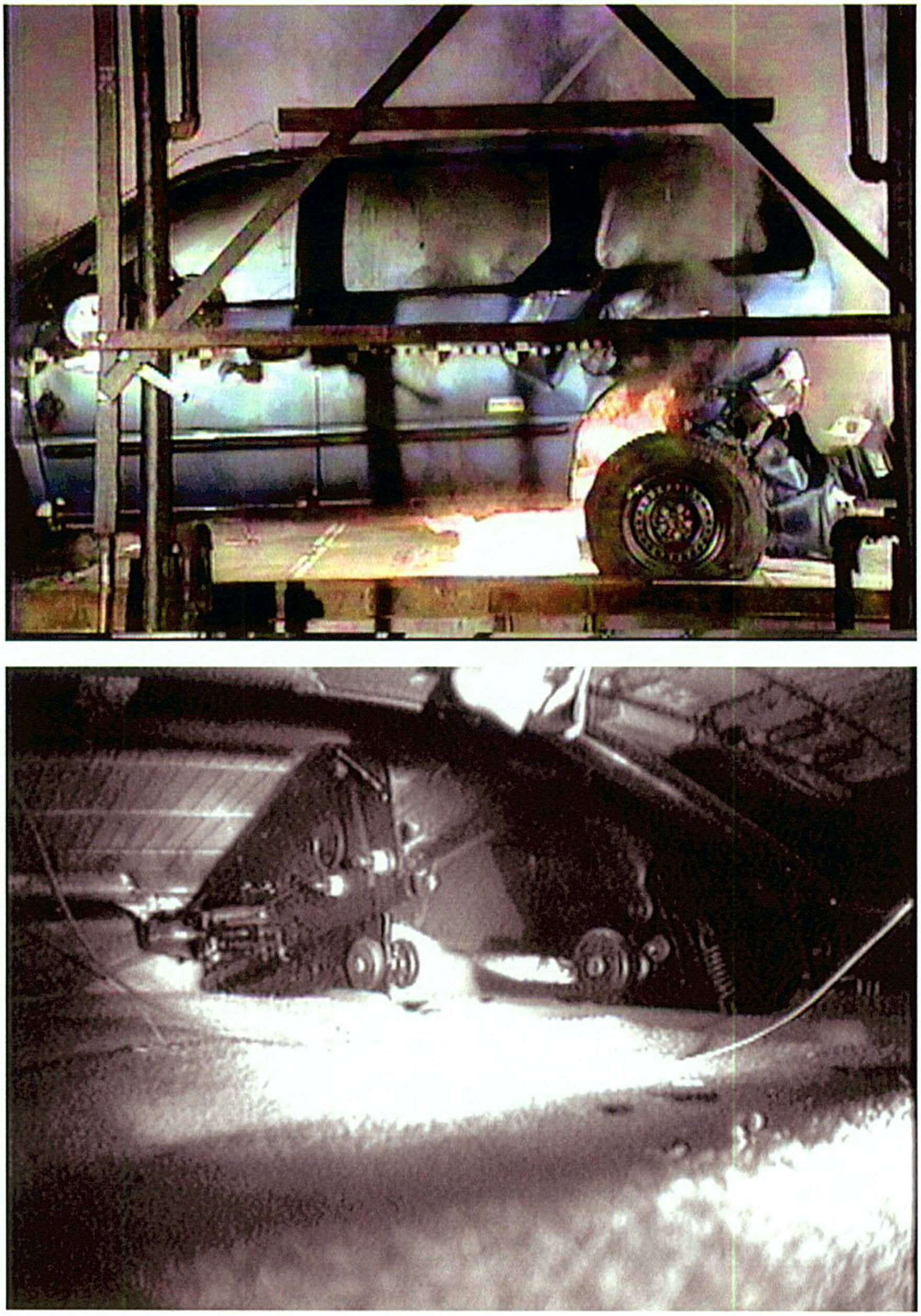

Figure 23. Fire Test F961116. Video stills from Camera 2 (upper) and Camera 6 (lower) at 50 seconds post-ignition.

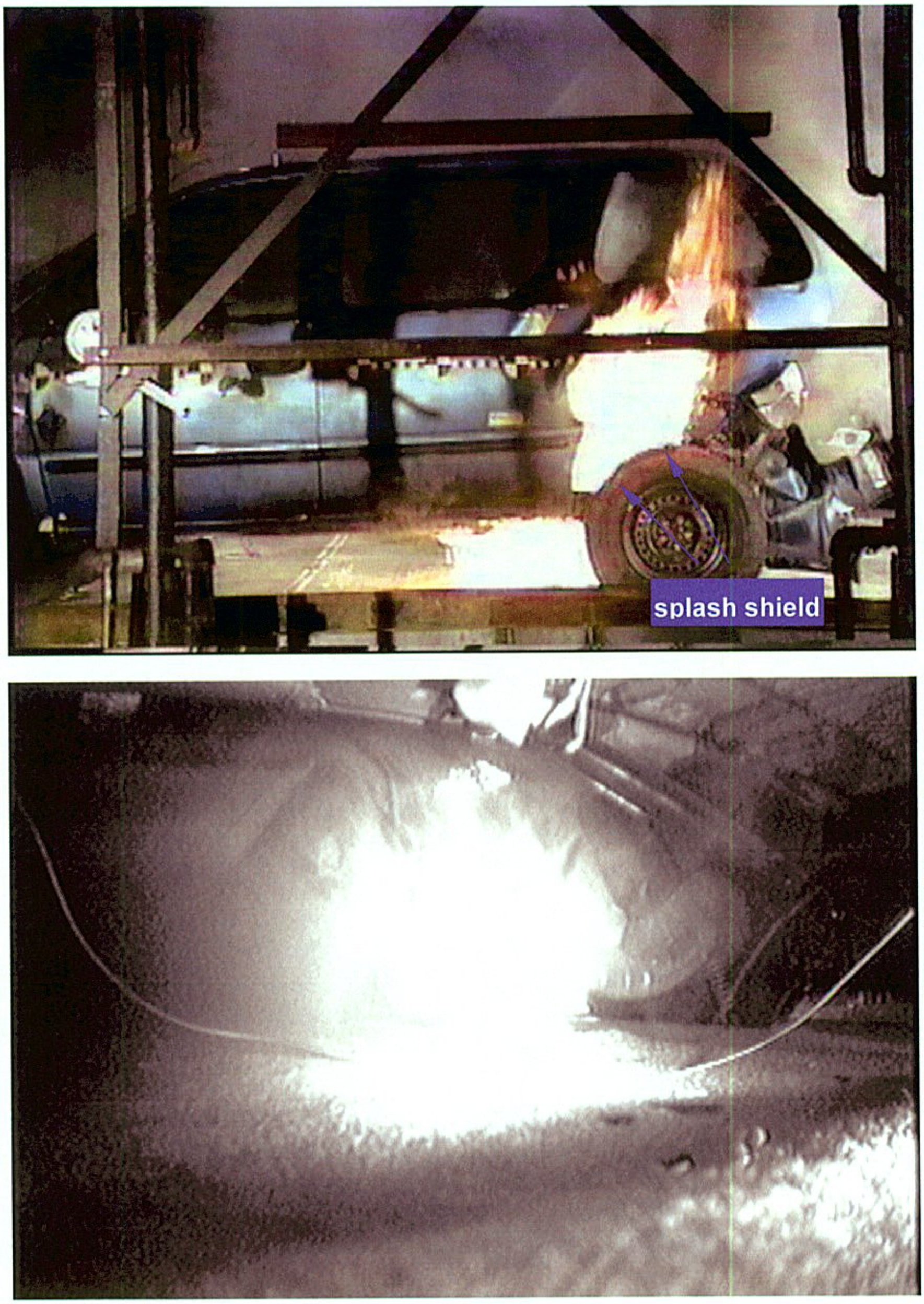


Figure 24. Fire Test F961116. Video stills from Camera 2 (upper) and Camera 6 (lower) at 100 seconds post-ignition.

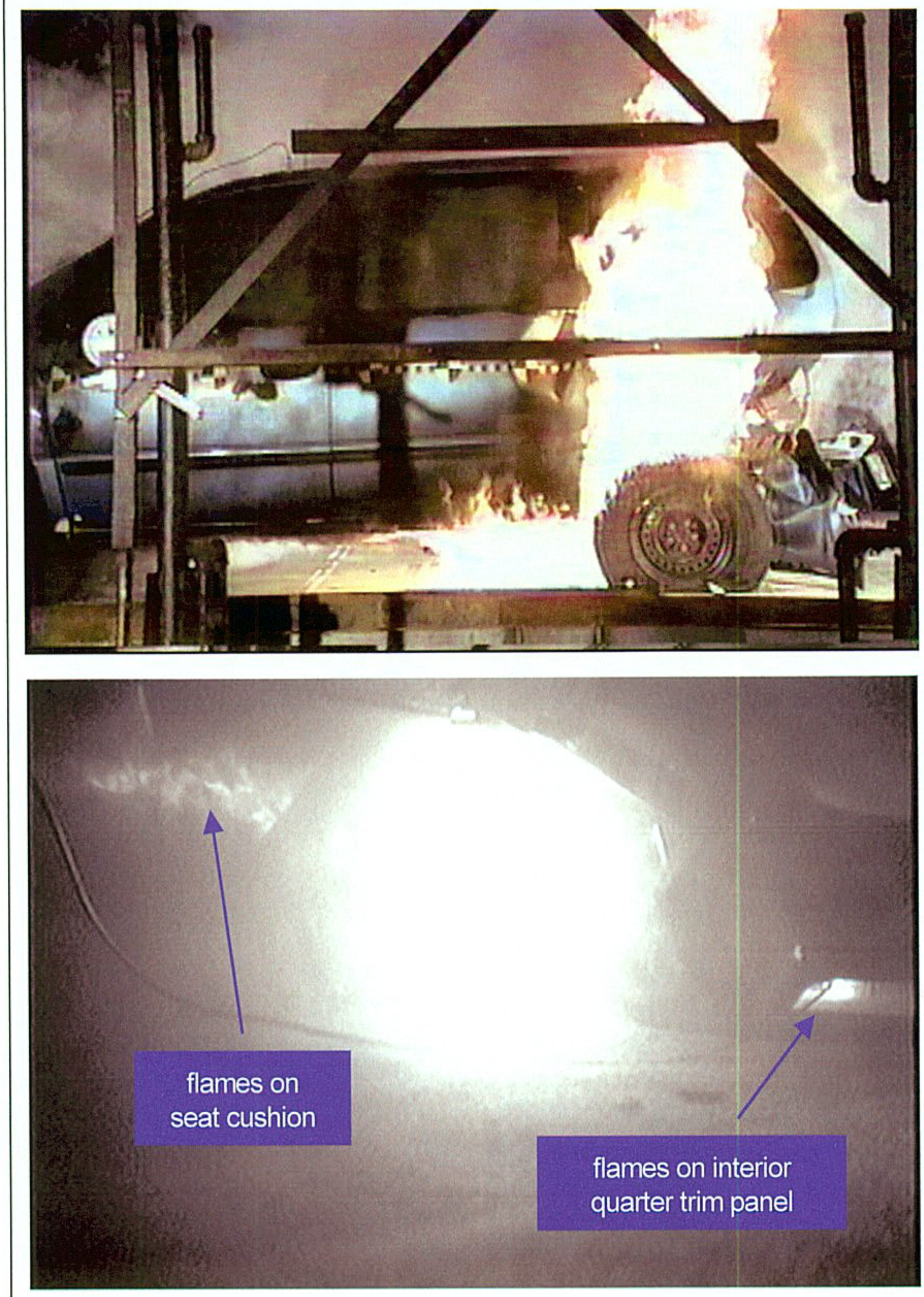


Figure 25. Fire Test F961116. Video stills from Camera 2 (upper) and Camera 6 (lower) at 150 seconds post-ignition.

The filler door, wheelhouse splash shield, and inner wheelhouse panel are visible in the view from Camera 2 (Fig. 21, upper video still). Camera 6, which was located on the carpet under the middle bench seat, provided an interior-view of the lower portion of the left rear wheelhouse and floor pan (Fig 21, lower video still). The left riser and track under the second bench seat blocked the view of the left quarter trim panel covering the rear section of the wheelhouse. A section of the open spot weld seam between the lower edge of the wheelhouse side panel and the floor pan was visible.

Flames entered the left rear wheelhouse between 10 and 15 seconds post-ignition (Fig. 22). Although the diameter of the pool fire remained constant for the first 90 seconds of the test, the fire plume in the wheelhouse increased in size during this time (Fig. 23). Flames were visible through the open spot weld seam along the lower edge of the wheelhouse side panel, but did not appear to have spread into the passenger compartment (Fig. 23). As the wheelhouse splash shield sagged onto the left rear tire and started to burn, the fire in the left rear wheelhouse grew substantially (Fig. 24). The intensity of light in the area of the open weld-seam increased during this time (Fig. 24). Details that were visible during the first 50 seconds of the test were now lost when a large area of the field-of-view of Camera 6 became overexposed (Fig.'s 24 and 25). By 100 seconds post-ignition, it was difficult to distinguish between flames actually inside the passenger compartment and light scattered by smoke entering the split spot weld seam (Fig. 24). At 150 seconds post-ignition, flames were discernable in the area around the lower edge of the wheelhouse under the left side of the second bench seat, and along the lower edge of the left quarter trim panel in front of the middle bench seat riser and track (Fig. 25).

The openings at the rear of the wheelhouse (*i.e.*, the open spot weld seam between the rear of the wheelhouse and the left quarter panel and the open spot weld seam between the inner and outer wheelhouse panels) were not in the fields-of-view of either Camera 2 or Camera 6. Flame-spread into the passenger compartment through either of these openings would not have been visible in the video stills shown in Figures 21 through 25.

The exact timing of flame-spread through the split spot weld seam was difficult to determine by examination of the video records alone. Temperature, heat-flux, and pressure data were used to determine the time of flame spread into the passenger compartment. Figure 26 shows the locations of five thermocouples and one heat-flux transducer/radiometer assembly in the left rear wheelhouse of the test vehicle.

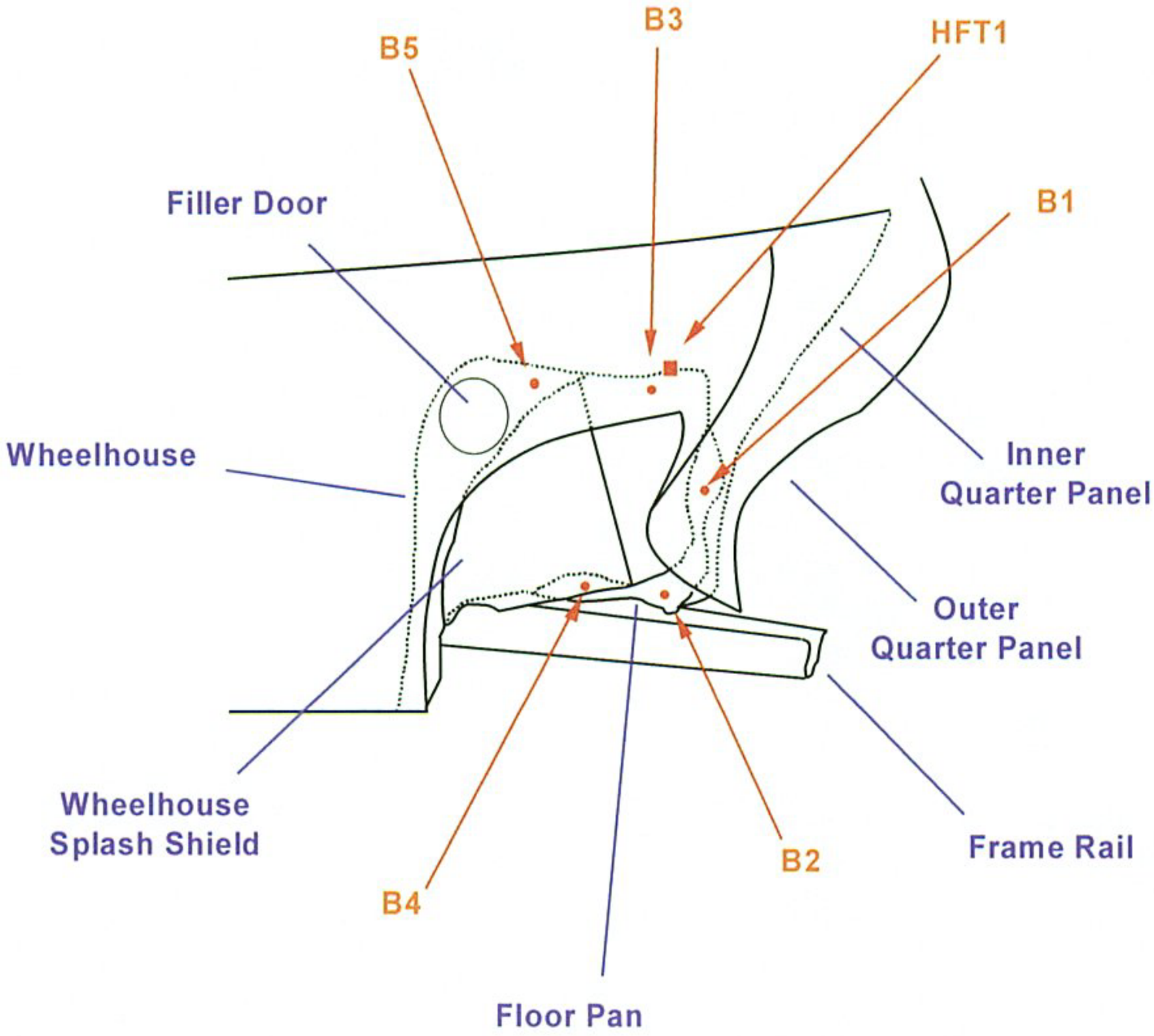


Figure 26. Fire Test F961116. Diagram of the left rear wheelhouse of the test vehicle. The wheelhouse splash shield was a poly(propylene) panel that covered the front of the wheelhouse. Thermocouple B1 was located in an split section of the weld-seam between the wheelhouse and interior quarter panel. Thermocouples B2 and B4 were located in an split section of the weld-seam between the wheelhouse and floor pan. Thermocouple B3 was located in the rear of the wheelhouse, extending approximately 1 cm below its upper, exterior surface. Thermocouple B5 was located in the front of the wheelhouse, extending approximately 1 cm below its upper, exterior surface. Before it melted and sagged onto the tire, the wheelhouse splash shield covered Thermocouple B5. Heat-flux Transducer 1 (HFT1) was inserted through the upper surface of the wheelhouse, rearward of the wheelhouse splash shield.

Thermocouples were placed at three locations in the openings created by split spot weld seams (Fig. 26). Two thermocouples and one heat flux transducer/radiometer assembly were placed just below the upper surface of the wheelhouse to monitor the intensity of the fire plume in the wheelhouse (Fig. 26).

Hot gas started to accumulate in the left rear wheelhouse before the fire plume from the burning gasoline pool entered the wheelhouse. Temperatures recorded by Thermocouples B3 and B5 started to increase shortly after the gasoline pool was ignited (Fig. 27), before flames were visible in the lower front section of the wheelhouse, but remained less than 500°C for the first 60 seconds of this test. [9] A net positive heat flux to the upper surface of the wheelhouse panel also was recorded approximately 5 seconds after the gasoline pool was ignited, but remained less than 20 $kW/m^2$ for the first 70 seconds post-ignition (Fig. 27).

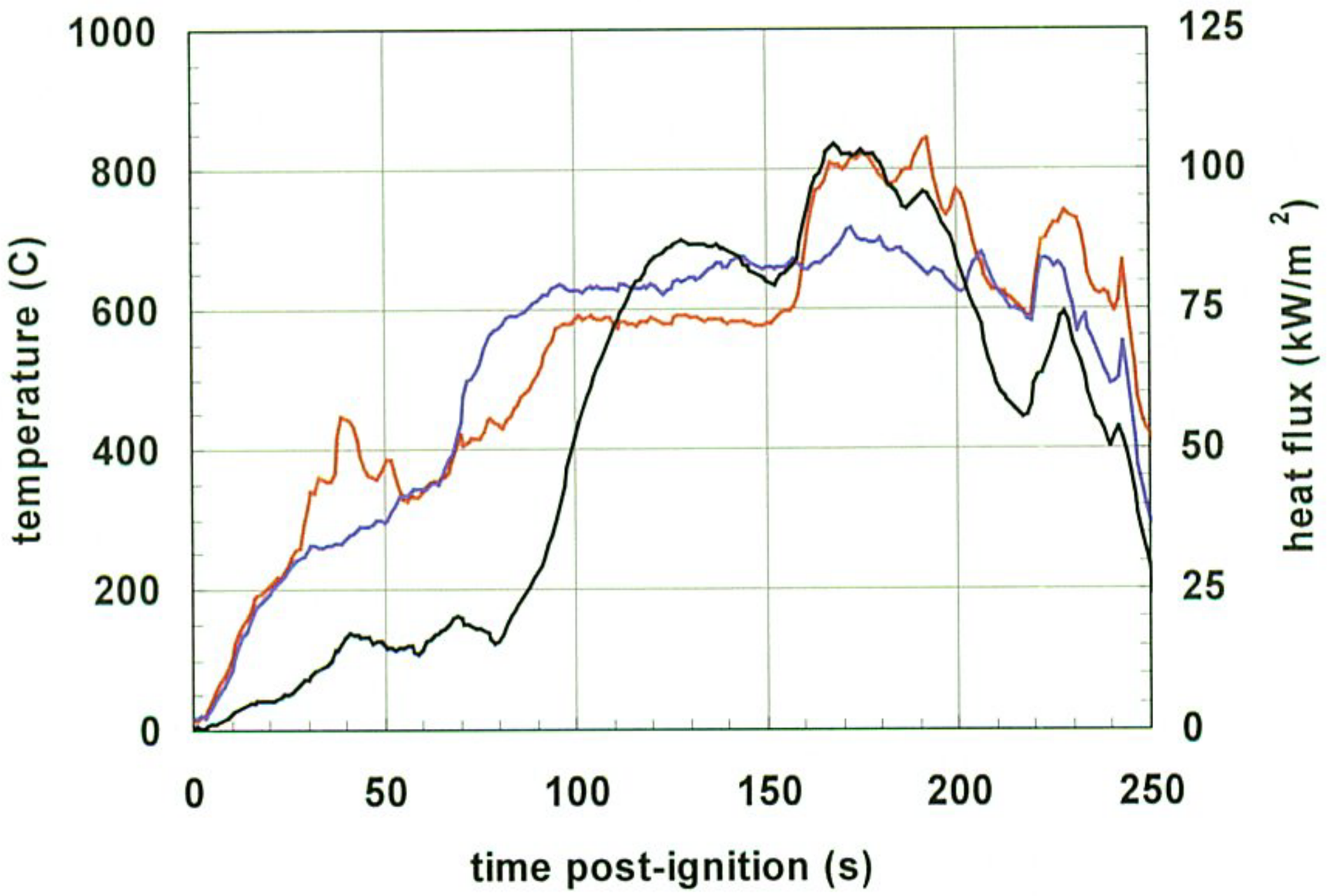


Figure 27. Fire Test F961116. Plots of temperatures recorded by Thermocouples B3 (—, left axis) and B5 (—, left axis), and heat flux recorded by HFT1 (—, right axis).

[9] In this report, one of the criteria for assessing the presence of flame is a thermocouple reading of 600°C or greater

Ignition of combustible material located in the wheelhouse, namely the wheelhouse splash shield, resulted in a large increase in heat transfer to the wheelhouse panels. As the splash shield sagged onto the tire and ignited between 60 and 90 seconds post-ignition, flames began to fill the left rear wheelhouse (see Fig.'s 23 and 24). Temperatures recorded by Thermocouples B3 and B5 increased rapidly to approximately 600°C during this time interval (Fig. 27). The heat flux to the top of the wheelhouse showed a similar trend, increasing to approximately 85 kW/m$^2$ between 80 and 120 seconds post-ignition (Fig 27).

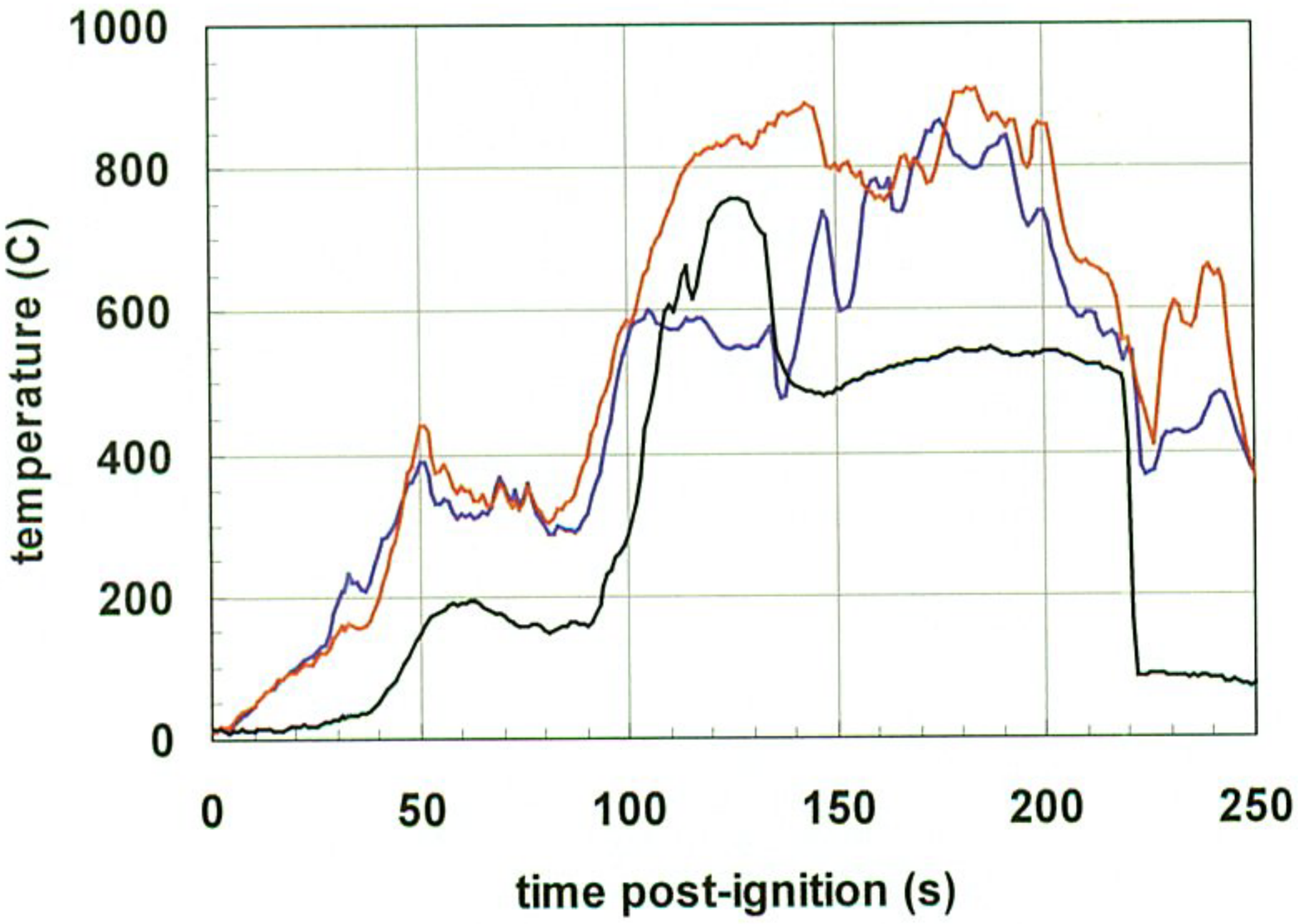


Figure 28. Fire Test F961116. Plots of temperatures recorded by thermocouples B1 (—), B2, (—) and B4 (—).

Data from Thermocouples B1, B2, and B4 indicate that flames first entered the passenger compartment through the osplit spot weld seams around the left rear wheelhouse between 80 and 120 seconds post-ignition. Hot gases also started to enter the passenger compartment through these openings shortly after the gasoline pool was ignited (Fig. 28). Thermocouples B1 and B2 recorded temperatures in the range of 300 to 400°C between 50 and 90 seconds post-ignition (Fig. 28), while Thermocouple B4, which was behind the wheelhouse splash shield (see Fig. 26), recorded temperatures of < 200°C.

Thermocouples B1 and B2 recorded rapid temperature increases between 80 and 120 seconds post-ignition, with Thermocouple B1 recording a temperature of greater than 800°C and Thermocouple B2 recording a temperature of slightly less than 600°C at 120 seconds post-ignition (Fig. 28). Thermocouple B4 recorded a rapid temperature increase between 90 and 130 seconds post-ignition, recording a temperature of approximately 750°C at 130 seconds post-ignition.

### 5.2 Flame-Spread through the Left Quarter Vent

Although the fire plume was approximately ½ the height of the test vehicle by 50 seconds post-ignition (Fig. 29), it had not extended laterally beyond the left rocker panel or the outer edge of the left wheelhouse.

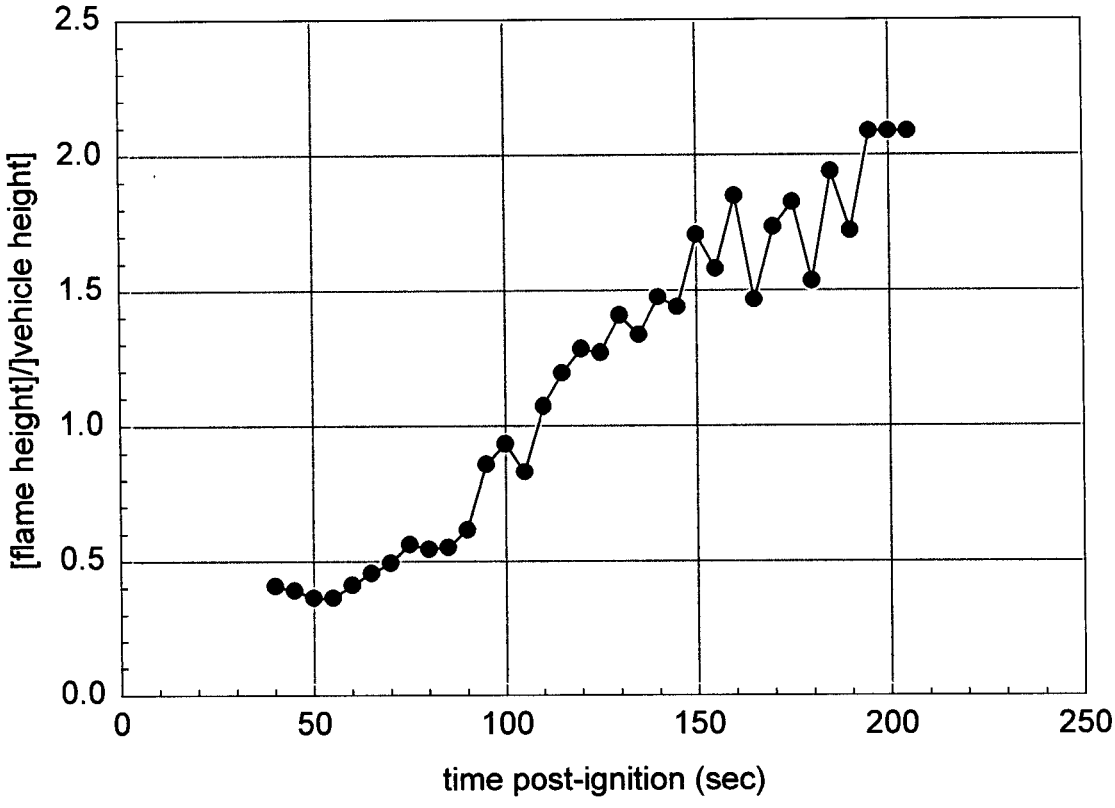


Figure 29. Fire Test F961116. Plot of the height of the fire plume versus time post-ignition. The height of the fire plume was the distance from the simulated road surface below the test vehicle to the highest extension of flame visible in the video from Camera 1.

As the splash shield sagged onto the tire and ignited between 60 and 90 seconds post-ignition, a fire plume was observed outside the left rear wheelhouse (see Fig. 24). Flames spread from the splash shield to the left rear tire between 100 and 150 seconds post- ignition (Fig. 25). An increase in the heat flux to the wheelhouse panels (Fig. 27) indicated that the intensity of the fire in the wheelhouse increased during this time interval. The height of the fire plume emerging from the wheelhouse also increased between 100 and 150 seconds post-ignition (Fig. 29).

The natural buoyancy of the fire plume emerging from the left rear wheelhouse caused the flames to move upward along the contour of the deformed outer left quarter panel (for example, refer to the video still in Figure 30). The tops of the flames reached the lower edge of the quarter vent glass between 100 and 105 seconds post-ignition. As the height of the flame increased further, the left quarter vent glass split the fire plume. Most of the flames were directed to the outside of the vent glass. However, a small fraction of the split fire plume was directed inward, between the vent glass and the quarter panel. Initially the fire plume did not reach the top of the vent glass, and there was no indication that flames entered the passenger compartment through the open vent (video still, Fig. 31). By 130 seconds post-ignition, flames along the interior surface of the vent glass sporadically reached the top of the vent. The angled glass appeared to have directed a portion of the fire plume into the passenger compartment through the left quarter vent (video still, Fig. 32). By 155 seconds post-ignition, the tops of the flames were consistently above the top of the test vehicle, and flames appeared to enter the left quarter vent continuously (video still, Fig. 33). Flames started to spread laterally to the right across the rear of the headlining between 170 and 180 seconds post-ignition (video still, Fig. 34).

### 5.3 Flame-Spread Across the Headlining

Flame-spread across the headlining cannot be attributed solely to the entry of flames through the left quarter vent. Hot gas started to enter the split spot weld seams around the left rear wheelhouse shortly after the gasoline pool was ignited (see Fig. 28). Hot gas rising from this area heated the upper left corner of the back panel of the second bench seat cover and left edge of the window opening in the liftgate. The temperatures of these objects were only slightly greater than the ambient temperature between 50 and 120 seconds post-ignition (Infrared thermograms, Fig.'s 31 and 32). The rising gas would have also heated the left rear corner of the headlining, but this could not be confirmed because the headlining was not in the field-of-view of IR3.

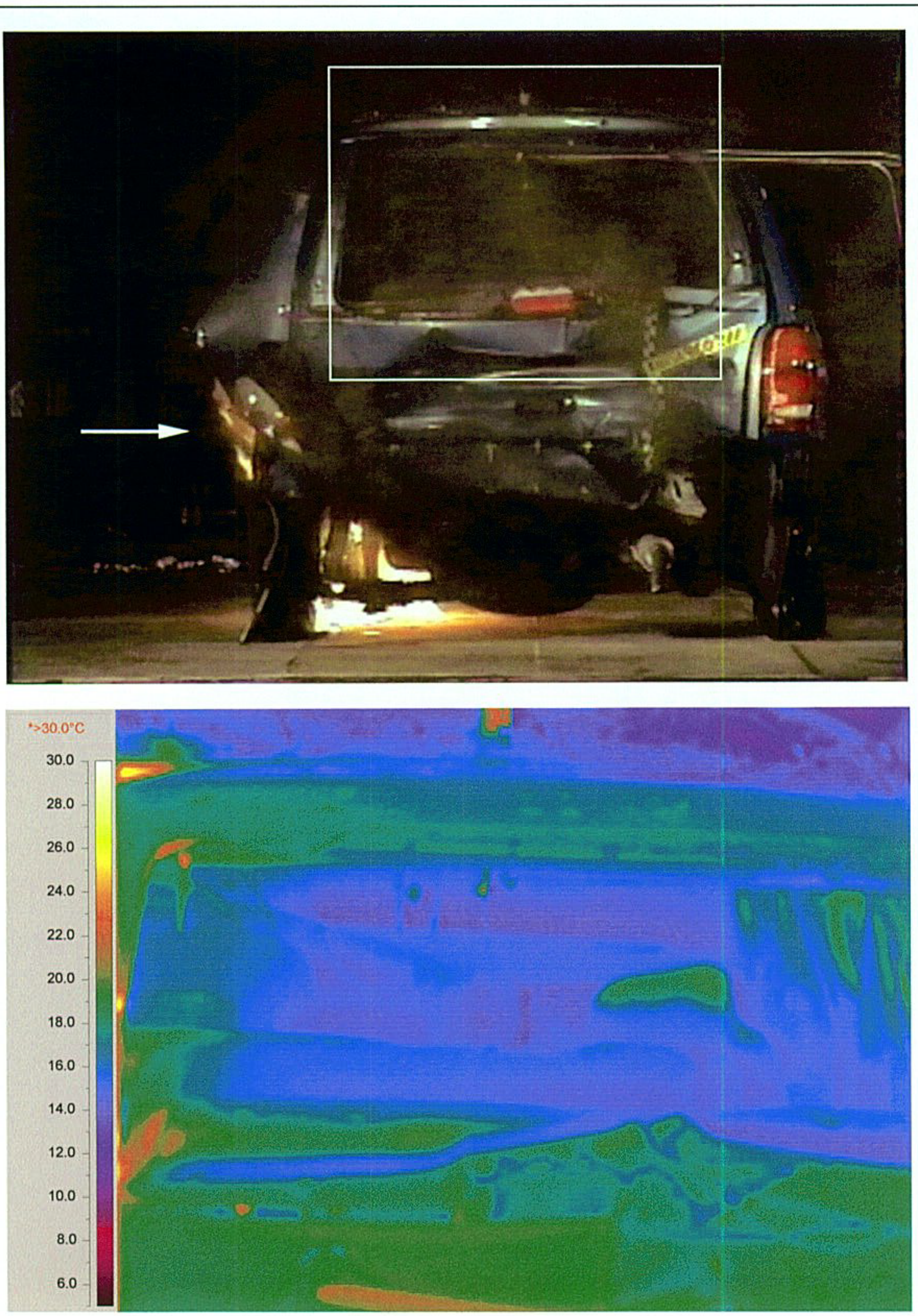


Figure 30. Fire Test F961116. Video still from Camera 1 (upper) and Infrared Thermogram from IR3 (lower) at 80 seconds post-ignition. The box in the video still shows the approximate field-of-view of IR3. The arrow indicates flames in the left rear wheelhouse.

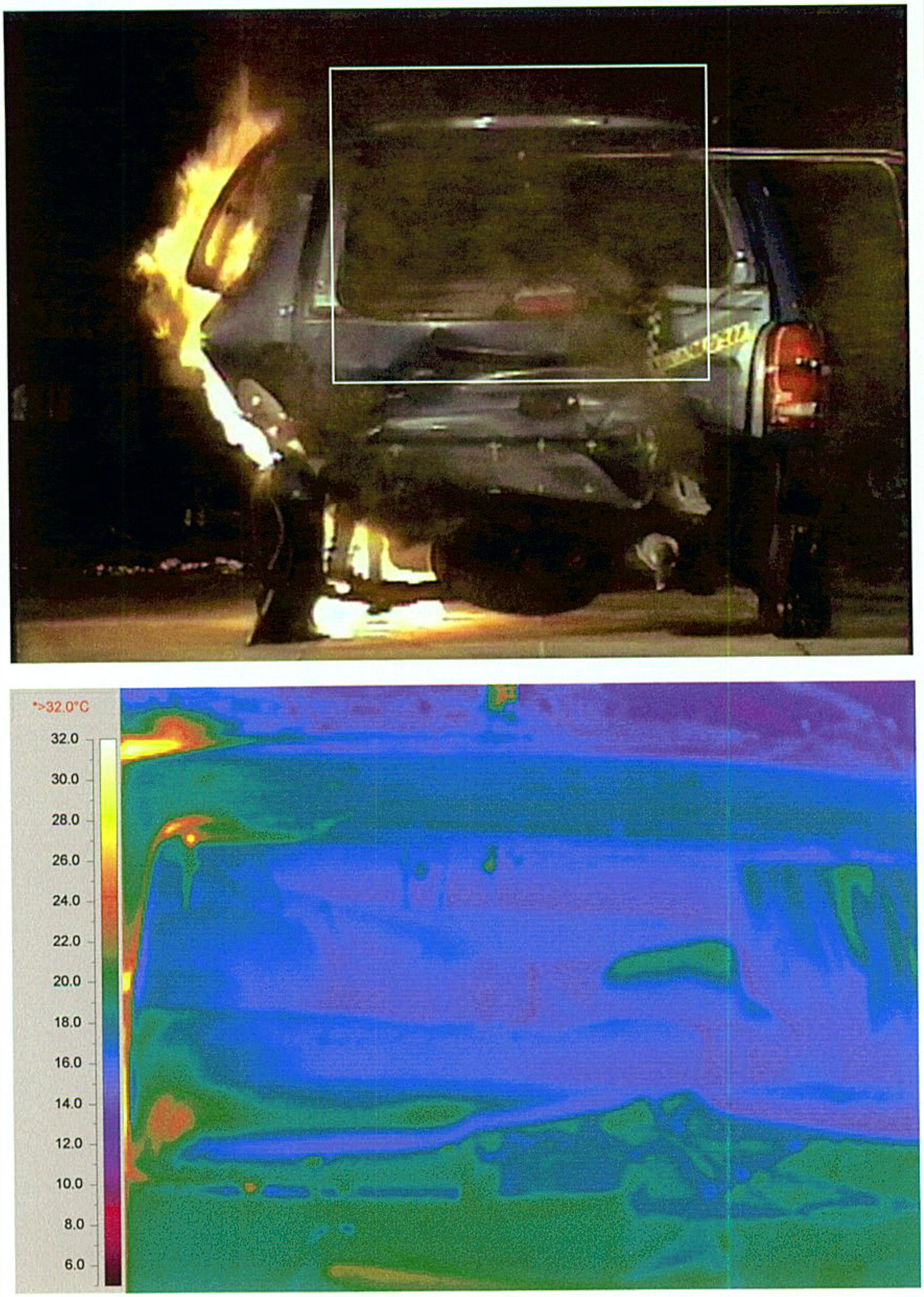


Figure 31. Fire Test F961116. Video stills from Camera 1 (upper) and Infrared Thermogram from IR3 (lower) at 110 seconds post-ignition. The box in the video still shows the approximate field-of-view of IR3.

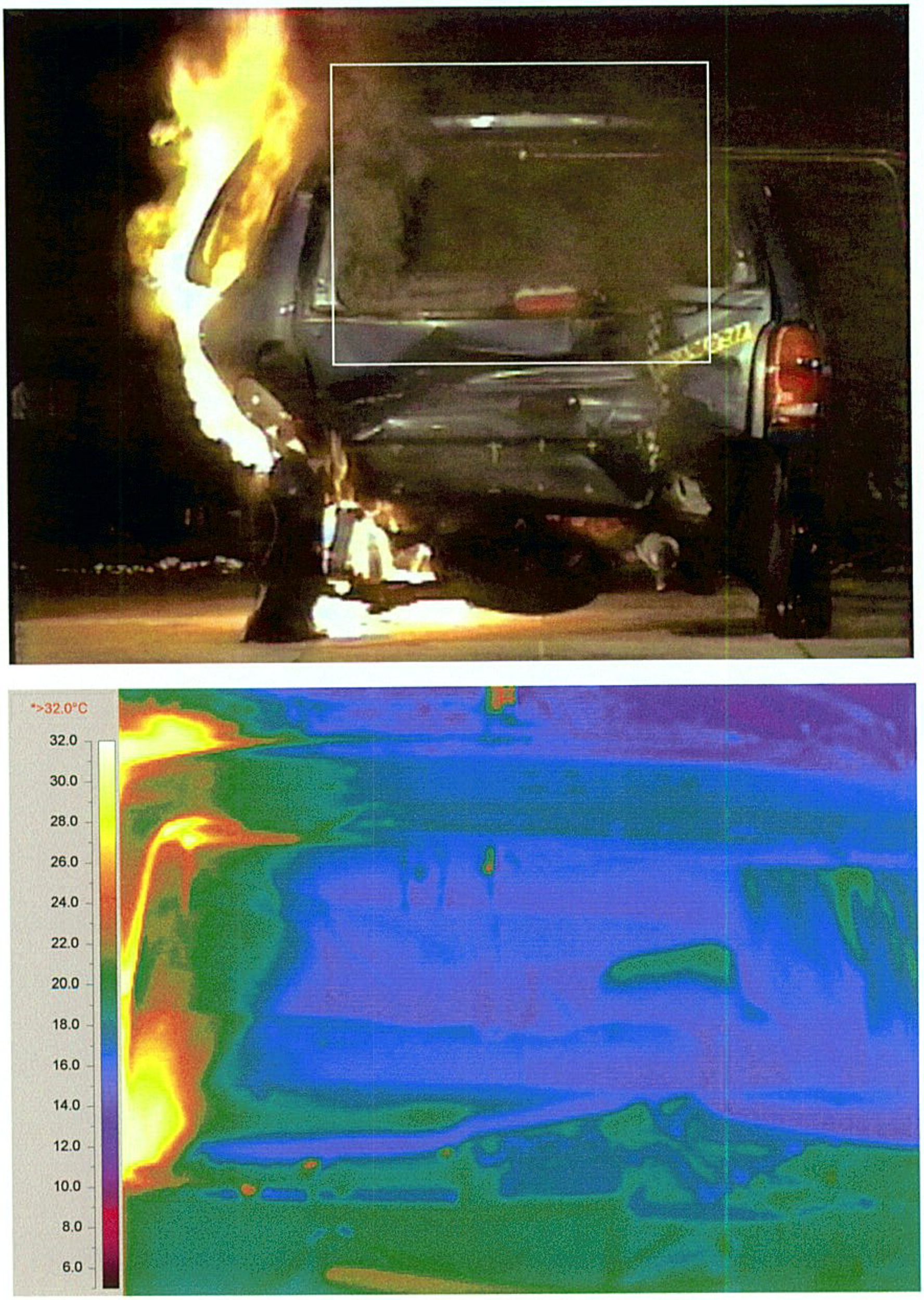


Figure 32. Fire Test F961116. Video stills from Camera 1 (upper) and Infrared Thermogram from IR3 (lower) at 130 seconds post-ignition. The box in the video still shows the approximate field-of-view of IR3.

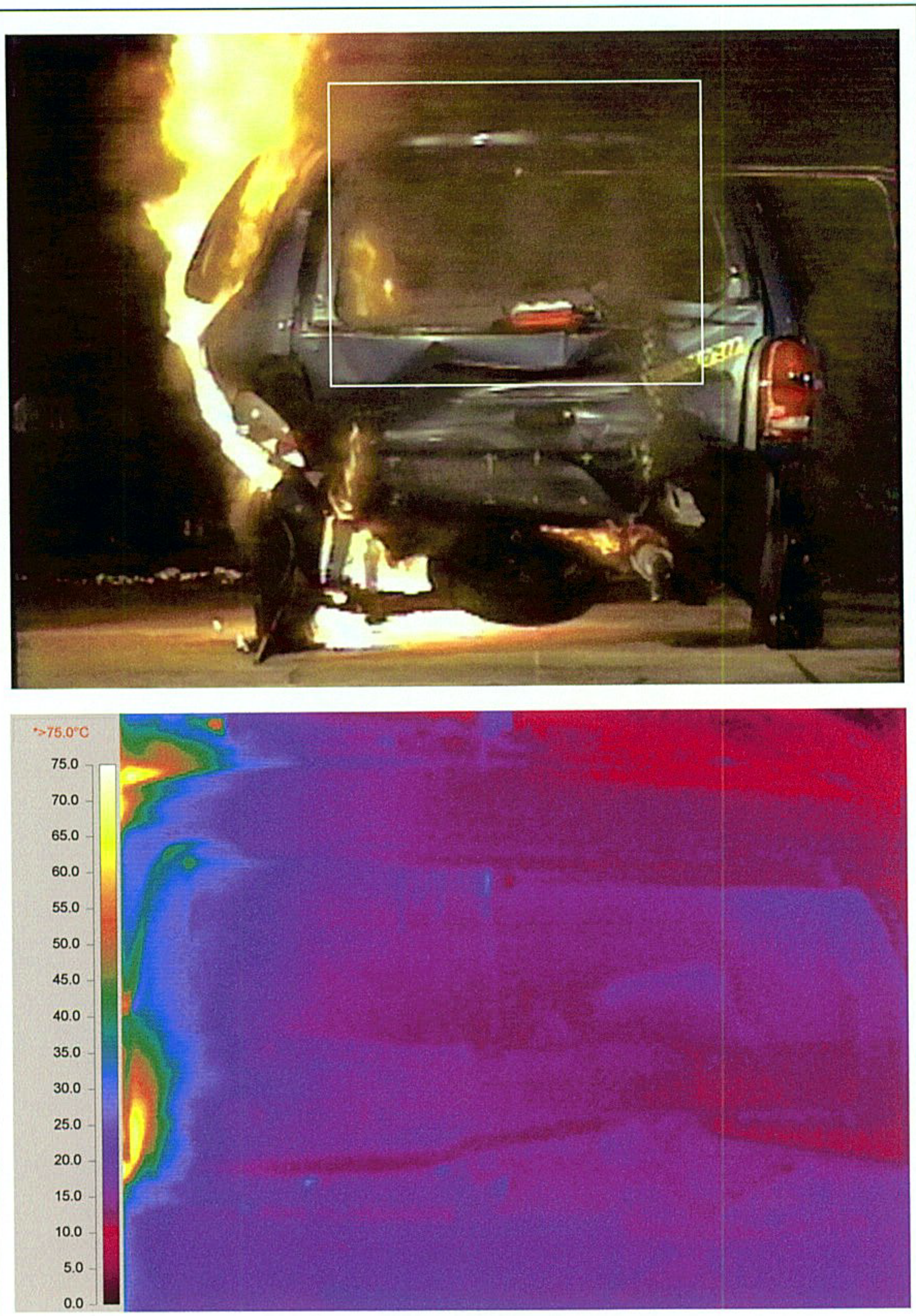


Figure 33. Fire Test F961116. Video stills from Camera 1 (upper) and Infrared Thermogram from IR3 (lower) at 155 seconds post-ignition. The box in the video still shows the approximate field-of-view of IR3. Note the change in temperature scale in the thermogram.

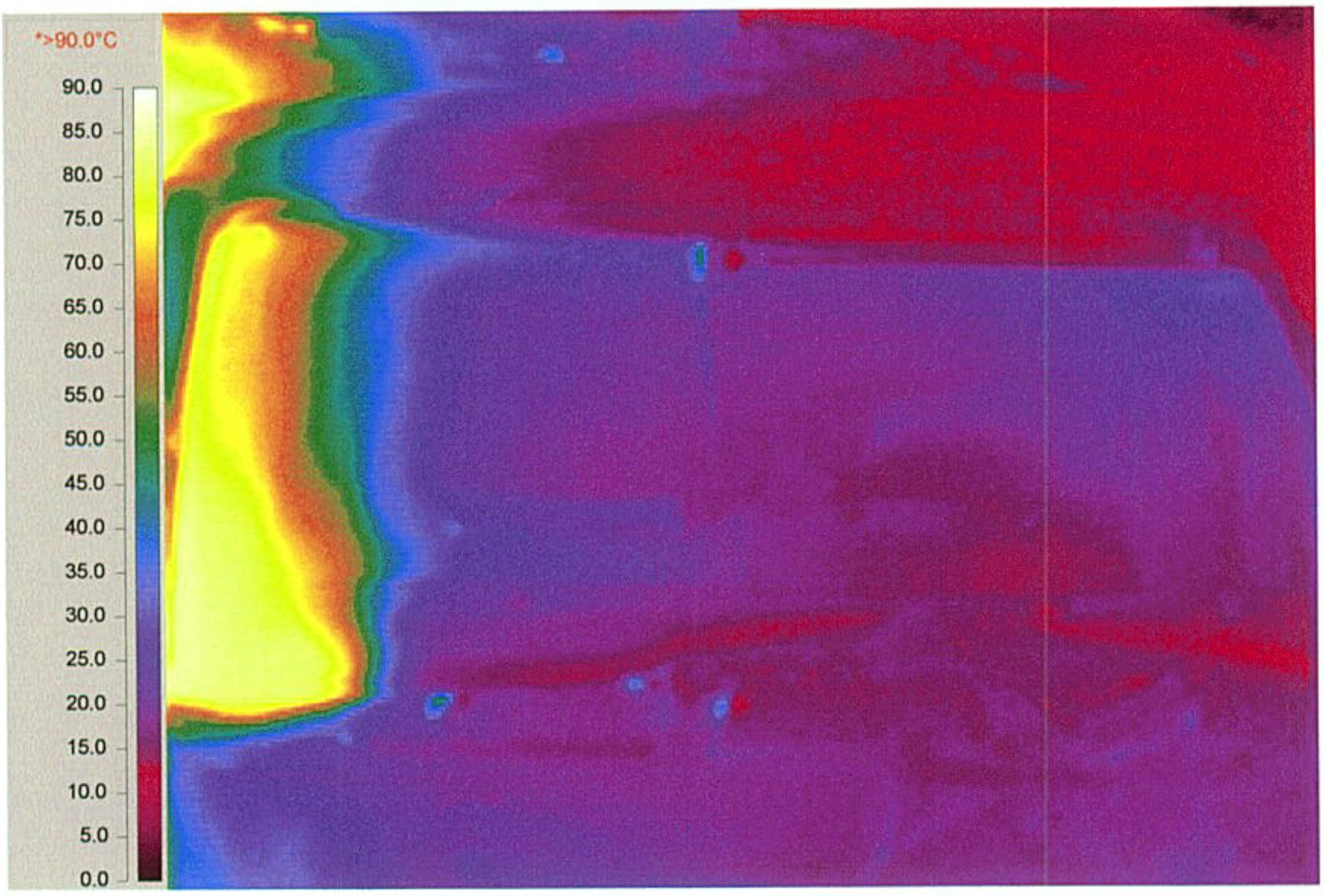


Figure 34. Fire Test F961116. Video stills from Camera 1 (upper) and Infrared Thermogram from IR3 (lower) at 175 seconds post-ignition. The box in the video still shows the approximate field-of-view of IR3. Note the change in temperature scale in the thermogram.

A thick gray plume of smoke started to emerge from inside the test vehicle between 105 and 110 seconds post-ignition (video still, Fig. 32). The density of the smoke column increased over the next 20 to 25 seconds (Fig. 30) until flames became visible through the left side of the liftgate window between 135 and 140 seconds post-ignition (video still, Fig. 31). The temperature of the upper left corner of the second bench seat back and left edge of the liftgate window opening increased from approximately 24°C to greater than 32°C between 120 and 130 seconds post-ignition -- before a fire plume was visible (Infrared thermogram, Fig. 32). The rate of heating of these objects increased rapidly once a fire plume started to emerge from the lower left rear corner of the test vehicle (Fig.'s 33 and 34).

Flames entering the left quarter vent appeared to combine with the fire plume emanating from the left rear wheelhouse and spread across the headlining between 170 and 200 seconds post-ignition. Figure 35 contains a series of diagrams showing plots of isothermal contours of the temperature along the lower surface of the headlining from 160 to 195 seconds post-ignition.[10] The temperature profiles shown in Figure 35 indicated that the fire plume had contacted the left rear corner of the headlining by 170 seconds post-ignition. Flames spread out radially along the lower surface of the headlining over the next 20 seconds. This is consistent with observation of a fire plume starting to spread toward the right across the rear of the headlining at 175 seconds post-ignition (see Fig. 34). By 190 seconds post-ignition, the flame front had moved forward along the headlining to a line approximately above the backs of the front seats.[11]

Isothermal contour plots shown in Figure 35 suggest that flames moved from the left to the right side of the headlining between 180 and 195 seconds post-ignition. By 195 seconds post-ignition, thermocouples below the left side of the headlining were recording temperatures < 600°C, suggesting that flames had disappeared from this area of the headlining. The video from Camera 1 shows the flames moved from left to right along the back of the headlining. Heavy smoke in the passenger compartment obscured the view of flame movement on more forward sections of the headlining. These observations suggest that fire consumed most of combustible material in the headlining within approximately 20 to 30 seconds after its ignition.

---

[10] Isothermal contours of the temperature below the headlining were estimated from the temperature data recorded from the A-Thermocouples using a three-dimensional interpolation command available in SigmaPlot® 4.0 for Windows® **[6]**. This command used an inverse distance method to generated temperature values for points on a uniformly spaced Cartesian grid from the [x,y,t] triple data from these thermocouples. Refer to Figure A3 in **APPENDIX A** for the approximate locations of the A-thermocouples below the headlining. Refer to **APPENDIX B** for the data from the A-Thermocouples.

[11] The location of the flame-front was based on based on a threshold temperature of 600°C used to establish the presence of flames in this study.

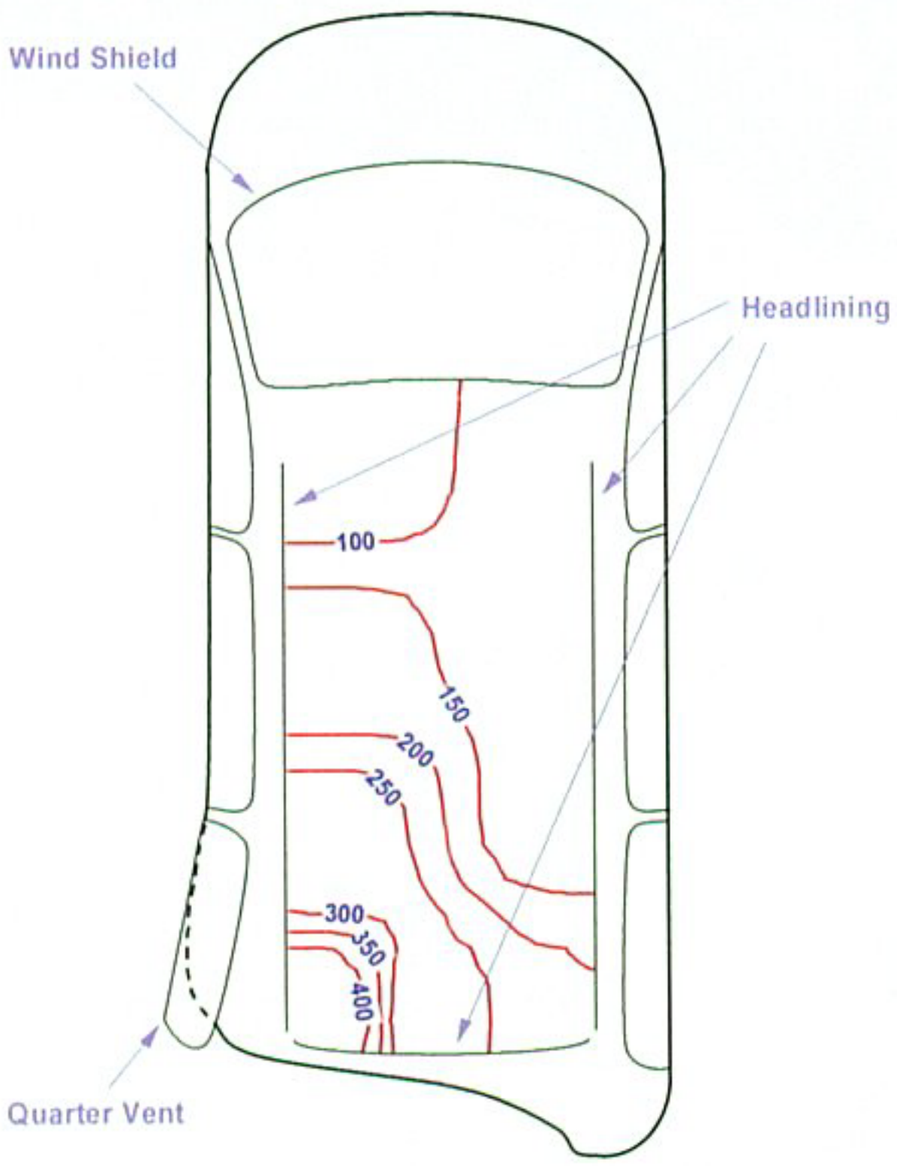


160 seconds post -ignition

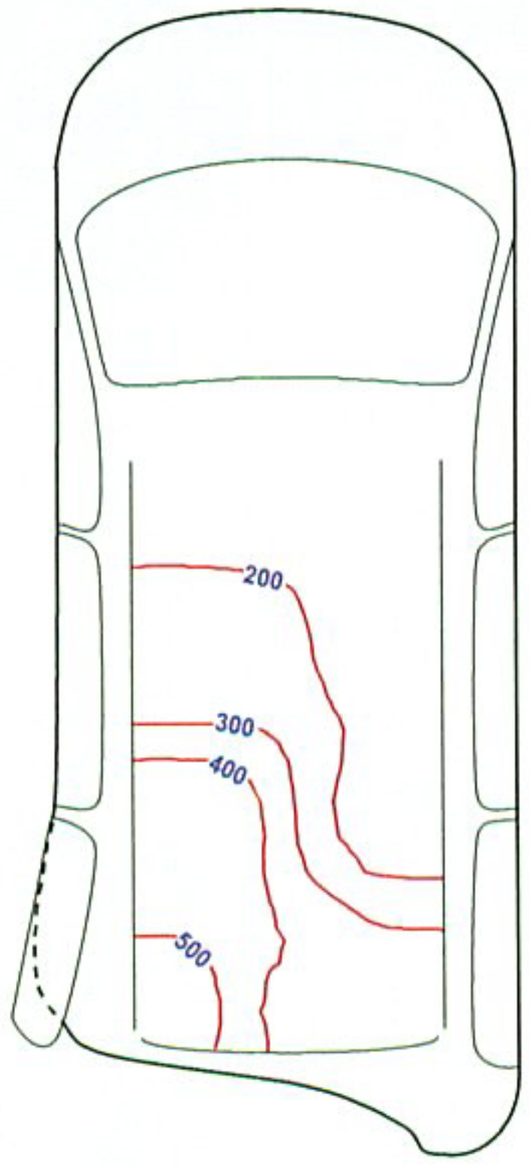


165 seconds post -ignition

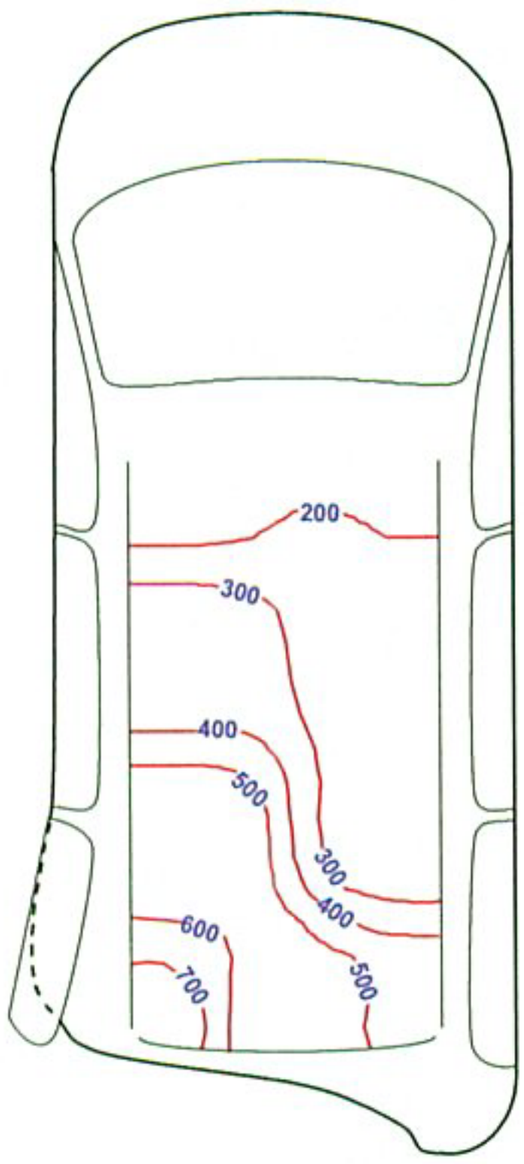


170 seconds post -ignition

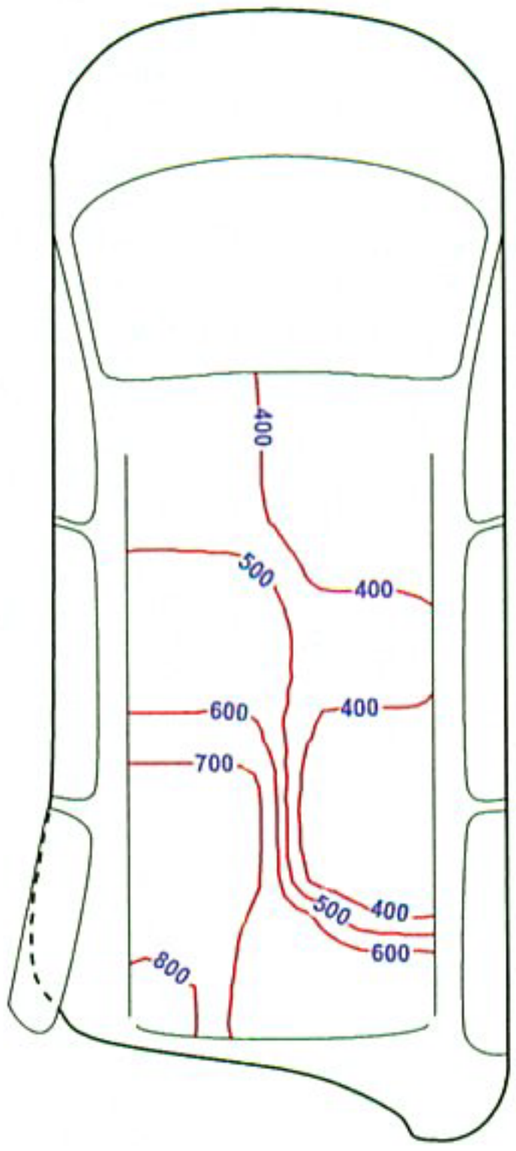


175 seconds post -ignition

Figure 35. Fire Test F961116. Isothermal contour plots showing temperature profiles along the lower surface of the headlining estimated from the responses of the A-thermocouples.

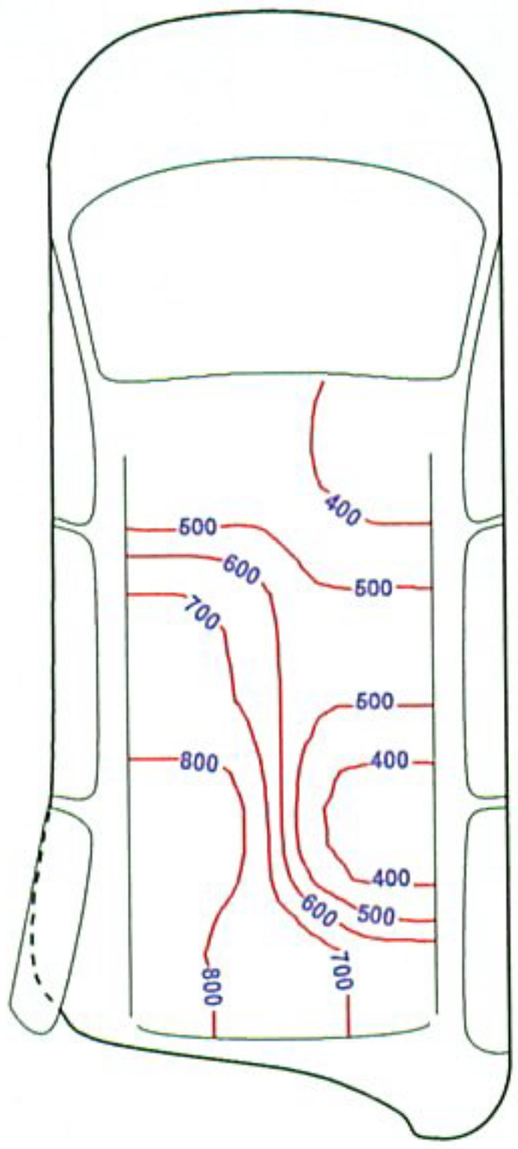


180 seconds post -ignition

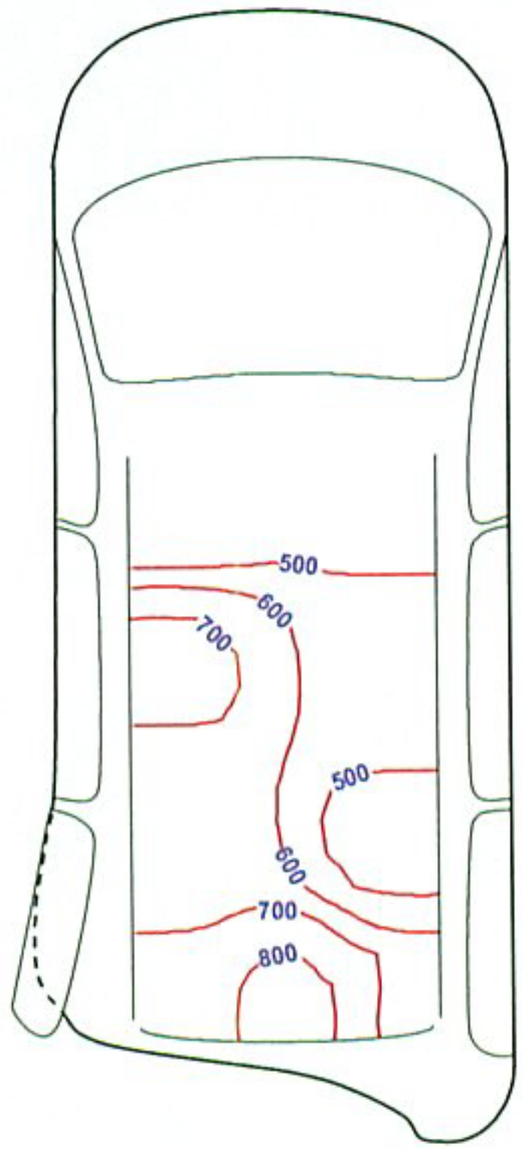


185 seconds post -ignition

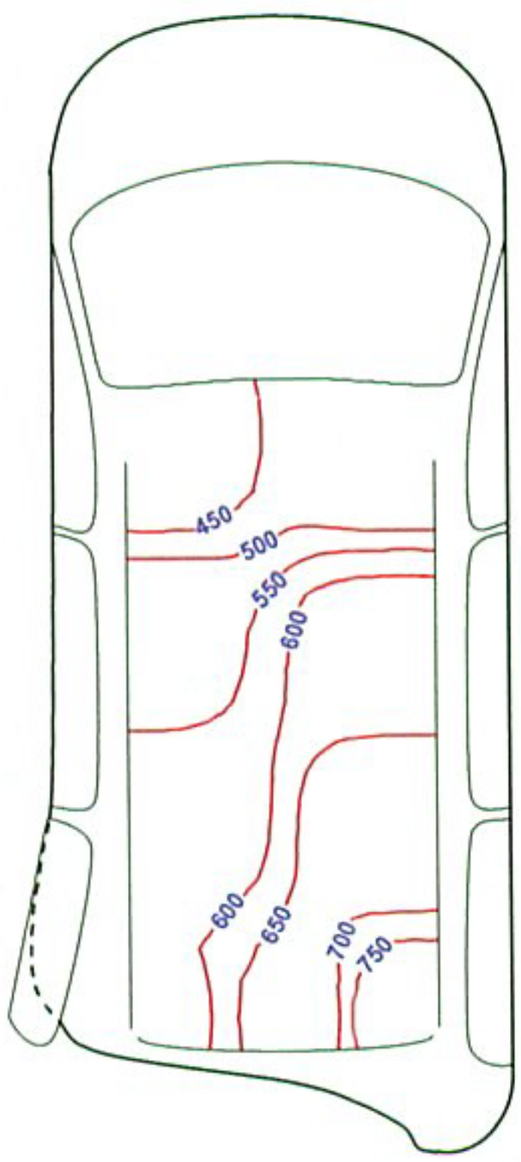


195 seconds post -ignition

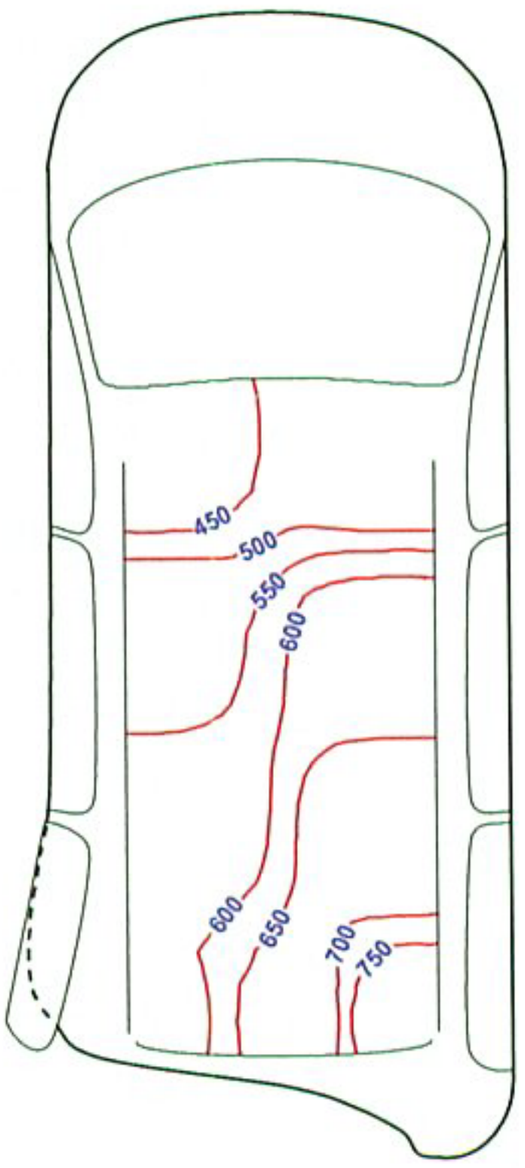


195 seconds post -ignition

Figure 35, continued. Fire Test F961116. Isothermal contour plots showing temperature profiles along the lower surface of the headlining estimated from the responses of the A-Thermocouples.

## 6 Ignition of Interior Components

Interior components around the left rear wheelhouse started to burn between 100 and 150 seconds post-ignition. Hot gas and flames that entered the split spot weld seams around the wheelhouse ignited the second bench seat and the left quarter trim panel. Flames spread to the back of the second bench seat, the liftgate trim panel, the C- and D-pillar moldings, and the headlining. Finally, radiation from these fires ignited the back panel of the seat cover on the first bench seat.

The plume of dark gray smoke emanating from the lower left rear corner of the test vehicle beginning approximately 130 seconds post-ignition (see **SECTION 5.3**), indicating that combustible materials around the left rear wheelhouse were exposed to heat and undergoing thermal decomposition at this time. Flames had entered the split spot weld seams at the rear of the wheelhouse by 100 seconds post-ignition (see **SECTION 5.1**). Sections of left quarter trim panel closest to the split spot weld seams and the left side of the second bench seat cushion were exposed directly to flames between 120 and 130 seconds post-ignition. The appearance of flames coming from the same area at approximately 150 seconds post-ignition indicated that some materials inside the passenger compartment had ignited by this time. Examination of the vehicle after the test revealed that fire damage to the interior was greatest in the left rear corner of the test vehicle (Fig. 36), which indicated that flames entered the passenger compartment in this area.

It was difficult to determine the exact times of ignition of individual components by examination of the video record because many components were obscured by smoke before they ignited. The thermocouple data augmented the video record by indicating the presence of flames at specific locations in the test vehicle. However, even this was not unambiguous evidence that the surface of a material adjacent to the thermocouple had ignited. Evidence of ignition would have required precise measurement of surface temperature either by a very small thermocouple in contact with the surface or by Infrared thermography. The thermoplastic materials used to fabricate the interior components of the test vehicle tend to melt and deform before they start to decompose and ignite. As these materials melted, it would have been nearly impossible to maintain contact between a thermocouple and the materials surfaces. Smoke in the passenger compartment obscured views of the thermocouples on the interior trim panels, so the video record could not be used to determine whether individual thermocouples remained in contact with the trim panel surfaces when they recorded flame temperatures. The accurate measurement of surface temperature by radiometric techniques is often impossible in sooty environments. Given these limitations, the

times-of-ignition of individual components that appear in the following discussion are estimates based on analysis of the video records of this test and thermocouple data acquired during the test.


Figure 36. Fire Test F961116. Photograph showing fire damage to the second bench seat, the left quarter trim panel, the C- and D-pillar trim panels, and the headlining.

## 6.1 Ignition of the Second Bench Seat

The video from Camera 6 shows flames spreading along the lower surface of the seat cushion in the second bench seat and lower edge of the left quarter trim panel by 150 seconds post-ignition (see Fig. 25). The image from the CCD camera became increasingly overexposed as flames entered the openings around the left rear wheelhouse, making it difficult to observe the ignition of objects in its field-of-view (see Fig's 20 through 24). In addition, smoke accumulating above the carpet in the rear of the test vehicle obscured the view from this camera, contributing to the difficulty in determining the exact times of ignition of the second bench seat and left quarter trim panel. Figure 37 shows a video still from Camera 6 at 190 seconds post-ignition, where few details of the interior of the test vehicle are discernable. Outlines of some of the components in

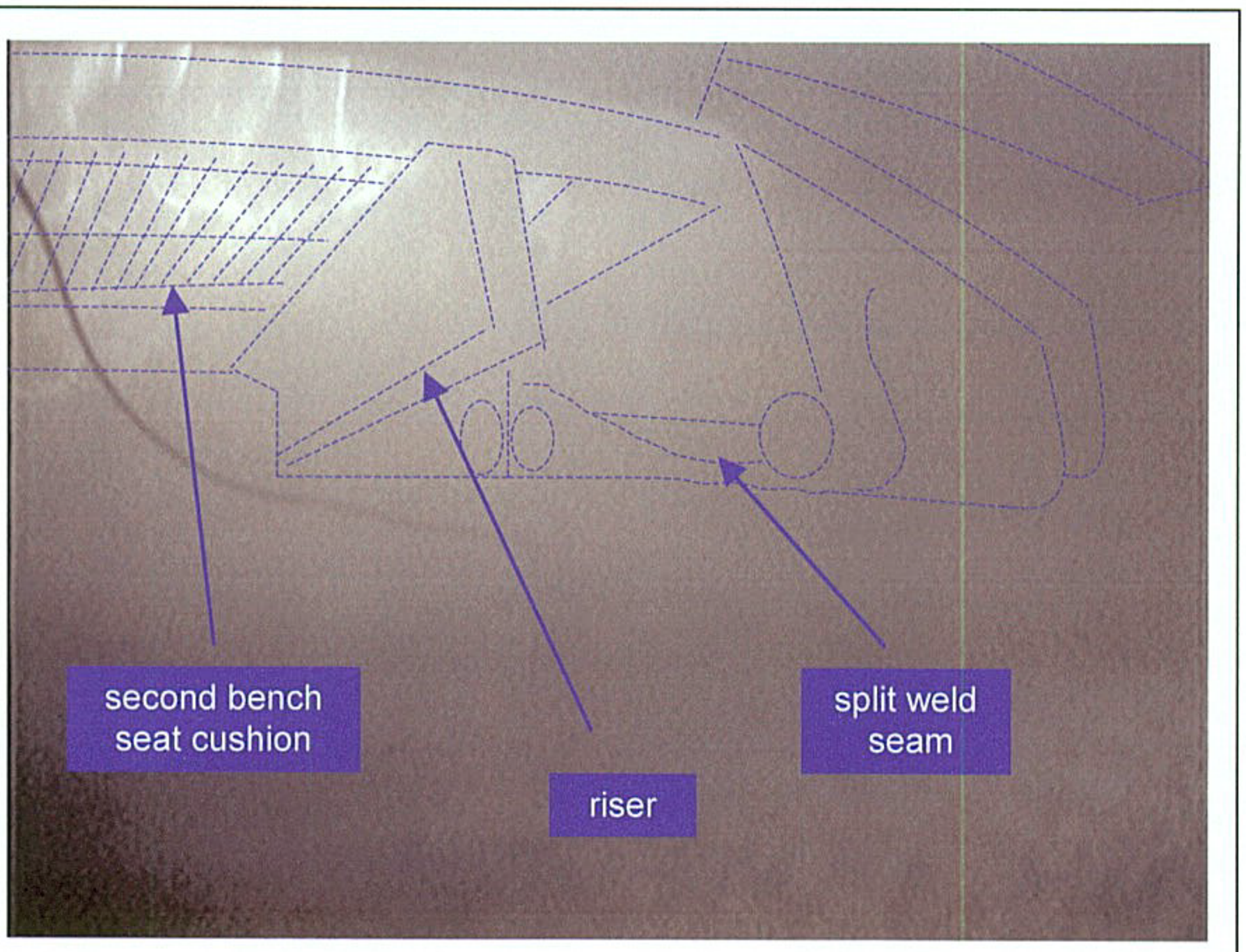


Figure 37. Fire Test F961116. Video still from Camera 6 at 190 seconds post-ignition showing flames filling the space below the left side of the second bench seat cushion. Refer to Figure 19 for the locations of objects obscured by smoke in this figure.

the field-of-view of Camera 6 (see Fig. 21) have been overlaid on the video still for reference. The foam pad in the seat cushion appears to have ignited by this time, with flames spreading along its lower surface toward the right side of the test vehicle. However, it was impossible to determine accurately the time of ignition of the foam pad and the rate of flame-spread along the seat cushion from this video.

Isothermal contours estimated from thermocouple data gave a clearer indication of time of ignition and rate of flame spread. Figure 38 shows a series of diagrams of the second bench seat with estimated isothermal contours of the temperature along the lower surface of the seat cushion. The isothermal contour plots in these diagrams are projected through the seat cushion.

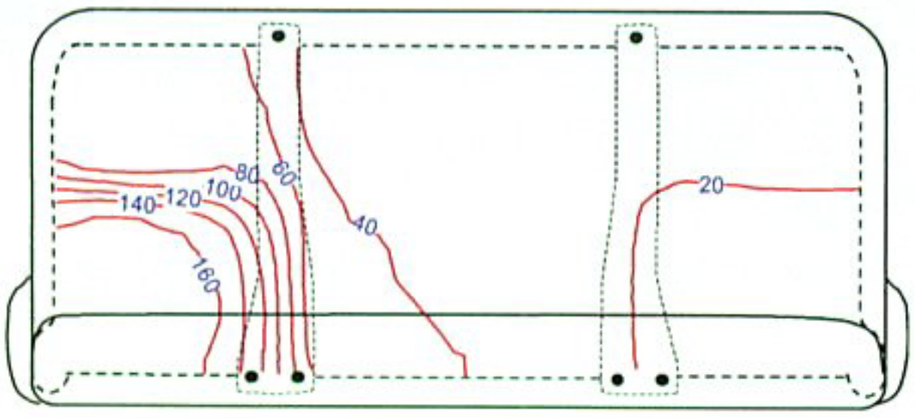


100 seconds post-ignition

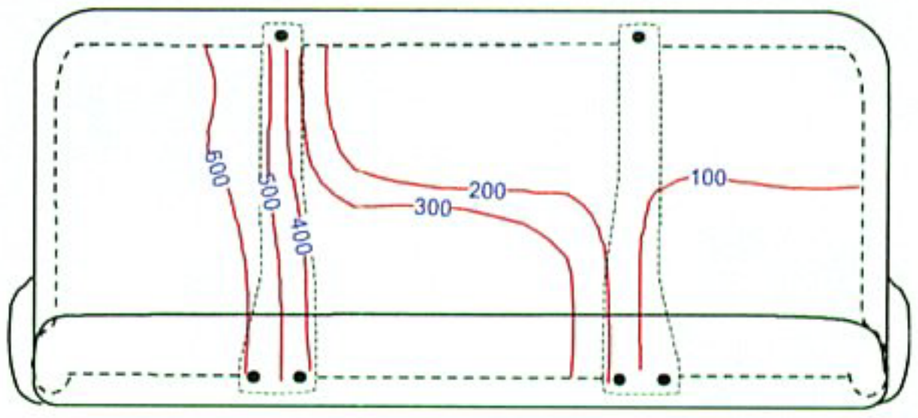


140 seconds post-ignition

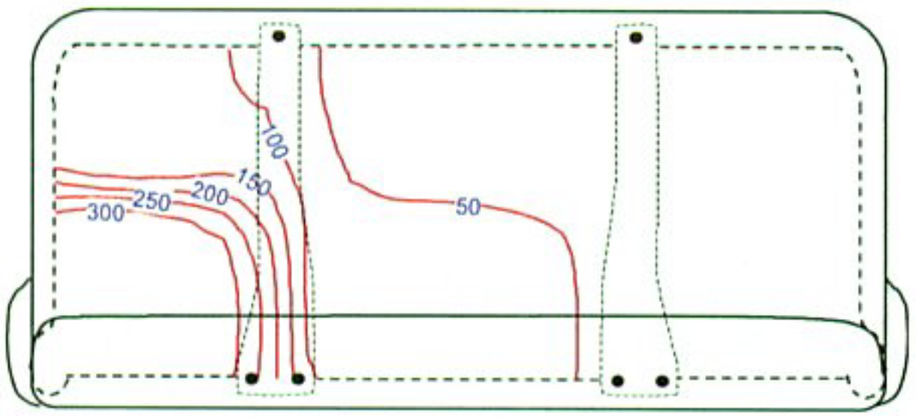


110 seconds post-ignition

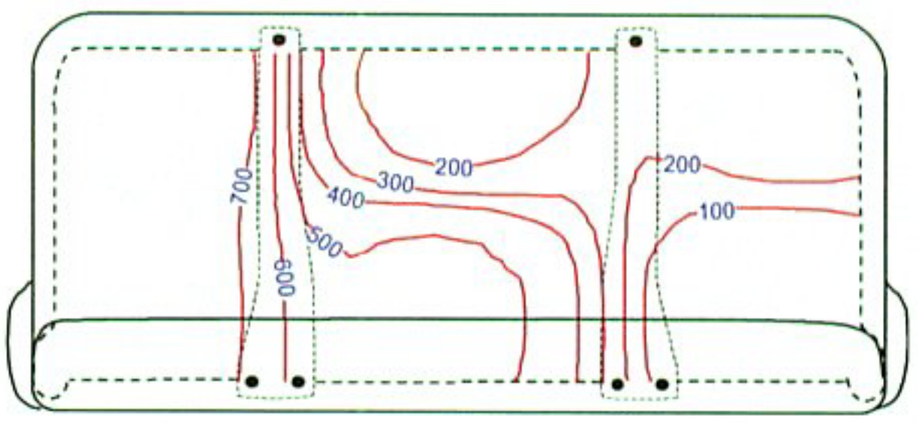


150 seconds post-ignition

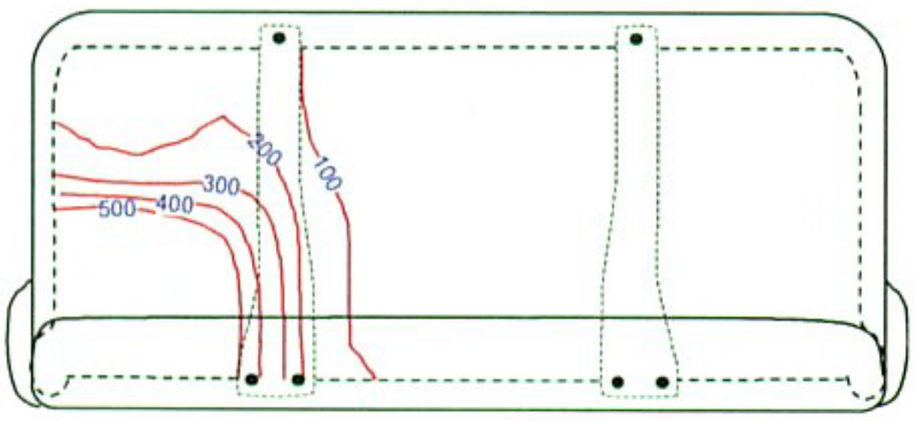


120 seconds post-ignition

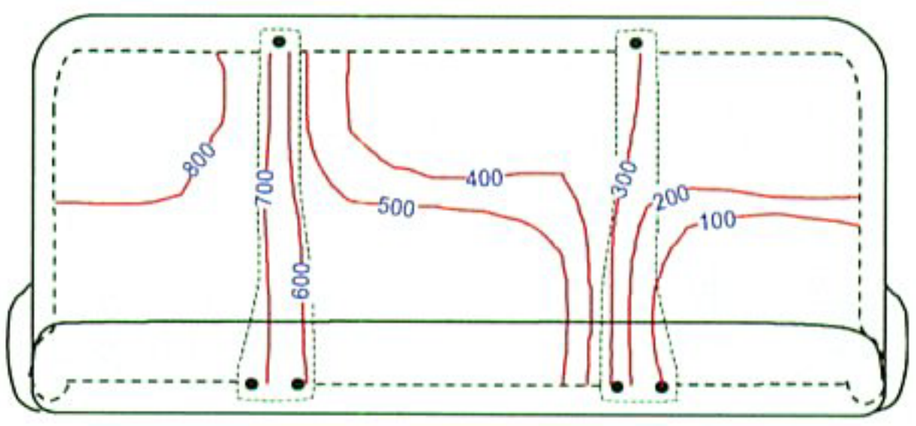


160 seconds post-ignition

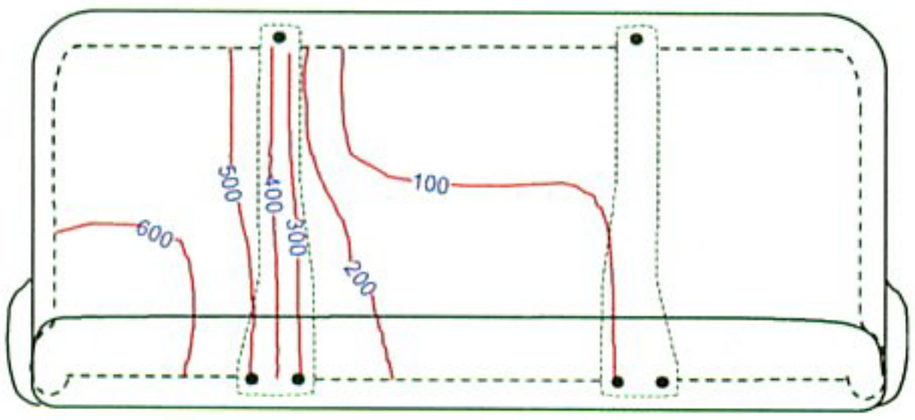


130 seconds post-ignition

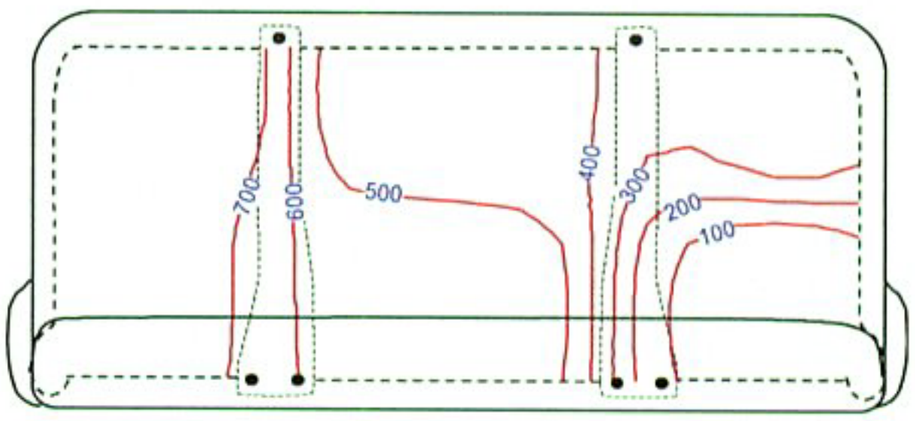


170 seconds post-ignition

Figure 38. Fire Test F961116. Diagrams showing isothermal contours along the lower surface of the foam pad in the second bench seat cushion between 100 and 170 seconds post-ignition. The view in these diagrams is from the top of the bench seat looking down through the seat cushion.

These diagrams are oriented so the back of the seat (which was against the liftgate trim panel) is down and the left side of the seat (which was adjacent to the left wheelhouse) is to the left. The outlines of the risers and the lower edge of the seat cover are shown as dashed lines. The isothermal contours were estimated from the S-Thermocouples data.[12]

The isothermal contour plots in Figure 38 indicate that hot gas entering the split spot weld seams around the wheelhouse was heating the left rear corner of the seat cushion by 100 seconds post-ignition. The temperature increased along the entire lower surface of the seat cushion between 100 and 130 seconds post-ignition. As indicated by temperatures greater than 600°C, flames were present along the lower surface of the foam pad in the left rear corner of the seat cushion by 130 seconds post-ignition. The isothermal contour plots in this figure indicate that flames spread forward toward the front seat cushion and laterally toward the right side of the seat cushion. The left riser appears to have hindered lateral flame-spread, confining flames to the left of the riser between 130 and 170 seconds post-ignition.

The video from Camera 1 indicated that material in the left rear corner of the test vehicle, including the second bench seat, ignited between 130 and 155 post-ignition (see Fig.'s 32 and 33 and **SECTION 5.3**). The development of an area on the lower surface of the foam pad exceeding the threshold temperature of 600°C by 130 seconds post-ignition suggests that this material was heated by direct flame contact and started to thermally decompose at this time, producing the smoke column shown in Figure 32. By 170 seconds post-ignition, flames appeared to have filled the space between the left riser and left edge side panel. The development of temperatures exceeding 600°C between 130 and 150 seconds post-ignition suggests that flames were spreading along the lower surface of the foam pad in the seat cushion at this time. The transition from thermal decomposition to flaming ignition of this material occurred around 130 seconds post-ignition, but the time of ignition of this material could not be determined more precisely from these data. The S-Thermocouples, which were located approximately 1 cm below the lower surface of the foam pad, could have been heated by flames entering the openings around the left rear wheelhouse before the foam pad started to burn.

[12]Isothermal contours of the temperature below the second bench seat cushion were estimated from the temperature data recorded from the S-Thermocouples using a three-dimensional interpolation command available in SigmaPlot® 4.0 for Windows® [6]. This command used an inverse distance method to generated temperature values for points on a uniformly spaced Cartesian grid from the [x,y,t] data from these thermocouples. Refer to **APPENDIX C** for thermocouple locations and temperature data.

Figure 39. Fire Test F961116. Photograph showing fire damage to the seating areas of the second bench seat.

The burn-pattern on the second bench seat indicated that flames were concentrated on the left side of the seat cushion and seat back. Sections of the seating- and side panels[13] on the left sides of the seat-back and seat-cushion had been consumed by fire, exposing the underlying foam pad (Fig.'s 39 and 40). The exposed foam contained the melted and charred residue from the seating- and side-panels of the seat cover (Fig. 39). The left hinge contained residue from the hinge cover and left quarter trim panel, which had apparently melted and sagged onto the left side of the second bench seat (Fig. 39). The upper left corner of the seat back contained residue from the D-Pillar trim, which had apparently melted and dripped onto the seat back (Fig. 39). This residue appeared to have trapped gas bubbles as it cooled and solidified as the fire was

[13]The seating panels in the seat covers were a poly(ethylene terphthalate) cut-pile fabric. The side panels were a vinyl fabric containing an isononyl phthalate plasticizer.

extinguished. This suggests that the temperature of this material was greater than its thermal decomposition temperature and had probably ignited by the time the test was ended.[14]

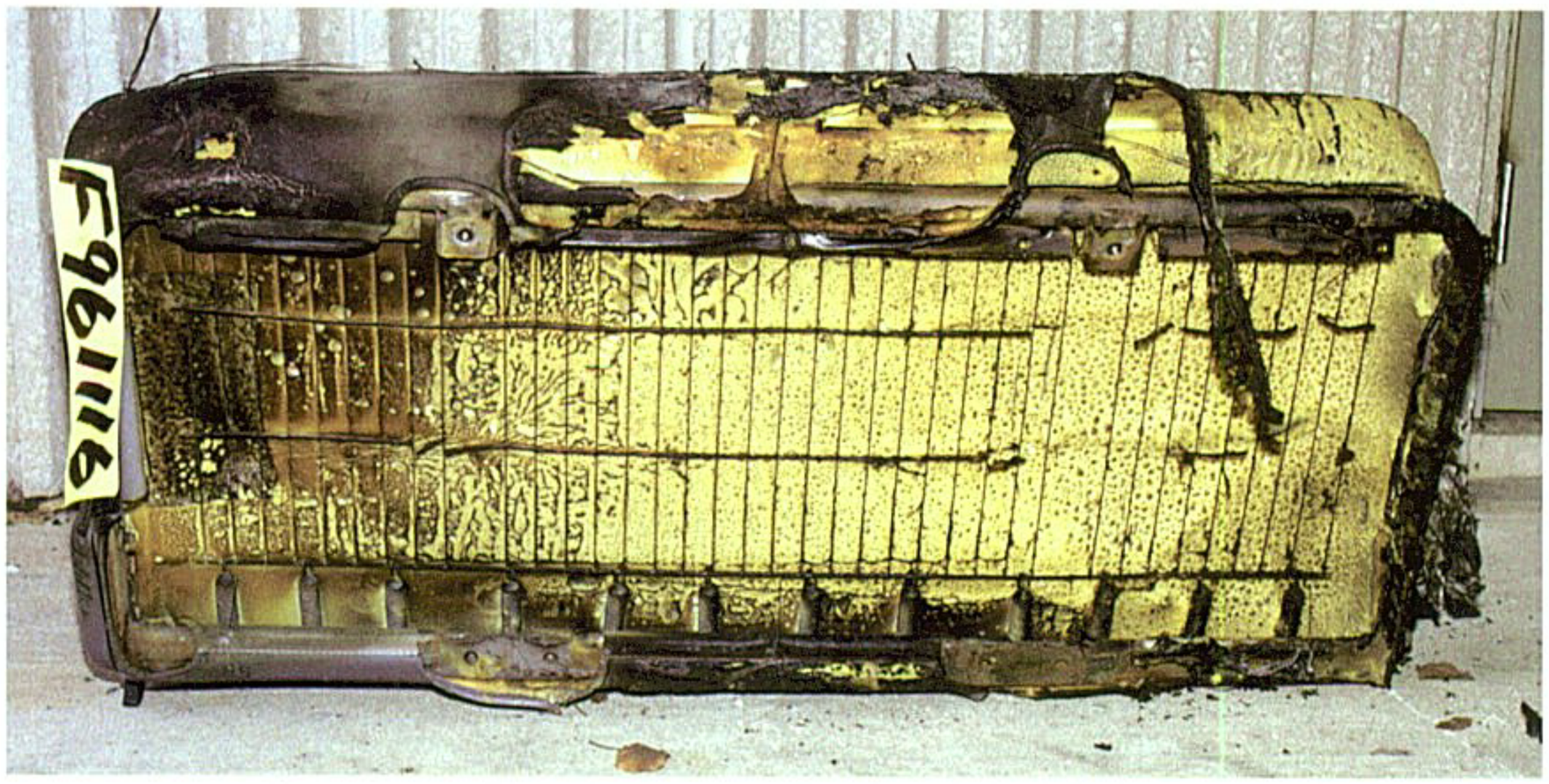


Figure 40. Fire Test F961116. Photograph showing fire damage to the lower surface of the foam pad in the second bench seat cushion.

Figure 40 is a photograph of the under-side of the second bench seat removed from the test vehicle after this fire test. The pattern of smoke and fire damage observed on the lower surface of the foam pad in the seat cushion is consistent with the pattern of flame-spread inferred from the estimated isothermal contours shown in Figure 38. Inspection of the seat revealed that material was eroded from lower surface of the foam pad[15] along the central (between the risers) and left (outboard of the left riser) sections[16] of the seat cushion (Fig. 40). Deposits of brown and black soot were observed evident on the right section. The isothermal contour plots in Figure 38 suggest that flames spread along the lower surface of the seat cushion up to the left riser by 170 seconds post-ignition. Smoke and gases produced in the fire plume spread to the right along the central and right sections of the seat cushion. The estimated temperatures along the central section of the seat cushion (Fig. 38) were greater that the thermal decomposition temperature of

---

[14]The trim panels in the test vehicle were poly(propylene) [**8**].

[15]The foam pads in the seat cushions and seat backs were a flexible TDI/poly(1,2-propylene glycol) urethane foam.

[15]In this report, the central section is defined as the portion of seat cushion between the risers, the left section is defined as the portion of seat cushion outboard of the left riser, and the right section is defined as the portion of seat cushion outboard of the right riser.

the urethane foam. The estimated temperatures along the central section of the seat cushion (Fig. 38) were less than the thermal decomposition temperature of the urethane foam.

## 6.2 Ignition of Interior Trim Panels

It was difficult to determine the exact times of ignition of the left quarter trim panel, the C- and D-pillar trim, and the lift-gate trim panel. In the view from Camera 6, the lower edge of the left quarter trim panel appears to have ignited between 90 and 110 seconds post-ignition. Smoke and flames in the left rear corner of the test vehicle obscured the view of the trim panel at this time. Flames appear to have channeled in the space between the inner quarter panel and the quarter trim panel, igniting the back surfaces of the left quarter trim panel first. The appearance of a fire plume emanating from this area between 130 and 155 seconds post-ignition (see **SECTION 4.3**) indicates that some of these components were burning at this time.

Figure 41 contains a series of four diagrams showing the left side of the test vehicle interior. The isothermal contours[17] in these diagrams indicate that the interior (exposed) surfaces of the left quarter trim panel, the left bolster, and the left D-pillar trim were burning by 170 seconds post-ignition. Hot gas entering the split spot weld seams around the wheelhouse was heating the upper section of the D-pillar trim and the lower edge of the left quarter trim panel along the wheelhouse at 140 seconds post-ignition. By 150 seconds post-ignition, flame temperatures (i.e., temperatures $\geq$ 600°C) were recorded on the interior (exposed) surface of the quarter trim panel near the front of the left wheelhouse. The temperatures recorded on these components increased so that, by 170 seconds post-ignition, flame temperatures were recorded on a number of areas on the left quarter trim panel, the left bolster, and the left D-pillar trim panel.

The pattern of smoke and fire damage observed in Figure 42 indicates that the rear half of the left quarter trim panel, the left C- and D-pillar trim panels, and the left edges of the liftgate trim panel and liftgate sill plate had ignited by the time flames in the interior of the test vehicle were extinguished. Inspection of the test vehicle after the fire was extinguished revealed that fire damage to the interior trim panels was localized to the left rear corner and headlining (Fig. 42). The section of the left quarter trim panel that was rearward of the C-Pillar was consumed by fire. The left C-pillar trim had ignited around the left quarter vent. Material covering the front-surface of the left C-pillar appeared to have melted and sagged, but not to have ignited. The left D-pillar trim

[17]Isothermal contours on the interior (exposed) surfaces of the left quarter trim panel, the D-Pillar trim, and the left bolster were estimated from the temperature data recorded from the E-Thermocouples using a three-dimensional interpolation command available in SigmaPlot® 4.0 for Windows® **[6]**. This command used an inverse distance method to generated temperature values

also had ignited, and was largely consumed by fire. And as mentioned in **SECTION 5.1**, residue from the left D-pillar trim was noted on the upper left corner of the second bench seat back. The exposed metal surfaces around the left quarter vent contained heavy deposits of black soot. The paint on the exposed inboard and forward surfaces of the left C-pillar was discolored by heat, but these surfaces were almost devoid of soot. Material along the left edge of the liftgate trim panel and sill plate was melted, and the melted material appeared to have trapped gas bubbles as it solidified when the fire was extinguished.

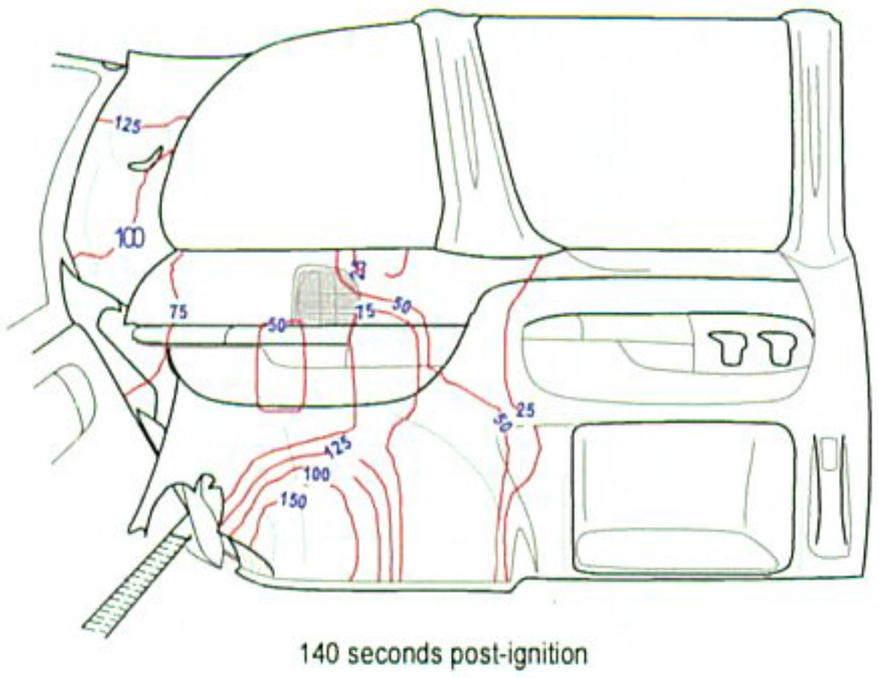


140 seconds post-ignition

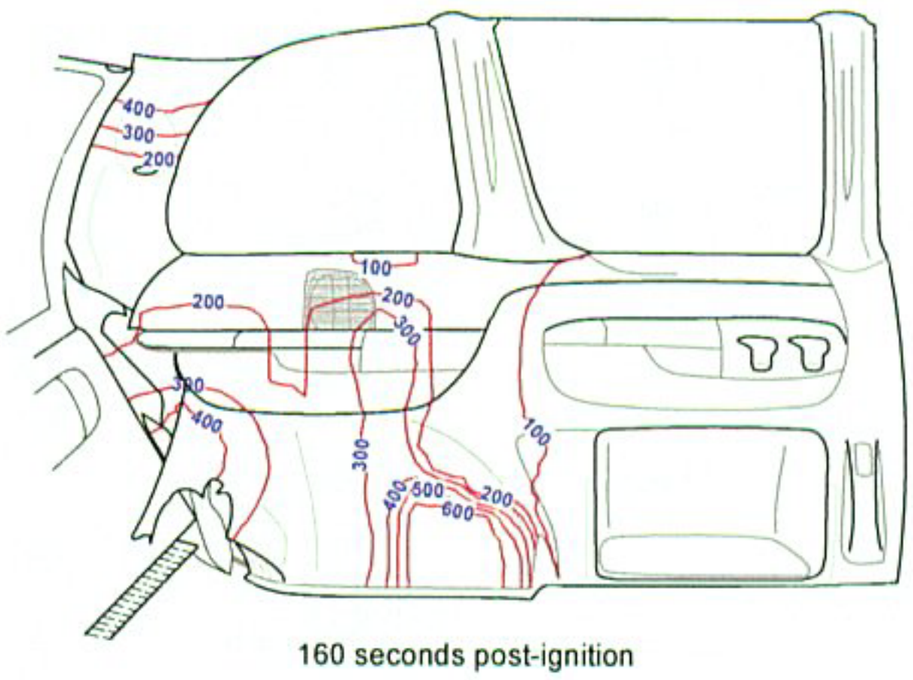


160 seconds post-ignition

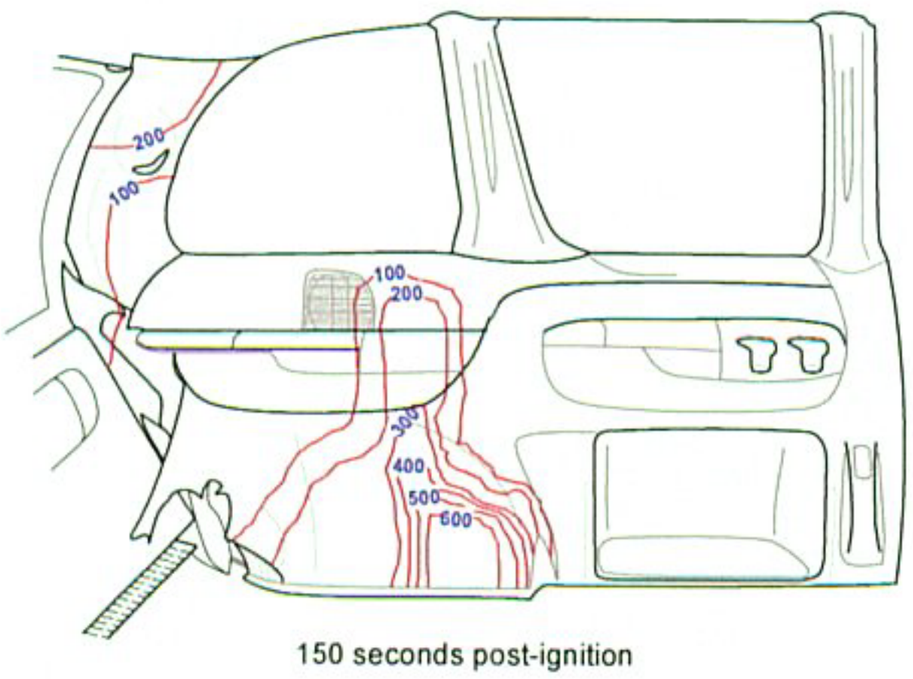


150 seconds post-ignition

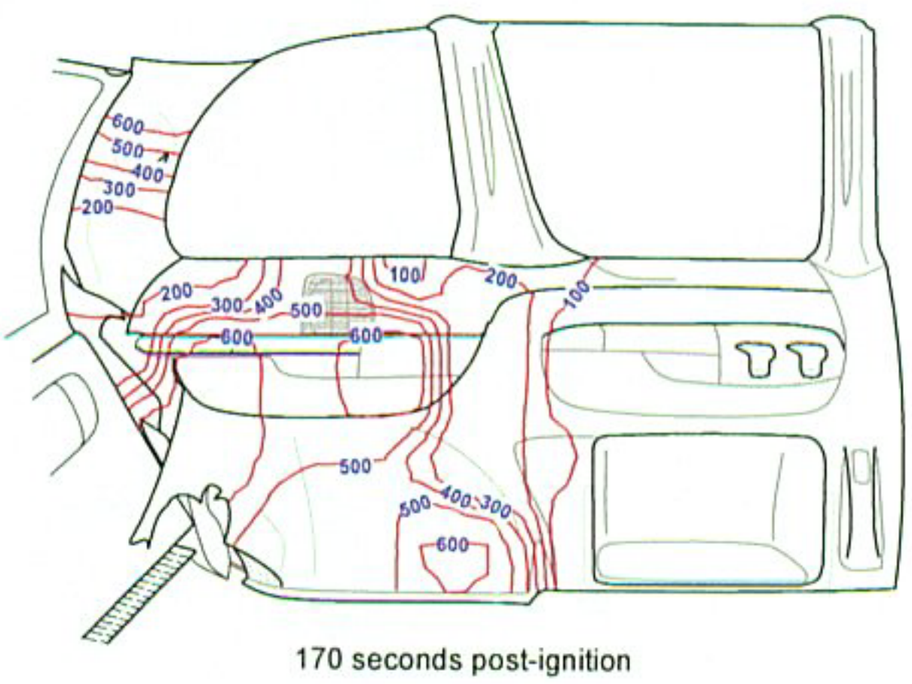


170 seconds post-ignition

Figure 41. Fire Test F961116. Diagrams showing isothermal contours on the interior (exposed) surfaces of the left quarter trim panel, the left quarter trim bolster, and the left D-pillar trim between 140 and 170 seconds post-ignition.

---

for points on a uniformly spaced Cartesian grid from the [x,y,t] triple data from these thermocouples. Refer **APPENDIX C** for thermocouple locations and data.


Figure 42. Fire Test F961116. Photograph showing the rear left corner of the passenger compartment of the test vehicle after this fire test. The storage box was not completely consumed by fire.

### 6.3 Ignition of the First Bench Seat and the Front Seats

Fire damage to the first bench seat indicated that the top and rear panels of the cover on the first bench seat back were ignited by radiation from flames in the left rear corner of the test vehicle and flames on the headlining (Fig. 43). Sections of the top- and back-panels of the cover had been consumed by fire. The exposed foam pad in these areas contained the charred residue of the vinyl fabric used to fabricate these panels. Material was eroded from the upper left corner of the foam pad, exposing sections of the frame in the seat back that had been covered. The foam also appeared to have melted and dripped onto the lower cross-member of the frame in this area, suggesting that the upper left corner of the pad in the seat back had ignited before the flames in the passenger compartment were extinguished.

Sections of the back- and side-panels in the seat back covers of the driver's and front passenger's seats were melted and charred (Fig. 44). The back-panel in the driver's seat back cover appeared to have been ignited by radiation from flames in the left rear corner of the test


Figure 43. Fire Test F961116. Photograph showing fire damage to the first bench seat.

vehicle. A section of the vinyl fabric in the upper left corner of the head restraint of the driver's seat had been consumed by fire. The exposed laminated sew-pad was charred.

The back- and side-panels were cracked and charred along the right edge of the front passenger side seat back cover (Fig. 44). The fabric in these areas also was coated with a layer of black soot. In contrast to the driver side seat, the back- and right side-panel in the front passenger side seat back cover appear to have been burned by flames entering the right front door, which was opened to extinguish flames in the front of the passenger compartment. The fluid containment pan retained liquid gasoline that escaped from the fuel tank of the test vehicle at the end of the test. The gasoline pool re-ignited several times during attempts to extinguish the fire. Flames from the burning gasoline in the pan appeared to enter the open right front door during this time and produce the fire damage to the front passenger side seat shown in Figure 44.

### 6.4 Conduction through the Floor Pan

Flames from the burning pool of gasoline started to heat the floor pan of the test vehicle within a few seconds after ignition. Figure 45 shows plots of the heat flux to the lower surface of the floor pan, the temperature recorded by a thermocouple (Thermocouple C3) located just below the floor


Figure 44. Fire Test F961116. Photograph showing fire damage to the driver's and front passenger's seats. (The yellow paint on the upper sections of the back panels and holes in the back panels were present when the test vehicle was received from Transportation Research Corporation.)

pan, and the temperature recorded by a thermocouple (Thermocouple B9) located on the upper surface body mastic covering the floor pan. These transducers were located in an area above the approximate center of the gasoline pool.

These data indicate that this area of the floor pan was exposed to flames starting at approximately 15 seconds post-ignition, and continued to be exposed to flames until the test was ended and the burning gasoline pool was extinguished. The heat flux to the lower surface of the floor pan ranged from approximately 75 $kW/m^2$ shortly after ignition to approximately 35 $kW/m^2$ just before fire suppression began.

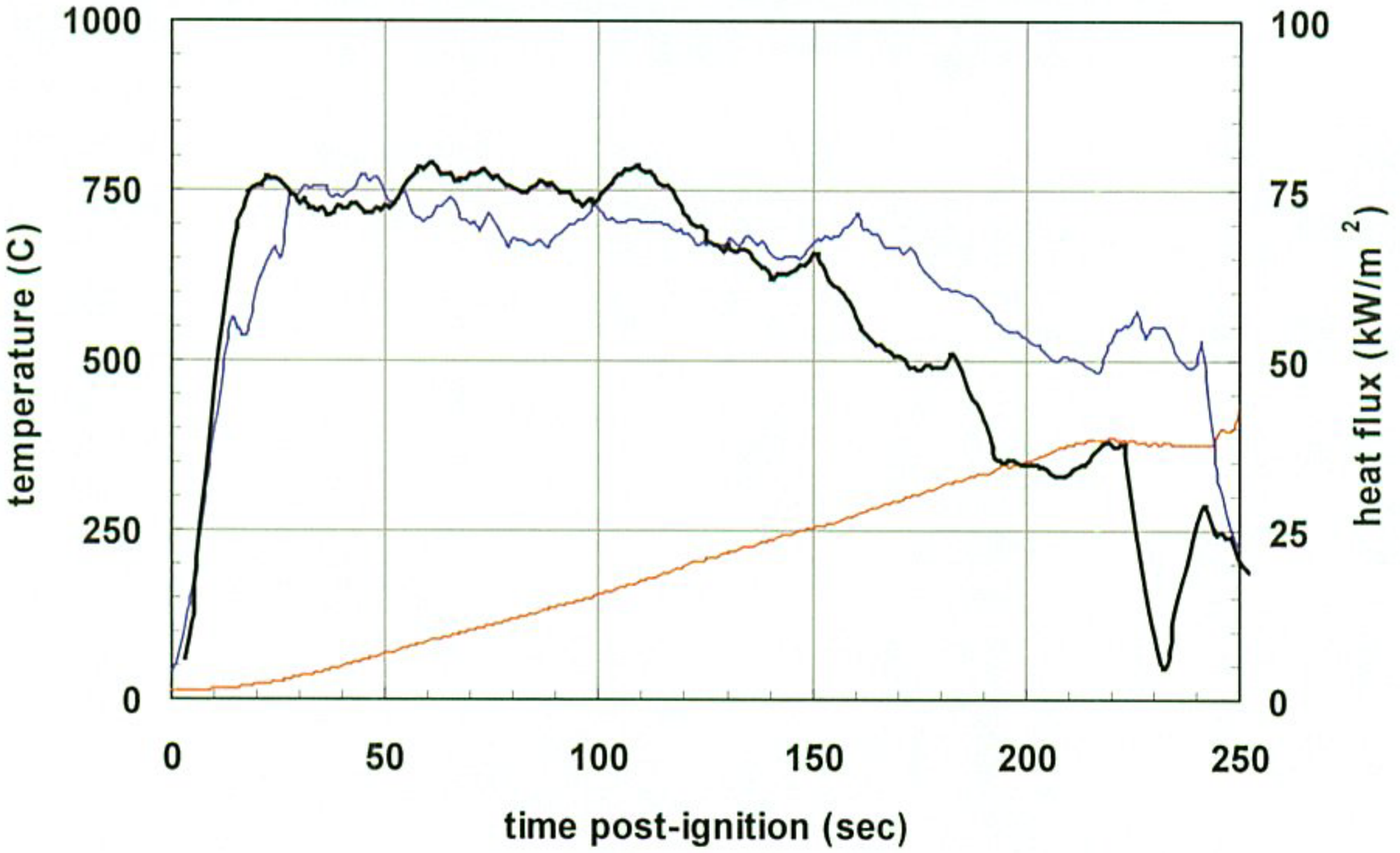


Figure 45. Fire Test F961116. Plots of the heat flux recorded by HFT 3 (—), the temperature recorded by Thermocouple C3 (—), and the temperature recorded by Thermocouple B9 (—). Refer to **APPENDIX E** for the location of and data from HFT3. Refer to **APPENDIX C** for the locations of and data from thermocouples C3 and B9.

Conduction through the floor pan heated the upper surface of the body mastic. Figure 46 shows isothermal contours[18] on the upper surface of the body mastic at 50, 100, 150, and 200 seconds post-ignition. The area of maximum conduction through the floor pan and temperature recorded on the upper surface of the floor pan (Fig. 46) corresponds roughly to the area of the floor pan that was above the hottest flames below the test vehicle (see Fig. 16).

---

[18]Isothermal contours on the upper surface of the body mastic on the floor pan were estimated from the temperature data recorded from the C-Thermocouples using a three-dimensional interpolation command available in SigmaPlot® 4.0 for Windows® [**6**]. This command used an inverse distance method to generated temperature values for points on a uniformly spaced Cartesian grid from the [x,y,t] triple data from these thermocouples. Refer to **APPENDIX C** for thermocouple locations and data.

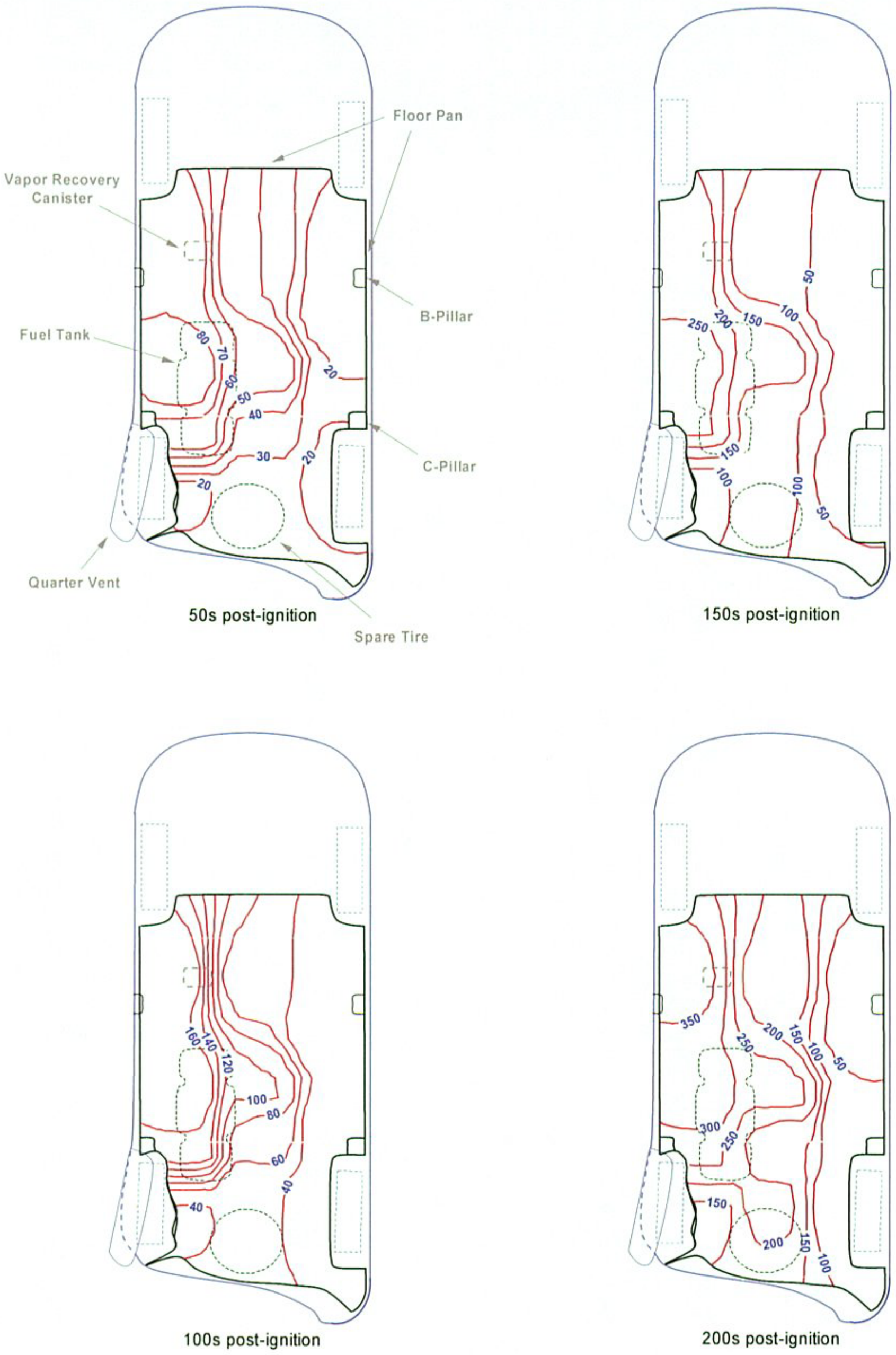


Figure 46. Fire Test F961116. Isothermal contours on the floor pan of the test vehicle.

The pattern of fire damage to the lower surface of the carpet pad indicated that, over most of the floor pan, conduction through the floor pan did not result in ignition of the carpet before fire was extinguished (Fig. 47).

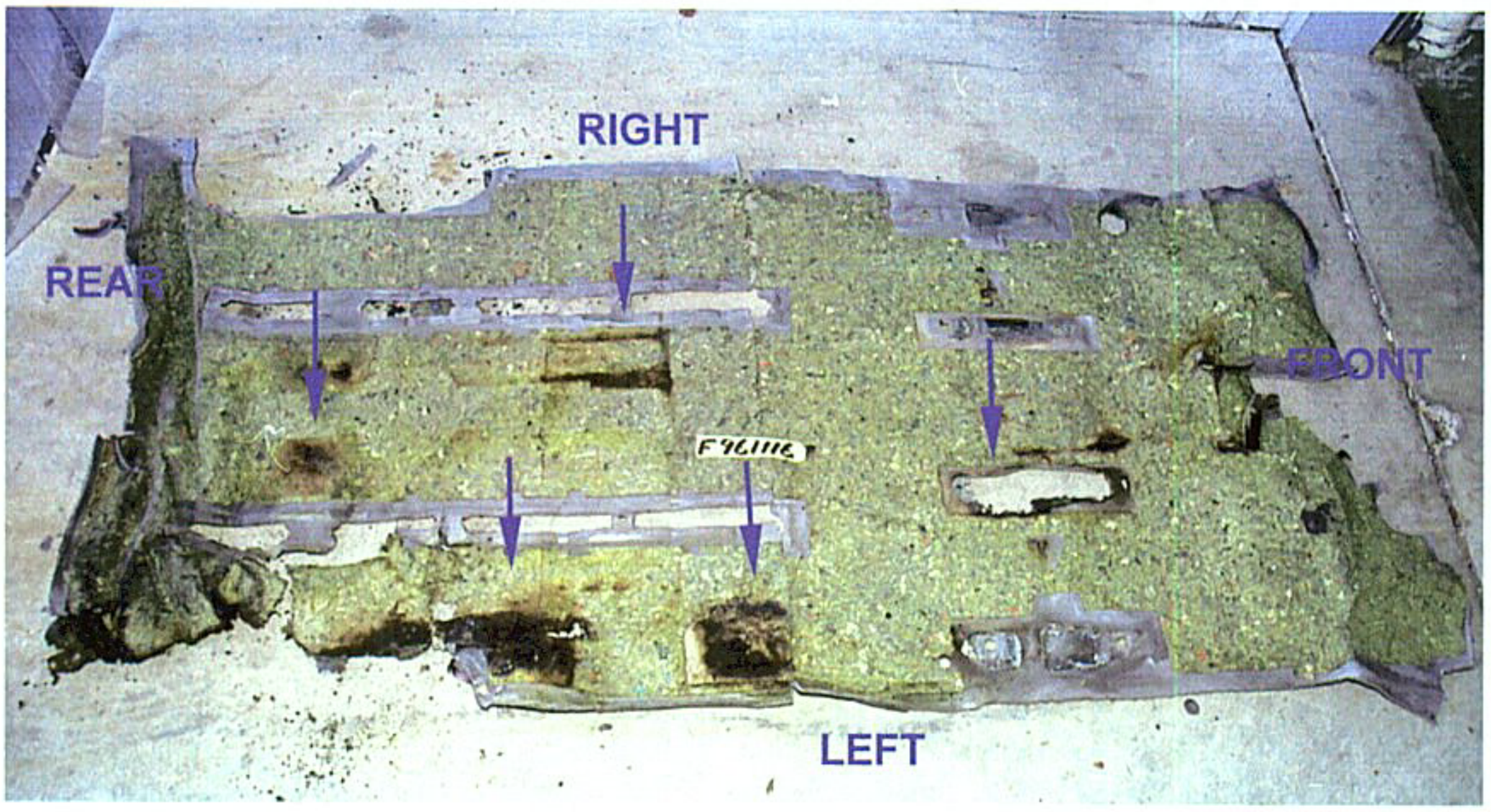


Figure 47. Fire Test F961116. Photograph showing the bottom of the carpet and carpet pad of the test vehicle after the test. The arrows indicate areas where the carpet or carpet were melted, burned, or charred.

The area of the carpet that abutted the left rear wheelhouse was burned and charred. In several areas (indicated by arrows in Figure 47), the temperature of the upper surface of the mastic on top of the floor pan was sufficiently high to have caused the carpet pad to char. In one area, under the inboard riser under the drivers seat where the carpet backing was not covered by pad, the carpet appeared to have ignited. The areas where the carpet pad was charred coincided with the sections of the floor pan where the surface temperature was greater than 200°C at 200 seconds post-ignition (Fig. 46).

## 7 Combustion Conditions

The output of combustion products from a fire depends on the material burning and on the supply of air to the flame. A well-ventilated fire is one in which the air supplied to the flames is sufficient for complete combustion. In partially enclosed spaces, such as an engine compartment or passenger compartment, airflow to the flames may be inadequate for complete combustion. In this case, called a ventilation-controlled or under-ventilated fire, the supply of air limits both the heat released by the fire and oxidation (combustion) of the gaseous fuel in the fire zone. As ventilation decreases, the output of carbon monoxide, hydrocarbons, smoke, and other products of incomplete combustion increase. The chemical composition of these gases depends on the chemical compositions of the materials burning and on the burning conditions, primarily ventilation. Accumulation of partially oxidized gases and gaseous unburned thermal decomposition products in an enclosed space can create a hazardous condition. In most cases, these gases are heated relative to the surrounding air and, because of their buoyancy, typically accumulate below the ceiling or roof, forming what is called the upper layer. The upper layer can be ignited by flames from burning objects (piloted ignition) or can ignite spontaneously (autoignition) when the temperature of the gases exceeds a minimum threshold temperature (autoignition temperature), which depends on the chemical composition and the fuel/oxygen ratio of the gaseous upper layer. Once ignited, radiation from the burning upper layer transfers heat downward, and may ignite combustible materials below the burning upper layer. Some of the partially oxidized gases and unburned thermal decomposition products may be toxic (see **SECTION 8**). Ventilation has a significant effect on the chemical composition of the gases produced in a fire.

The equivalence ratio $\Phi$ is a quantitative measure of ventilation:

$$\Phi = \frac{\left[fuel/O_2\right]_{fire}}{\left[fuel/O_2\right]_{stoichiometric}}$$

where $\Phi$ is the equivalence ratio, $[fuel/O_2]_{fire}$ is the fuel-to-oxygen ratio in the fire, and $[fuel/O_2]_{stoichiometric}$ is the fuel-to-oxygen ratio required for complete combustion. In most instances, the equivalence ratio cannot be measured directly in a large-scale test such as this. Different materials burned at different times and in different environments. Ventilation, and thus the equivalency ratio is not uniform in situations where objects are burning in different physical environments, such as burning motor vehicle. It was impossible to isolate and measure the fire products produced by each of the materials burning, and to measure airflow into each of the

unique environments that existed during this test. Estimates of the average ventilation was obtained from the data acquired during this test.

Heat and combustion gases produced by all burning objects in the test vehicle rose into the Fire Products Collector at the test facility. Thus, data from the Fire Products Collector can be used to estimate an average ventilation for the burning vehicle. A similar approach can be used to estimate an average ventilation for the passenger compartment from the gas concentration measurements from the FTIR gas analyzer and the air temperature data from the aspirated thermocouples. Estimation of ventilation from the data is done by comparison to the results obtained from testing individual materials in small-scale flammability tests,[19] where the equivalence ratio can be measured precisely [9].

Five derived parameters were used in this comparison. Values of these parameters for polymeric materials similar to those used in the test vehicle are shown in Table 2.

Table 2

Fire Products for Well-ventilated Fires[1,2]

| material | $Y(CO)/Y(CO_2)$ (g/g) | $Y(HC)/Y(CO_2)$ (g/g) | $Y(CO_2)/\Delta H_{CON}$ (g/kJ) | $Y(CO)/\Delta H_{CON}$ (g/kJ) | $Y(HC)/\Delta H_{CON}$ (g/kJ) |
|---|---|---|---|---|---|
| gasoline[3] | 0.011 – 0.014 | 0.0032 – 0.0039 | 0.14 – 0.16 | 0.0021 – 0.0026 | 0.00058 – 0.00073 |
| poly(ethylene) | 0.0087 | 0.0025 | 0.13 | 0.0011 | 0.00032 |
| poly(propylene) | 0.0086 | 0.0022 | 0.12 | 0.0011 | 0.00027 |
| poly(styrene) | 0.026 | 0.0060 | 0.21 | 0.0054 | 0.00127 |
| polyester | 0.05 | 0.019 | 0.15 | 0.0065 | 0.00185 |
| Nylon | 0.018 | 0.0078 | 0.13 | 0.0035 | 0.00098 |
| Flexible urethane foams | 0.006 - 0.027 | 0.0013 - 0.0033 | 0.15 - 0.21 | 0.0012 - 0.0055 | 0.00023 - 0.00069 |
| Rigid urethane foams | 0.015 - 0.046 | 0.006 - 0.036 | 0.17 - 0.23 | 0.0028 - 0.0081 | 0.00011 - 0.00070 |

[1]Values reported in Table 2 were calculated from data reported in Table 3-4.11 in reference 9.

[2]Y(CO) is the mass-yield of carbon monoxide (g). $Y(CO_2)$ is the mass-yield of carbon dioxide (g). Y(HC) is the mass-yield of gaseous hydrocarbons (g). $Y(CO_2)/\Delta H_{con} = (C_{CO_2}/c_p\Delta T)(\rho_{CO_2}/\rho_{air})$, $Y(CO)/\Delta H_{con} = (C_{CO}/c_p\Delta T)(\rho_{CO}/\rho_{air})$, and $Y(HC)/\Delta H_{con} = (C_{HC}/c_p\Delta T)(\rho_{HC}/\rho_{air})$. $\Delta H_{CON}$ is the convective heat of combustion per unit fuel vaporized (kJ/g). The $C_j$ are the gas-phase concentrations (volume fraction) of carbon dioxide, carbon monoxide, and total hydrocarbons. The $\rho_j$ are the gas-phase densities ($g/m^3$) of carbon dioxide, carbon monoxide, total hydrocarbons, and air. $c_p$ is the heat capacity of air (kJ/g-K). $\Delta T$ is the difference between the gas temperature and the temperature of the ambient air (K).

[3]Values for gasoline were estimated from the data in Table 3-4.11 in reference 9 assuming an aliphatic hydrocarbon content of 60 to 70 % and an aromatic hydrocarbon content of 30 to 40%.

[19] Small-scale flammability tests to determine combustion properties of materials were conducted in the Factory Mutual Research Corporation Flammability Apparatus (see reference 9).

These parameters include $Y(CO)/Y(CO_2)$, $Y(HC)/Y(CO_2)$, $Y(CO_2)/\Delta H_{CON}$, $Y(CO)/\Delta H_{CON}$, $Y(HC)/\Delta H_{CON}$. The values in Table 2 were determined for the well-ventilated combustion of a poly(ethylene), a poly(propylene), a poly(styrene), a polyester, a Nylon, a group of flexible urethane foams, and a group of rigid urethane foams.[20]

Figures 48 and 49 show plots of $[G_{CO}]/[G_{CO2}]$ and $[G_{HC}]/[G_{CO2}]$, respectively, versus time post-ignition calculated from the carbon monoxide-, hydrocarbon-, and carbon dioxide-release rates measured using the Fire Products Collector. The ratios $[G_{CO}]/[G_{CO2}]$ and $[G_{HC}]/[G_{CO2}]$ are equivalent to ratios $[Y(CO)]/[Y(CO_2)]$ and $[Y(HC)]/[Y(CO_2)]$, respectively, listed in Table 2. Before ignition, $[G_{CO}]/[G_{CO2}] = [G_{HC}]/[G_{CO2}] = 0$ because $G_{CO} = G_{HC} = G_{CO2} = 0$.

The values of $[G_{CO}]/[G_{CO2}]$ and $[G_{HC}]/[G_{CO2}]$ in Figure 48 are greater than the reference values for $[Y(CO)]/[Y(CO_2)]$ and $[Y(HC)]/[Y(CO_2)]$ in Table 2 for the first 60 to 90 seconds after ignition. Gasoline was the predominant material burning during this time. Values of $[G_{CO}]/[G_{CO2}] > 0.011$ to 0.014 and $[G_{HC}]/[G_{CO2}] > 0.0032$ to 0.0039 indicate that airflow into the flame was insufficient for stoichiometric combustion of the hydrocarbons vaporizing from the gasoline pool. Values of $[G_{HC}]/[G_{CO2}] > 0.0032$ to 0.0039 also indicates that unoxidized or partially oxidized gasoline vapor was entrained in the air drawn into to the Fire Products Collector. At least two factors may have contributed to the under-ventilated combustion conditions. The low clearance between test surface and the underbody of the test vehicle may have restricted airflow into the flames.

Also, the lower surfaces of the fuel tank and floor pan were cool relative to the flame at the beginning of this test, which may have slowed the combustion reactions in the impinging flames. Inefficient combustion would have resulted in higher rates of vaporization of unburned hydrocarbons from the periphery of the gasoline pool and of carbon monoxide-production during the early stages of the fire.

Increases in the overall heat release rate and the combustion efficiency of the fire, and a decrease in the heat flux to the floor pan were coincident with lateral expansion of the burning pool under the test vehicle starting at about 110 seconds post-ignition (see Fig. 7). For example, the heat release rate of the fire increased exponentially between 90 and 240 seconds post-ignition (**APPENDIX H**). The values of $[G_{CO}]/[G_{CO2}]$ and $[G_{HC}]/[G_{CO2}]$ started to decrease between 90 and 100 seconds post-ignition, approaching the ranges expected for well-ventilated combustion by the time fire suppression began. The heat flux to the floor pan was approximately

[16] The compositions and physical properties such as density, thermal conductivity, and heat capacity of these materials were not specified.

constant at 75 W/m$^2$ from about 20 to 110 seconds post-ignition, started to decrease after 110 seconds post-ignition (see Fig. 11).

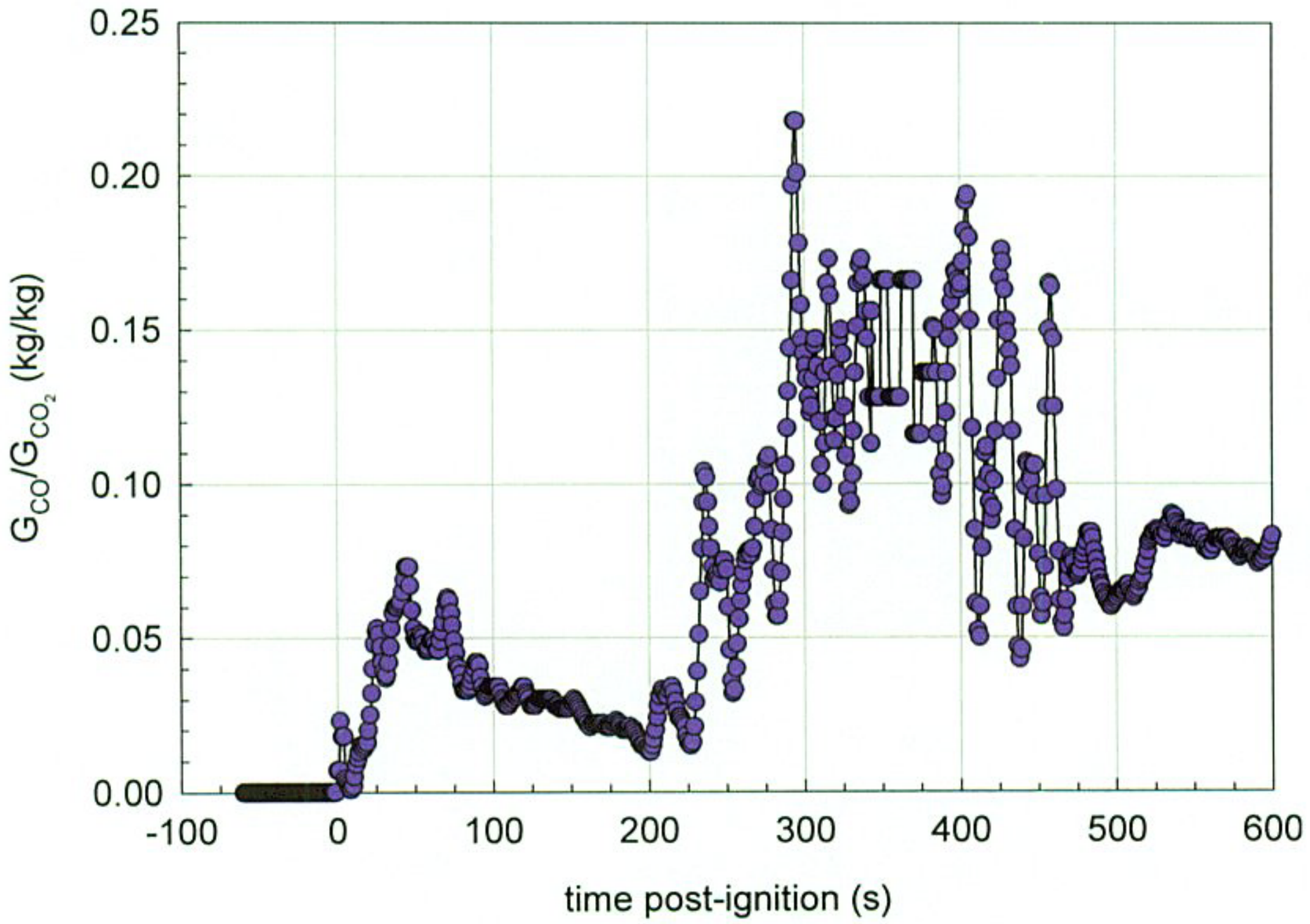


Figure 48. Fire Test F961116. Plot of $[G_{CO}]/[G_{CO2}]$ versus time post-ignition determined from the carbon dioxide- and carbon monoxide-release rates measured by the Fire Products Collector.

Lateral expansion of the burning pool (an increase in pool diameter) was caused by the additional input to the burning pool of melted thermoplastic material dripping from the fuel tank. One consequence of flame-spread to these materials was that a significant portion of the growing fire plume extended out from the restricted space below the test vehicle. This may have allowed higher buoyant flow and greater air entrainment into the flames extending away from the vehicle, resulting in an increase in the overall combustion efficiency observed to have occurred between 80 and 100 seconds post-ignition. At the same time, the heat flux to an area of the floor pan near the center of the pool decreased from approximately 75 to 30 kW/m$^2$ (see Fig. 11). One possible explanation of this is a decrease in oxygen. Expansion of the flames laterally may have resulted in a decrease in air entrainment into the space under the vehicle by oxygen before it reached the center of the flame. Reduction in the amount of oxygen supplied to the flames in this area would have partially inhibited the flame chemistry and reduced its heat output. A correlation between

heat output and ventilation has been demonstrated in laboratory experiments during combustion for a number of solid materials similar to the materials used in the test vehicle [**8**].

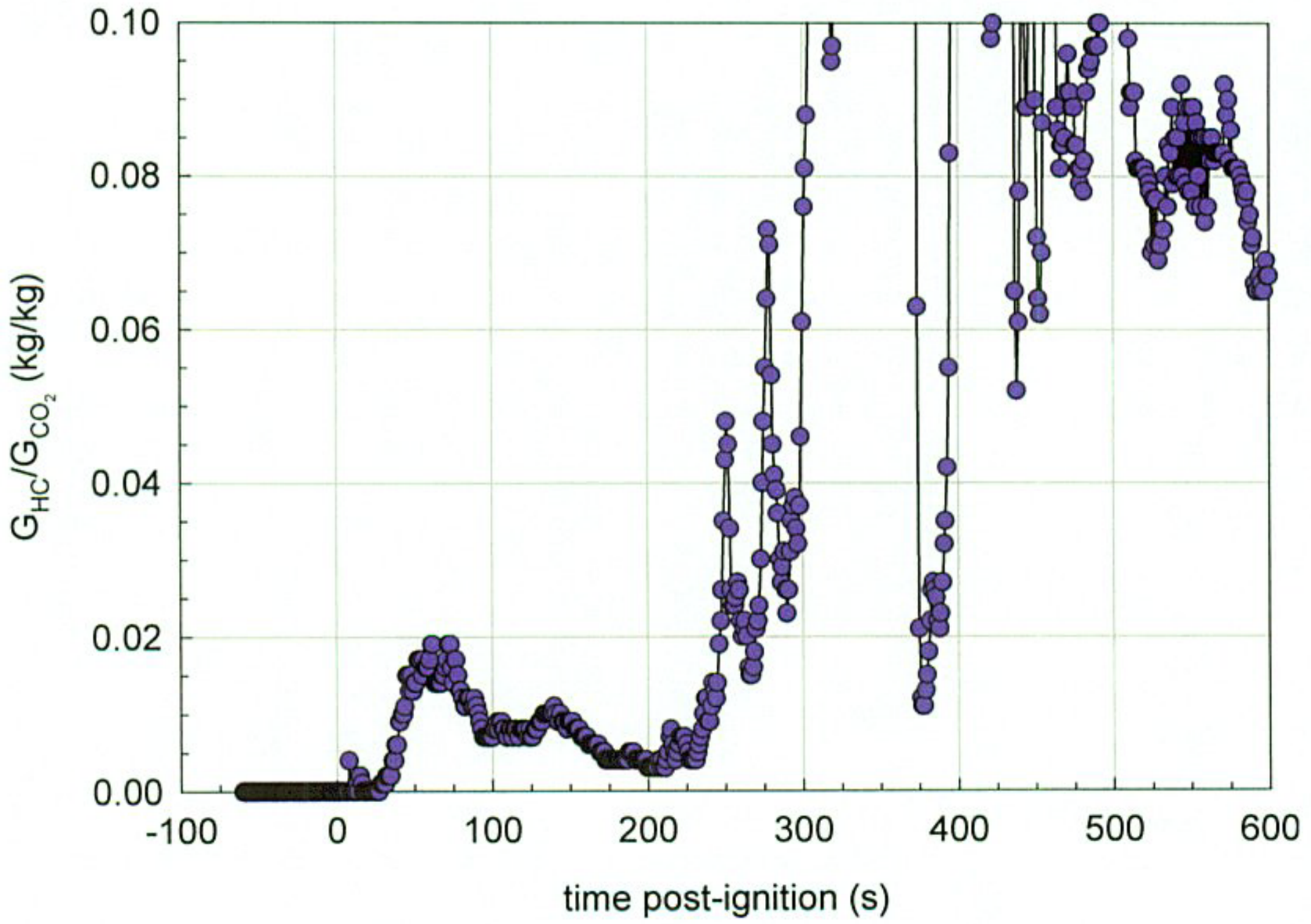


Figure 49. Fire Test F961116. Plot of $[G_{HC}]/[G_{CO2}]$ versus time post-ignition determined from the carbon dioxide- and carbon monoxide-release rates measured by the Fire Products Collector.

The values of $[G_{CO}]/[G_{CO2}]$ and $[G_{HC}]/[G_{CO2}]$ increased sharply at the onset of fire suppression, indicating a transition from well-ventilated combustion to non-flaming combustion or pyrolysis occurred as the flames were being extinguished. Although flames were visibly suppressed relatively quickly, many materials in the test vehicle remained hot enough to produce smoke, indicating thermal decomposition of the materials continued after the flames were visibly extinguished.

Analysis of the gas concentration and air temperature data in the passenger compartment suggests that combustion of materials inside the test vehicle progressed from an under-ventilated toward a well-ventilated condition. Figures 50 through 54 show plots of $M_{CO}/M_{CO2}$, $M_{HC}/M_{CO2}$, $[C_{CO2} \times \rho_{CO2}]/[t_{air} \times Cp]$, $[C_{CO} \times \rho_{CO}]/[t_{air} \times Cp]$, and $[C_{CO2} \times \rho_{CO2}]/[t_{air} \times Cp]$ calculated from this data. These ratios are equivalent to $Y(CO)/Y(CO_2)$, $Y(HC)/Y(CO_2)$, $Y(CO_2)/\Delta H_{CON}$, $Y(CO)/\Delta H_{CON}$, $(HC)/\Delta H_{CON}$, respectively, shown in Table 2. In these calculations, the quantity M(HC) was the

sum of the concentrations of methane, ethane, ethylene, and acetylene measured inside the passenger compartment (**APPENDIX I**).

The trends in the plots reflect combustion conditions in the passenger compartment. For example, the timing of peaks in the plots of $M_{CO}/M_{CO2}$, $M_{HC}/M_{CO2}$, $[C_{CO2} \times \rho_{CO2}]/[t_{air} \times Cp]$, $[C_{CO} \times \rho_{CO}]/[t_{air} \times Cp]$, and $[C_{CO2} \times \rho_{CO2}]/[t_{air} \times Cp]$ correlated with ignition of the left interior quarter trim finishing panel and rear left seat cushion (SECTION 6). The values of $M_{CO}/M_{CO2}$, $M_{HC}/M_{CO2}$, $[C_{CO2} \times \rho_{CO2}]/[t_{air} \times Cp]$, $[C_{CO} \times \rho_{CO}]/[t_{air} \times Cp]$, and $[C_{CO2} \times \rho_{CO2}]/[t_{air} \times Cp]$ during this time are greater than the respective ranges in Table 2, indicating under–ventilated combustion conditions. Prior to ignition, the materials in these components were heated by gases and flames entering the openings around the wheelhouse and would have undergone thermal decomposition chemical reactions. In the absence of combustion, thermal decomposition reactions are typically endothermic (do not produce heat) and yield complex mixtures of un-oxidized or partially oxidized organic gases. Transition from purely thermal decomposition to well-ventilated combustion of these materials would account for the initial peaks and decreasing values of $M_{CO}/M_{CO2}$, $M_{HC}/M_{CO2}$, $[C_{CO2} \times \rho_{CO2}]/[t_{air} \times Cp]$, $[C_{CO} \times \rho_{CO}]/[t_{air} \times Cp]$, and $[C_{CO2} \times \rho_{CO2}]/[t_{air} \times Cp]$ in Figures 50 through 54.

The air temperature and concentrations of all combustion gases in the passenger compartment decreased when the fire was extinguished. The values of $M_{CO}/M_{CO2}$, $M_{HC}/M_{CO2}$, $[C_{CO2} \times \rho_{CO2}]/[t_{air} \times Cp]$, $[C_{CO} \times \rho_{CO}]/[t_{air} \times Cp]$, and $[C_{CO2} \times \rho_{CO2}]/[t_{air} \times Cp]$ increased approximately 10 fold at this time (Fig. 50 through 54), but it is difficult to interpret the meaning of these increases. Although flaming combustion had ceased, several objects in the passenger compartment continued to thermally decompose. Thus, these increases in these indexes may reflect the transition to non-flaming combustion or pyrolysis. Also, the use of a water mist to extinguish the fire appeared to cool the gases in the passenger compartment, resulting in a rapid decreased in $t_{air}$. and increases in the values of $[C_{CO2} \times d_{CO2}]/[t_{air} \times Cp]$, $[C_{CO} \times \rho_{CO}]/[t_{air} \times Cp]$, and $[C_{CO2} \times \rho_{CO2}]/[t_{air} \times Cp]$.

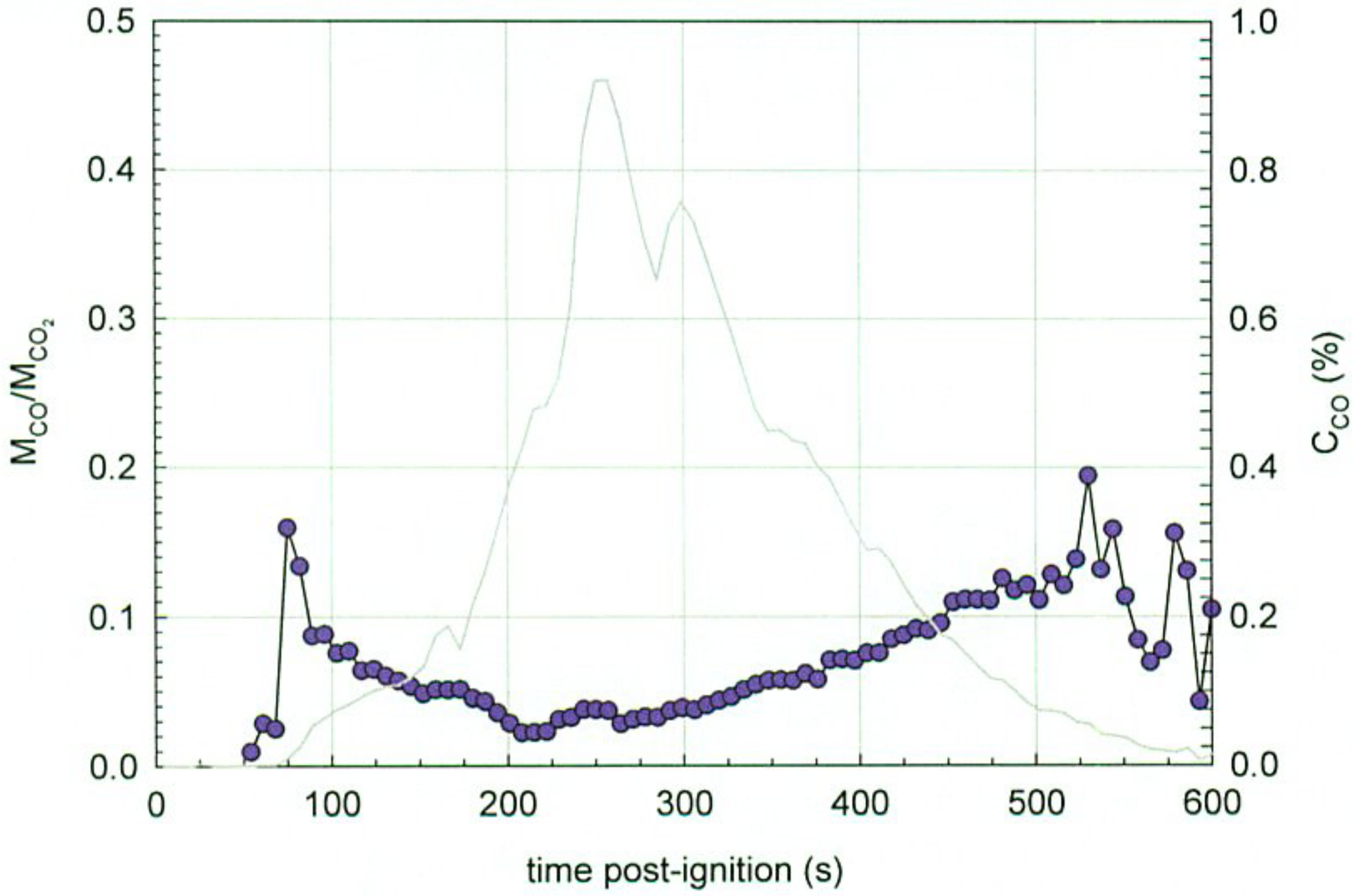


Figure 50. Fire Test F961116. Plots of $[M_{CO}]/[M_{CO2}]$ (—●—, left axis) and $C_{CO}$ (—, right axis) in the passenger compartment.

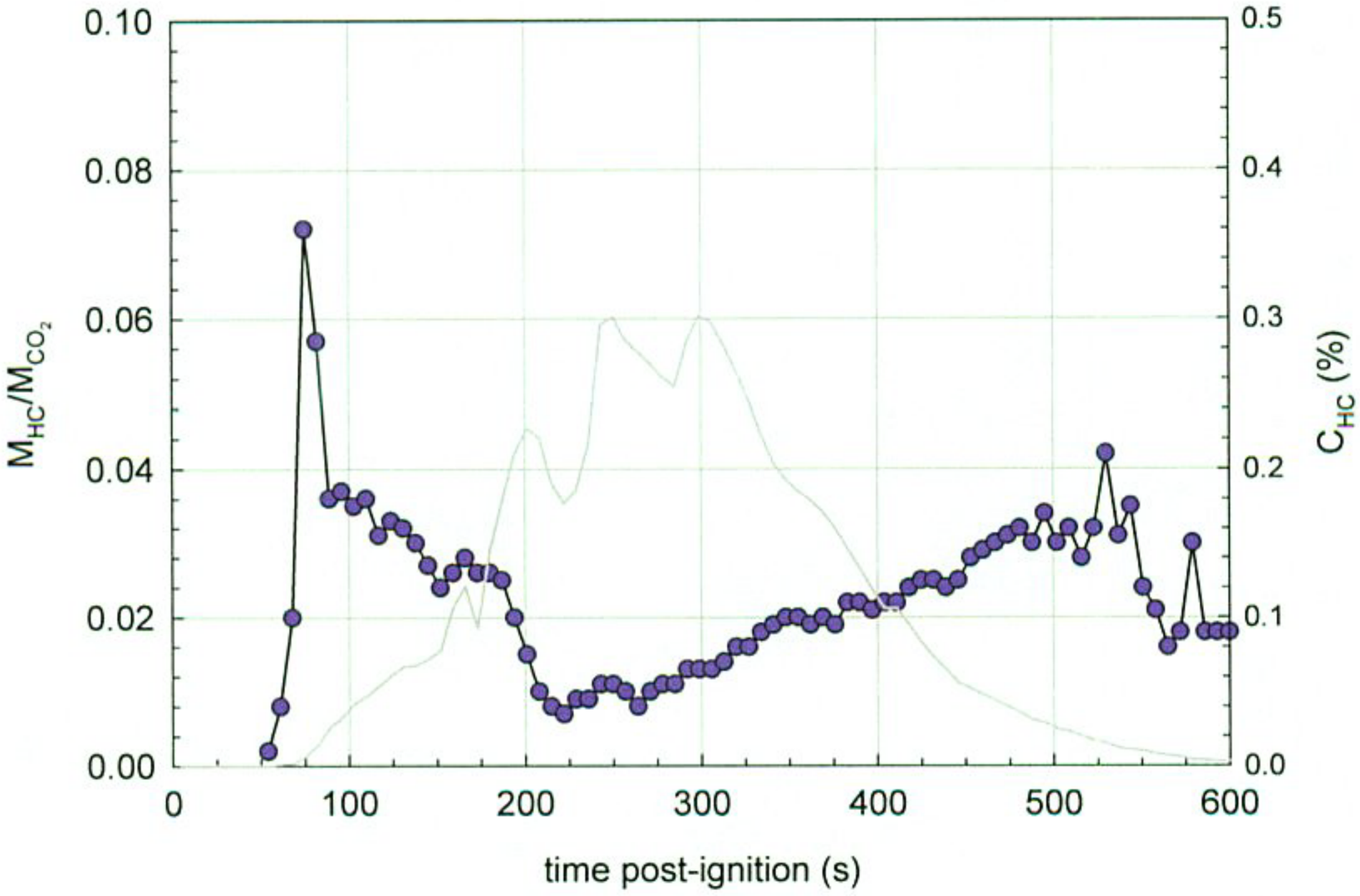


Figure 51. Fire Test F961116. Plots of ratio $[M_{HC}]/[M_{CO2}]$ (—●—, left axis) and $C_{HC}$ (—, right axis) in the passenger compartment.

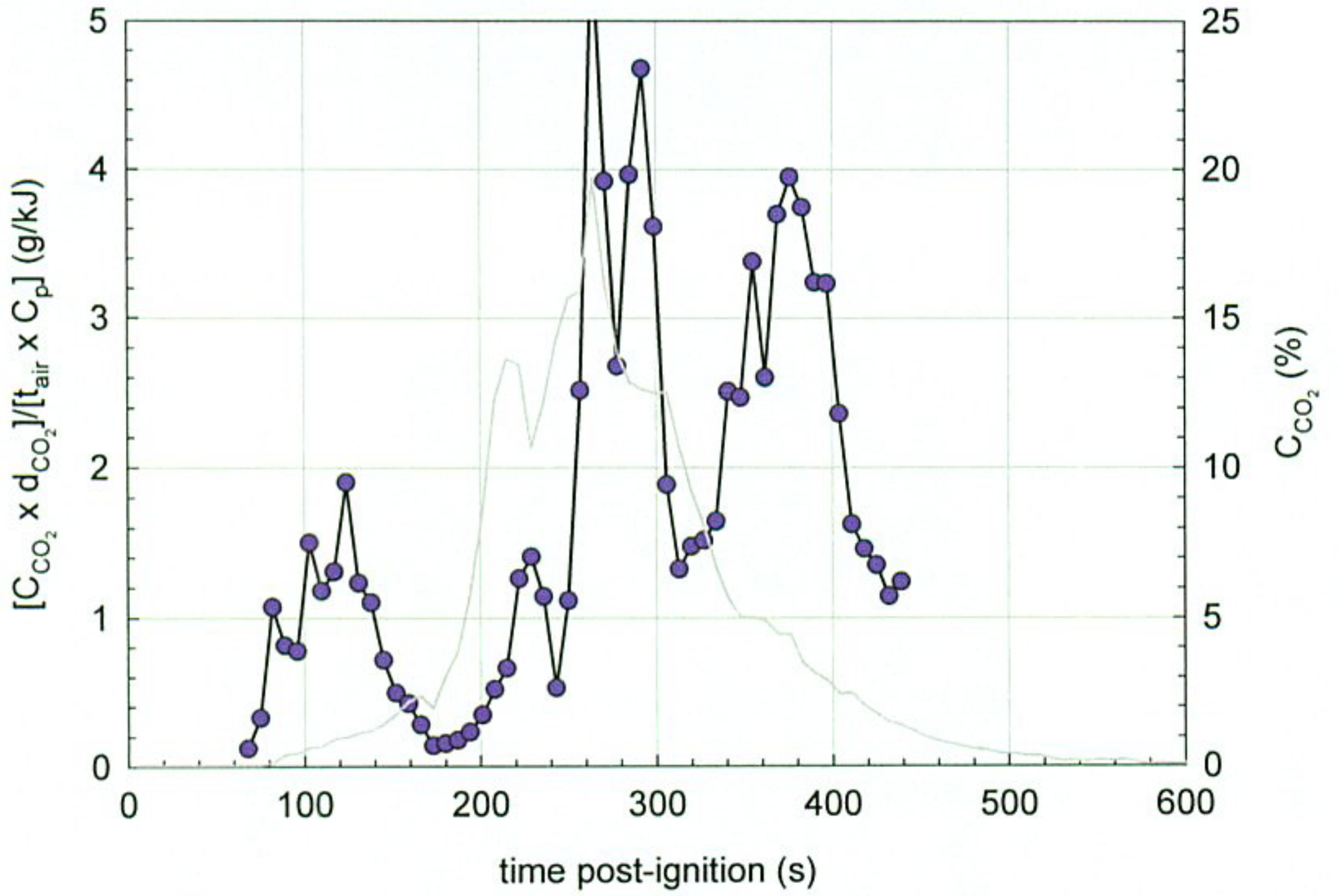


Figure 52. Fire Test F961116. Plots of $[C_{CO2} \times d_{CO2}]/[t_{air} \times Cp]$ (—●—, left axis) $C_{CO2}$ (—, right axis) in the passenger compartment.

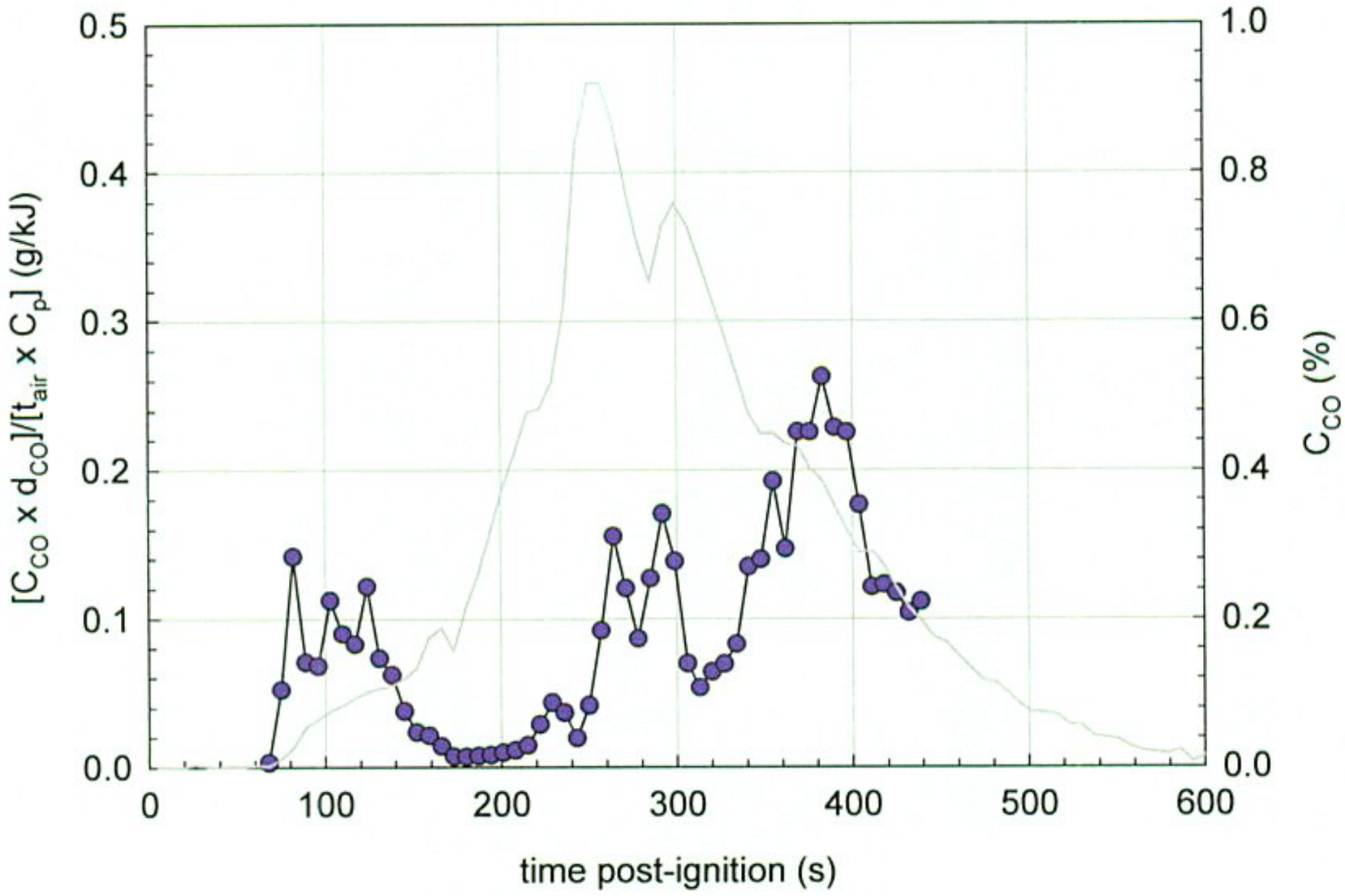


Figure 53. Fire Test F961116. Plots of $[C_{CO} \times d_{CO}]/[t_{air} \times Cp]$ (—●—, left axis) and $C_{CO}$ (—, right axis) in the passenger compartment.

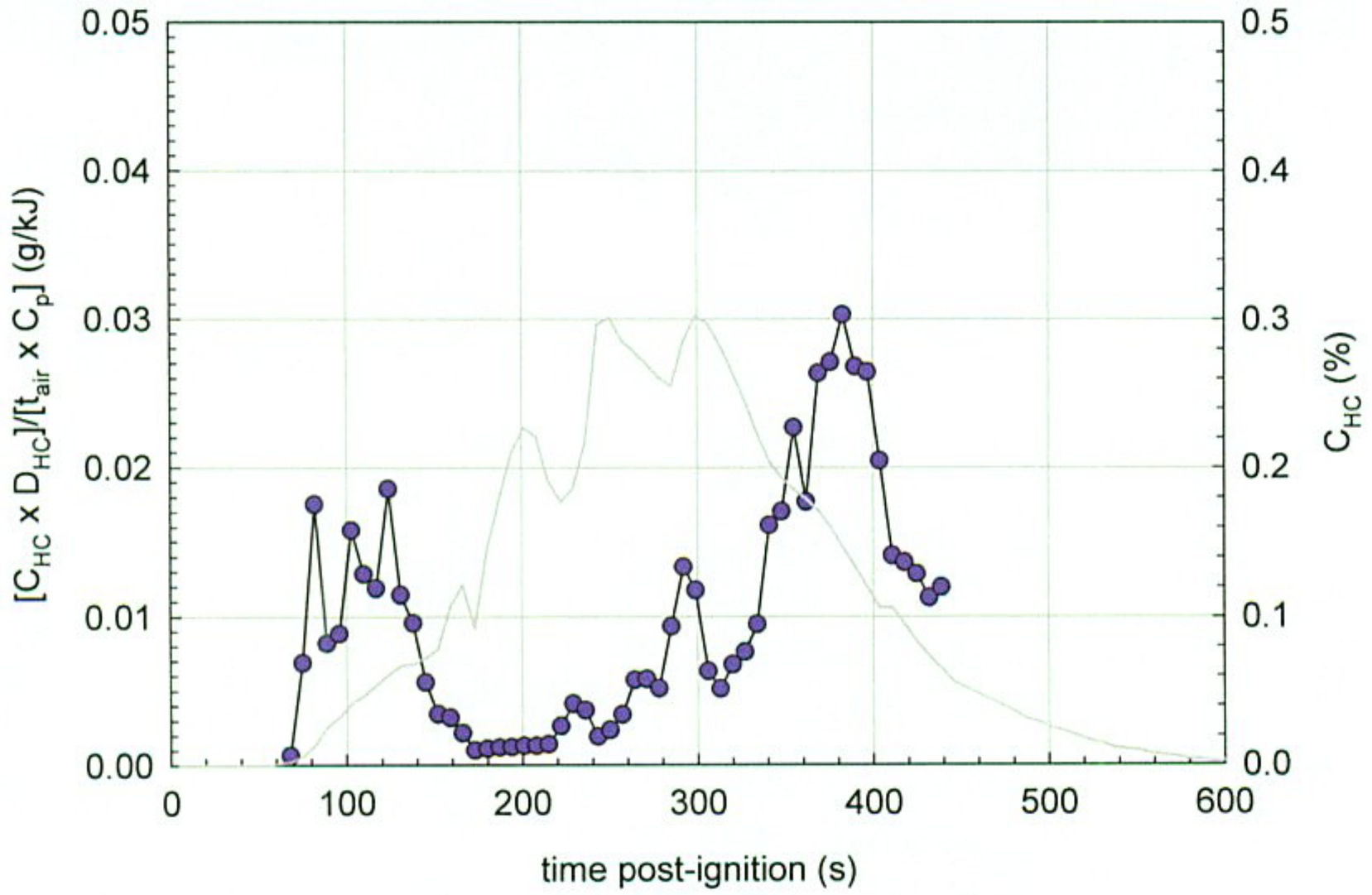


Figure 54. Fire Test F961116. Plots of $[C_{HC} \times d_{HC}]/[t_{air} \times Cp]$ (—●—, left axis) and $C_{HC}$ (—, right axis) in the passenger compartment.

## 8 Estimation of Skin Temperature Profiles from Exposure to Heat and Fractional Equivalent Dose Parameters from Exposure to Combustion Gases

The mathematical model "BURNSIM: A Burn Hazard Assessment Model" [10] was used to estimate the time and depth of burns to exposed skin. The inputs to this model were heat fluxes derived from the directional flame thermometer measurements and air temperatures measured using the aspirated thermocouple probe.

Two models were used to estimate the potential for toxicity from exposure to the combustion gases measured in the passenger compartment. The Federal Aviation Administration (FAA) Combined Hazard Survival Model [11] was used to estimate the time to incapacitation and the time to lethality. A model described by Purser [12] also was used to estimate the time to incapacitation. Both models estimate the risk from exposure to hot air, reduced oxygen, carbon monoxide, carbon dioxide, hydrogen cyanide, hydrogen chloride, hydrogen fluoride, hydrogen bromide, acrolein, and nitrogen dioxide. Both models also account for the physiological effect of carbon dioxide-induced hyperventilation, which increases the respiratory uptake.

### 8.1 The BURNSIM Model

The computer model BURNSIM was the analytical tool chosen to estimate skin temperature depth profiles from the heat flux data in **APPENDIX G**. The BURNSIM model divides the skin into a series of ten layers, with a uniform thickness of 0.2 mm per layer. The top layer was divided into 8 layers each with a uniform thickness of 0.025 mm to better account for the non-instantaneous heat transfer from the epidermal surface into the first layer.

Skin Model of BURNSIM

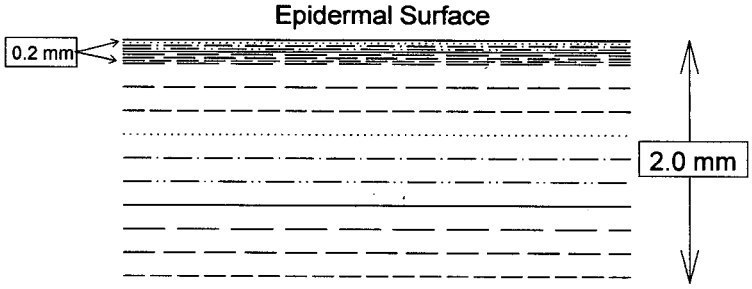


The BURNSIM analysis used here incorporated the following assumptions to estimate skin temperature profiles. The absorbtivity of exposed skin was assumed to be 0.60 (i.e., the skin absorbs 60% of the radiation incident upon the epidermal surface). The absorbtivity of surface

hair was assumed to be 0.05 (i.e., surface hair absorbs 5% of the incident radiation before it reached the skin). Exposed skin was assumed to absorb 100% of the measured convective heat flux to its surface. The temperature of each layer was estimated as a function of the time of exposure to an external heat flux. A portion of the absorbed heat is removed from the skin by the circulatory system. Thermal damage to a layer of skin exceeds the capacity of the physiological repair processes when the temperature of that layer exceeds 45°C.

In estimating skin temperature, the analysis presented in this paper using BURNSIM did not account for the presence of facial or head hair, or clothing covering the skin, all of which may block direct heat transfer to the skin. This analysis also did not account for variations in skin thickness among individuals, or variations in skin thickness at different parts of the body on the same individual. For example, skin thickness can vary from 1 to 5 mm with body location. This analysis also did not account for effect of skin pigmentation on absorbtivity. In using the radiative and convective heat flux estimates shown in **APPENDIX G** to estimate skin temperature profiles, this analysis assumed that the location and orientation of the skin was identical to that of the transducers used to measure heat flux. Small changes in position or angle of the surface of the skin relative to the DFT's in this test can lead to large differences between the actual incident heat flux to exposed and that measured by the DFT (see below). The accuracy of the estimated skin temperature depth profiles obtained by analysis of heat flux data, such as measured in this test, using BURNSIM cannot be determined from currently available information and data.

### 8.1.1 Estimation of Skin Temperature Profiles using BURNSIM

Figures 54 through 61 show skin temperature depth profiles estimated for exposed skin at three locations in the passenger compartment of the test vehicle. These include above the driver's seat, above the center of the first bench seat, and above the center of the second bench seat.

The DFT located above the center of the second bench seat was oriented so that the active surface of the transducer was parallel to the seat cushion and facing downward (Plot F12, **APPENDIX G**). Toward the end of the test, this transducer was heated by radiation from the flames on the seat cushion and by convection from hot gases accumulating just below the headlining. The estimated radiative and convective heat fluxes peaked between 200 and 210 seconds post-ignition at approximately 42 and 8 $Kw/m^2$, respectively (Plot G12, **APPENDIX G**). The estimates of skin temperature at the epidermal surface and sub-dermal interface reached maximums of 137 and 46°C, respectively, between 210 and 230 seconds post-ignition.

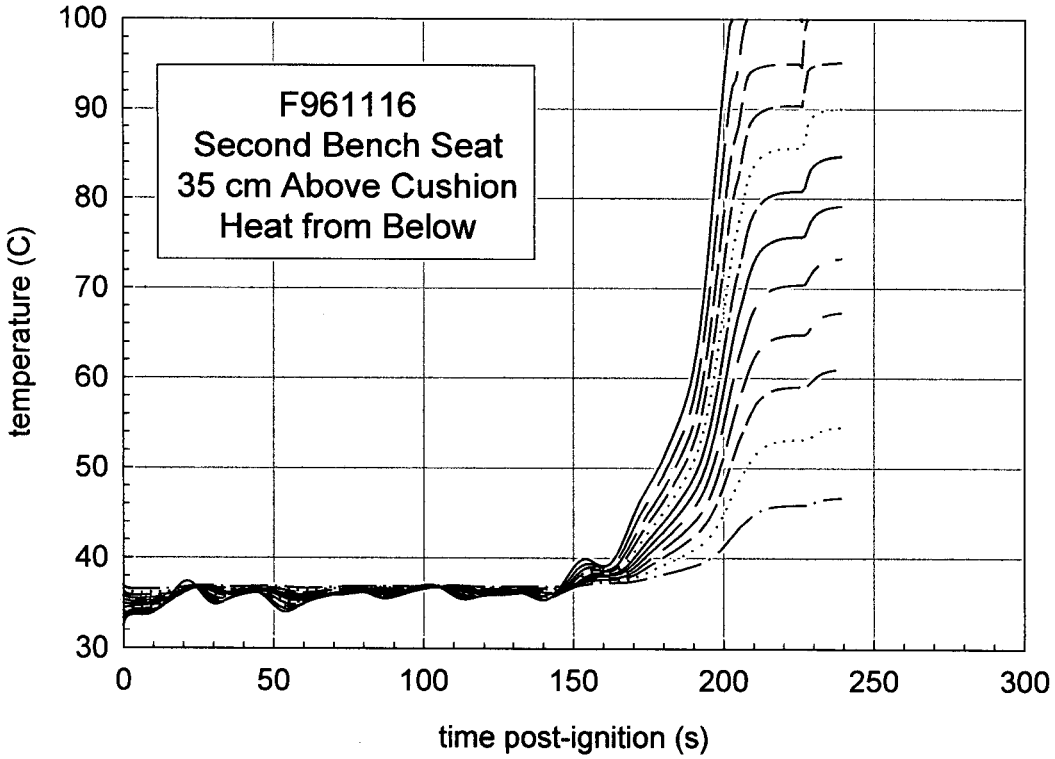


Figure 55. Fire Test F961116. Skin temperature profiles estimated from the heat flux to a downward-facing horizontal surface approximately 35 cm above the second bench seat.

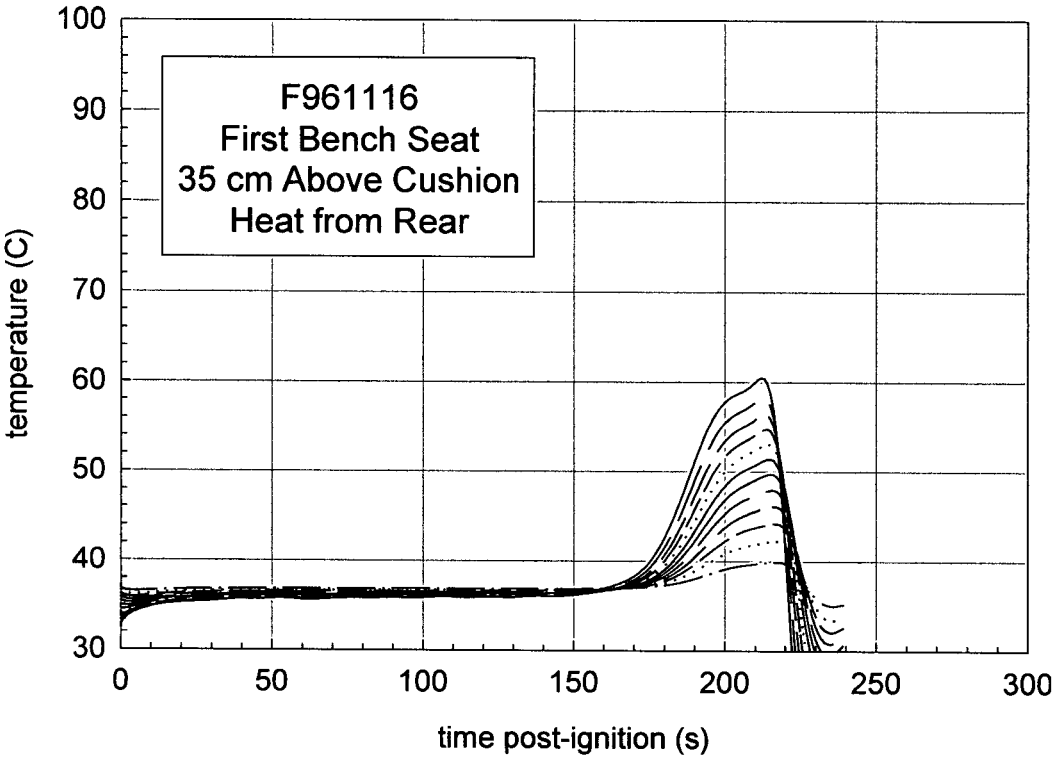


Figure 56. Fire Test F961116. Skin temperature profiles estimated from the heat flux to a rear-facing vertical surface approximately 35 cm above the first bench seat.

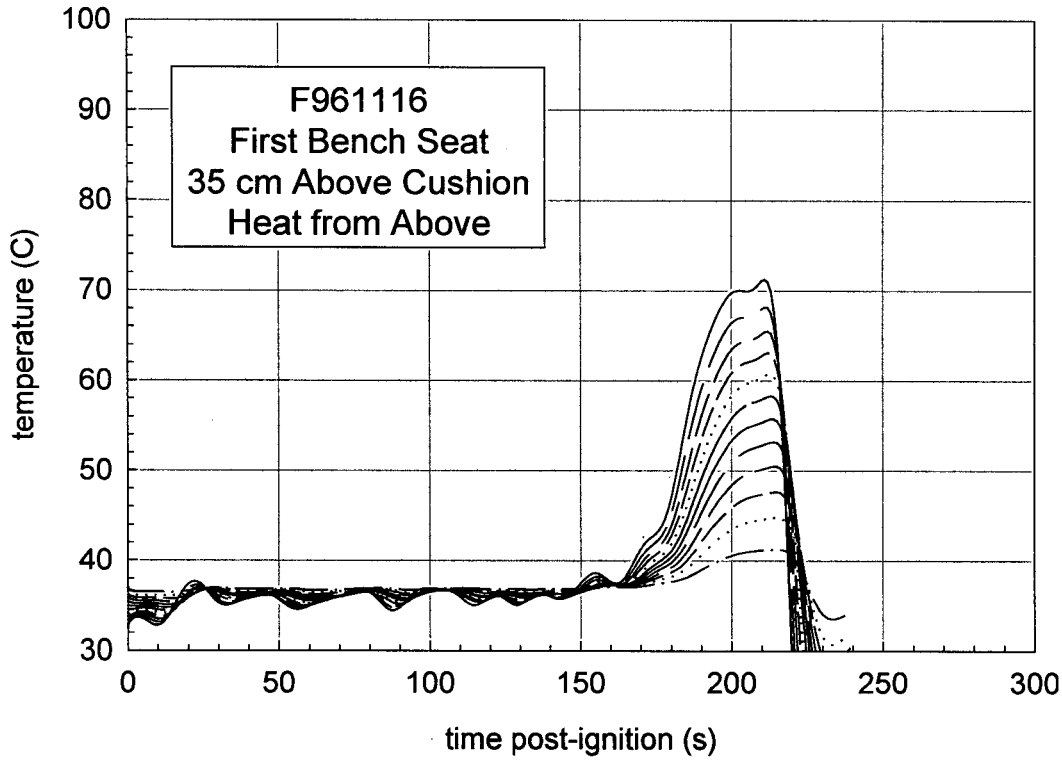


Figure 57. Fire Test F961116. Skin temperature profiles estimated from the heat flux to an upward-facing horizontal surface approximately 35 cm above the first bench seat.

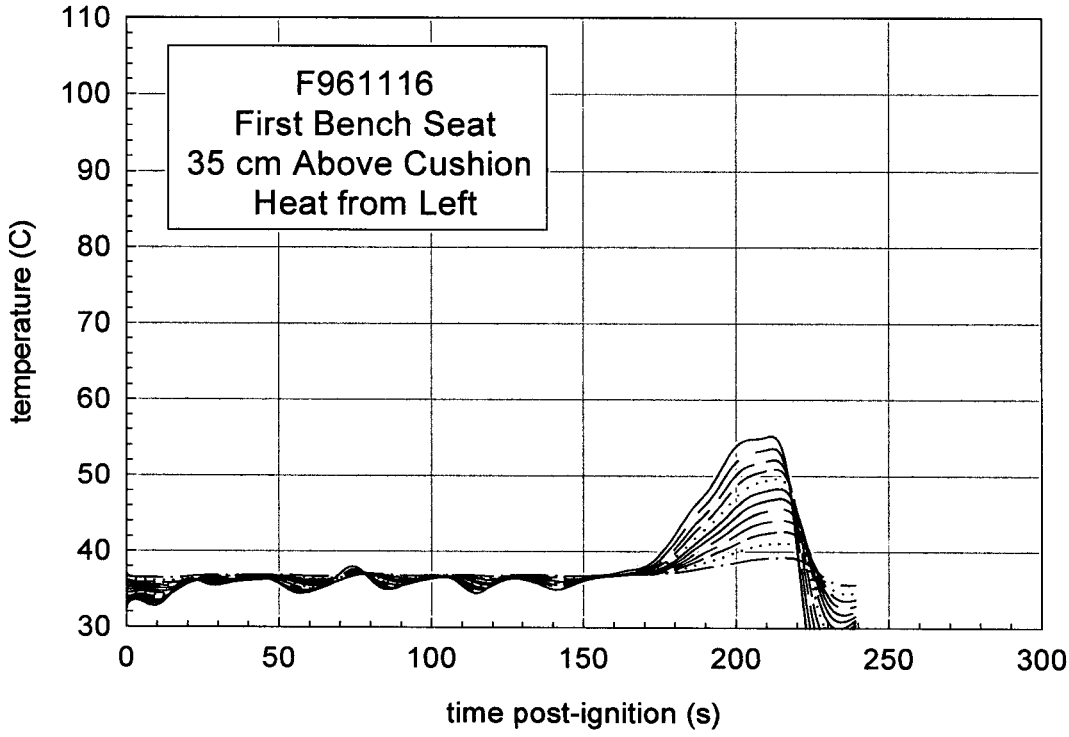


Figure 58. Fire Test F961116. Skin temperature profiles estimated from the heat flux to a left-facing vertical surface approximately 35 cm above the first bench seat.

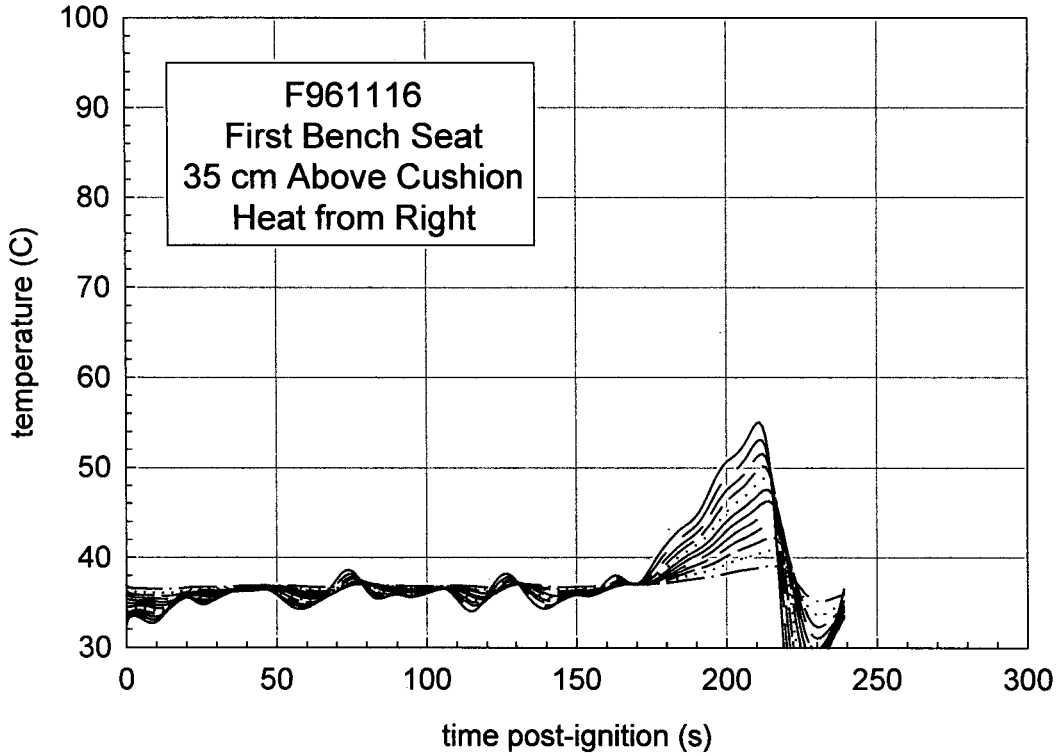


Figure 59. Fire Test F961116. Skin temperature profiles estimated from the heat flux to a right-facing vertical surface approximately 35 cm above the first bench seat.

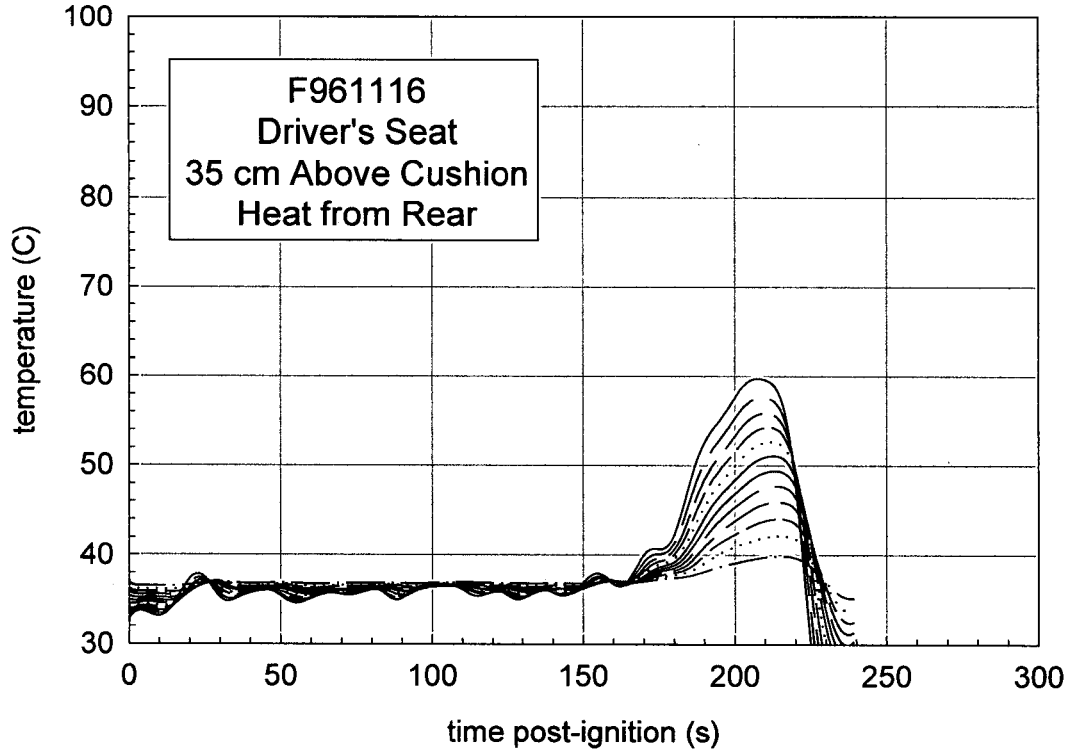


Figure 60. Fire Test F961116. Skin temperature profiles estimated from the heat flux to a rear-facing vertical surface approximately 35 cm above the driver's seat.

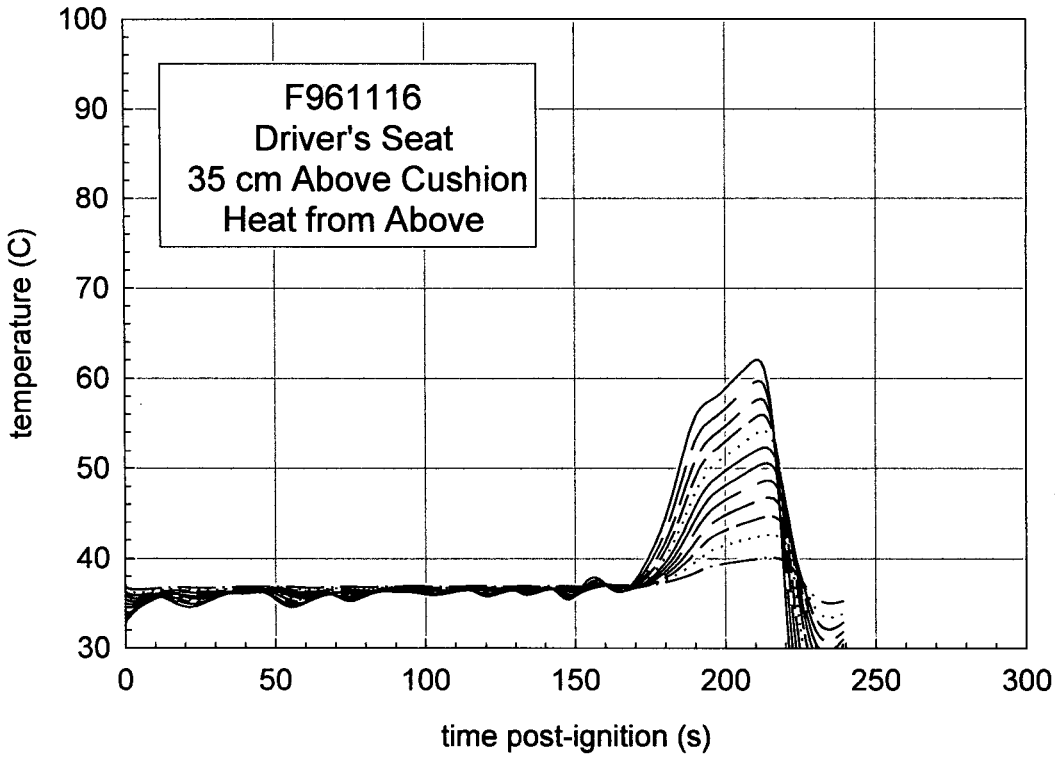


Figure 61. Fire Test F961116. Skin temperature profiles estimated from the heat flux to an upward-facing horizontal surface approximately 35 cm above the driver's seat.

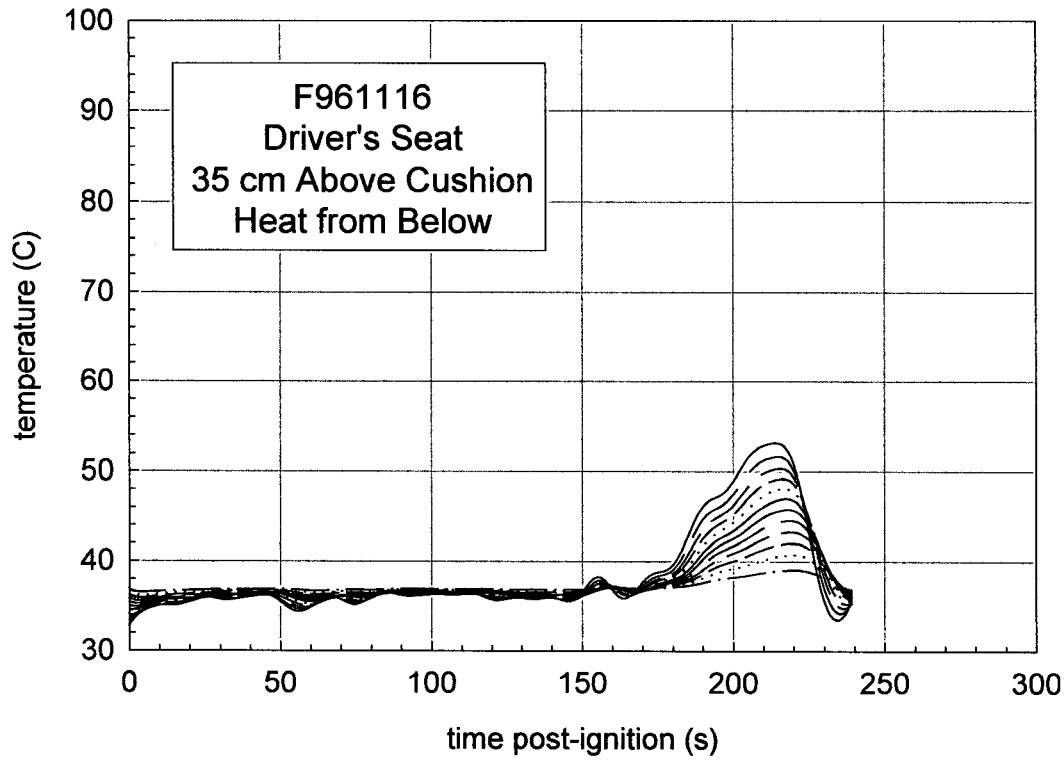


Figure 62. Fire Test F961116. Skin temperature profiles estimated from the heat flux to a downward-facing horizontal surface approximately 35 cm above the driver's seat.

It should be noted that this analysis did not account for the presence of an occupant in the second bench seat. An occupant below the transducer would have attenuated radiative heat transfer from the burning seat cushion upward to the transducer.

The estimated convective heat flux to the DFT's located above first bench seat and above the driver's seat appeared to be independent of transducer orientation and location in the vehicle, and reached peak values ranging from 2.5 to 4.5 $kW/m^2$ between 180 and 210 seconds post-ignition. As would be expected for convective heat transfer to objects located at different heights in an air mass with a large vertical temperature gradient, the estimated convective heat fluxes to these transducers appeared to correlate directly with the height of the transducer in the passenger compartment (see **APPENDIX G**).

The estimated radiative heat fluxes to the DFT's located above the first bench seat and driver's seat appeared to correlate most closely with the orientation of the transducer (Plots G2, G4, G6, G8, G10, and G16 **APPENDIX G**). For example, the estimated peak radiative heat fluxes to DFT's 4 and 14, which were facing up and parallel to the headlining panel, were 13 and 10 $kW/m^2$, respectively, and occurred at approximately 190 seconds post-ignition. The estimated peak radiative heat fluxes to DFT's 1, 2, 3, and 11, which were perpendicular to the headlining, were in the range of 7 to 8 $kW/m^2$ and occurred between 190 and 210 seconds post-ignition (Plots G2, G4, G6, and G10, **APPENDIX G**). The estimated radiative heat flux to DFT 13, which was parallel to the headlining but facing downward, peaked at 4.5 $kW/m^2$ between 200 and 210 seconds post-ignition. The timing of the estimated peak heat fluxes to these transducers correlated with the timing of flame-spread across the headlining above this area (Fig. 34). These results suggest that the predominant mechanism of heat transfer was radiation form the burning headlining. In this case, the angle of the surface of the skin relative to the flames can lead to large differences in the incident heat flux and discrepancies between estimated and actual skin temperatures at a given location.

The skin temperature depth profile estimates from the BURNSIM analysis correlated directly with the total (convective + radiative) heat flux estimates. In general, the highest estimated skin temperatures were obtained with data from the transducers that were facing upward: approximately 71 and 62°C for the first bench and driver's seats, respectively, and both occurring at approximately 210 seconds post-ignition (fig.'s 57 and 61, respectively). The maximum skin temperatures estimated using data from the other DFT's were lower (Fig.'s 56, 58, 59, 60, and 62).

## 8.2 The FAA Combined Hazard Survival Model and Purser's Model of Combustion Gas Toxicity

The FAA Combined Hazard Survival Model and Purser's model utilize the concept of a Fractional Effective Dose [FED] to estimate the cumulative effects of exposure to a mixture of gases produced by burning materials. For exposure to a single gas with an unchanging concentration in air, the Fractional Effective Dose for Incapacitation [FED(I)] is defined as the product of the gas-phase concentration and the time of exposure ($C \times t$) normalized to the concentration-time product that results in incapacitation of 50% of an exposed population [8, 9]. Similarly, the Fractional Effective Dose for lethality [FED(L)] is defined as the product of the gas-phase concentration and the time of exposure normalized to the concentration-time product that results in the death of 50% of an exposed population [see references in 8 and 9]. The estimates of FED(I) and FED(L) obtained using the FAA Combined Hazard Survival Model or Purser's model of combustion gas toxicity and presented in this report cannot be used to predict precisely when the gas concentrations measured in this test would have resulted in incapacitating narcosis or death for a vehicle occupant. Whether exposure to these gases results in toxicity depends on a number of complex physical and physiological variables.

Some of the physical variables include the exact chemical composition of the gaseous mixture, the concentration of each component of the gaseous mixture, and the time of exposure. Exposure to these gases in a burning vehicle can be highly variable, and depend on factors such as elevation in the passenger compartment and airflow through the passenger compartment. As mentioned in the previous section, combustion gases are hotter that the ambient air and form an upper-layer. The air temperature data from the aspirated thermocouples indicated that a steep air-temperature gradient developed in the front of the passenger compartment during this test (see **SECTION 8.3**). Since both heat and mass are conserved in a fire, the existence of a steep vertical air-temperature gradient implies the existence of similarly steep vertical concentration gradients for gaseous combustion products accumulating in the passenger compartment. The location of the head and nose in the passenger compartment will effect the exposure concentration. An occupant whose head was located below the level where gases were measured, such as an occupant bent over in the seat, would have been exposed to lower concentrations of combustion gases than those shown in **APPENDIX I** and in Figures 62 through 65. Airflow through the passenger compartment will dilute or remove these gases.

Uncertainties in the responses of humans exposed to these gases also complicated the determination of when and whether toxicity occurs. The mathematical equations for the calculation of FED(I) and FED(L) were derived by analysis of data from controlled experiments in

which different species of laboratory animals were exposed to a range of concentrations of each gas. In using data from these laboratory animal experiments to define FED(I) and FED(L), both models implicitly assume that humans respond the same as laboratory animals to exposure to these gases – an assumption that is largely untested and may not be accurate. For example, except for incapacitation from exposure to carbon dioxide, none of the model predictions using either the FAA Combined Hazard Survival Model or Purser's model have been validated for humans. That is, the accuracy of FED(I) and FED(L) in predicting human responses to exposure to the combustion gases measured in this test has not been determined. Consequently, there is a high degree of uncertainty as to the effect exposure to these levels of combustion gases would actually have on a human vehicle occupant. In addition, neither of these models accounts for variation in individual responses to these gases nor the effect of trauma suffered during the crash on an occupant's response to these gases.

The equations presented in both the FAA Combined Hazard Survival Model and in Purser's model divide the exposure into one-minute intervals when the concentration of the gaseous species changes with time. In this test, Fourier Transform Infrared spectra were obtained at seven-second intervals to characterize the changing gas concentrations observed in the passenger compartment. The equations presented in the FAA Combined Hazard Survival Model and in Purser's model were modified to account for the faster sampling times used in this test. These modified equations are shown below and were used to derive the estimated of FED(I) and FED(L) shown in **SECTION 8.2.1.**

Carbon dioxide-induced hyperventilation can increase the respiratory uptake of airborn combustion products. The FAA Combined Hazard Survival Model uses a multiplication factor to account for the increased respiratory uptake of gaseous combustion products because of exposure to elevated levels of carbon dioxide [$V_{CO2}$]:

$$V_{CO_2} = \frac{\exp(1.9086 + 0.2496 \times C_{CO_2})}{6.8} \qquad (1)$$

where the units of $C_{CO2}$ are %. This equation was not modified for the analysis presented in **SECTION 8.2.1**.

The Fractional Effective Doses for Incapacitation from exposure to carbon dioxide, carbon monoxide, hydrogen chloride, hydrogen cyanide and decreased oxygen were calculated using the following equations modified to account for sampling intervals of less than 1 minute:

$$FED(I)_{CO_2} = \left(\frac{t}{60}\right) \times \sum \left\{ \frac{1}{2193.8 - \left(311.6 \times C_{CO_2}\right)} \right\} \quad (2)$$

when $5.5 \leq C_{CO2} \leq 7.0\%$,

$$FED(I)_{CO_2} = \left(\frac{t}{60}\right) \times \sum \left\{ \frac{1}{\exp\left(6.1623 - \left(0.5189 \times C_{CO_2}\right)\right)} \right\} \quad (3)$$

when $C_{CO2} > 7.0\%$,

$$FED(I)_{CO} = \left(\frac{t}{60}\right) \times \left(\frac{1}{3.4250}\right) \times \sum \left\{ V_{CO_2} \times C_{CO} \right\} \quad (4)$$

when $V_{CO2} \times C_{CO} > 0.01\%$,

$$FED(I)_{HCl} = \left(\frac{t}{60}\right) \times \sum \left\{ \frac{1}{3 + \frac{336{,}000}{\left(V_{CO_2} \times C_{HCl}\right) - 300}} \right\} \quad (5)$$

when $V_{CO2} \times C_{HCl} > 300$ ppm;

$$FED(I)_{HCN} = \left(\frac{t}{60}\right) \times \left(\frac{1}{564}\right) \times \sum \left\{ \left(V_{CO_2} \times C_{HCN}\right) - 63 \right\} \quad (6)$$

when $V_{CO2} \times C_{HCN} > 63$ ppm; and

$$FED(I)_{O_2} = \left(\frac{t}{60}\right) \times \sum \left\{ \frac{1}{\exp\left(8.55 - \left(0.511 \times \left(20.9 - C_{O_2}\right)\right)\right)} \right\} \quad (7)$$

when $C_{O2} < 11\%$. The value of t in these equations was the time in seconds between acquisition of FTIR spectra. The overall Fractional Effective Dose for Incapacitation was calculated by summing the terms in equations 2 through 7:

$$FED(I)_{TOTAL} = FED(I)_{CO_2} + FED(I)_{CO} + FED(I)_{HCl} + FED(I)_{HCN} + FED(I)_{O_2} \quad (8)$$

The Fractional Effective Doses for Lethality from exposure to carbon monoxide and hydrogen cyanide were calculated using the following equations modified to account for sampling intervals of less than 1 minute:

$$FED(L)_{CO} = \left(\frac{t}{60}\right) \times \sum \left\{ \frac{1}{\exp\left(5.85 - \left(0.00037 \times V_{CO_2} \times C_{CO}\right)\right)} \right\} \qquad (9)$$

when $2000 \leq V_{CO2} \times C_{CO} \leq 9000$ ppm,

$$FED(L)_{CO} = \left(\frac{t}{60}\right) \times \sum \left\{ \frac{1}{0.4 + \left(\frac{58{,}000}{V_{CO_2} \times C_{CO}}\right)} \right\} \qquad (10)$$

when $V_{CO2} \times C_{CO} > 9000$ ppm, and

$$FED(L)_{HCN} = \left(\frac{t}{60}\right) \times \left(\frac{1}{2586}\right) \times \sum \left\{ \left(V_{CO_2} \times C_{HCN}\right) - 43.2 \right\} \qquad (11)$$

when $V_{CO2} \times C_{HCN} > 43.2$ ppm;

The overall Fractional Effective Dose for Lethality was calculated by summing the terms in equations 8 through 10:

$$FED(L)_{TOTAL} = FED(L)_{CO} + FED(L)_{HCN} \qquad (12)$$

The model described by Purser also uses a multiplication factor to account for the enhanced respiratory uptake of toxic gases because of exposure to elevated levels of carbon dioxide:

$$V_{CO_2} = \frac{\exp\left(1.9086 + \left(0.2496 \times C_{CO_2}\right)\right)}{6.8} \qquad (13)$$

The Fractional Effective Doses for Incapacitation from exposure to carbon monoxide and hydrogen cyanide were calculated using the following equations modified to account for sampling intervals of less than 1 minute:

$$FED(I)_{CO_2} = \left(\frac{t}{60}\right) \times \sum \left\{ \frac{1}{\exp\left(6.1623 - \left(0.5189 \times C_{CO_2}\right)\right)} \right\} \quad (14)$$

when $C_{CO2} > 5\%$,

$$FED(I)_{CO} = \left(\frac{t}{60}\right) \times V_{CO_2} \times \sum \left\{ \frac{0.00082925 \times C_{CO}}{30} \right\} \quad (15)$$

where the units of $C_{CO}$ are ppm,

$$FED(I)_{HCN} = \left(\frac{t}{60}\right) \times V_{CO_2} \times \sum \left\{ \frac{4.4}{185 - C_{HCN}} \right\} \quad (16)$$

when $80 \leq C_{HCN} \leq 180$ ppm,

$$FED(I)_{HCN} = \left(\frac{t}{60}\right) \times V_{CO_2} \times \sum \left\{ \frac{1}{\exp\left(5.396 - \left(0.023 \times C_{HCN}\right)\right)} \right\} \quad (17)$$

when $C_{HCN} > 180$ ppm; and

$$FED(I)_{O_2} = \left(\frac{t}{60}\right) \times \sum \left\{ \frac{1}{\exp\left(8.13 - \left(0.54 \times \left(20.9 - C_{O_2}\right)\right)\right)} \right\} \quad (18)$$

when $C_{O2} < 11.3\%$.

As in the FAA model, the value of t in these equations was the time in seconds between acquisition of FTIR spectra. The overall Fractional Effective Dose for Incapacitation was calculated by summing the terms in equations 14 through 18:

$$FED(I)_{TOTAL} = FED(I)_{CO_2} + FED(I)_{CO} + FED(I)_{HCN} + FED(I)_{O_2} \quad (19)$$

Both the FAA Combined Hazard Survival model and Purser's model predict that 50% of an exposed population would experience incapacitating narcosis (*i.e.*, an occupant loses consciousness and would be unable to exit a vehicle without assistance) when $FED(I)_{TOTAL} = 1.0$. Similarly, both of these models predict that 50% of an exposed population would die when $FED(L)_{TOTAL} \geq 1.0$.

### 8.2.1 Estimation of Fractional Equivalent Dose Parameters

The analysis presented in this report includes estimates of FED(I) and FED(L) for carbon dioxide, carbon monoxide, and hydrogen cyanide obtained using the FAA Combined Hazard Survival Model, and estimates of FED(I) for carbon dioxide, carbon monoxide, and hydrogen cyanide obtained using Purser's model for assessment of the toxicity of combustion products. The estimated FED(I) and FED(L) shown in Figures 63 through 67 were obtained using the equations presented in Section 8.2. The concentration of hydrogen chloride exceeded the lower limit of detection of the FTIR gas analysis system after the test was ended and fire suppression began, and therefore was not included in the estimation of any of the FED(I) or FED(L). The other gaseous species included in the FAA Combined Hazard Model and Purser's model were not measured during this test.

Figures 63 through 66 show plots of the estimated $FED(I)_{co2}$, $FED(I)_{co}$, $FED(I)_{HCN}$, and $FED(I)_{TOTAL}$ computed using the FAA Combined Hazard Survival Model and Purser's model for assessment of the toxicity of combustion products. Both models predicted values of $FED(I)_{co2} > 1$ starting at approximately 240 seconds post-ignition, and exceeded a value of $FED(I)_{co2} \approx 5$ at about 260 seconds post-ignition (Fig. 63). The FAA Combined Hazard Survival Model and Purser's model yielded different estimates of $FED(I)_{CO}$ (Fig. 64). In Purser's model, the equation for computation of $FED(I)_{co}$ includes a term for respiratory minute volume. Values of 8.5 and 25 L/min, representing rest or light activity, respectively [11], were used to calculate $FEC(I)_{CO}$. Purser's model yielded estimates of $FED(I)_{CO} > 1$ starting at approximately 245 seconds post-ignition with a respiratory minute volume of 8.5 L/min and $FED(I)_{CO} > 1$ starting at approximately 210 seconds post-ignition with a respiratory minute volume of 25 L/min. The FAA Combined Survival Hazard Model yielded estimates of $FED(I)_{co} > 1$ starting at approximately 215 seconds post-ignition. Both yielded estimated $FED(I)_{HCN} > 1$ starting between 200 and 210 seconds post-ignition, and $FED(I)_{HCN} \approx 5$ by 220 seconds post-ignition (Fig. 65).

Figure 66 shows estimates of $FED(I)_{TOTAL}$ versus time post-ignition computed using the FAA Combined Hazard Survival Model and Purser's model for assessment of the toxicity of combustion products. The FAA Model indicated that hydrogen cyanide, carbon monoxide, and carbon dioxide accounted for 70, 23, and 12%, respectively, of $FED(I)_{TOTAL}$. Purser's model indicated hydrogen cyanide accounted for between 91 and 96% of $FED(I)_{TOTAL}$, carbon monoxide accounted for between 2 and 7% of $FED(I)_{TOTAL}$, and carbon dioxide accounted for less that 2% of $FED(I)_{TOTAL}$.

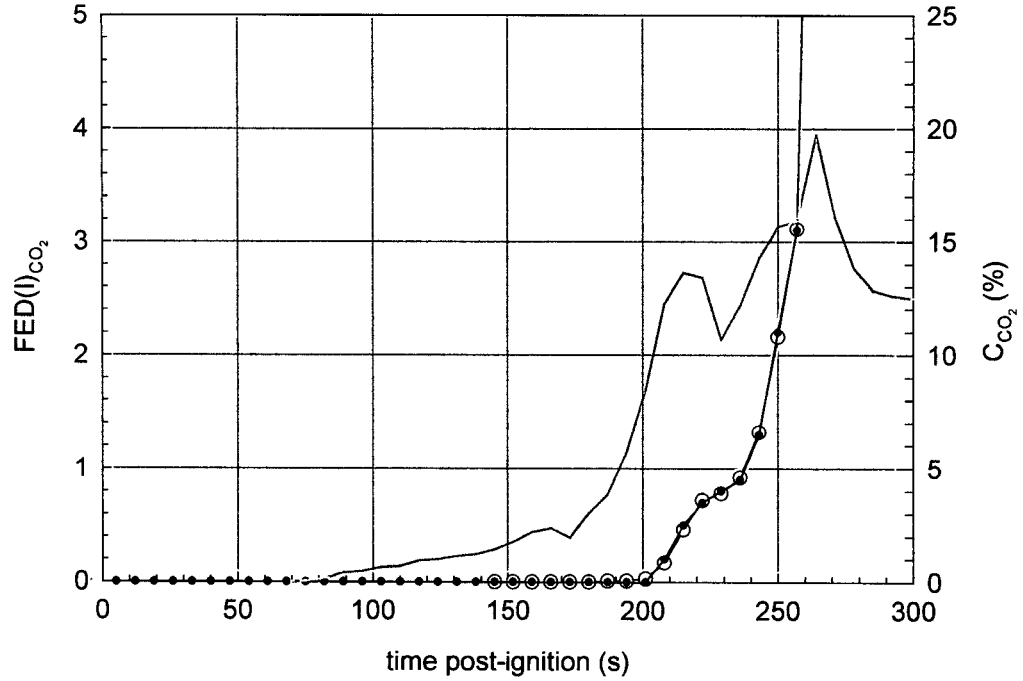


Figure 63. Fire Test F961116. Plots of FED(I)$_{CO2}$ versus time post-ignition: FAA Combined Hazard Survival Model (—O—); and Purser's model (—●—). A plot of $C_{CO2}$ (——) is included for reference.

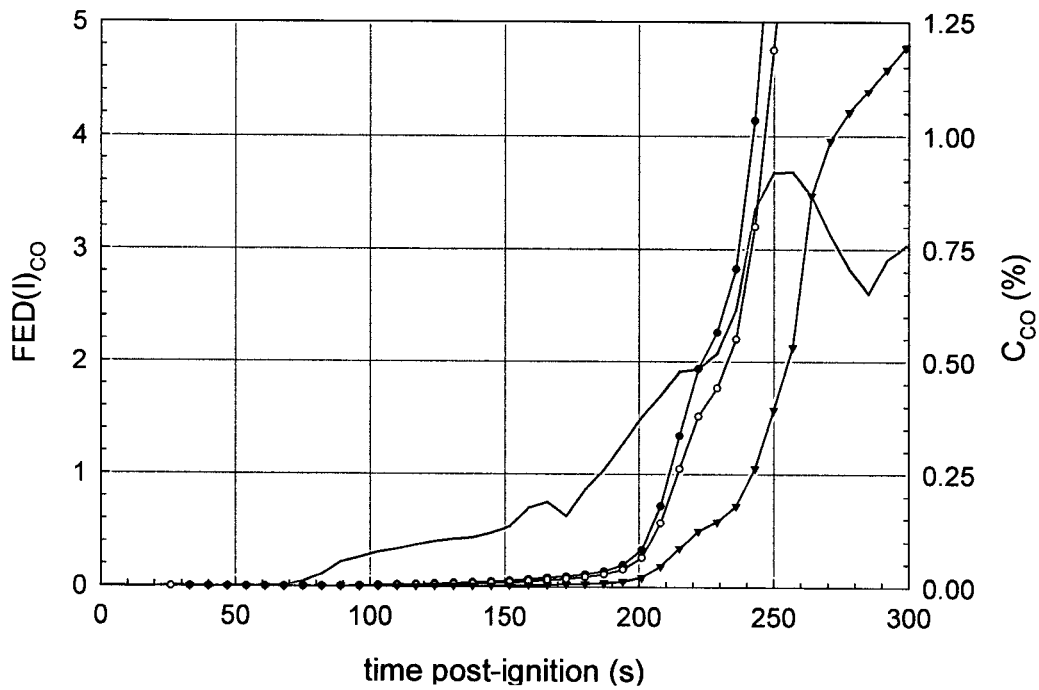


Figure 64. Fire Test F961116. Plots of estimates of FED(I)$_{CO}$ versus time post-ignition computed using the FAA Combined Hazard Survival Model (—O—), the Purser model with a respiratory minute volume of 8.5 L/min (—▼—), and the Purser model with a respiratory minute volume of 25 L/min (—●—). A plot of $C_{CO}$ (——) is included for reference.

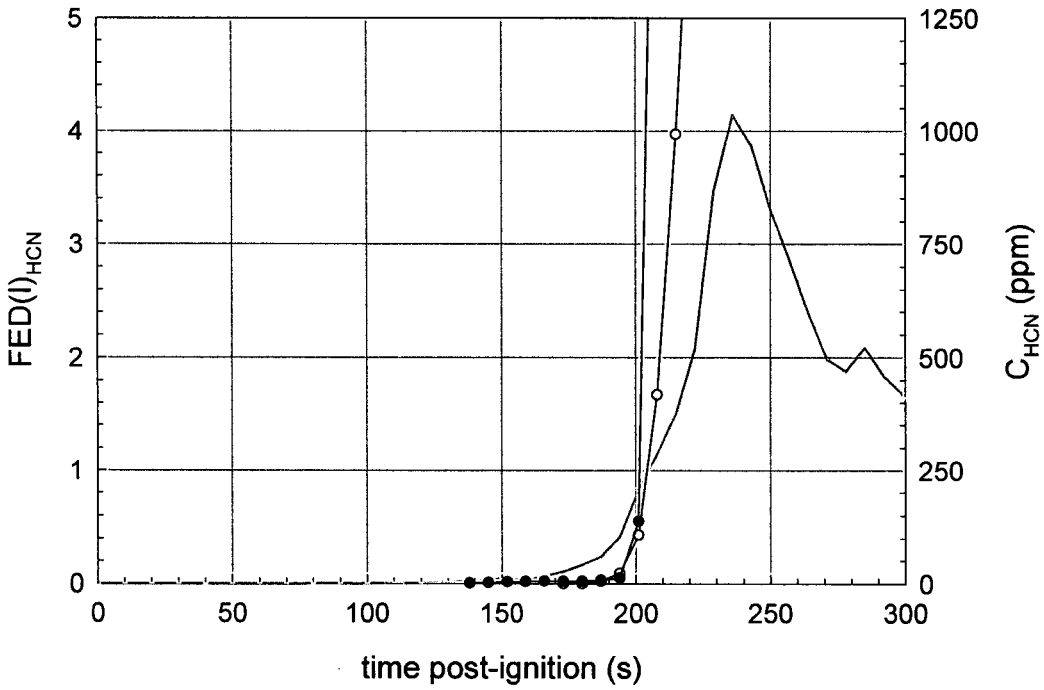


Figure 65. Fire Test F961116. Plots of estimates of $FED(I)_{HCN}$ versus time post-ignition computed using the FAA Combined Hazard Survival Model (—○—) and Purser's model for assessment of the toxicity of combustion products (—●—). A plot of $C_{HCN}$ (——) is included for reference.

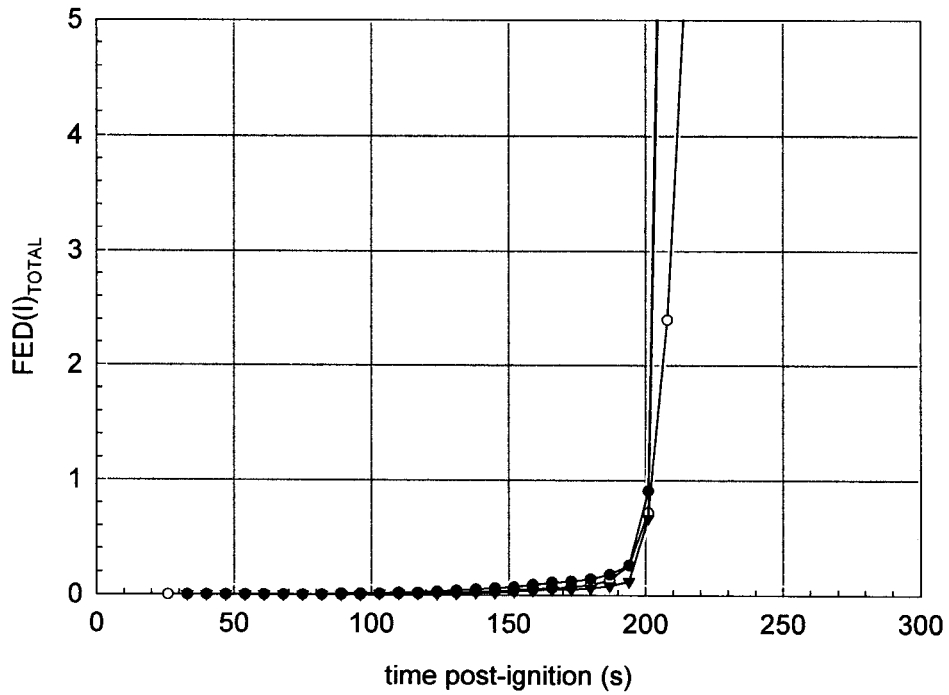


Figure 66. Fire Test F961116. Plots of $FED(I)_{TOTAL}$ versus time post-ignition: FAA Combined Hazard Survival Model (—○—); Purser's model with RMV = 8.5 L/min (—▼—); and Purser's model with RMV = 25 L/min (—●—).

Figure 67 shows plots of $FED(L)_{CO}$, $FED(L)_{HCN}$, and $FED(L)_{TOTAL}$ computed using the FAA Combined Survival Hazard Model.

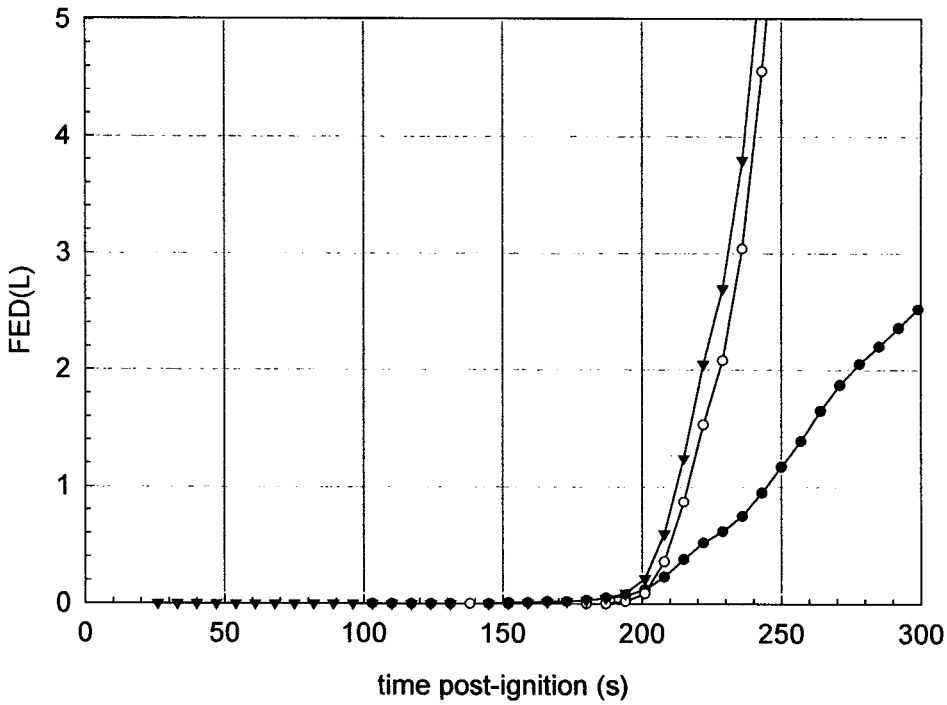


Figure 67. Fire Test F961116. Plots of $FED(L)_{CO}$ (—●—), $FED(L)_{HCN}$ (—○—), and $FED(L)_{TOTAL}$ (—▼—) versus time post-ignition computed using the FAA Combined Hazard Survival Model.

The estimate of $FED(L)_{HCN}$ increased sharply between 180 and 240 seconds post-ignition, exceeding a value of 1 at approximately 200 seconds post-ignition. In contrast, the estimate of $FED(L)_{CO}$, started to increase gradually at the same time, exceeding a value of 1 at approximately 245 seconds post-ignition. And $FED(L)_{TOTAL}$, which is the sum of $FED(L)_{CO}$ and $FED(L)_{HCN}$, also increased sharply between 180 and 240 seconds post-ignition, exceeding a value of 1 at approximately 205 seconds post-ignition, where $FED(L)_{HCN}$ accounted for 70% and $FED(L)_{CO}$ accounted for 30% of $FED(L)_{TOTAL}$. These estimates suggest that the concentrations of combustion gases may have exceeded lethal levels in the front of the passenger compartment after approximately 205 seconds post-ignition.

### 8.3 Estimation of Burn-Injury to the Respiratory Tract

Figure 68 shows plots of the air temperature measured at 1, 4, 7, 10, 13, and 16 inched below the lower surface of the headlining panel versus time post-exposure. These plots show that the average air temperature in the front of the passenger compartment was in the range of 453°C (1

inch below the headlining panel) to 182°C (16 inch below the headlining panel) between 180 and 210 seconds post-ignition.

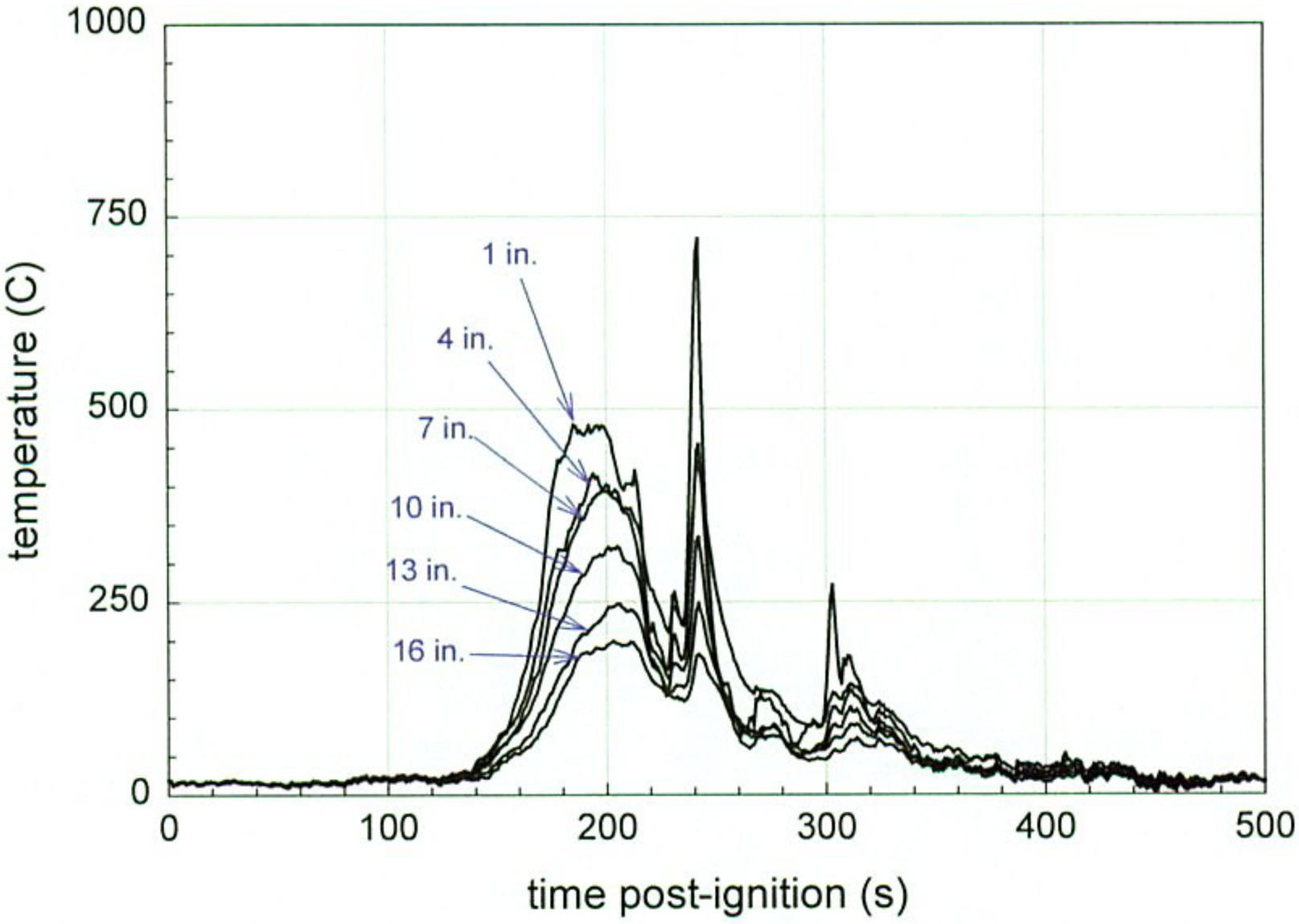


Figure 68. Fire Test F961116. Plots of air temperature at 1, 4, 7, 10, 13, and 16 inches below the lower surface of the headlining panel versus time post-ignition.

As the data in Figure 68 shows, the temperature of the air inhaled by an occupant in the front of the test vehicle at this time would have depended on the height of the occupant's head. It is impossible to estimate the potential for burn injury to the respiratory tract caused by inhalation of hot air from this air temperature data alone. Water and particulate produced by the fire increase the heat capacity of the air. The concentrations of these species in the inhaled air have been shown to affect both the severity and depth of burn injury in the respiratory system. Neither the water- nor the particulate-concentrations of air in the passenger compartment were measured in this test. Purser states that a robust quantitative relationship between the temperature, water-content, and particulate-content of inhaled air and subsequent burn injury to respiratory airways has not been established [11]. A few controlled animal studies indicate that inhalation of steam at 100°C caused burns to the larynx and trachea similar to those produced by inhalation of dry air at 350°C or flames at 500°C [see references in 11]. In these controlled animal studies, death was not immediate, but resulted from obstructive edema in the burned airways a few to twenty-four hours after the exposure. As neither water nor particulate were measured in the air sampled from the passenger compartment during this test, the potential for burn injury to the respiratory airways

from inhalation of hot gas cannot be determined accurately from the air temperature data shown in Figure 68.

## ACKNOWLEDGEMENTS

Dr. Thomas Ohlemiller and Thomas Cleary of the Building and Fire Research Laboratory, National Institute of Standards and Technology were responsible for video taping this fire test, and provided an initial analysis of the test data for fire propagation. Dr. Archibald Tewarson of Factory Mutual Research Corporation provided the data from the Fire Products Collector at the test facility that was collected during this test.

## REFERENCES


1. Jack L. Jensen and Jeffrey Santrock. Evaluation of Motor Vehicle Fire Initiation and Propagation. Part 1: Vehicle Crash Test and Fire Propagation Test Program. Submitted to the National Highway Transportation Safety Administration pursuant to the Settlement Agreement between General Motors and the Department of Transportation. Submitted July 31, 1997.

2. Final Report of Deformable Impactor into Rear of 1996 Plymouth Voyager Minivan at 80 kph with 70% Overlap. April 19, 1996. NHTSA Technical Reference Division. Washington, DC. Report No. TRC-95-V006.

3. Federal Safety Standards. Motor Vehicle Safety Standard No. 214 Side Impact Protection - Passenger Cars, Trucks, Buses & Multipurpose Passenger Vehicles with GVWR of 10,000 Pounds or Less. 60FR57838-39 (November 22, 1995).

4. Federal Safety Standards. Motor Vehicle Safety Standard No. 301 Fuel System Integrity - Passenger Cars; MPV's, Trucks and Busses with GVWR of 10,000 Pounds or Less; and School Buses with GVWR Greater than 10,000 Pounds. 61FR19201-02 (May 1, 1996)

5. Thomas J. Ohlemiller and Thomas G. Cleary. Aspects of the Motor Vehicle Fire Threat from Flammable Liquid Spills on a Road Surface. National Institute of Standards and Technology Internal Report NISTIR 6147. March 1998. Submitted to the National Highway Transportation Safety Administration in partial fulfillment of the General Motors/Department of Transportation Settlement Agreement. Submitted on September 9, 1998.

6. SigmaPlot® 4.0 for Windows®, SPSS Inc., 444 North Michigan Avenue, Chicago, IL 60611. Copyright © 1997 by SPSS Inc..

7. Thomas J. Ohlemiller and John R. Shields. Burning Behavior of Selected Automotive Parts from a Minivan. National Institute of Standards and Technology Internal Report NISTIR 6143. August 1998. Submitted to the National Highway Transportation Safety Administration pursuant to the Settlement Agreement between General Motors and the Department of Transportation. Submitted September 9, 1998.

8. Ismat A. Abu-Isa, David R. Cummungs, Douglas E. La Due, and Archibald Tewarson. Thermal Properties and Flammability Behavior of Automotive Polymers. Submitted to the National Highway Transportation Safety Administration pursuant to the Settlement Agreement between General Motors and the Department of Transportation. Submitted on March 23, 1999.

9. Archibald Tewarson. "Generation of Heat and Chemical Compounds in Fires" Section 3/Chapter 4, SFPE Handbook of Fire Protection Engineering, 2nd Edition, 1995, pp. 3:53-124.

10. F. S. Knox III, Dena Bonetti, and Chris Perry. User's Manual for BRNSIM/BURNSIM: A Burn Hazard Assessment Model. United States Army Aeromedical Research Laboratory Report No. 93-13. Fort Rucker, Alabama 36362-5292. February 1993.

11. L. C. Speitel. Toxicity Assessment of Combined Gases and Development of a Survival Model. DOT/FAA/AR-95-5. July 1995.

12. David A. Purser. "Toxicity Assessment of Combustion Products" Section 2/Chapter 8, SFPE Handbook of Fire Protection Engineering, 2nd Edition, 1995, pp. 2:85-146.

# APPENDIX A
# VIDEO CAMERAS

Six video cameras were used in this test. Figure A1 shows the approximate locations of the video cameras relative to the test vehicle during this test.

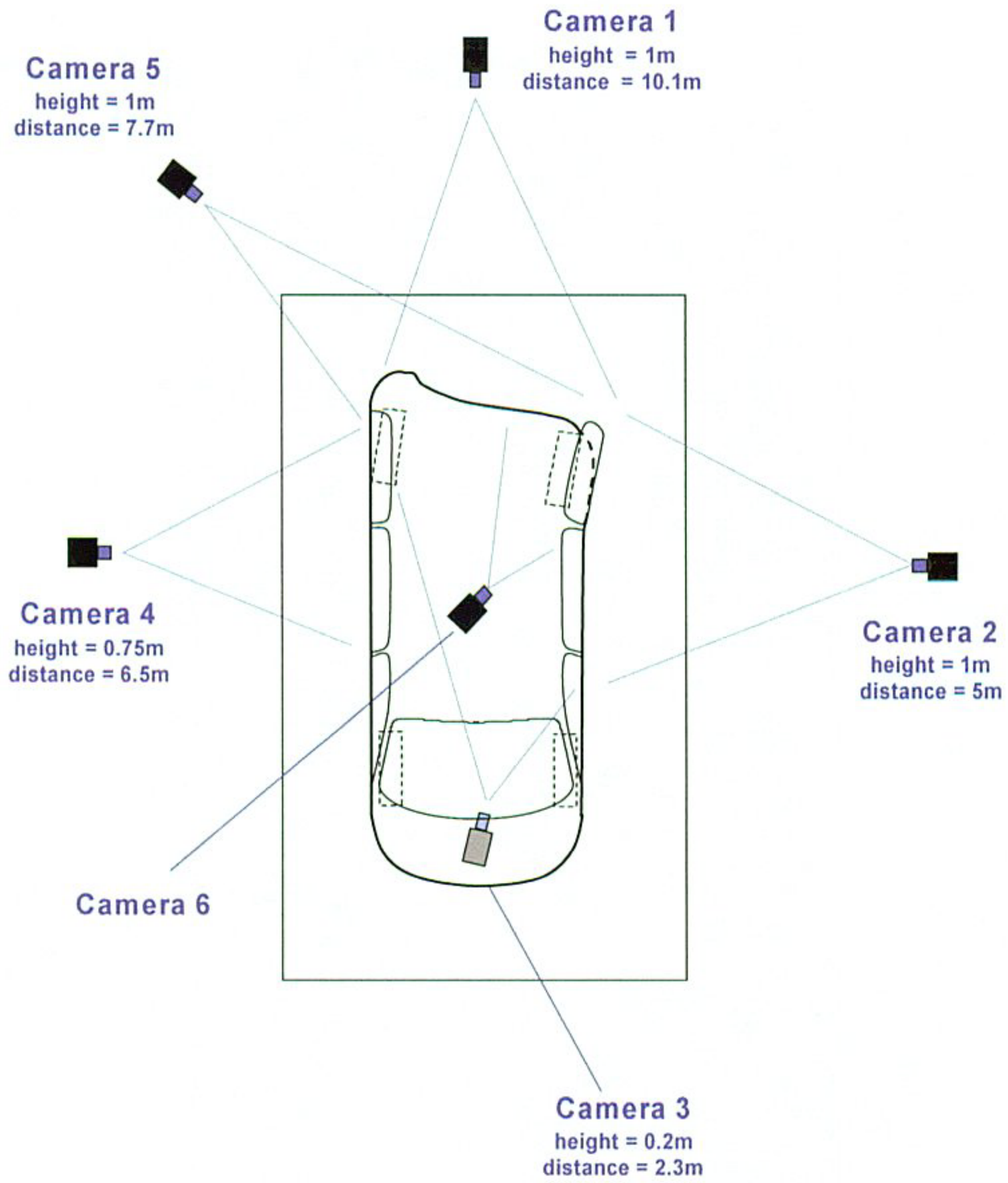


Figure A1. Fire Test F961116. Diagram showing the approximate locations of the video cameras during this test. Distances in this figure are not to scale in this diagram.

Cameras 1, 2, 4, and 5 were Hi-8 camcorder mounted on tripods. Camera 1 had a field-of-view that included the full height and width of the rear of the test vehicle. Camera 2 had a field-of-view that included the full height of the vehicle from the rear bumper fascia to the left front door. Camera 4 had a field-of-view that included the full height and length of the right side of the test

vehicle. Camera 5 was focused through the broken rear lift-gate window on the interior trim above the left rear wheelhouse.

Camera 3 was a Hi-8 camcorder mounted on a sled, which was located under the vehicle just forward of the transaxle. Its field-of-view included the area under the full width of the rear of the test vehicle. This camera provided a view of the area on the floor under the test vehicle where gasoline was expected to pool.

Camera 6 was a black-and-white CCD device with a fixed focal length located on the floor under the center of the middle bench-seat. Its field-of-view included the carpet and interior trim around the left rear wheelhouse, and a section of the lower surface of the foam cushion on the rear bench-seat. The output from the CCD camera was sent to a video recorder external to the vehicle. All video cameras were started before the test. A microphone on each camera recorded the air horn, which signaled removal of the plug from the hole in filler neck, ignition of the gasoline flowing from the hole with a propane torch, and the end of the test.

All video cameras were started before the test. A microphone on each camera recorded the air horn, which signaled the start and end of the test.

Quartz-halogen floodlights were used to illuminate the exterior of the vehicle. The level of illumination provided by these lamps was insufficient to balance the intensity of light reflecting from the vehicle surfaces with the brightness of the flames. To compensate for this imbalance, the light sensitivity adjustments on the Hi-8 camcorders were set to the manual position so that the apparent brightness of the vehicle surfaces did not change as the fire developed. As a result, the flames were overexposed, causing them to appear more opaque than they actually were.

# APPENDIX B
# INFRARED THERMOGRAPHY

Infrared thermal imaging radiometers were used to help determine fire propagation, flame, and surface temperatures during this test. These imaging systems measure thermal radiation within a definite waveband, over a variable field of view. The data obtained from these measurements can be analyzed to produce a two-dimensional map of apparent temperature called a thermogram.

Thermal imaging systems produce a spatially resolved map of surface temperatures from the radiant energy emitted in the field of view. The response time of these systems is nanoseconds, giving them the capability to acquire over 1 million discrete measurements per second. The capability of high-speed data acquisition is advantageous in that it can provide a tremendous amount of thermal data during a vehicle fire test, which can be over in only a few minutes. Thermal imaging radiometers can be used concurrently as a vision system and a measurement system. However, the thermal sensitivity, scan speed, and spatial resolution must be optimized for a particular application.

## B.1 Infrared Camera Location

Three thermal imaging systems were used in this test. Figure B1 shows the approximate locations of the infrared cameras relative to the test vehicle during this test. All of these systems were mounted on tripods positioned outside the vehicle. IR 1 was an Inframetrics Model SC1000 ThermaCam (Inc, Billerica, MA) with an optical window of 3 to 5μ, and was fitted with a 3.9μ cut-off filter. Its field-of-view included the full height and width of the rear of the test vehicle, and the simulated road surface under the fuel tank. IR 2 was an Inframetrics 740 thermal imaging radiometer with an optical window of 8 to 12μ. Its field-of-view included the full height and width of the rear of the test vehicle, and the left side of the test vehicle from the front door (US driver) rearward. IR 3 was an Inframetrics Model 760 thermal imaging radiometer with an optical window of 3 to12μ, and was fitted with a 3.9μ cut-off filter. It was focused on the interior of the vehicle through the broken window in the rear lift gate.

## B.2 Data Systems

The analog output signals from the Inframetrics Models 740 and 760 radiometers were recorded to videotape during the fire test. The thermal images stored on the tapes were converted to an 8-bit digital format and stored to a computer hard drive. The Inframetrics Model *SC1000* ThermaCam output an 8-bit digital signal, which was stored directly to a computer hard drive during the fire test. In both cases, the data acquisition software (*ThermaGram Pro version 1.3*) was configured to sample data at 5-sec. intervals. The computer data system used to process

the IR thermograms was a PC with a 90 MHz Pentium Processor, 64 MB of RAM, 2.0 GB hard drive, and a thermal A/D conversion card (*Inframetrics and ThermoTeknix Systems*).

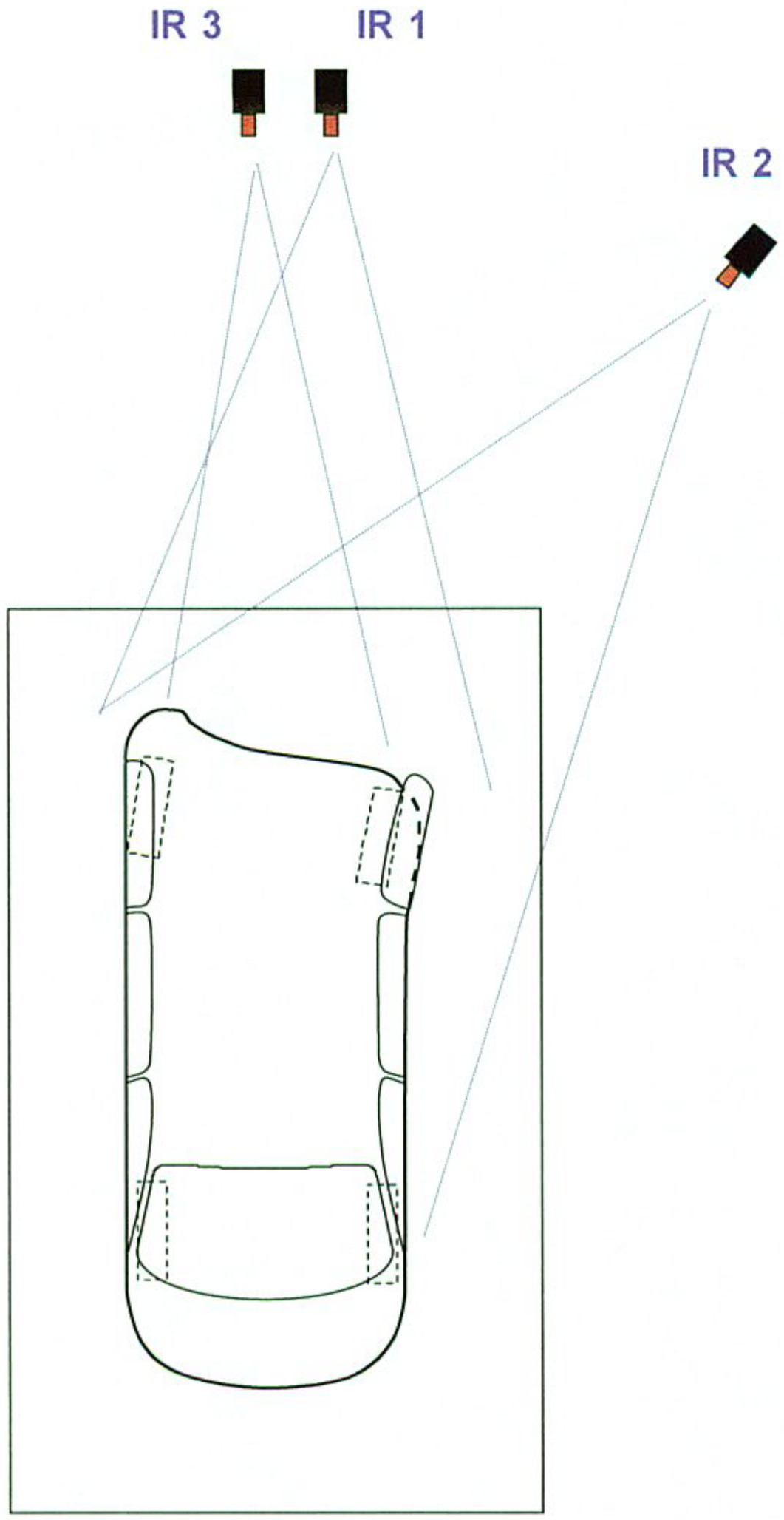


Figure B1. Fire Test F961116. Diagram showing the locations of the infrared thermal imaging systems during this test. Distances in this duagram are not to scale in this diagram.

## B.3 Data Analysis

Thermal imaging systems measure infrared radiation within a certain spectral band and must be calibrated to convert radiant intensity in that spectral band to temperature. Due to variations in system response, every system has to be calibrated. Calibration curves for the basic thermal imaging radiometers are measured at the factory and stored in read-only memory or in analysis software programs. Additional calibrations are needed for the optical filters. These calibrations are stored in the analysis software programs. Since thermal imaging radiometers are AC coupled devices, they measure differences in thermal radiation. To get absolute temperatures, there must be a reference to provide DC restoration. In these instruments, the reference is an internal blackbody reference source that is viewed periodically by the detector.

The general radiometric equation was used to convert radiant energy to temperature:

$$\hat{I} = [E_t \times F(T_t)] + [(1 - E_t) \times F(T_b)] - [E_r \times F(T_r)] - [(1 - E_r) \times F(T_b)] \qquad \text{(B1)}$$

Where $\hat{I}$ is the difference in radiance between the target and a reference surface; $E_t$ is the emittance of the target surface, generally unknown; $E_r$ is the emittance of the reference surface, $T_t$ is the temperature of the target surface; $T_b$ is the temperature of background surfaces (i.e., ambient temperature), or other emitters such as flames reflected from the target; $T_r$ is the temperature of the reference surface; $F(T_t)$ is the radiance from an ideal emitting surface (i.e., black body) at the temperature of the target surface ($T_t$); $F(T_r)$ is the radiance from an ideal emitting surface at the temperature of the reference ($T_r$); and $F(T_b)$ is the radiance from the background relative to the radiance value from the reference surface when $E_r = 1$. Factors other than temperature determine the emittance of an object. These factors include the type of material, the texture of the surface, the wavelength of the detector, and the view-angle. In determining temperatures from the radiant energy from an object, the operator can set the emittance of an unknown target surface to a value of between .01 and 1.0.

Radiant intensity measured by the thermal imaging system is converted to a gray-scale value. An 8 bit system provides gray scale values from 0 to 255 for the radiant energy at each pixel in the instantaneous field of view. A 12 bit system provides gray scale values from 0 to 4095. As the radiometer scans the image, each pixel is assigned a gray scale value, and the gray scale image is stored either in a computer memory or onto videotape. When stored in computer memory, a single frame (1 thermogram) can contain up to 68,000 pixels (discrete measurements) with an assigned 8 bit or 12 bit value. Videotape provides a temporal resolution of 30 frames per second. Depending on the thermal range of the thermal imaging radiometer, a temperature value was

assigned to each pixel using either the factory calibration curves accompanying each instrument, or calibration curves stored in IR analysis software.

Separation of the apparent temperatures of various surfaces on and inside a burning vehicle from the captured data is not a trivial task. The data represent a complex combination of emitted infrared energy from those surfaces as well as reflected infrared energy from the flames, and reflected infrared energy from high intensity lights used to illuminate the vehicle for visual data capture. In addition, the flames themselves were emitting infrared radiation due to their sooty content, some part of which was captured by the infrared thermal imaging systems. Also, some of the infrared radiation being emitted by the vehicle surfaces had to pass through flames containing soot from incomplete combustion of synthetic polymers or through clear (clean) flames where more complete combustion was occurring, and/or a combination of both types of flames. In all of these cases, gases in the flame absorbed some of the infrared radiation emitted by objects behind the flame.

The following steps were taken to minimize the impact of unwanted infrared radiation being captured by the thermal imaging systems.

- Anti-reflection tapes, paint, and glazes were applied to highly reflective surfaces on the test vehicle.
- The thermal imaging systems were located in the shadows of the vehicle to block the video lights from shining directly into the radiometer.
- Two of the thermal imaging systems were fitted with flame filters (3.9 μm) to screen out a portion of the infrared radiation from both sooty and clear flames.

Despite these precautions, accurate surface temperatures could not be determined for areas of the vehicle blocked by intense flame. As a result, only surface temperatures determined to be reliable by the IR analysts are reported here. In some cases, specialized data analysis techniques were used to obtain reliable surface temperatures from areas in close proximity to, but not shielded by flame. Where possible, temperature data were reported from areas that lie in the shadow of the flames, which comes from highly emissive surfaces not affected by the flame radiation, and/or is deemed reliable based on the experience of the analysts. Data from nearby thermocouples were compared to IR temperature readings for a more comprehensive analysis.

During the data analysis, the videotapes were reviewed frame-by-frame to observe the burn sequence. The analyst captured images from selected frames on a video board. The image was processed to produce a digitized gray scale value for each element in the pixel matrix utilizing the

camera settings automatically documented between video frames on the videotape during data acquisition. Thermograms were produced from the digitized image matrix using a commercial software package (Thermogram Pro V1.3, sold by Inframetrics, Inc., Billerica, MA). This software utilized the NIST traceable calibration tables supplied by the manufacturer with each thermal imaging system.

# APPENDIX C
# THERMOCOUPLE DATA

Type-N thermocouples were fabricated by Medtherm Corporation (Huntsville, AL). They consisted of an enclosed, grounded thermocouple junction (30 AWG thermocouple wire) in an Inconel 600 sheath with magnesium oxide insulation (o.d. = 0.040 in. (1 mm), length = 50 ft. (15.2 m)). A transition to a duplex thermocouple extension cable (24 AWG) with fiberglass insulation and a stainless steel over-braid (length = 50 ft. (15.2 m)) was made through a stress-relief bushing. The thermocouple extension cables were connected directly to the multiplex thermocouple input cards in the data acquisition system (see below).

Type-K thermocouples with exposed, bead-type junctions were prepared from thermocouple duplex wire with glass fiber insulation (26 AGW, length = 10 ft (3.04 m). Each thermocouple was connected to a Type-K thermocouple extension cable using compensated ceramic thermocouple connectors. The extension cables consisted of Type-K thermocouple wire (24 AWG) with fiberglass insulation and a Teflon-jacketed stainless steel over-braid (length = 25 m (15.2 m)). The extension cables were connected directly to the multiplex thermocouple input cards in the data acquisition system (see below).

A PC-based data system was used for data acquisition from the thermocouples. The PC contained a 75 MHz Pentium Processor, 16 MB RAM, an 814 MB hard disk, and a 16-bit (Model BG45-AP5CP, ACER Inc., Taiwan R. O. C.). A 100 kHz I/O board with 16 analog input channels (DaqBoard 200A, IOTech, Inc., Cleveland, OH) was installed in one of the expansion slots in the PC. Thermocouple multiplex expansion cards (DBK-19, IOTech, Inc., Cleveland, OH) were used for data acquisition from the Type-N and Type-K thermocouples. The electrical shields on the thermocouple cables were connected to the electronic chassis grounds on the thermocouple mutliplex extension cards. The vehicle chassis was connected to the electronic chassis ground by a large-gauge cable. The data acquisition software (DASYLab, Daten System Technik GmbH, Mönchengladbach, Germany) was configured to sample each channel at a rate of 10 Hz and store the data in 10-point block averages.

Figures C1 through C7 show the approximate locations of thermocouples installed in the test vehicle for this test. Plots C1 through C84 show that temperature data recorded from these thermocouples.

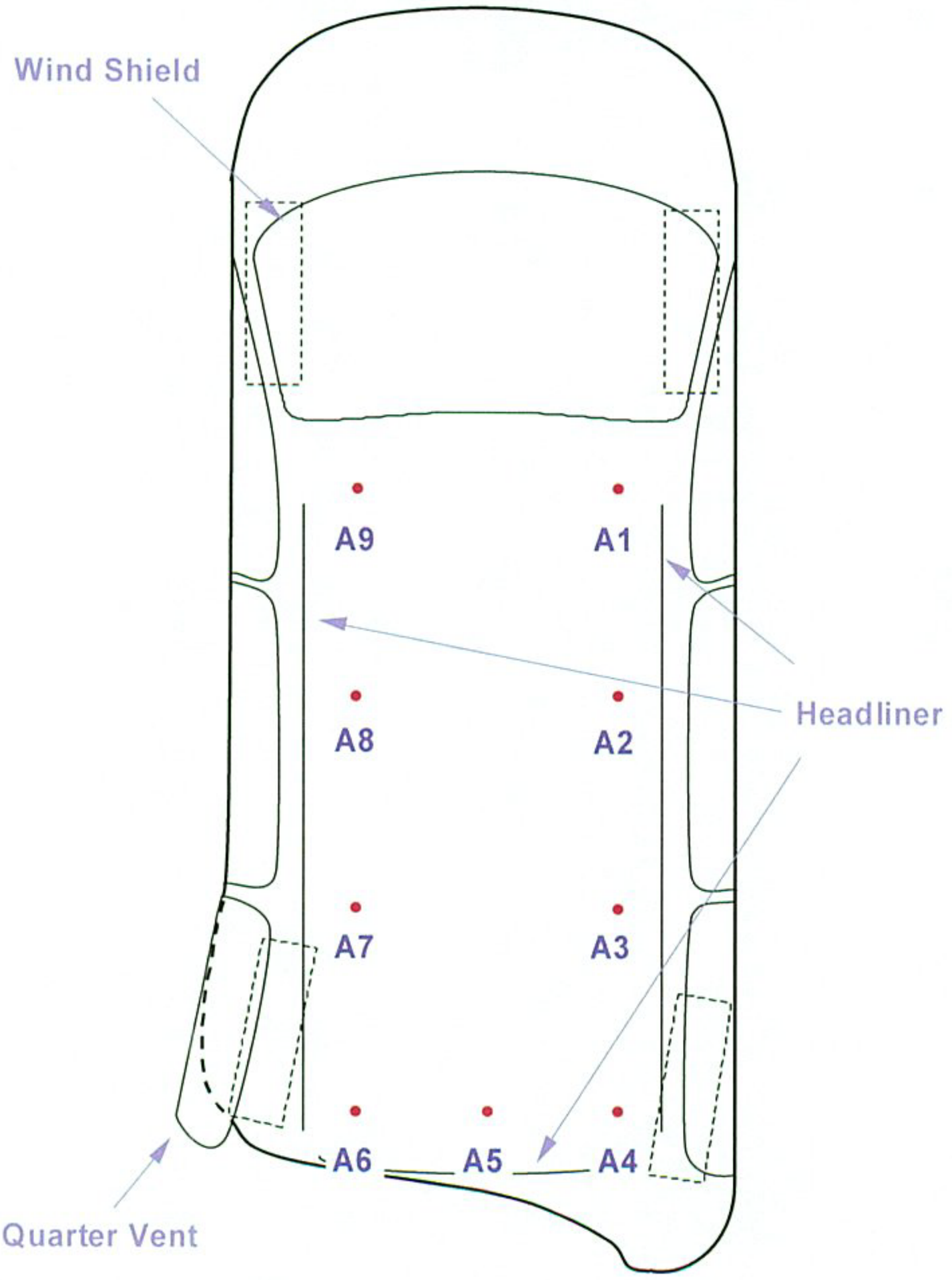


Figure C1. Fire Test F961116. Top view of the test vehicle showing the approximate locations of Thermocouples A1 through A9 below the lower surface of the headlining of the test vehicle. The thermocouples were inserted through the roof and headliner so that the thermocouple junction was approximately 1 cm below the lower surface of the headliner.

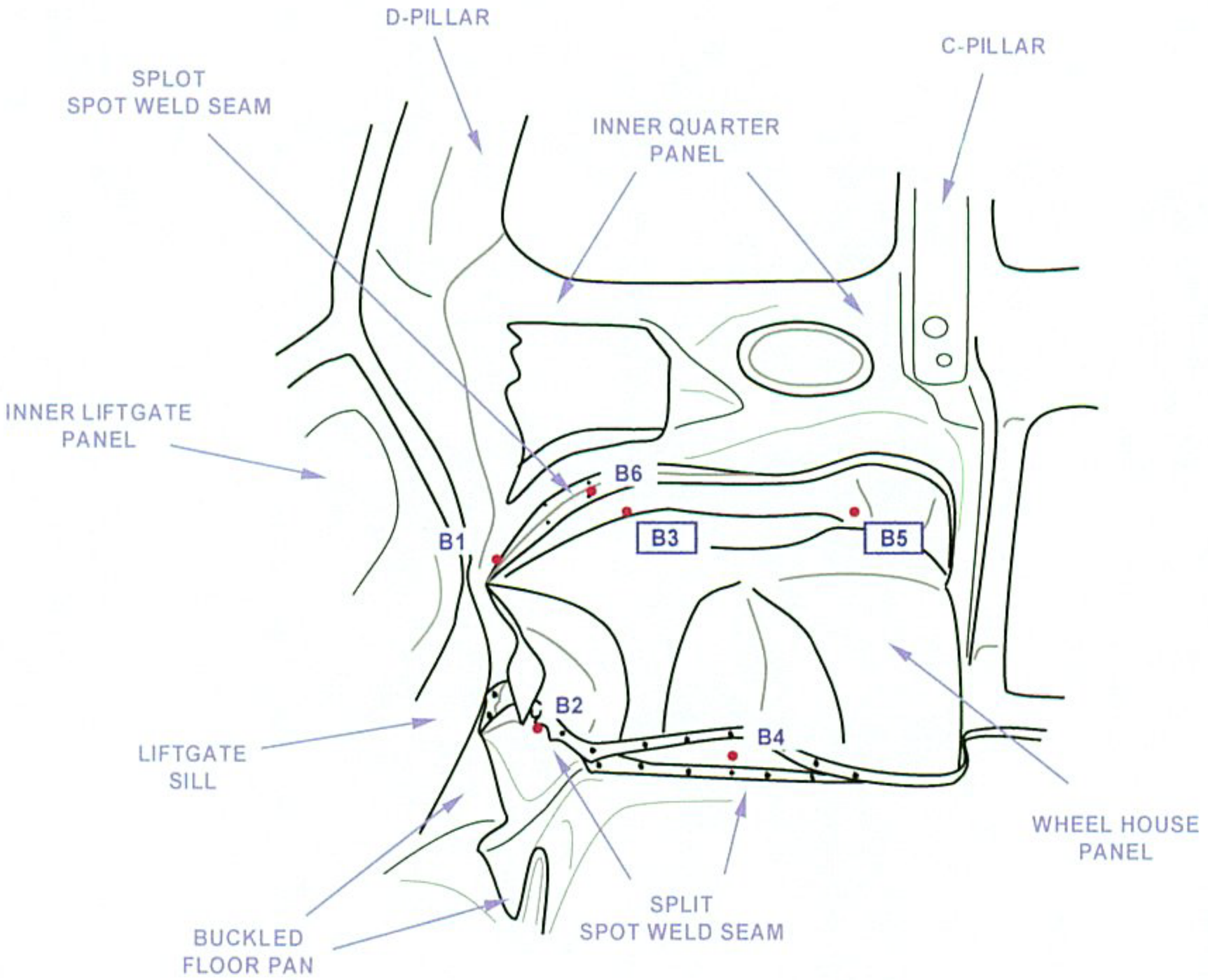


Figure C2. Fire Test F961116. Interior view of the rear left corner of the test vehicle (trim panels removed) showing the approximate locations of Thermocouples B1 through B6 on the inner quarter panel and wheelhouse panels. Thermocouple B1 was located in a seam opening at the rear of the wheelhouse. Thermocouples B2 and B4 were located in the seam opening between the inner wheelhouse panel and floor pan. Thermocouples B3 and B5 were inserted through the wheelhouse panel with the thermocouple junctions approximately 1 cm below the lower (exterior) surface of the sheet metal. Thermocouple B6 was located in a seam opening between the wheelhouse panel and the interior quarter panel.

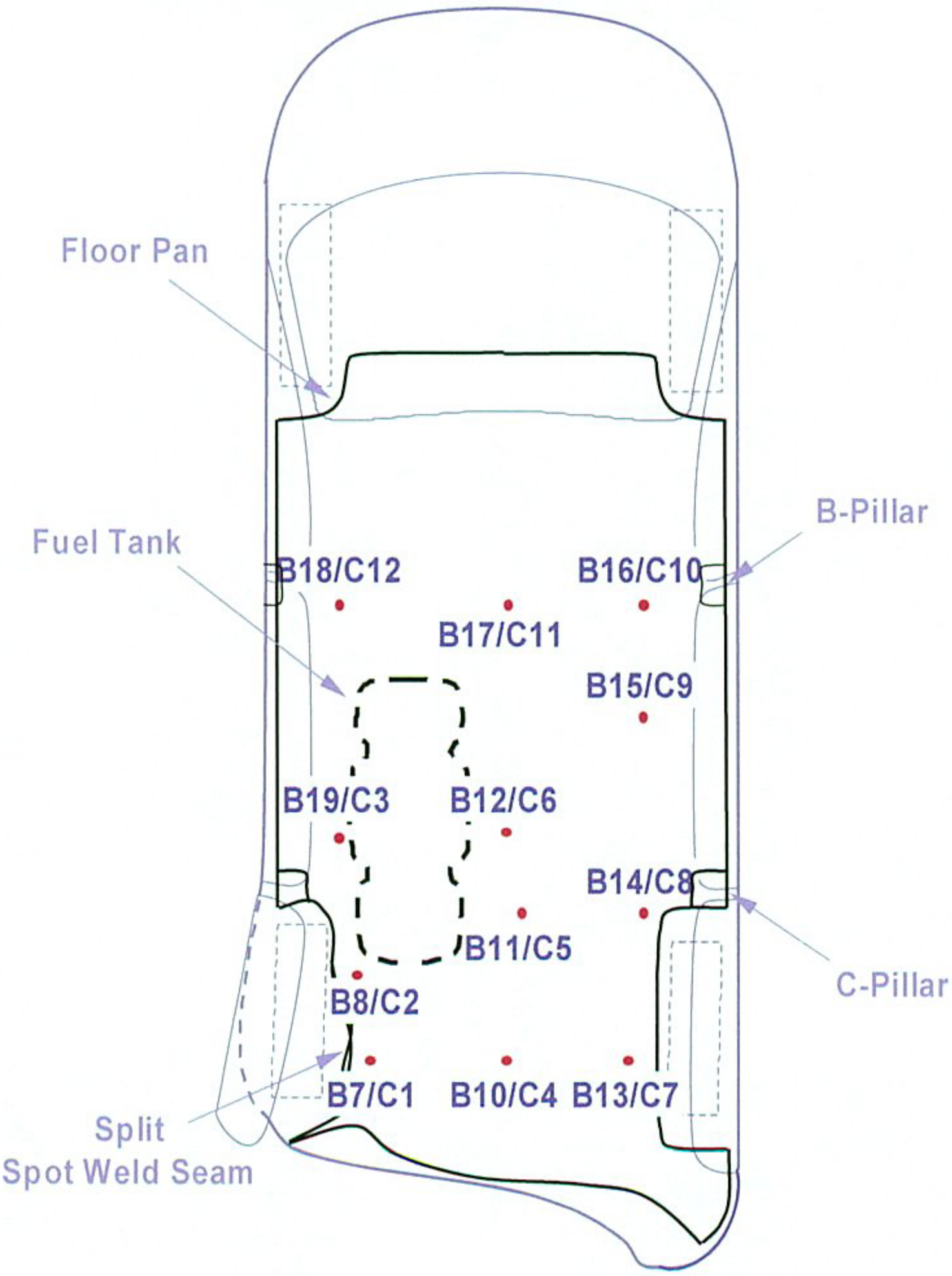


Figure C3. Fire Test F961116. Top view of the test vehicle showing the approximate locations of Thermocouples B7 through B18 and C1 through C12 in the floor pan of the test vehicle. Thermocouples B7 through B18 were attached to the interior (upper) surface of the floor pan with thermally conducting ceramic cement. Thermocouples C1 through C12 extended through the floor pan so that each thermocouple junction was approximately 1 cm below the exterior (lower) surface of the floor pan.

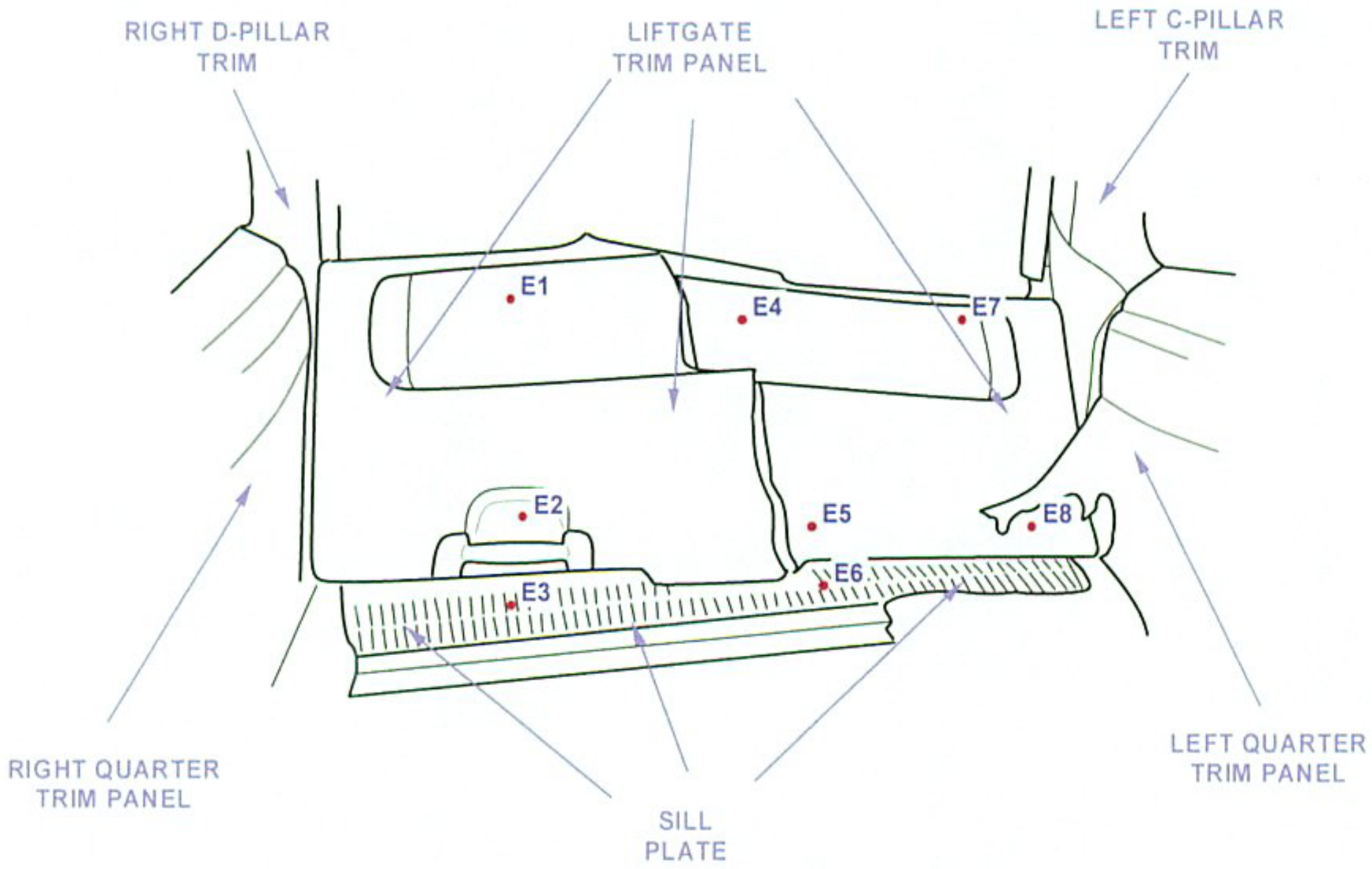


Figure C4. Fire Test F961116. Interior view of the rear of the test vehicle showing the approximate locations of Thermocouples E1 through E8 on the Liftgate Trim Panel and Sill Plate. Thermocouples E1, E2, E4, E5, E7, and E8 were located on the exterior (exposed) surface of the Liftgate Trim Panel. Thermocouples E3 and E6 were located on the exterior (exposed) surface of the Sill Plate.

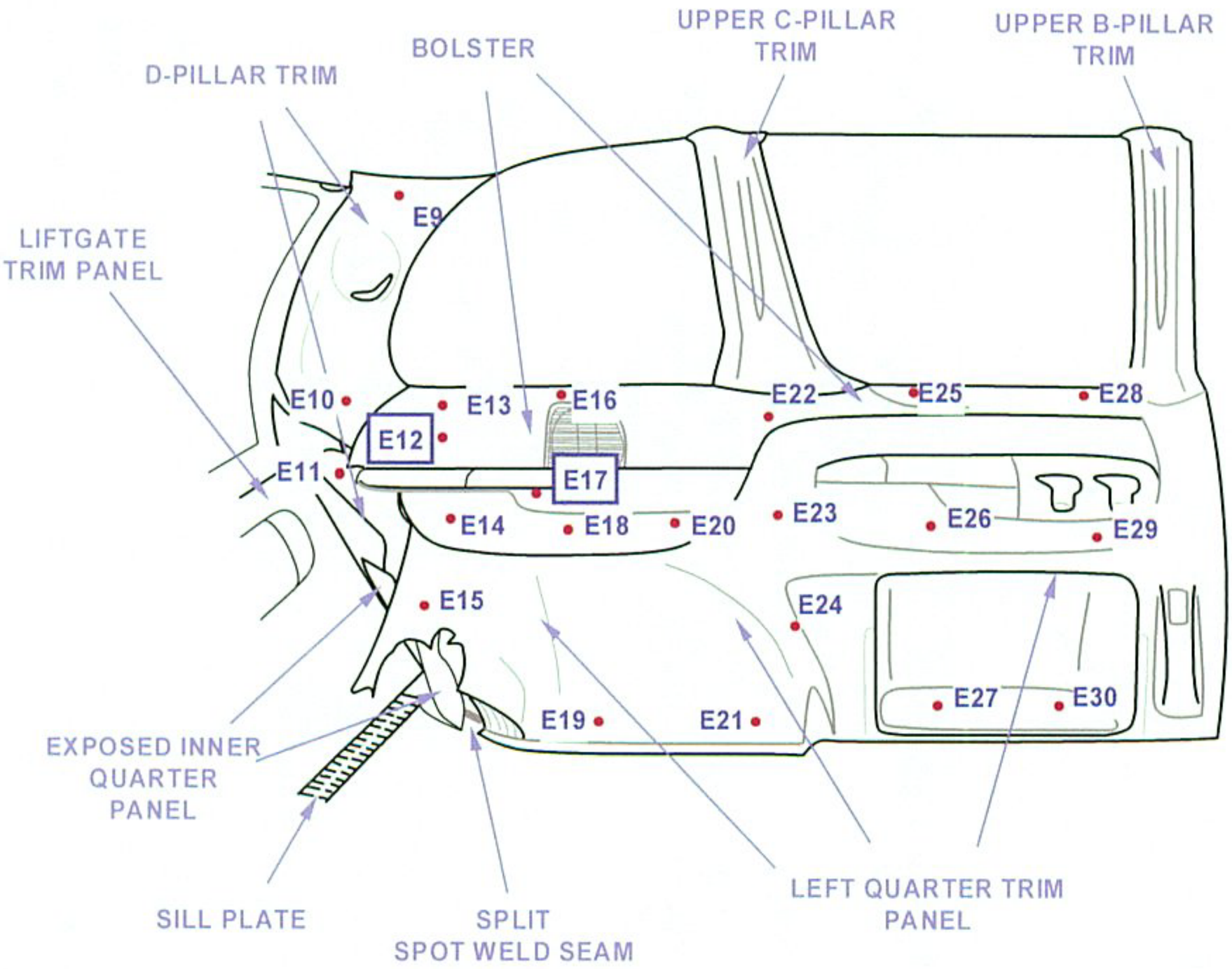


Figure C5. Fire Test F961116. Interior view of the left side of the test vehicle showing the approximate locations of Thermocouples E9 through E30 on the Left Quarter Trim Panel, Bolster and Left D-Pillar Trim Panel. Thermocouples E9, E10, and E11 were located on the exterior (exposed) surface of the D-Pillar Trim Panel. Thermocouples E13, E16, E22, E25, and E28 were located on the Exterior (exposed) surface of the Bolster. Thermocouples E14, E15, E18, E19, E20, E21, E23, E24, E26, E27, E29, and E30 were located on the exterior (exposed) surface of the Left Quarter trim panel. Thermocouple E12 was located on the interior (unexposed) surface of the3 Left Quarter Trim Panel above a split spot-weld seam at the top of the wheelhouse. Thermocouple E17 was located in the Storage Box in the Left Quarter Trim Panel.

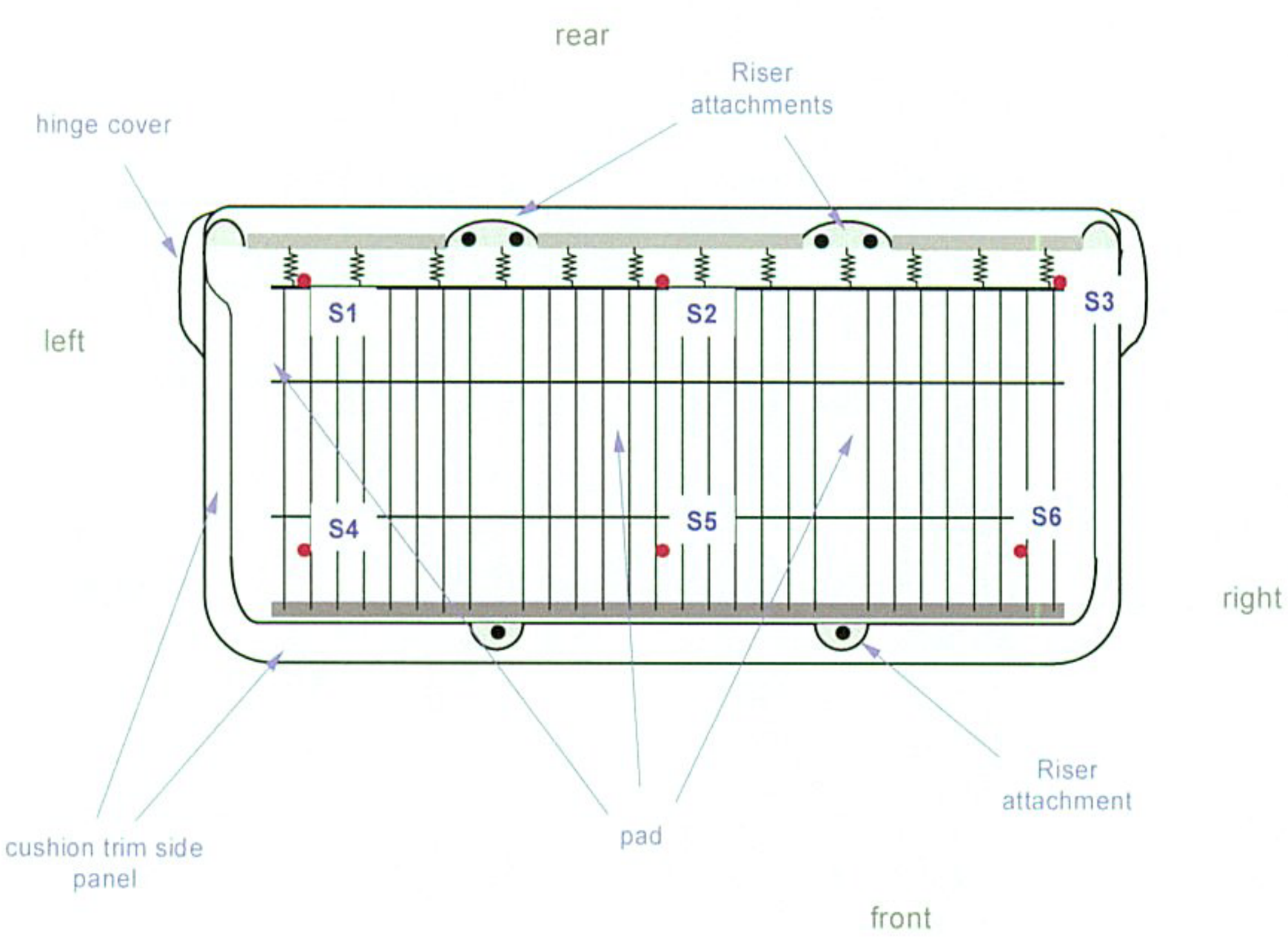


Figure C6. Fire Test F961116. View of the under-side of the second bench seat in the test vehicle showing the approximate locations of Thermocouples S1 through S6 below the seat cushion. The thermocouple junctions were located approximately 1 cm below the lower surface of the foam pad in the seat cushion.

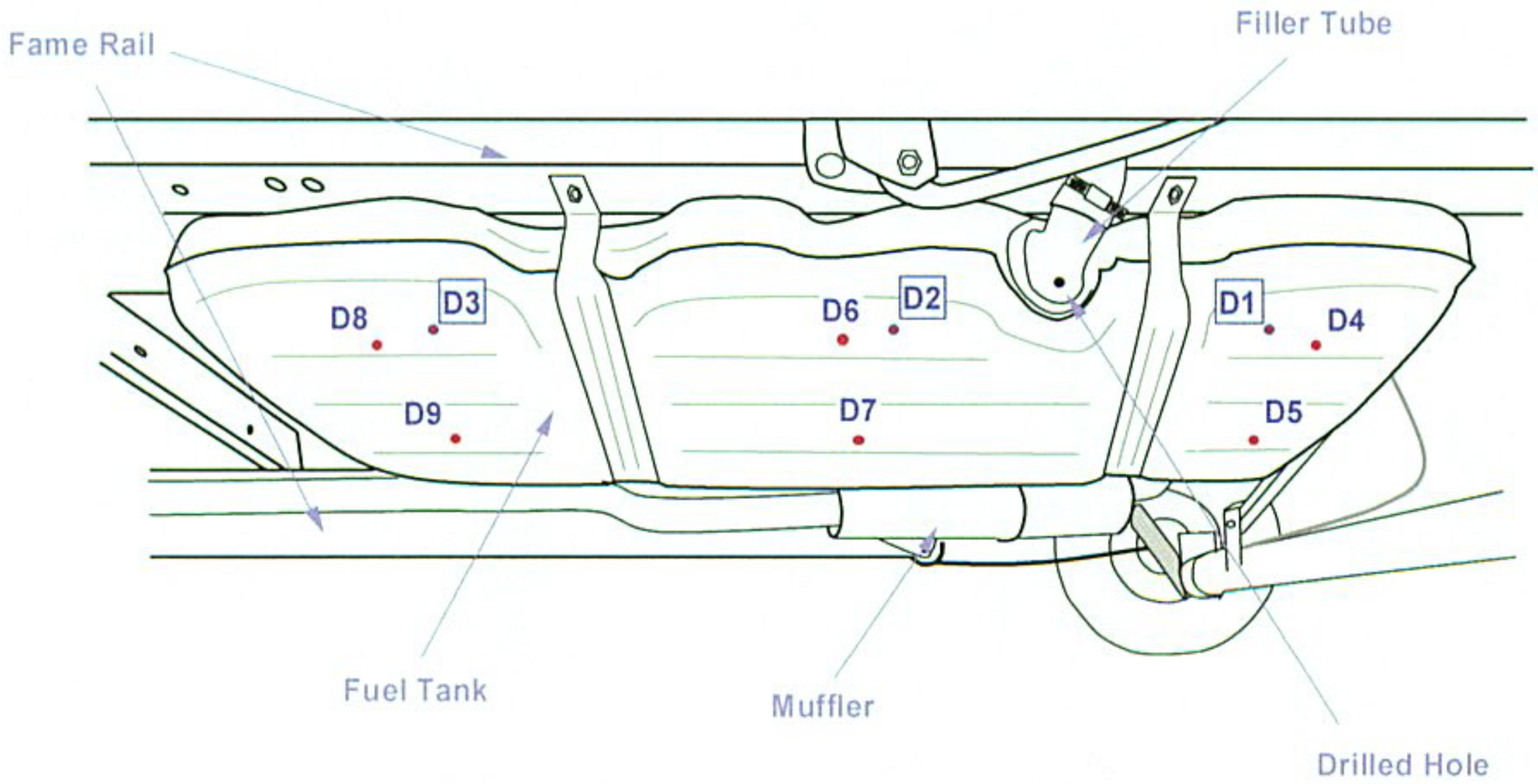


Figure C7. Fire Test F961116. View of the underbody of the test vehicle showing the approximate locations of Thermocouples D1 through D3 inside the fuel tank and Thermocouples D4 through D9 on the bottom of the fuel tank. Thermocouples D1 through D3 were located inside the fuel tank immersed in the gasoline at the start of the test. Thermocouples D4 through D9 were located on the lower surface of the bottom panel of the fuel tank.

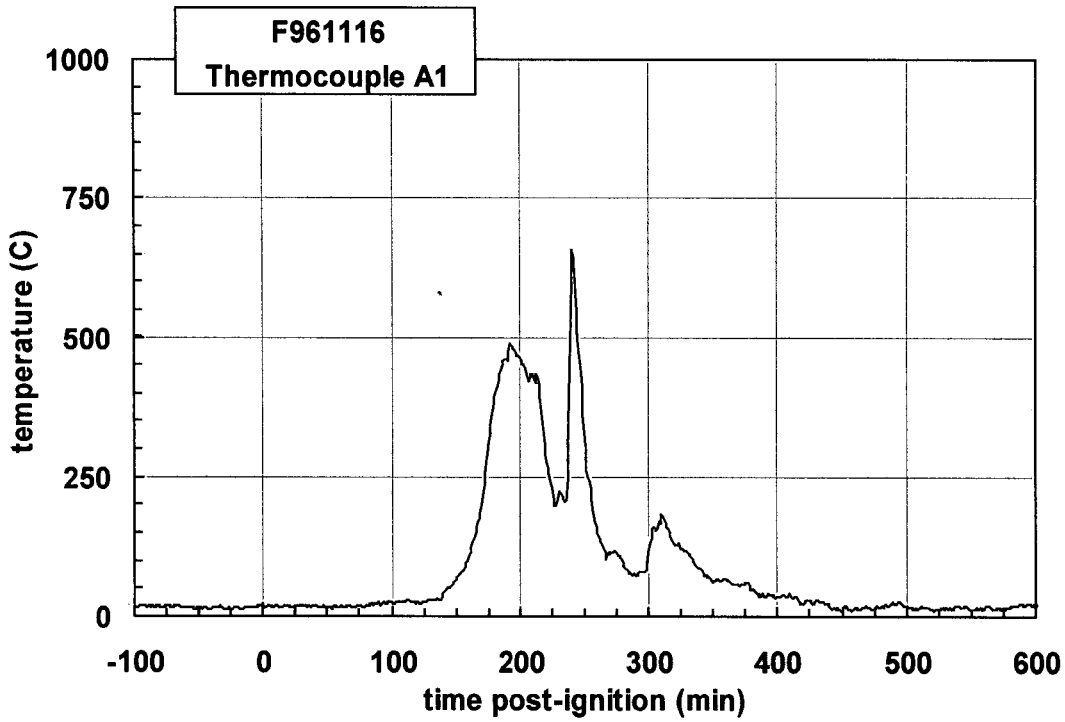


Plot C1. Fire Test F961116. Data plot from thermocouple A1.

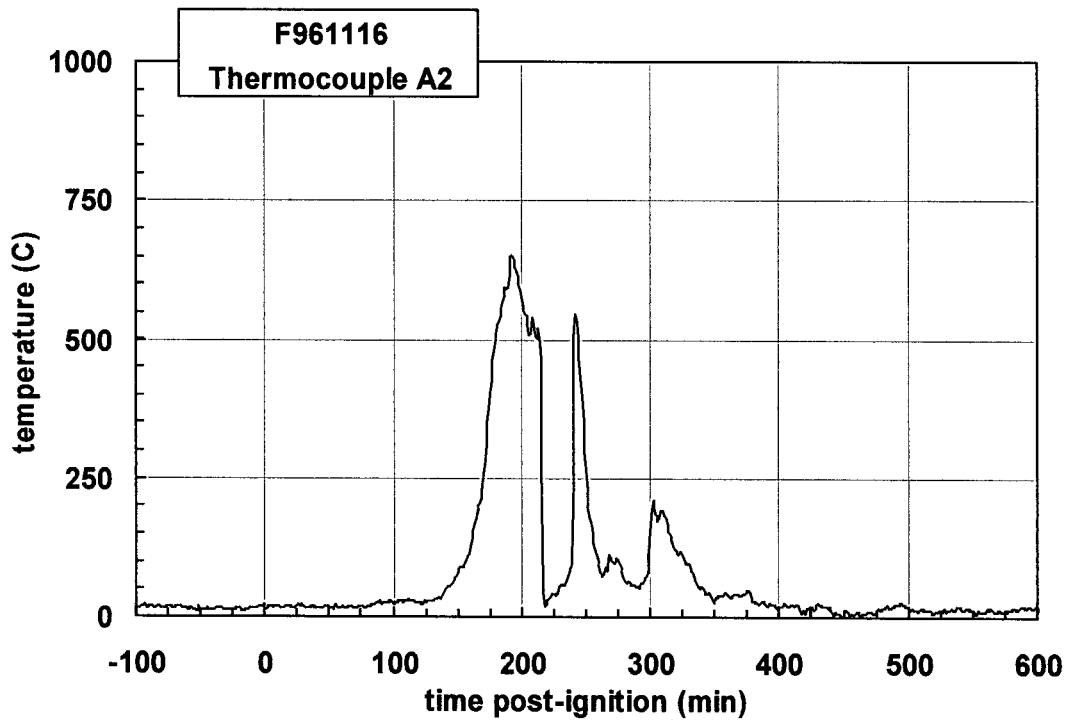


Plot C2. Fire Test F961116. Data plot from thermocouple A2.

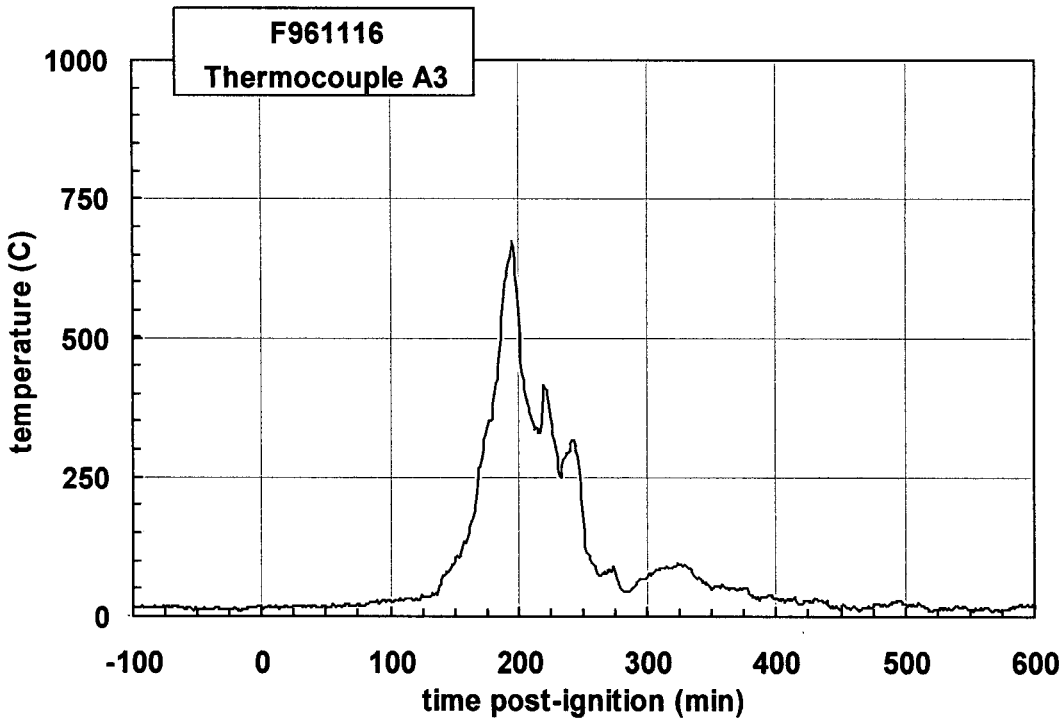


Plot C3. Fire Test F961115. Data plot from thermocouple A3.

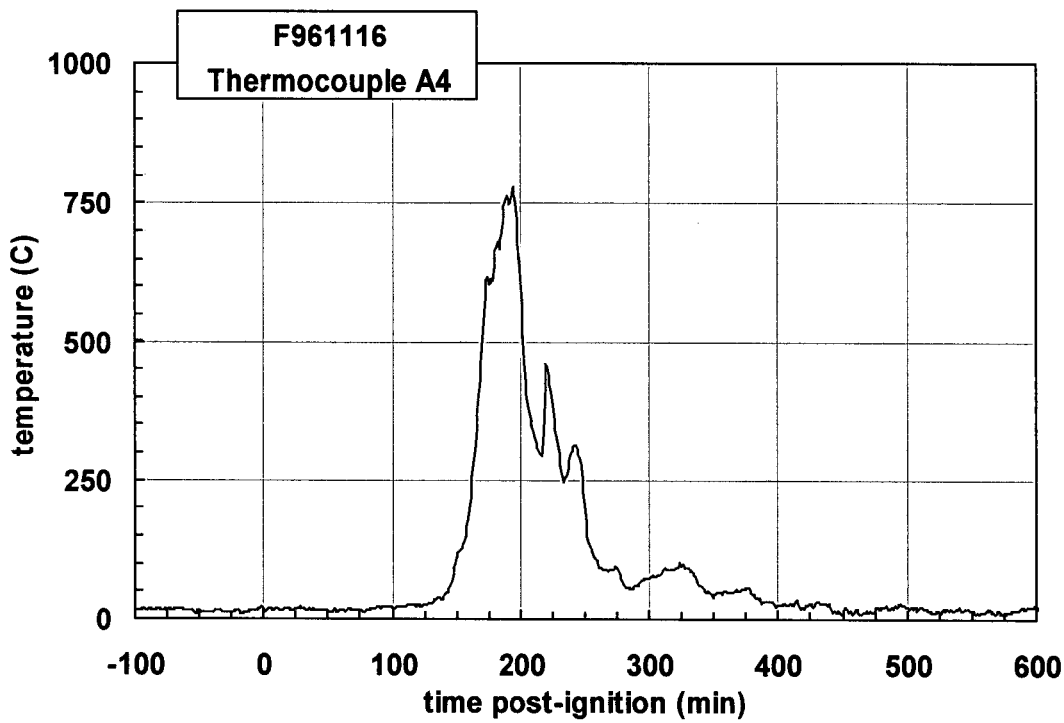


Plot C4. Fire Test F961116. Data plot from thermocouple A4.

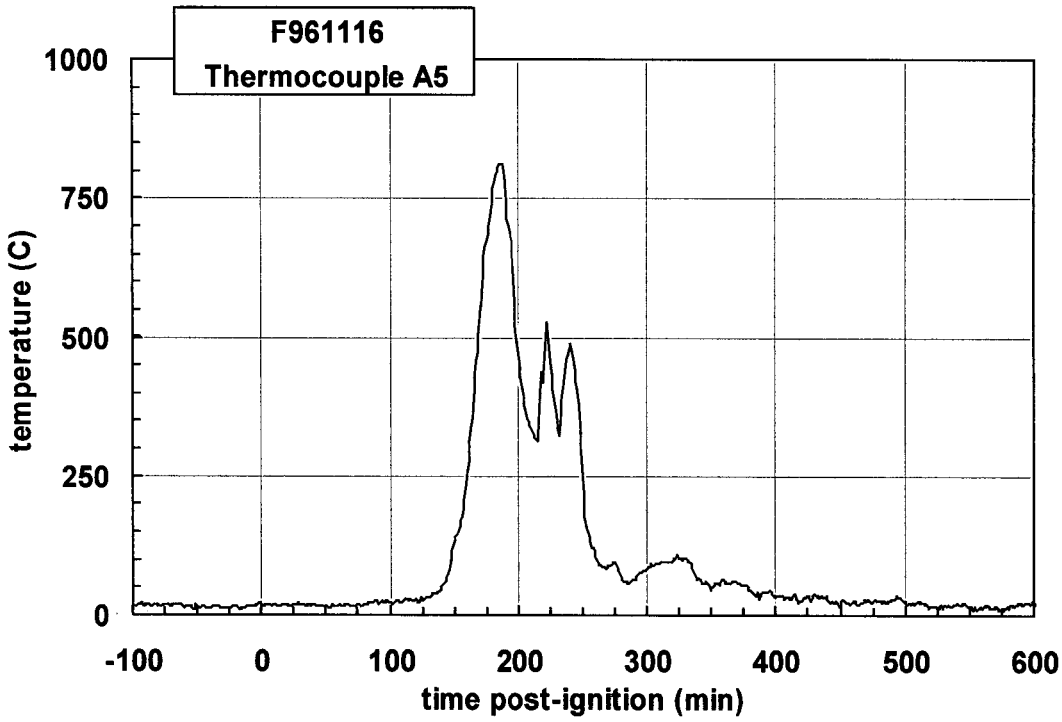


Plot C5. Fire Test F961116. Data plot from thermocouple A5.

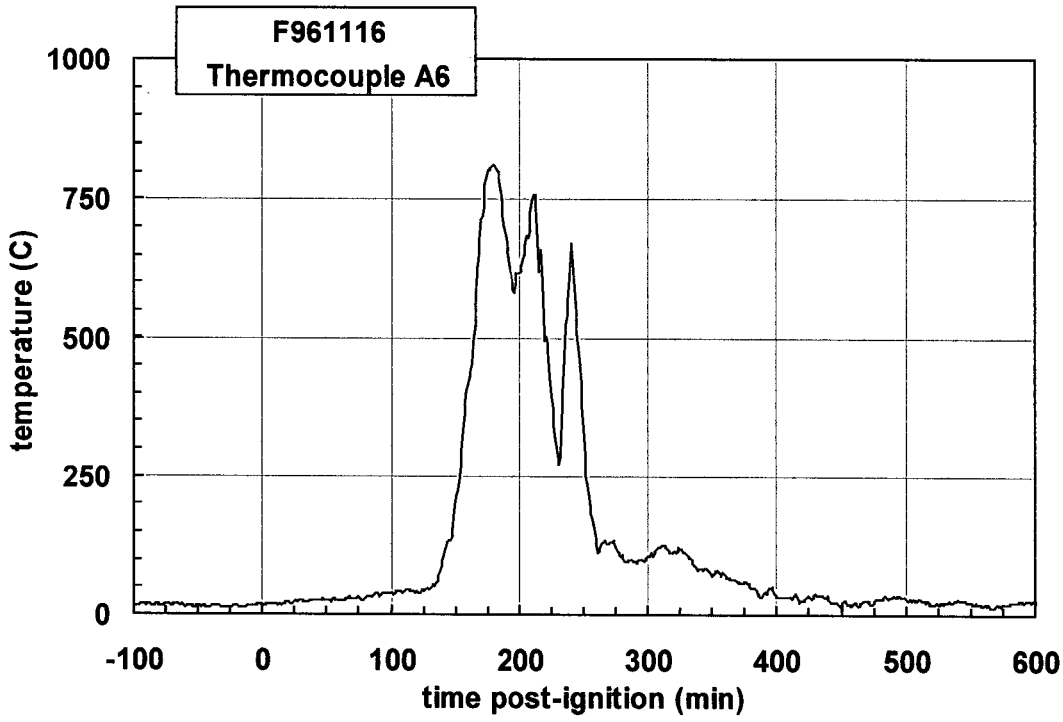


Plot C6. Fire Test F961116. Data plot from thermocouple A6.

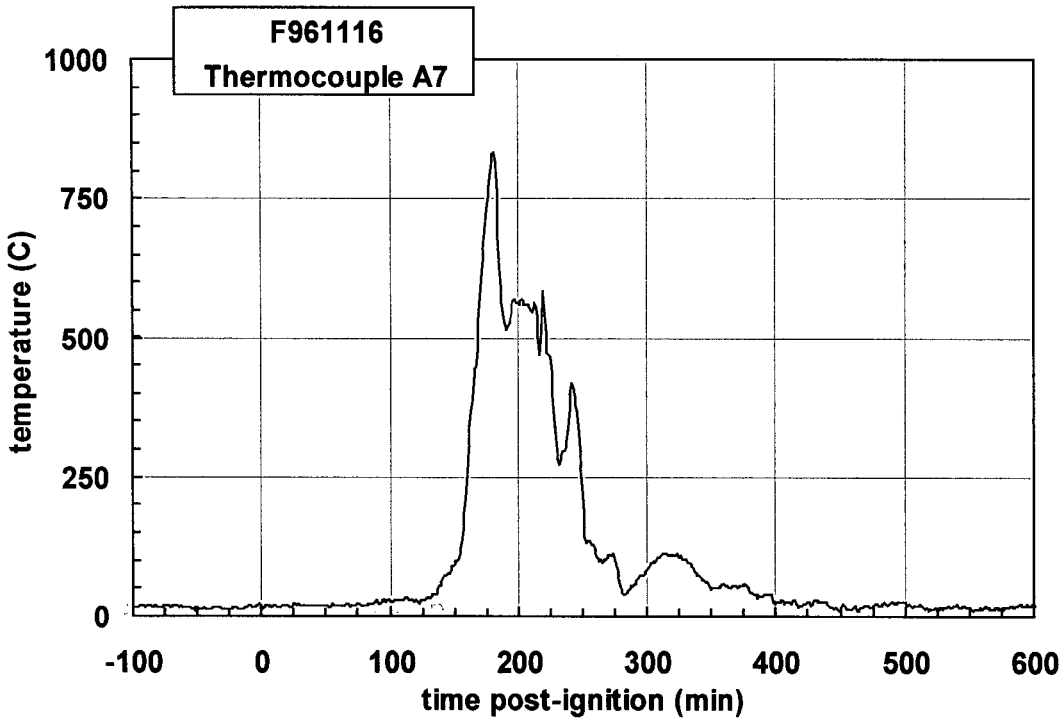


Plot C7. Fire Test F961116. Data plot from thermocouple A7.

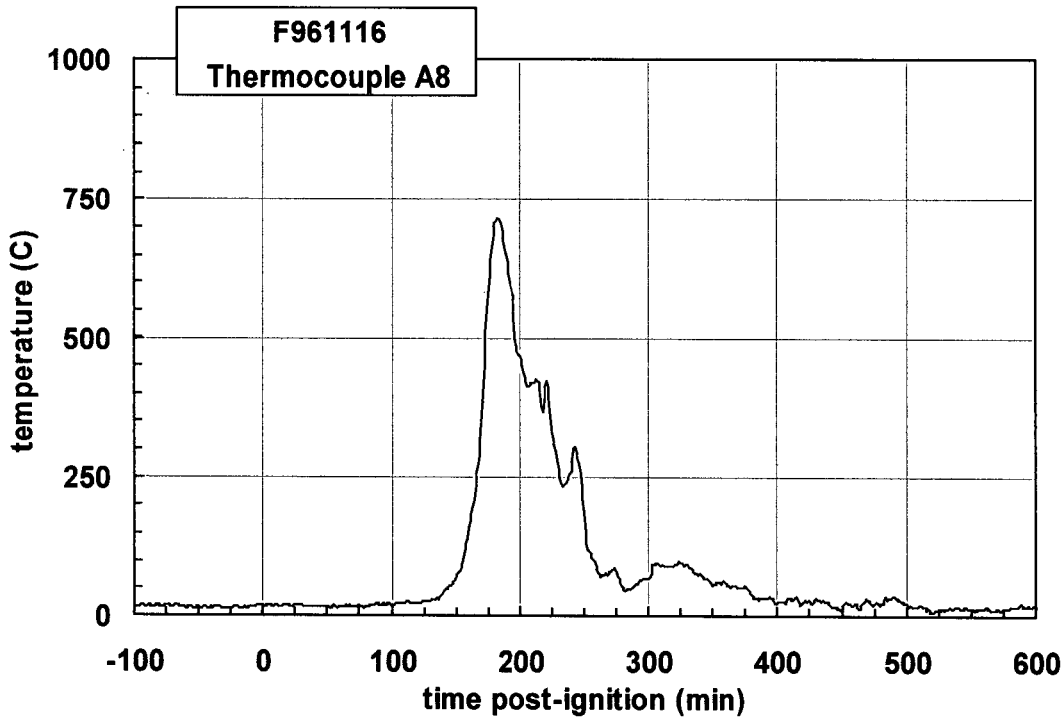


Plot C8. Fire Test F961116. Data plot from thermocouple A8.

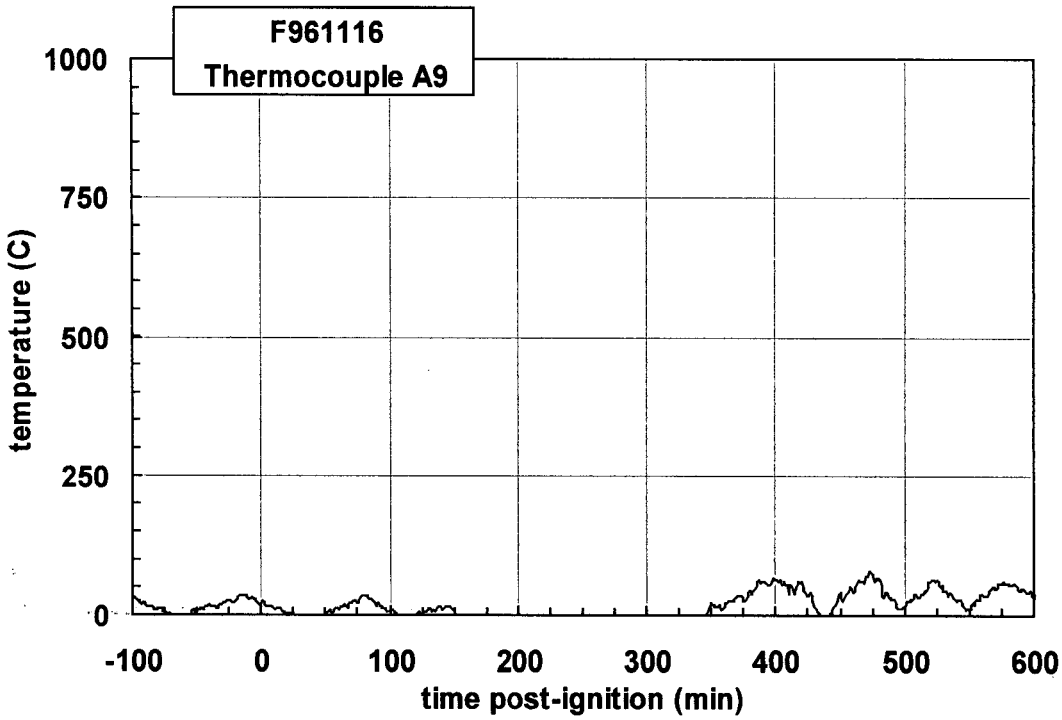


Plot C9. Fire Test F961116. Data plot from thermocouple A9.

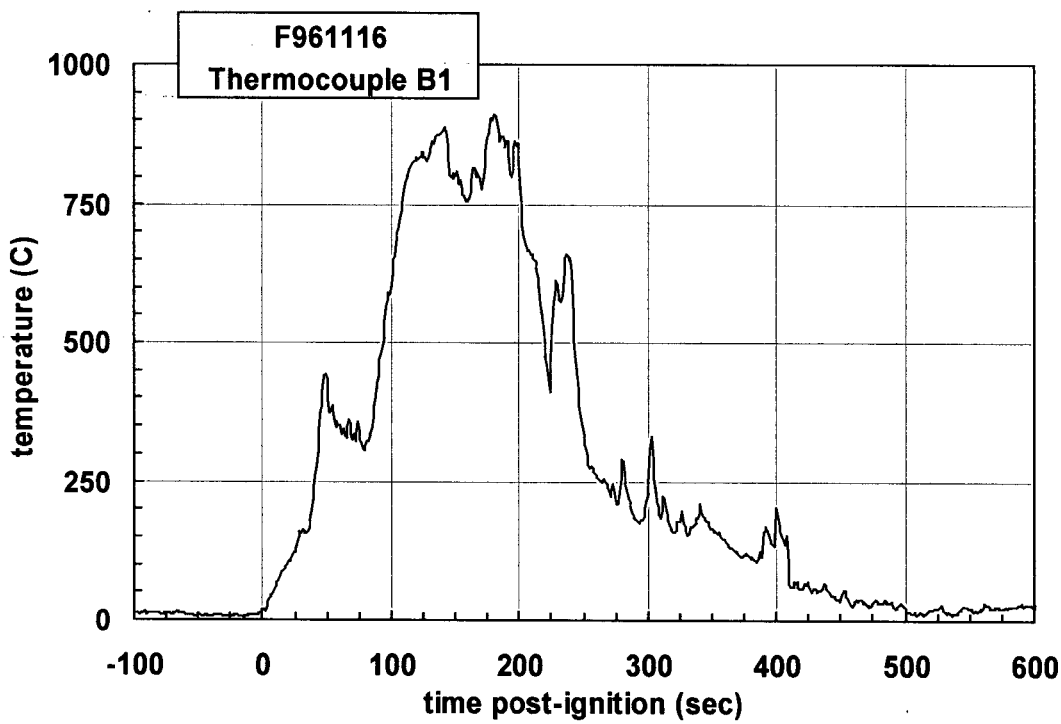


Plot C10. Fire Test F961116. Data plot from thermocouple B1.

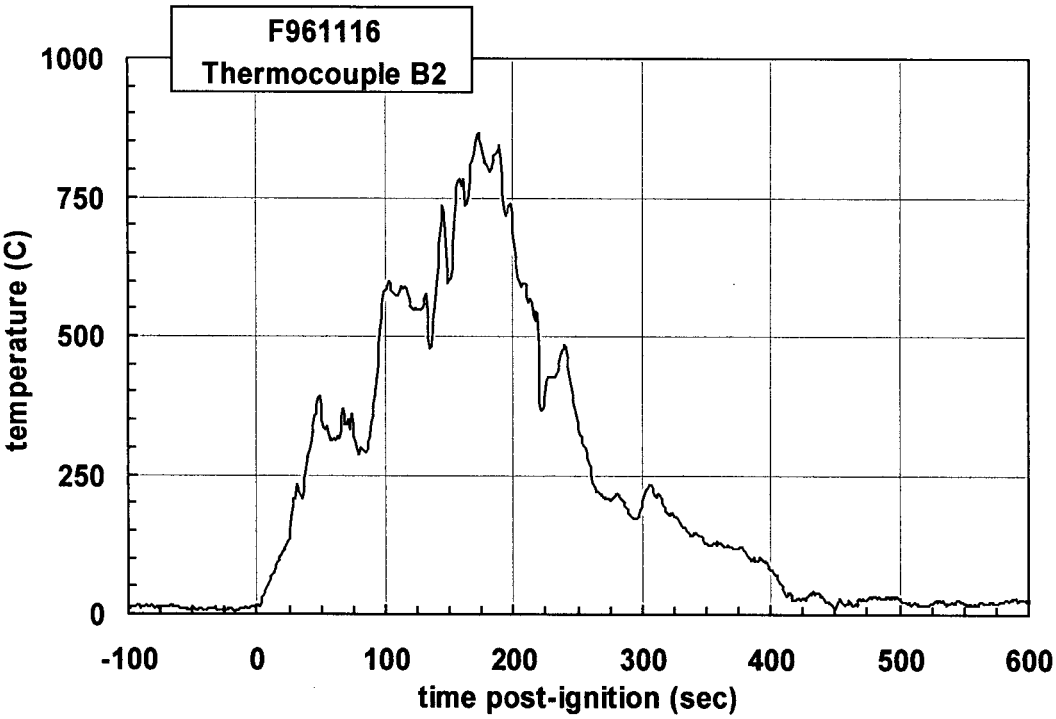


Plot C11. Fire Test F961116. Data plot from thermocouple B2.

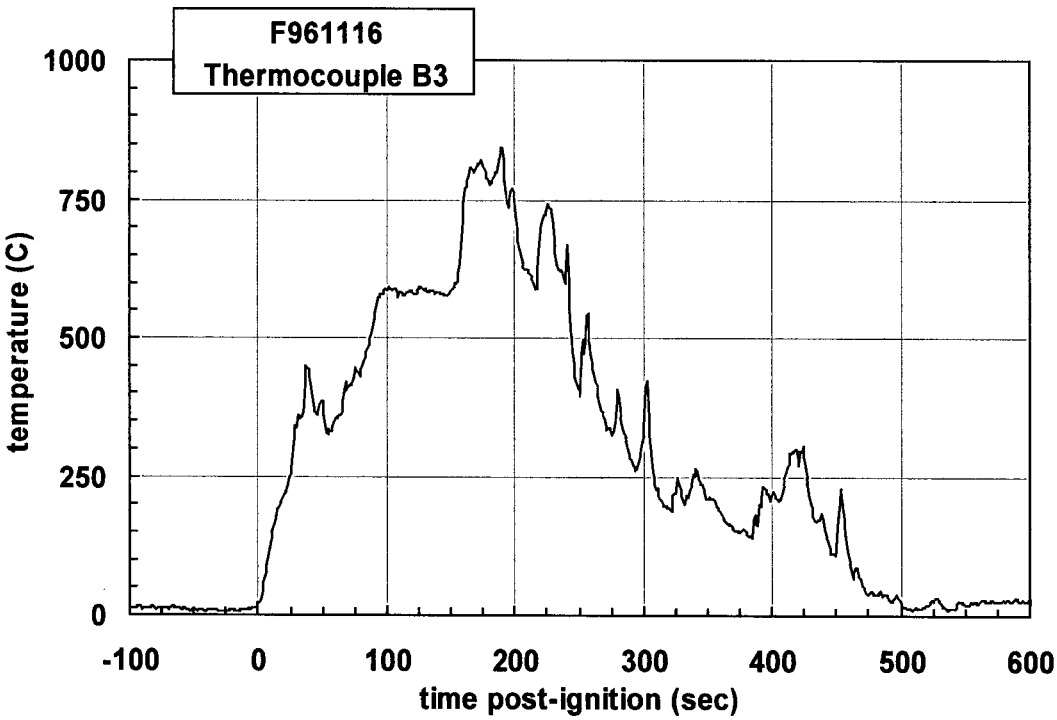


Plot C12. Fire Test F961116. Data plot from thermocouple B3.

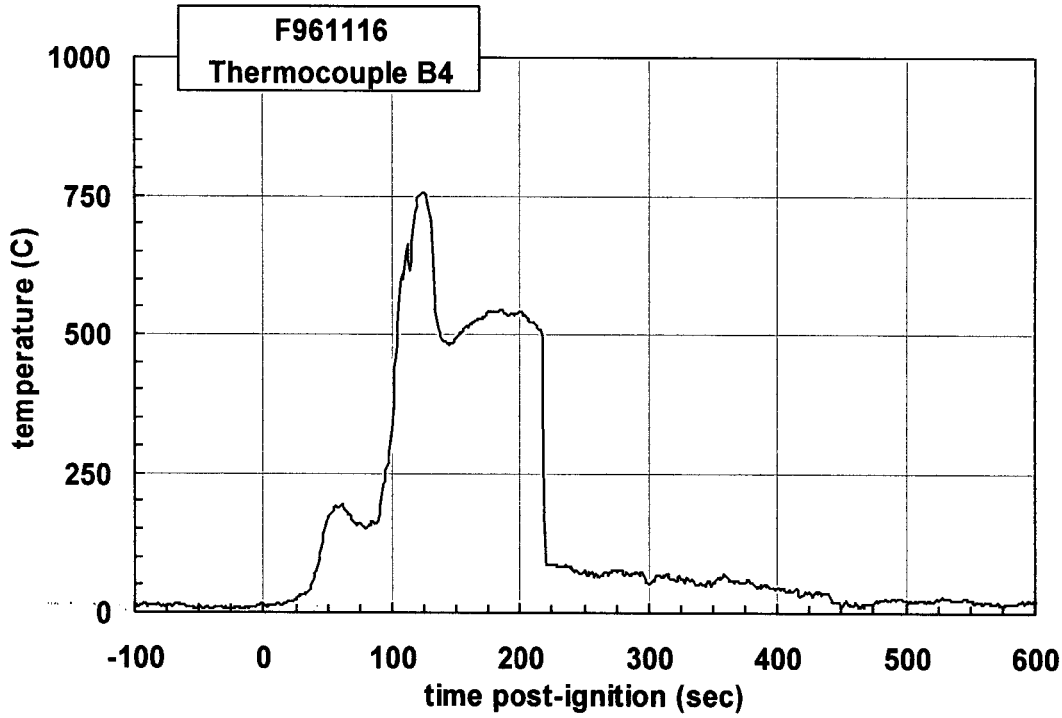


Plot C13. Fire Test F961116. Data plot from thermocouple B4.

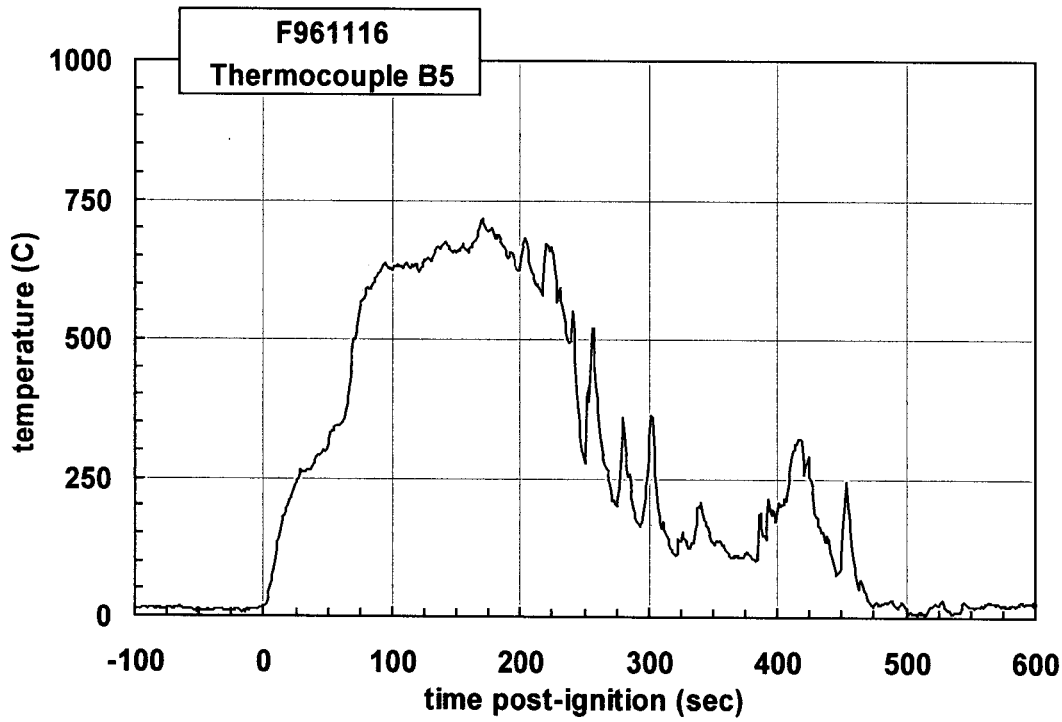


Plot C14. Fire Test F961116. Data plot from thermocouple B5.

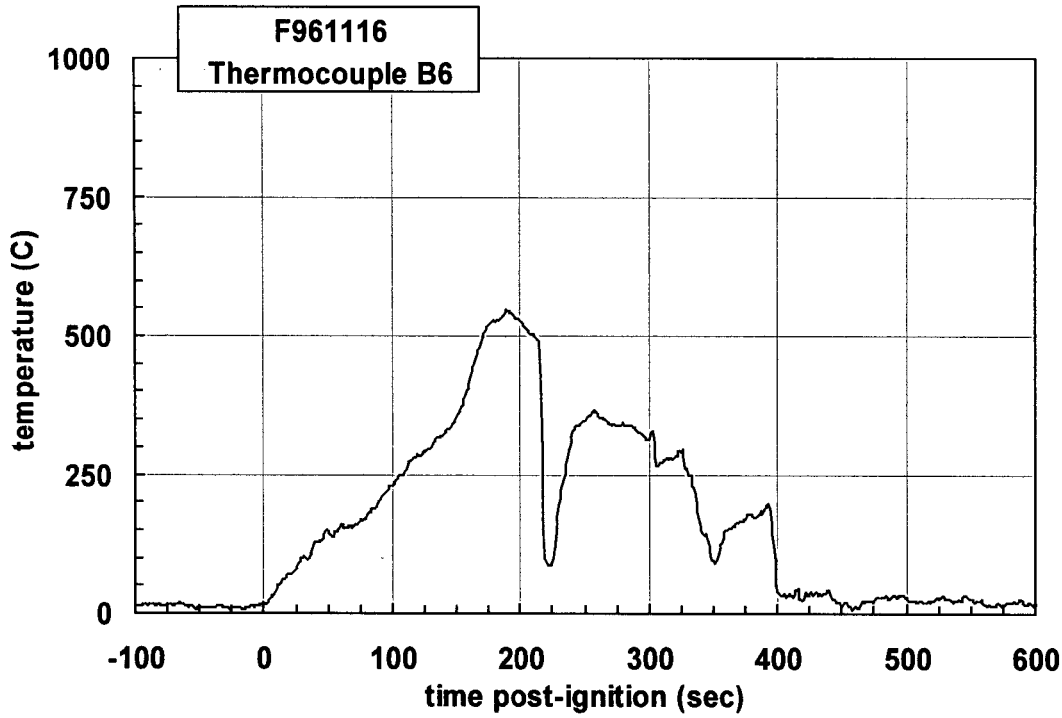


Plot C15. Fire Test F961116. Data plot from thermocouple B6.

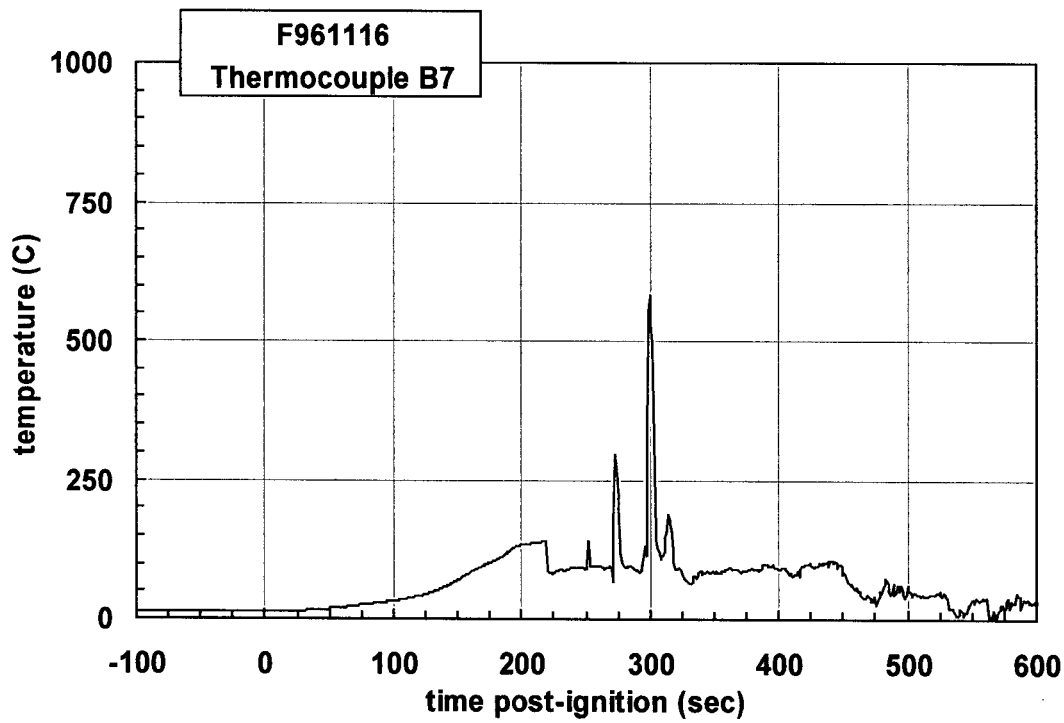


Plot C16. Fire Test F961116. Data plot from thermocouple B7.

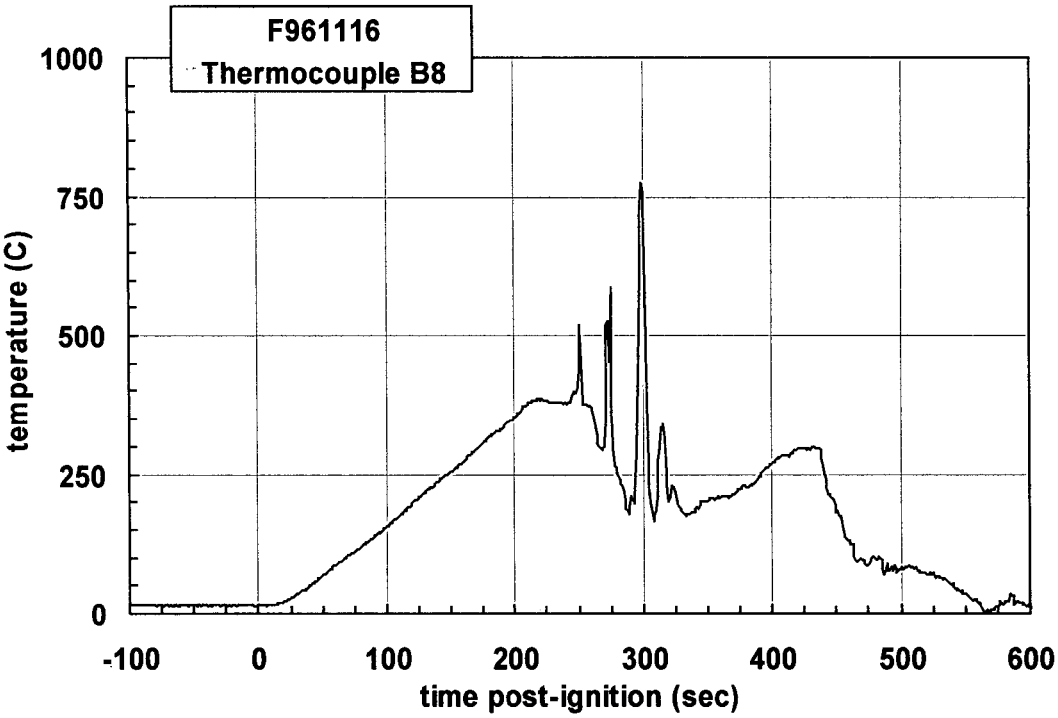


Plot C17. Fire Test F961116. Data plot from thermocouple B8.

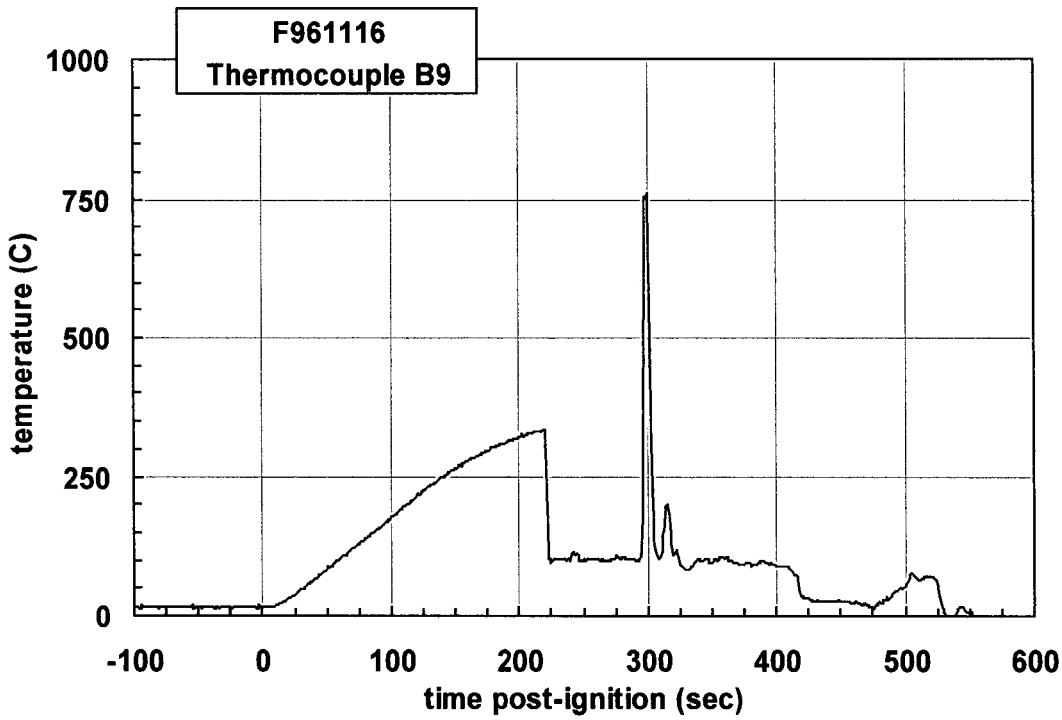


Plot C18. Fire Test F961116. Data plot from thermocouple B9.

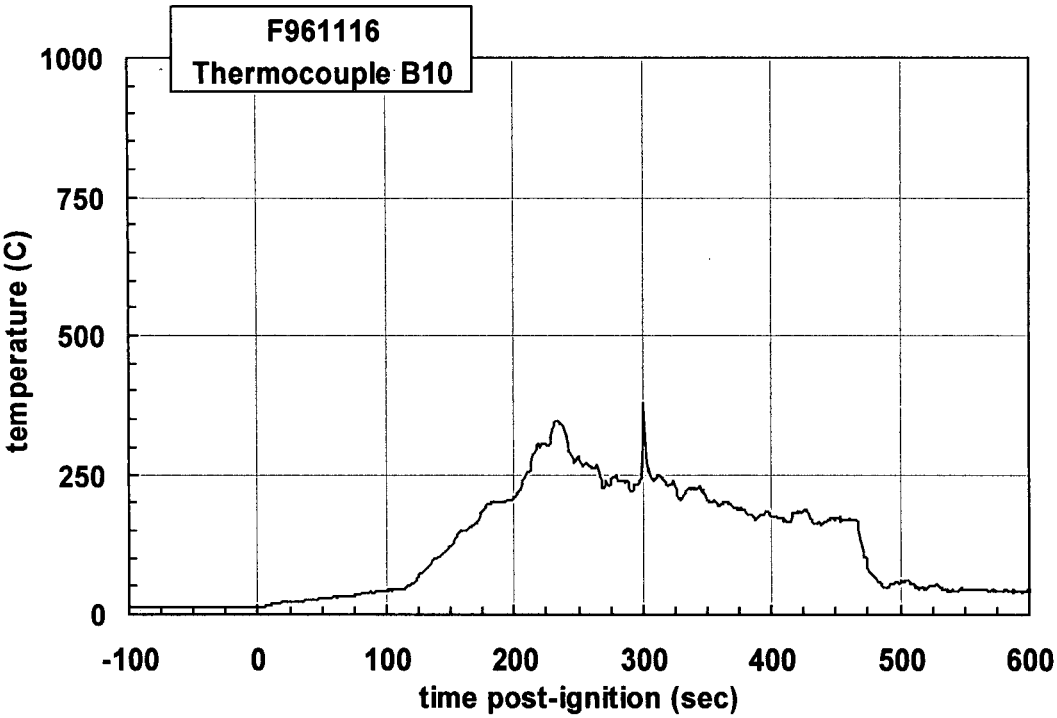


Plot C19. Fire Test F961116. Data plot from thermocouple B10.

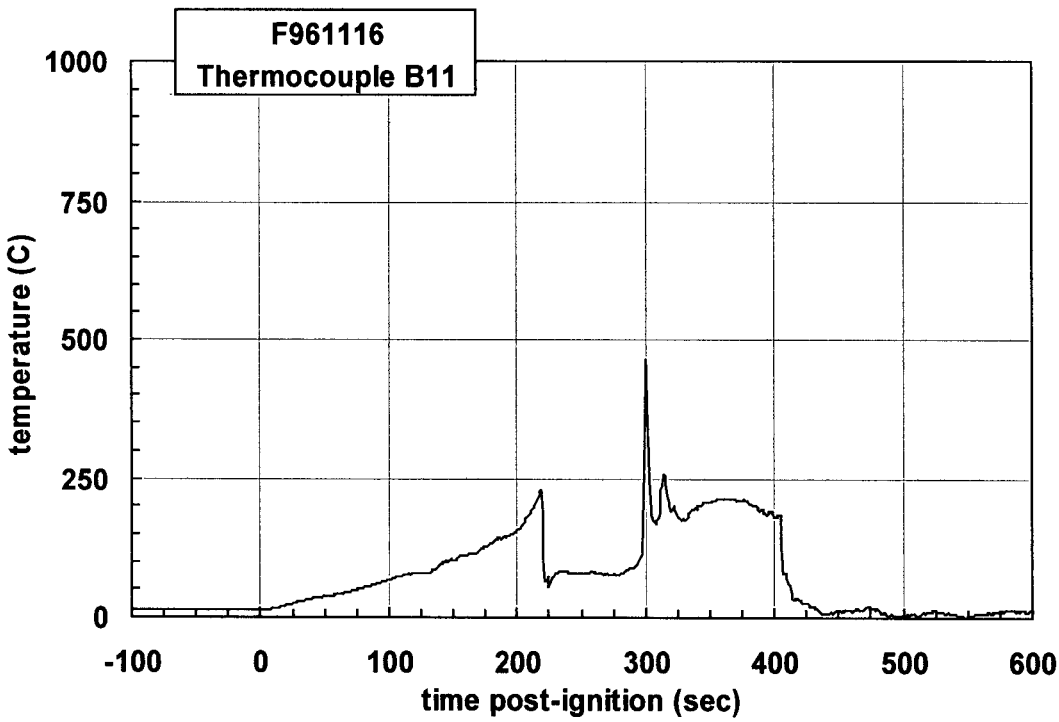


Plot C20. Fire Test F961116. Data plot from thermocouple B11.

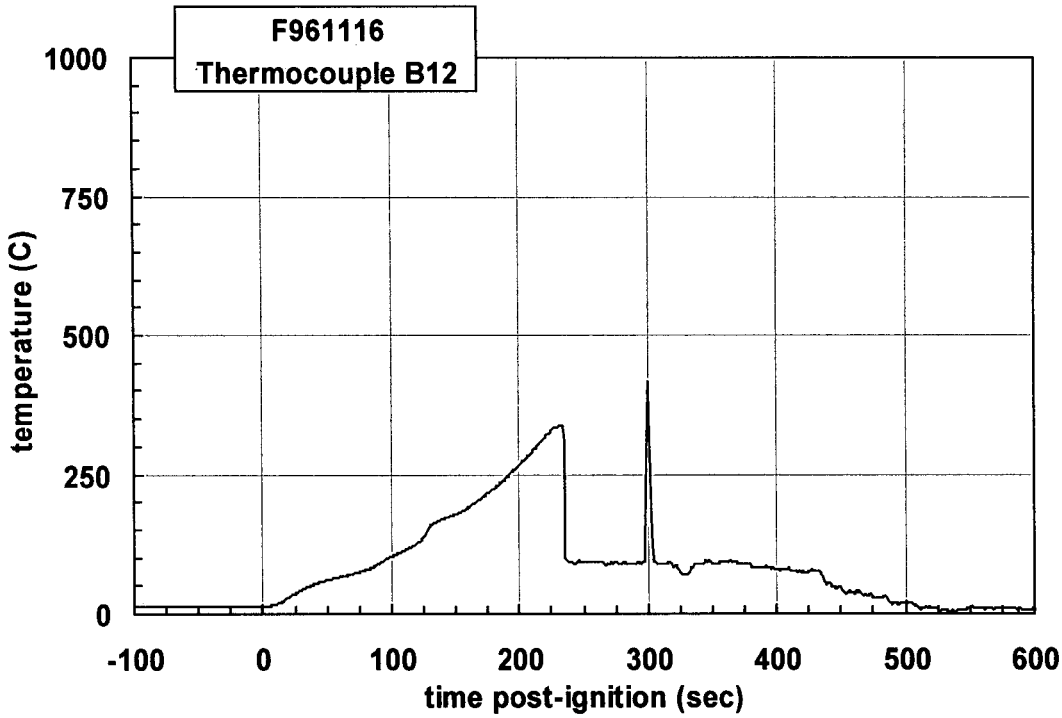


Plot C21. Fire Test F961116. Data plot from thermocouple B12.

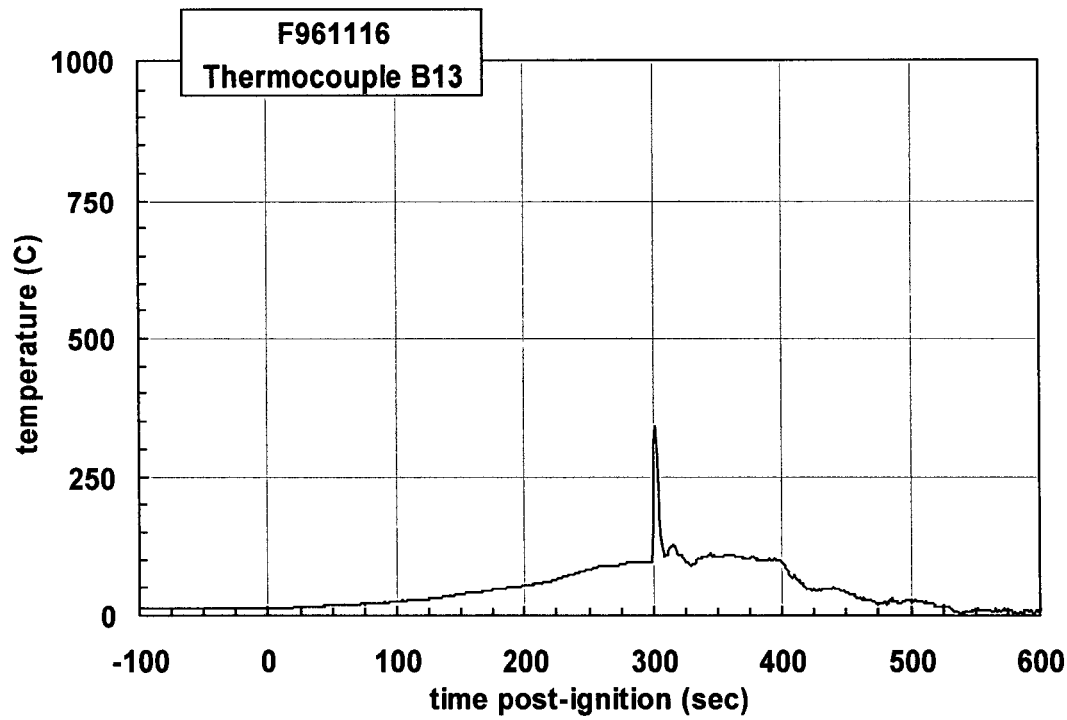


Plot C22. Fire Test F961116. Data plot from thermocouple B13.

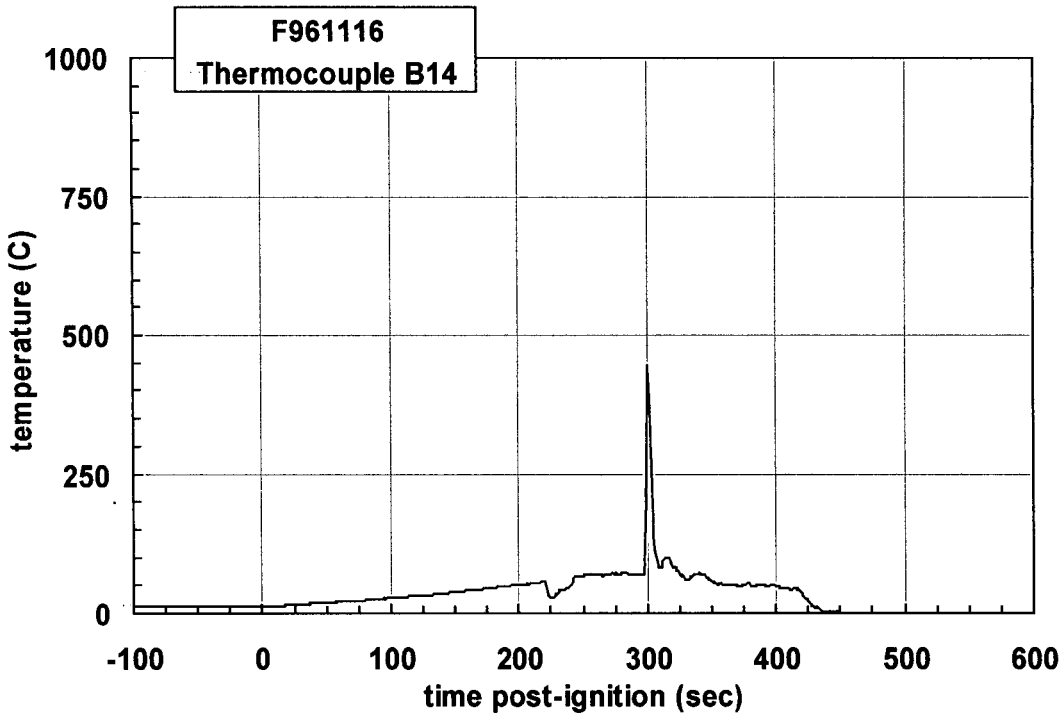


Plot C23. Fire Test F961116. Data plot from thermocouple B14.

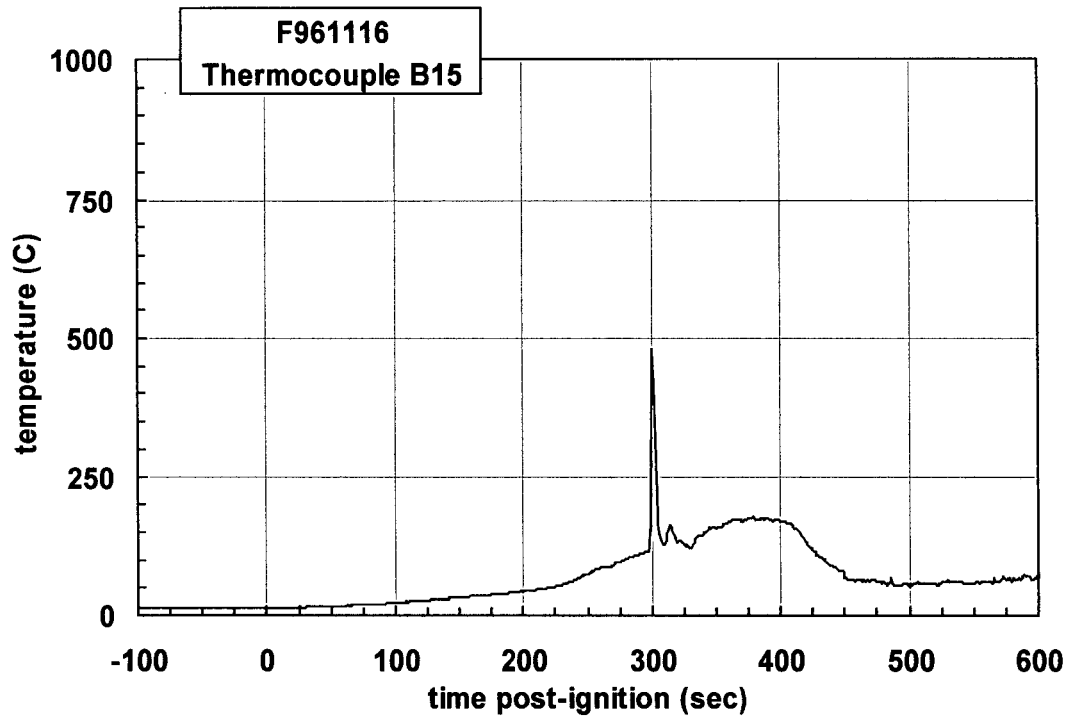


Plot C24. Fire Test F961116. Data plot from thermocouple B15.

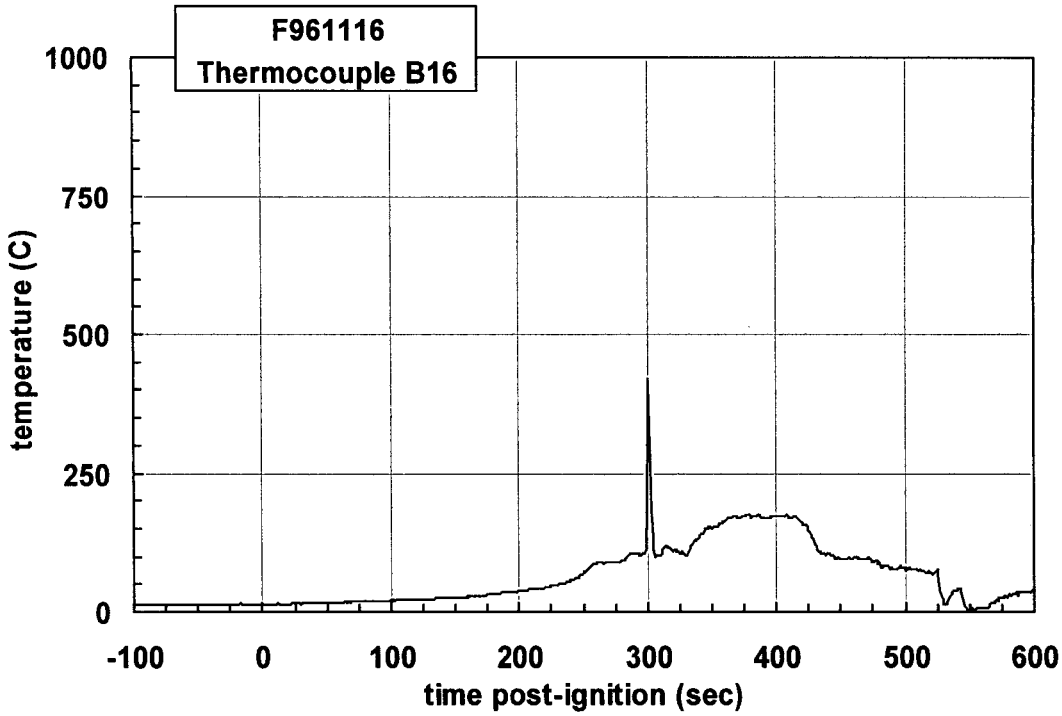


Plot C25. Fire Test F961116. Data plot from thermocouple B16.

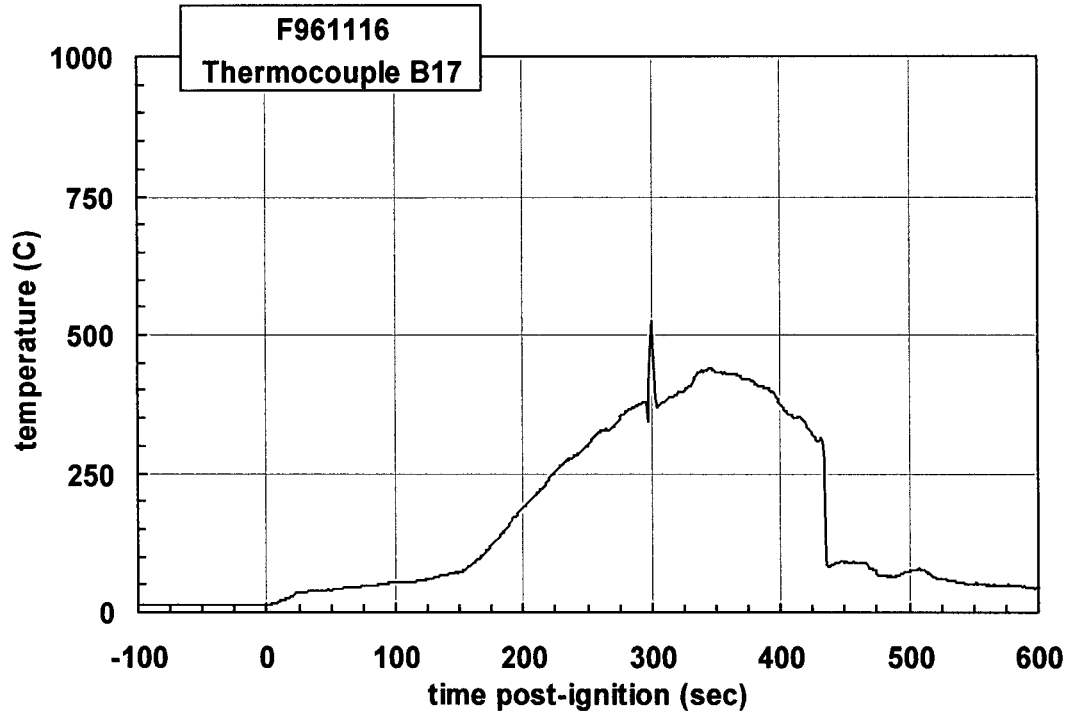


Plot C26. Fire Test F961116. Data plot from thermocouple B17.

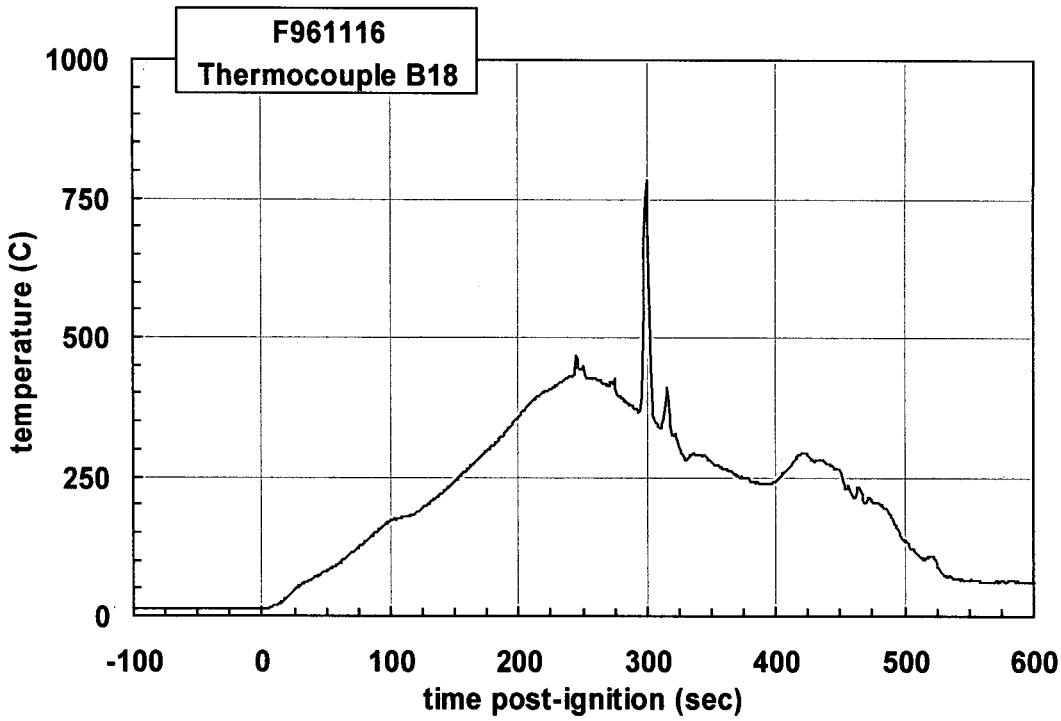


Plot C27. Fire Test F961116. Data plot from thermocouple B18.

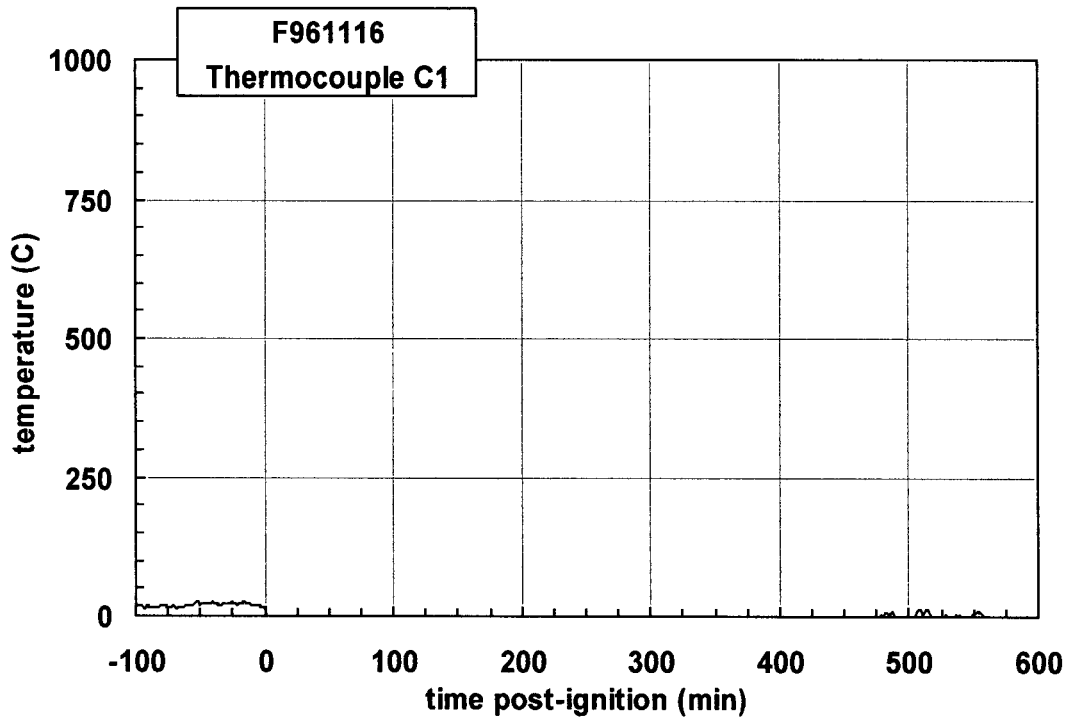


Plot C28. Fire Test F961116. Data plot from thermocouple C1. The thermocouple began to malfunction at 7 sec post-ignition.

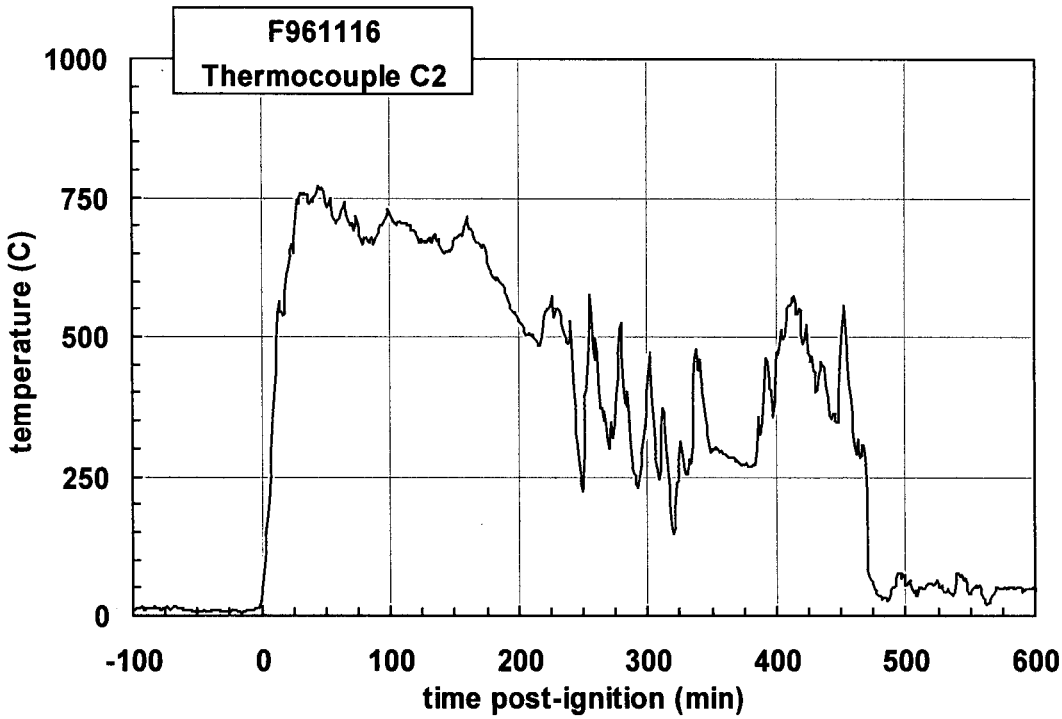


Plot C29. Fire Test F961116. Data plot from thermocouple C2.

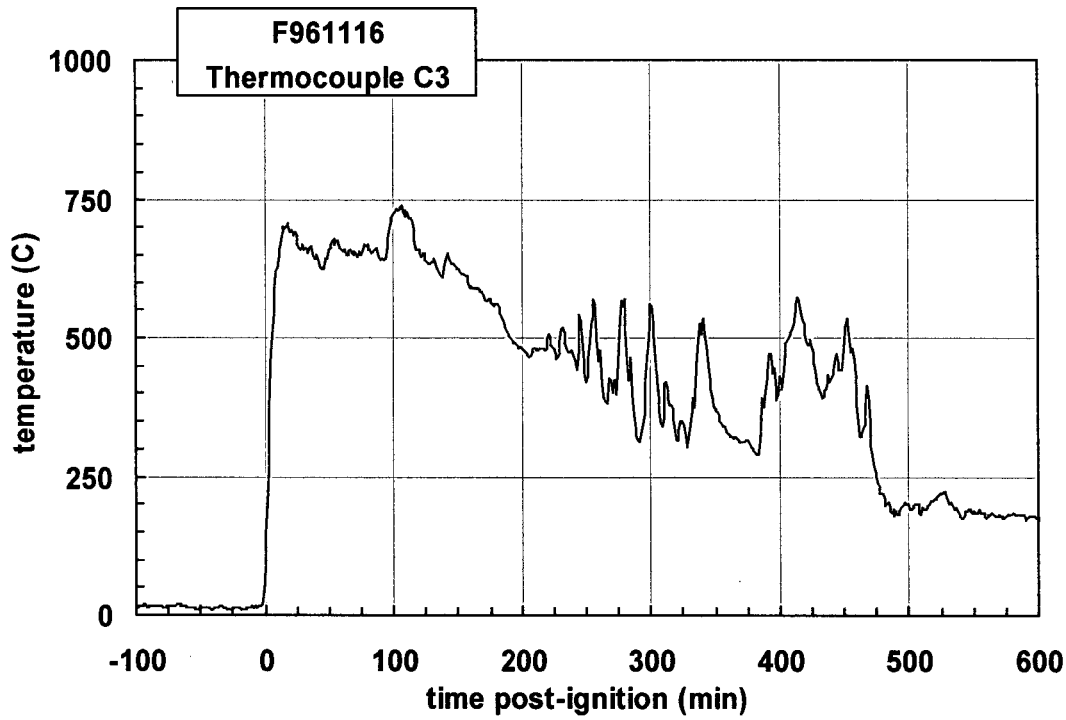


Plot C30. Fire Test F961116. Data plot from thermocouple C3.

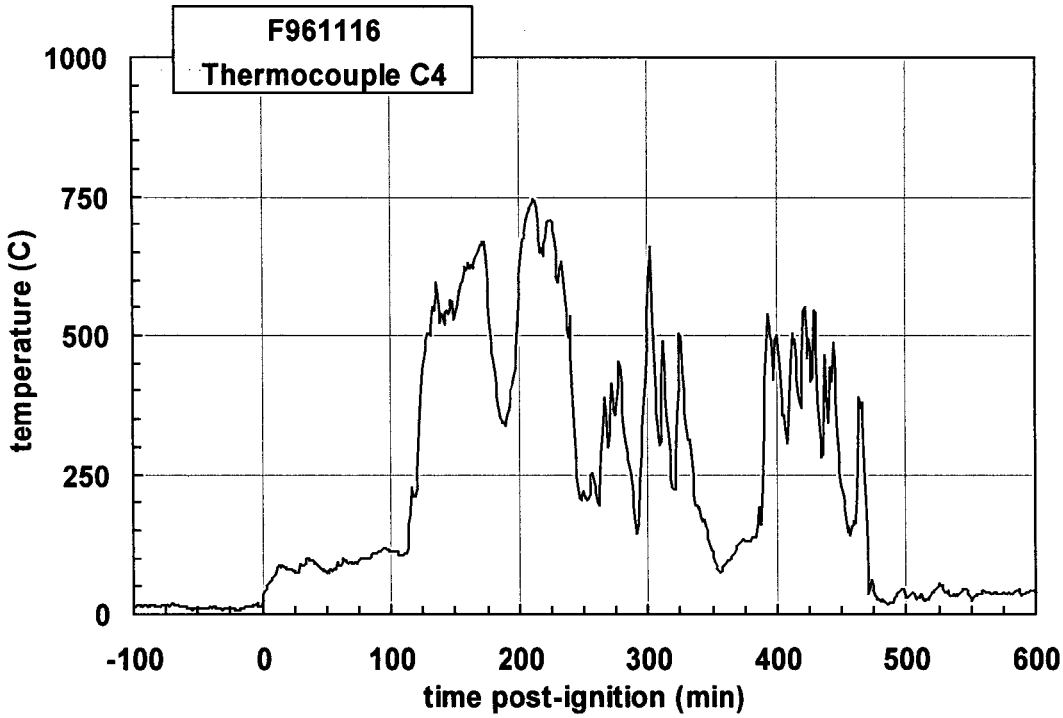


Plot C31. Fire Test F961116. Data plot from thermocouple C4.

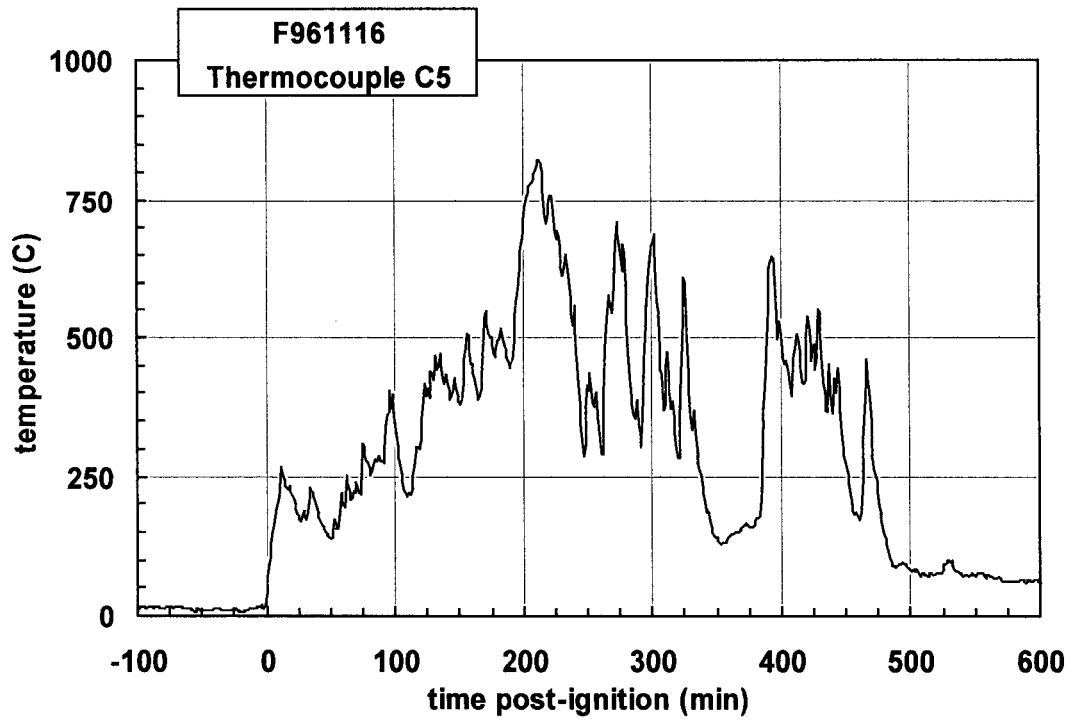


Plot C32. Fire Test F961116. Data plot from thermocouple C5.

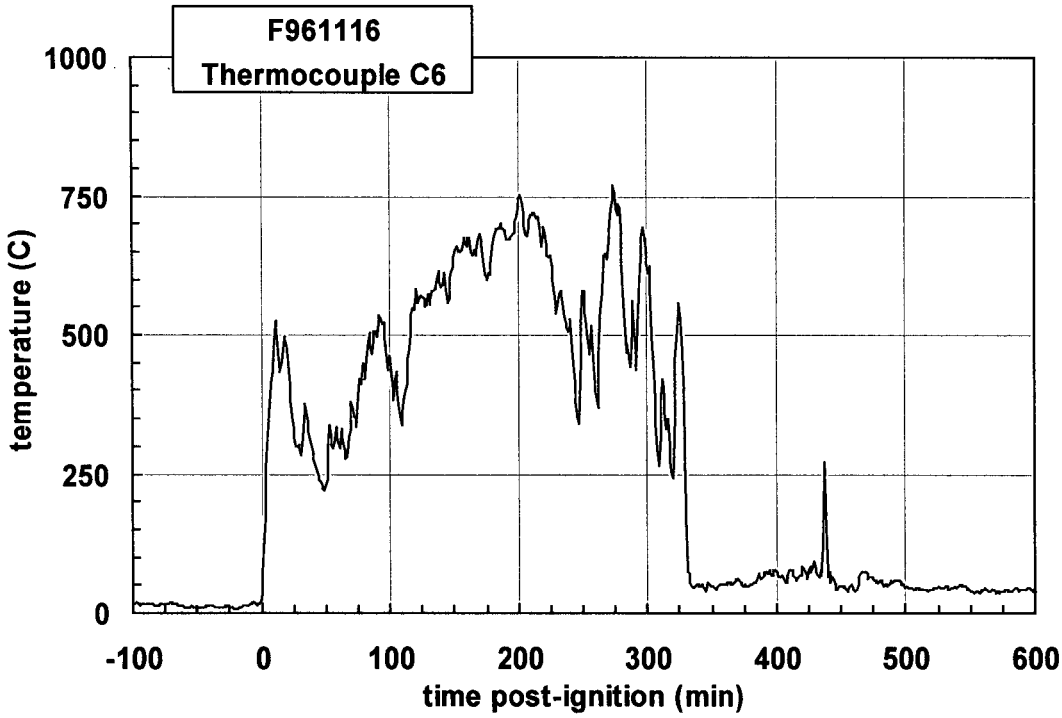


Plot C33. Fire Test F961116. Data plot from thermocouple C6.

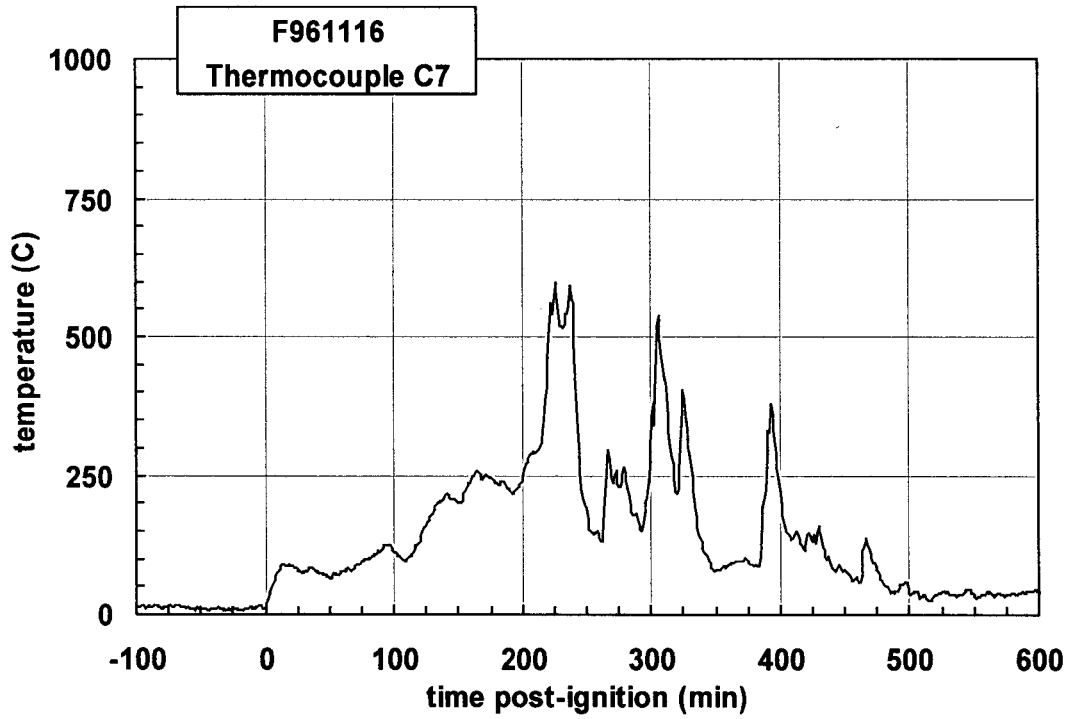


Plot C34. Fire Test F961116. Data plot from thermocouple C7.

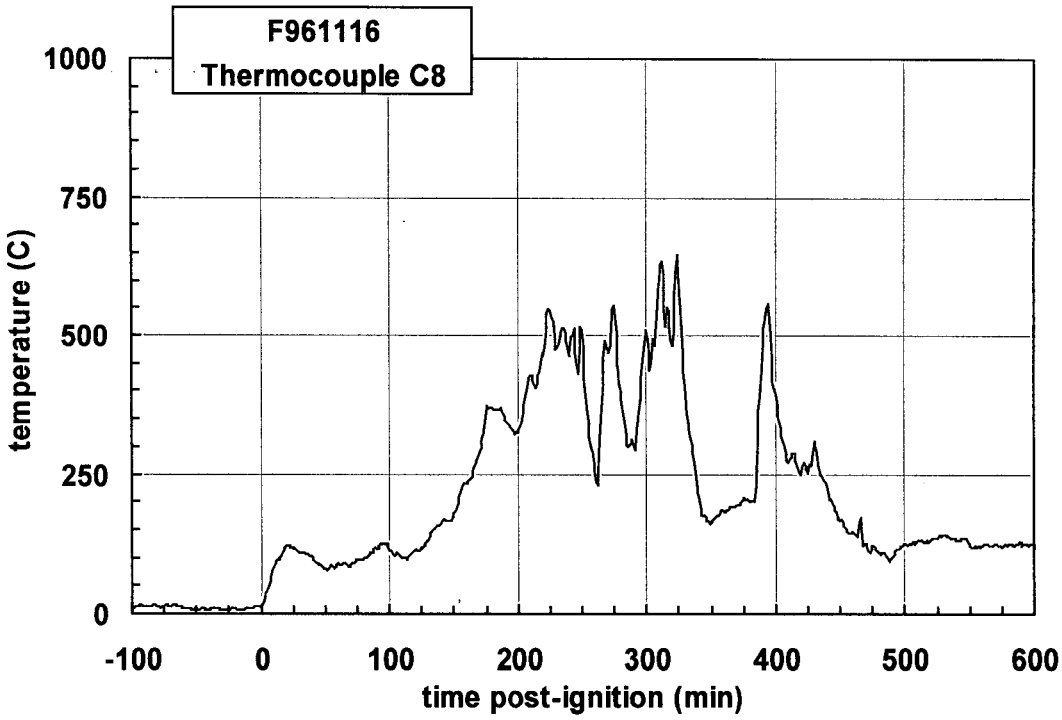


Plot C35. Fire Test F961116. Data plot from thermocouple C8.

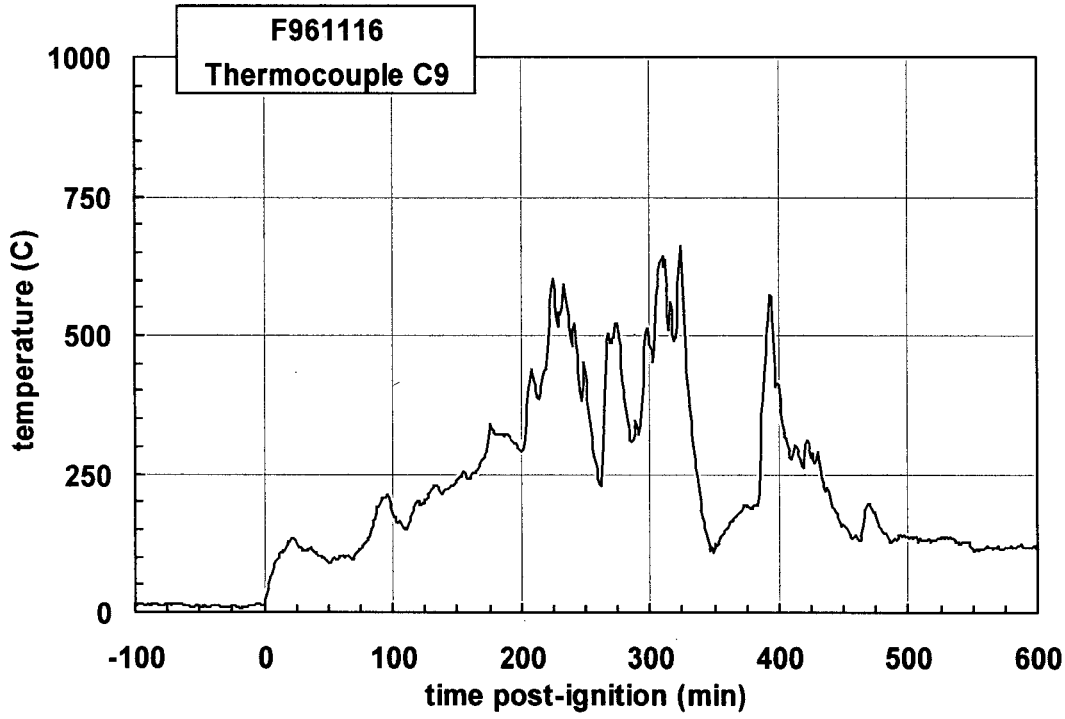


Plot C36. Fire Test F961116. Data plot from thermocouple C9.

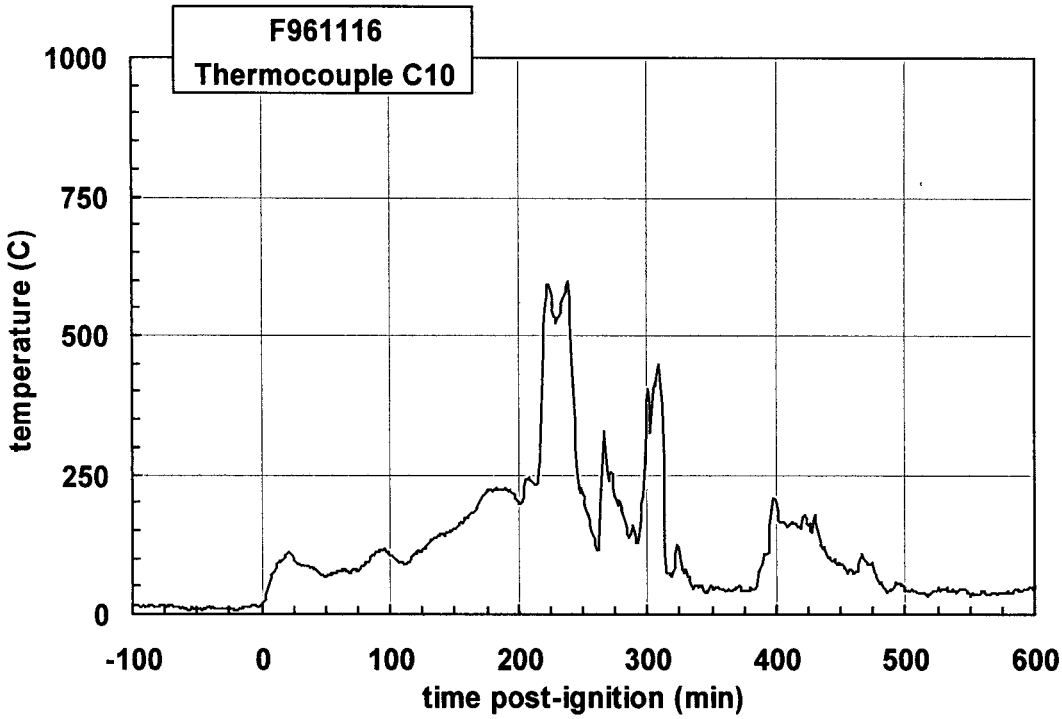


Plot C37. Fire Test F961116. Data plot from thermocouple C10.

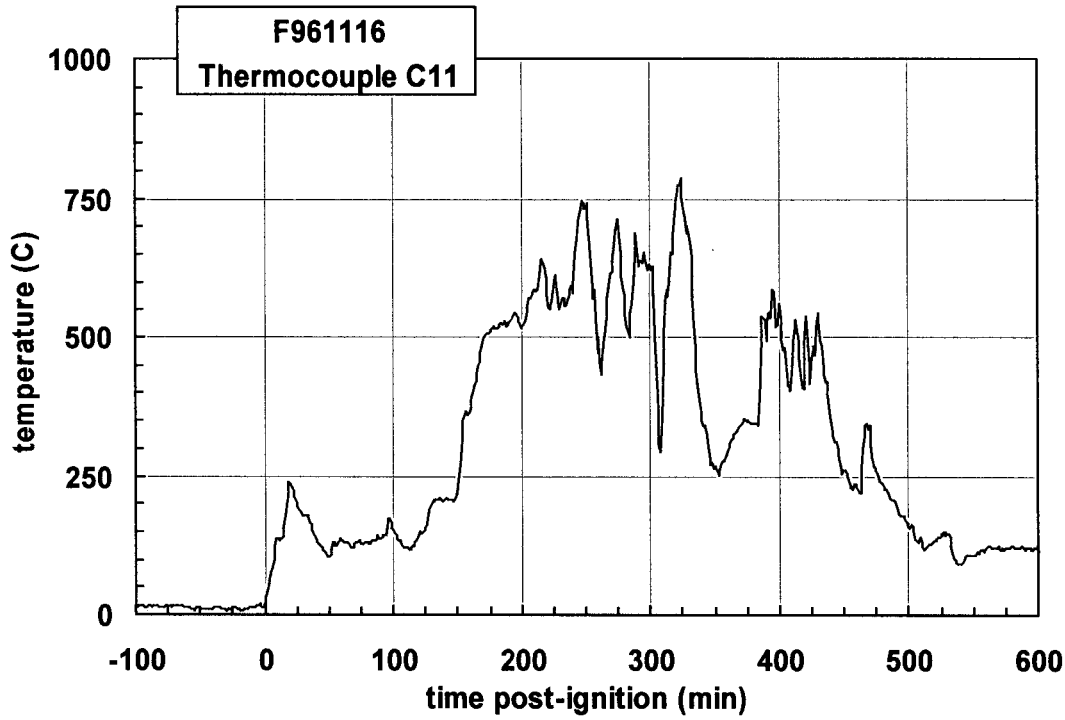


Plot C38. Fire Test F961116. Data plot from thermocouple C11.

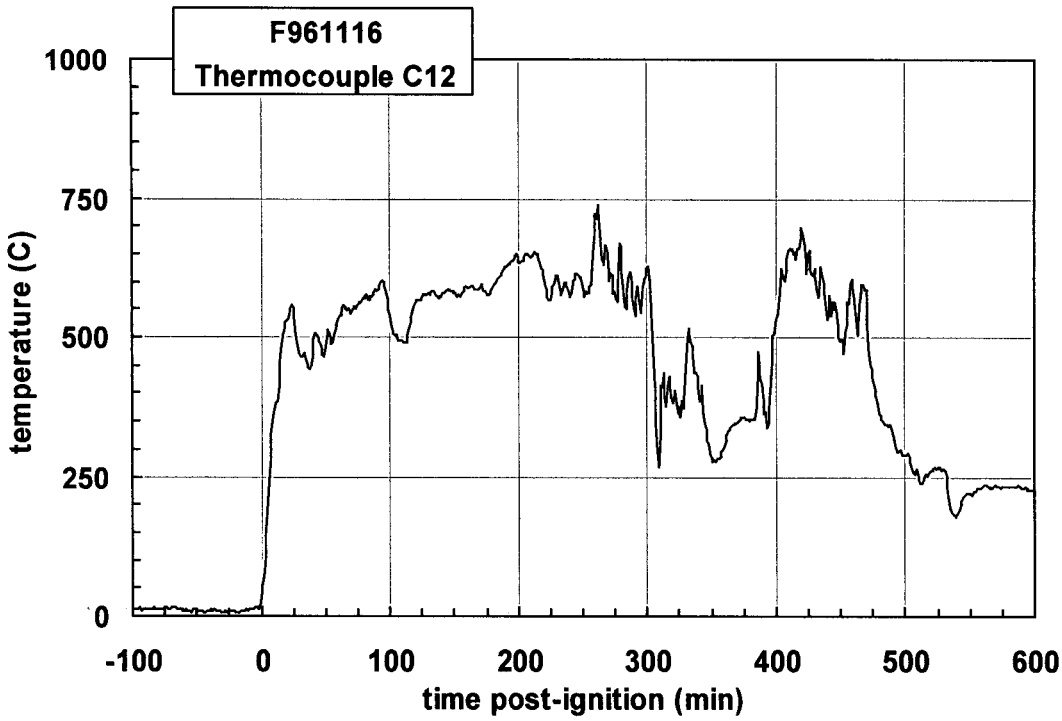


Plot C39. Fire Test F961116. Data plot from thermocouple C12.

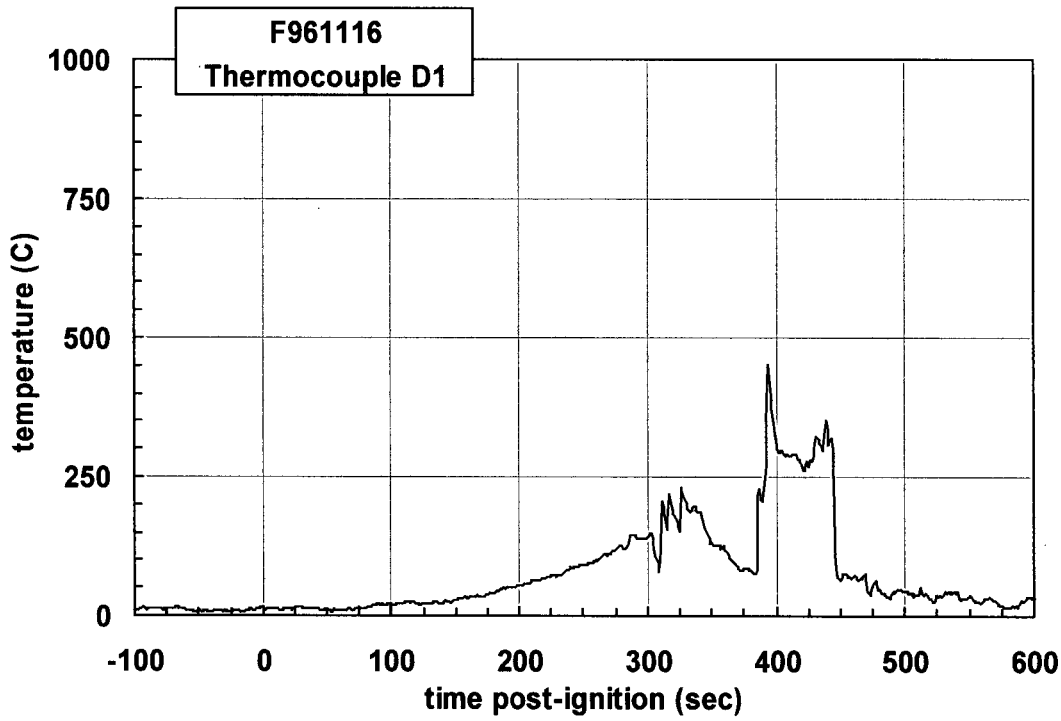


Plot C40. Fire Test F961116. Data plot from thermocouple D1.

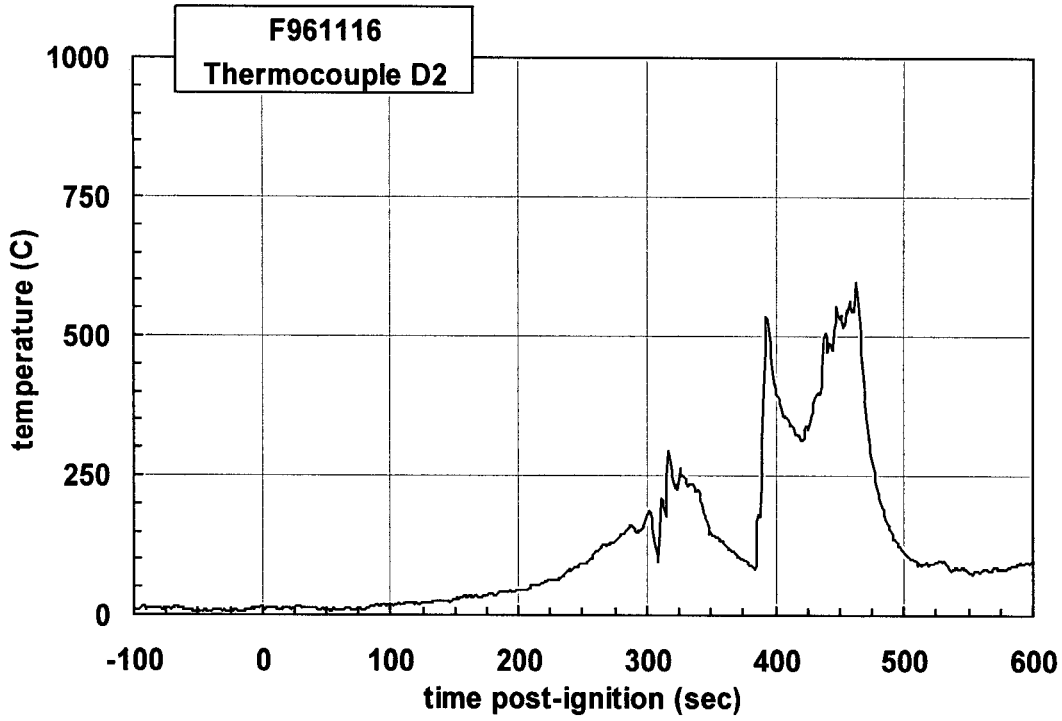


Plot C41. Fire Test F961116. Data plot from thermocouple D2.

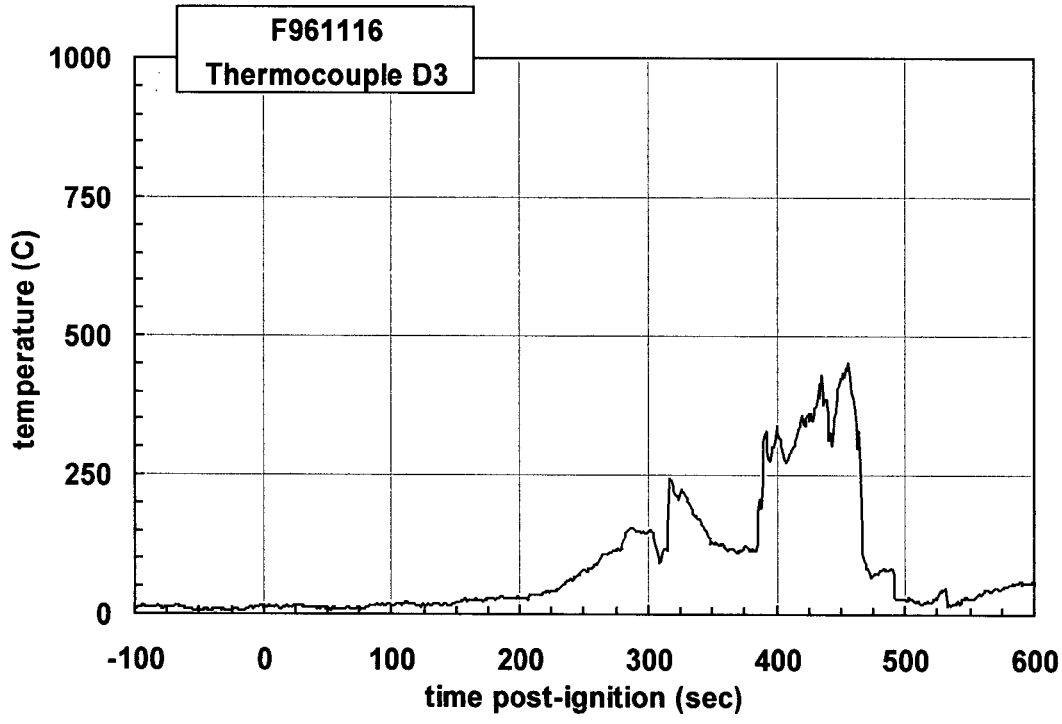


Plot C42. Fire Test F961116. Data plot from thermocouple D3.

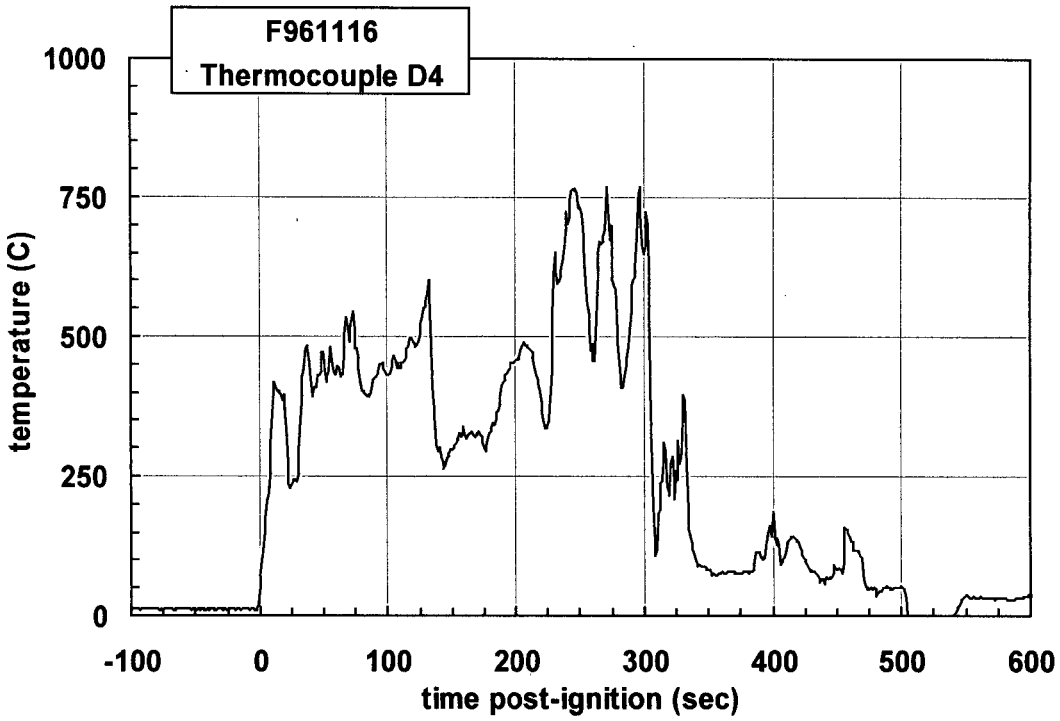


Plot C43. Fire Test F961116. Data plot from thermocouple D4.

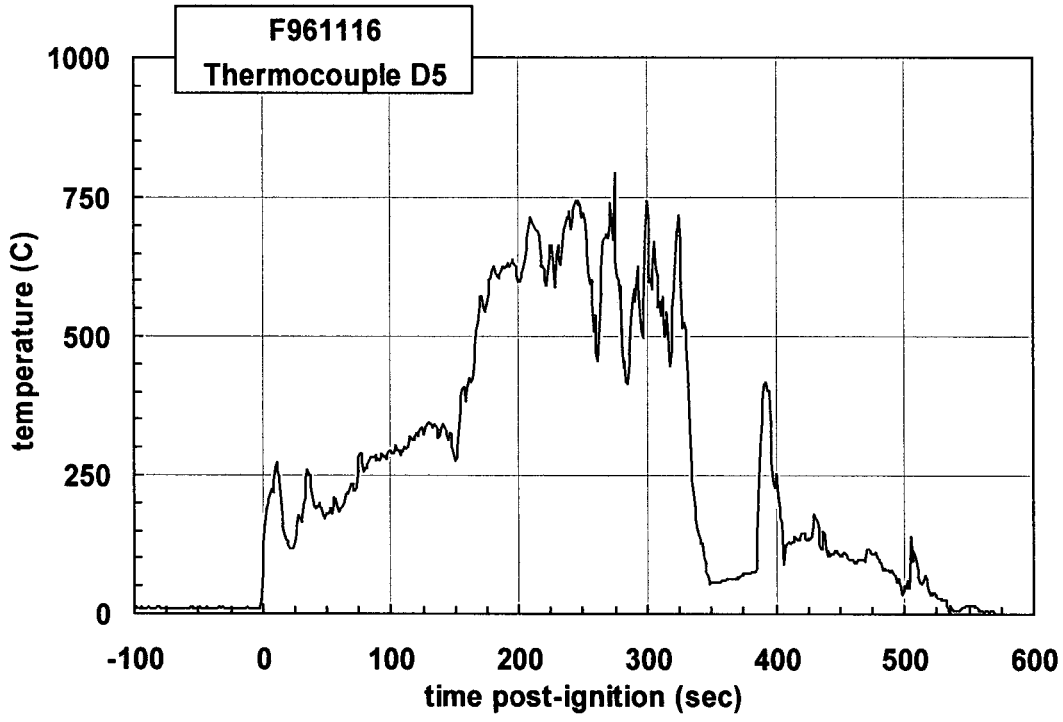


Plot C44. Fire Test F961116. Data plot from thermocouple D5

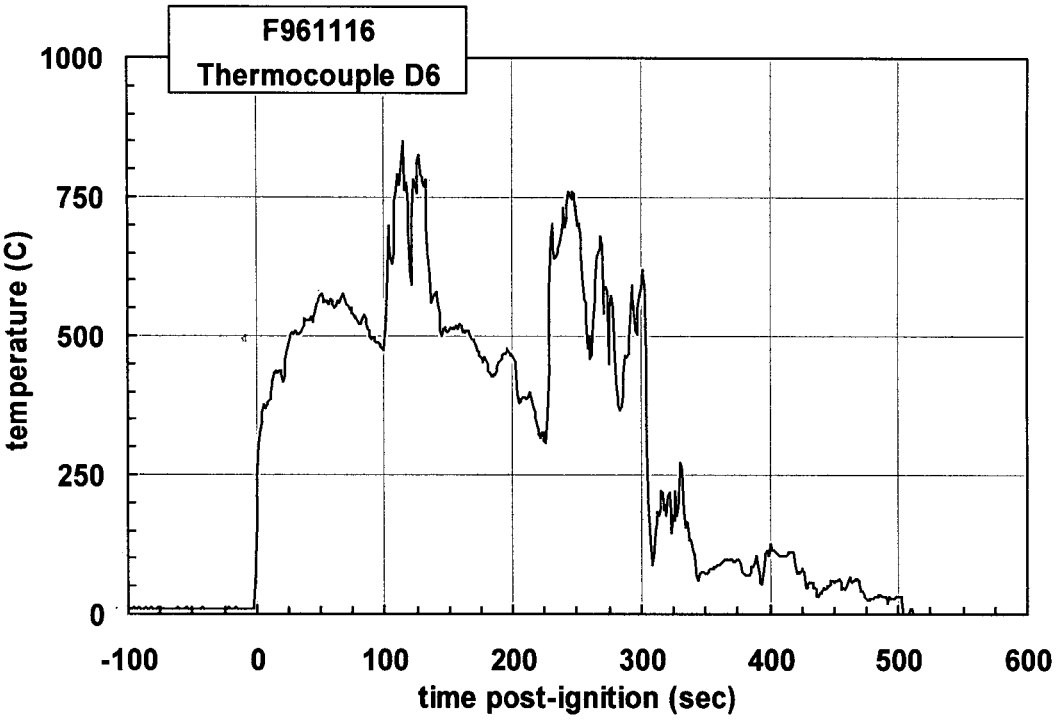


Plot C45. Fire Test F961116. Data plot from thermocouple D6.

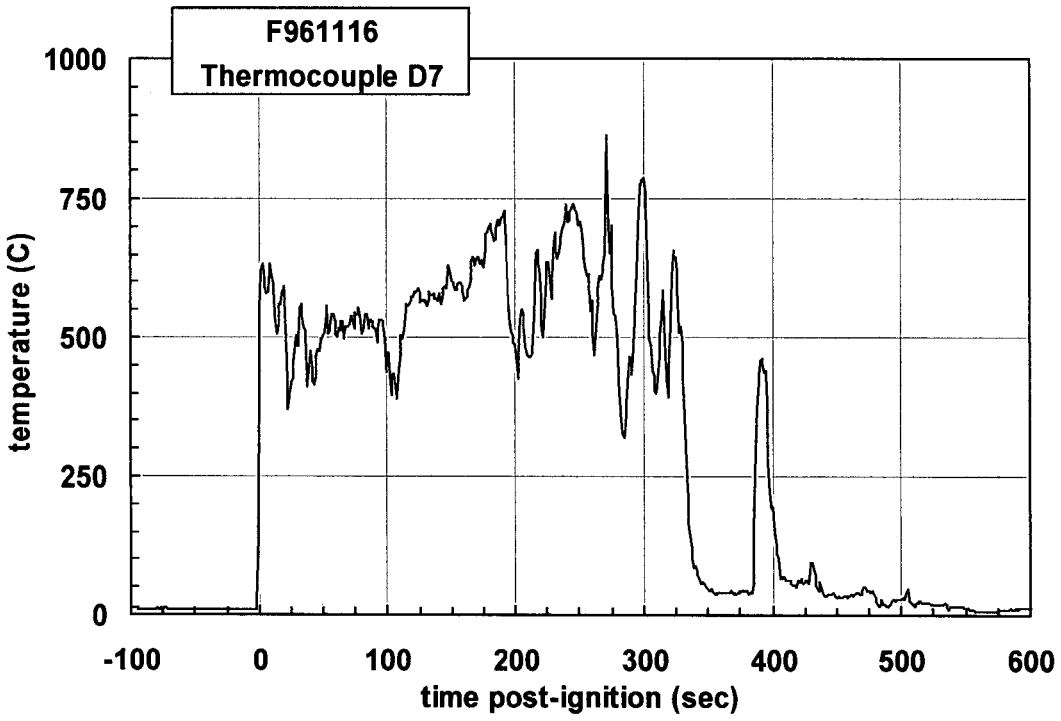


Plot C46. Fire Test F961116. Data plot from thermocouple D7.

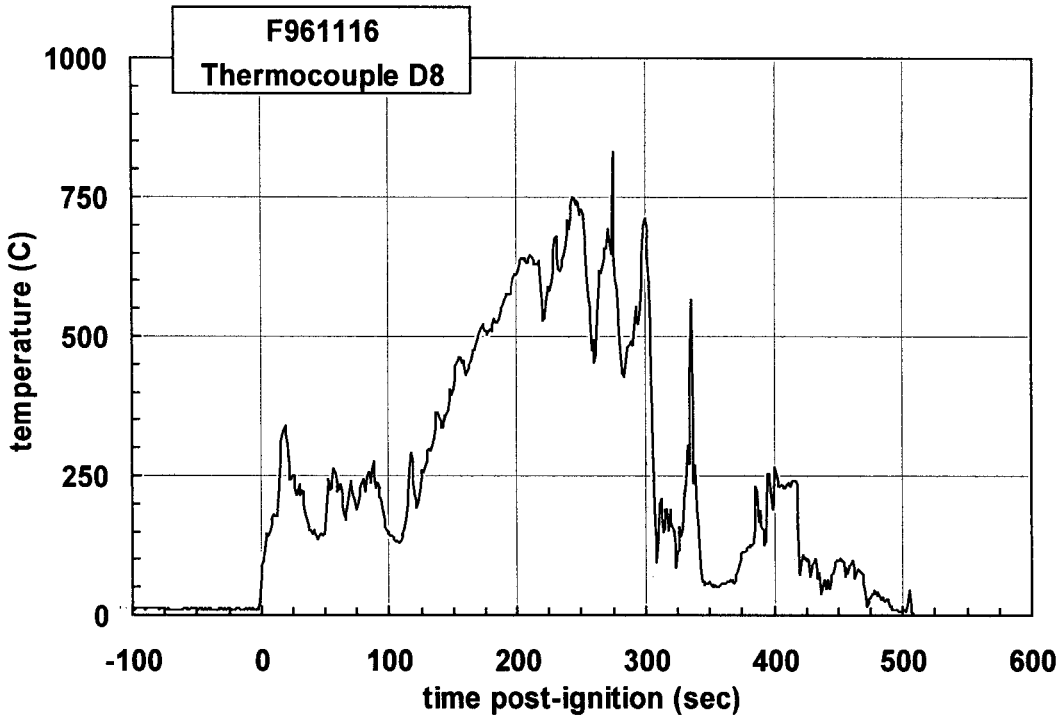


Plot C47. Fire Test F961116. Data plot from thermocouple D8.

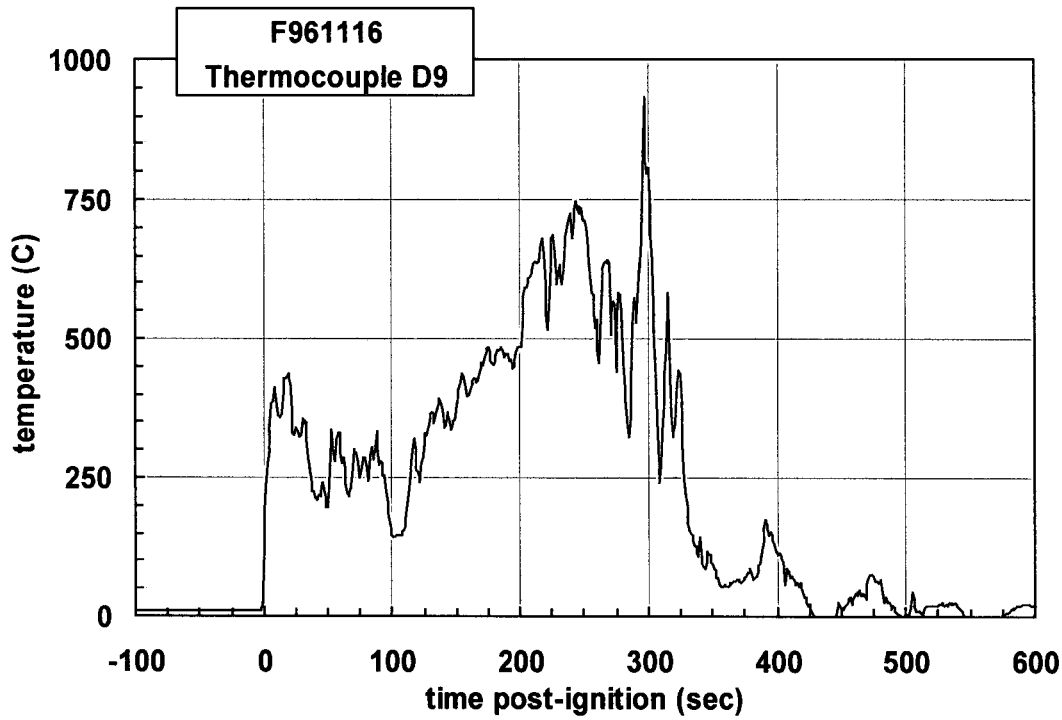


Plot C48. Fire Test F961116. Data plot from thermocouple D9.

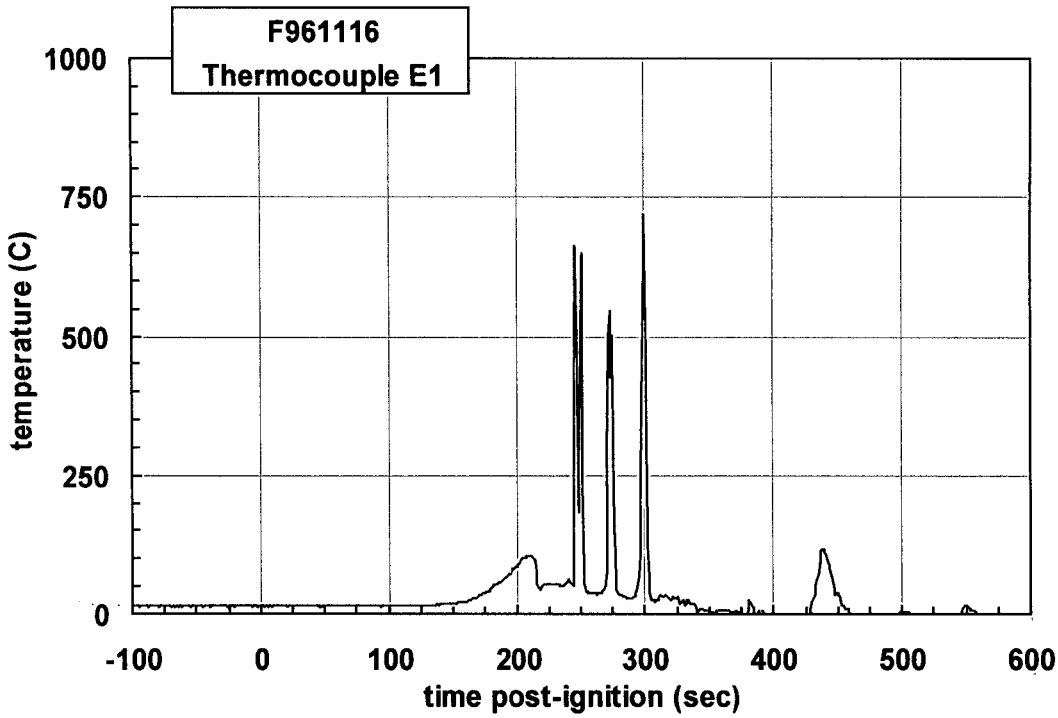


Plot C49. Fire Test F961116. Data plot from thermocouple E1.

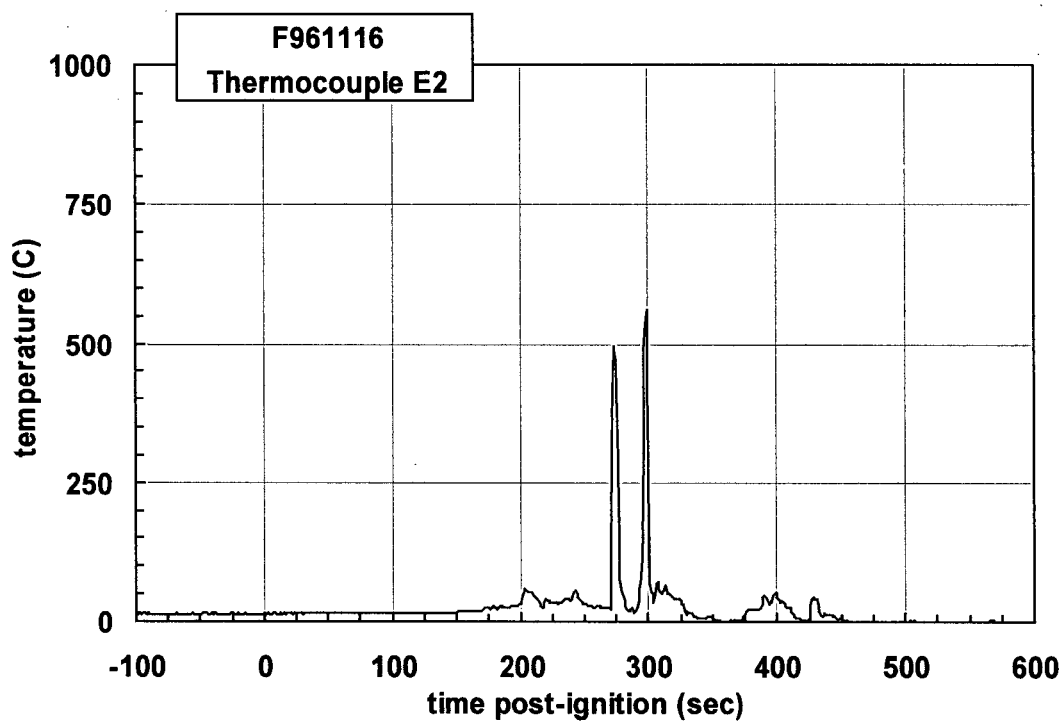


Plot C50. Fire Test F961116. Data plot from thermocouple E2.

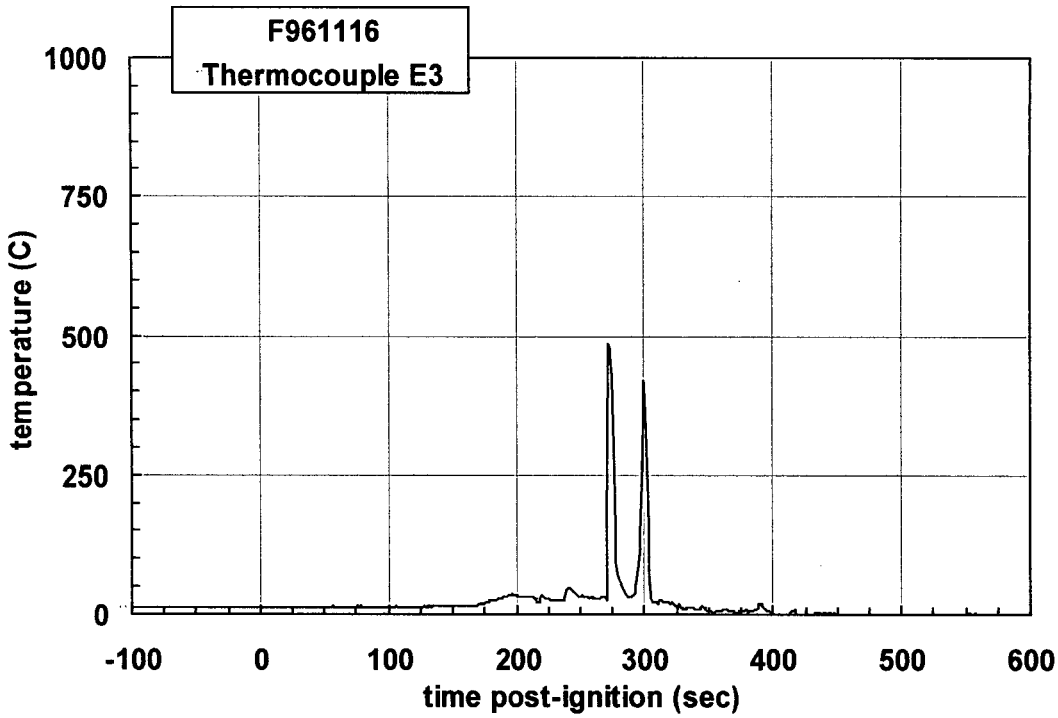


Plot C51. Fire Test F961115. Data plot from thermocouple E3.

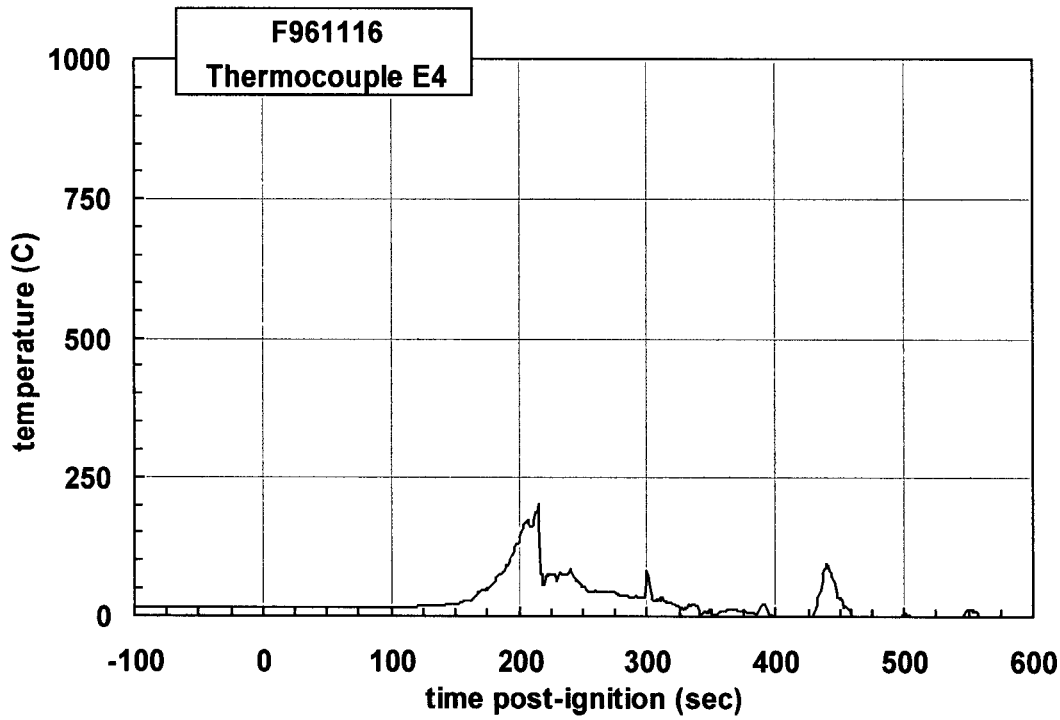


Plot C52. Fire Test F961116. Data plot from thermocouple E4.

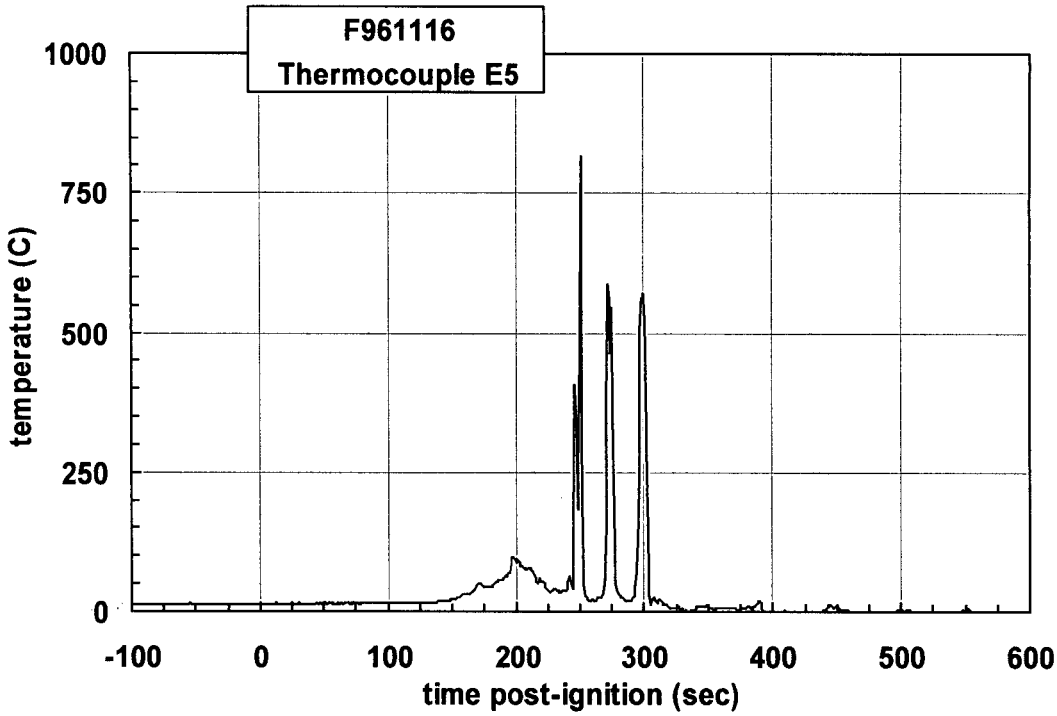


Plot C53. Fire Test F961116. Data plot from thermocouple E5.

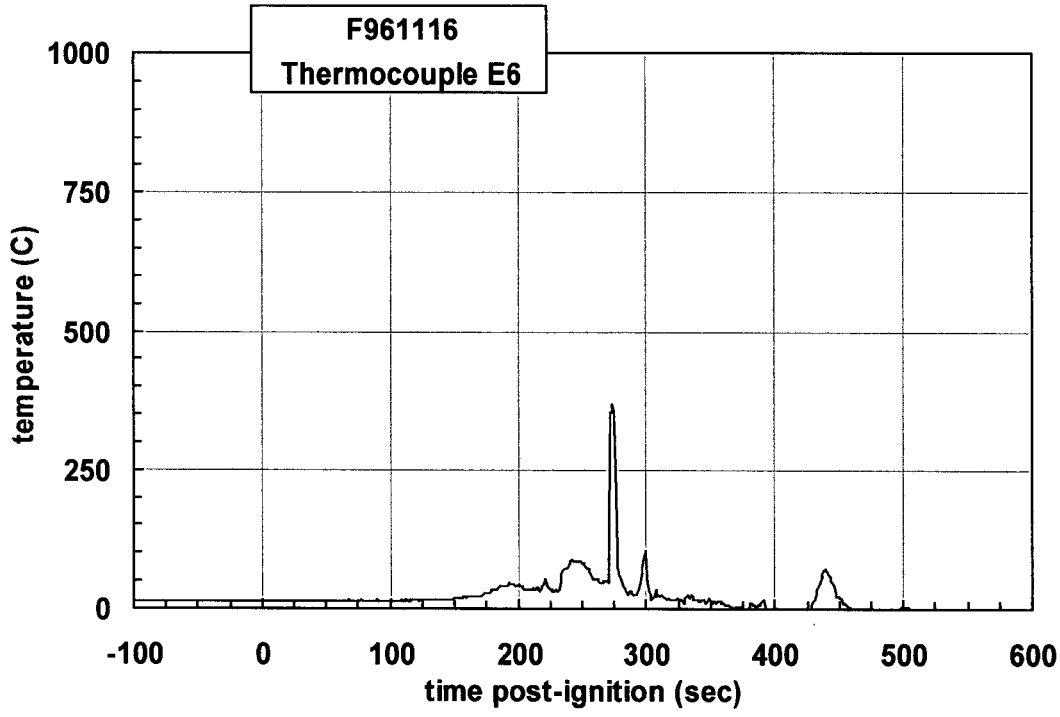


Plot C54. Fire Test F961116. Data plot from thermocouple E6.

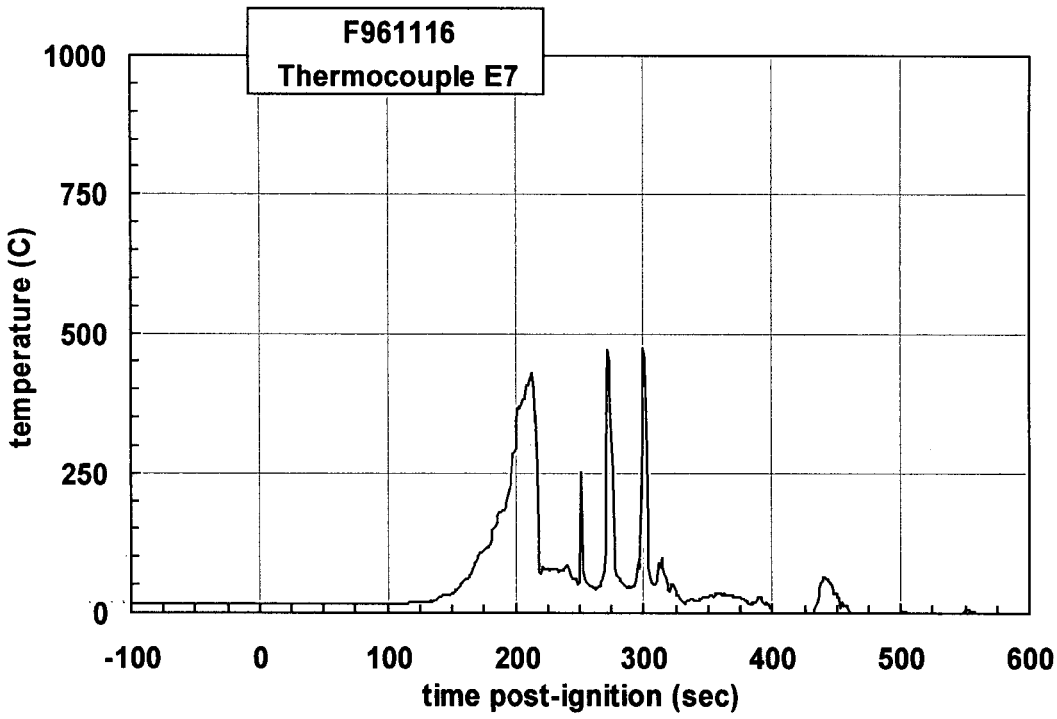


Plot C55. Fire Test F961116. Data plot from thermocouple E7.

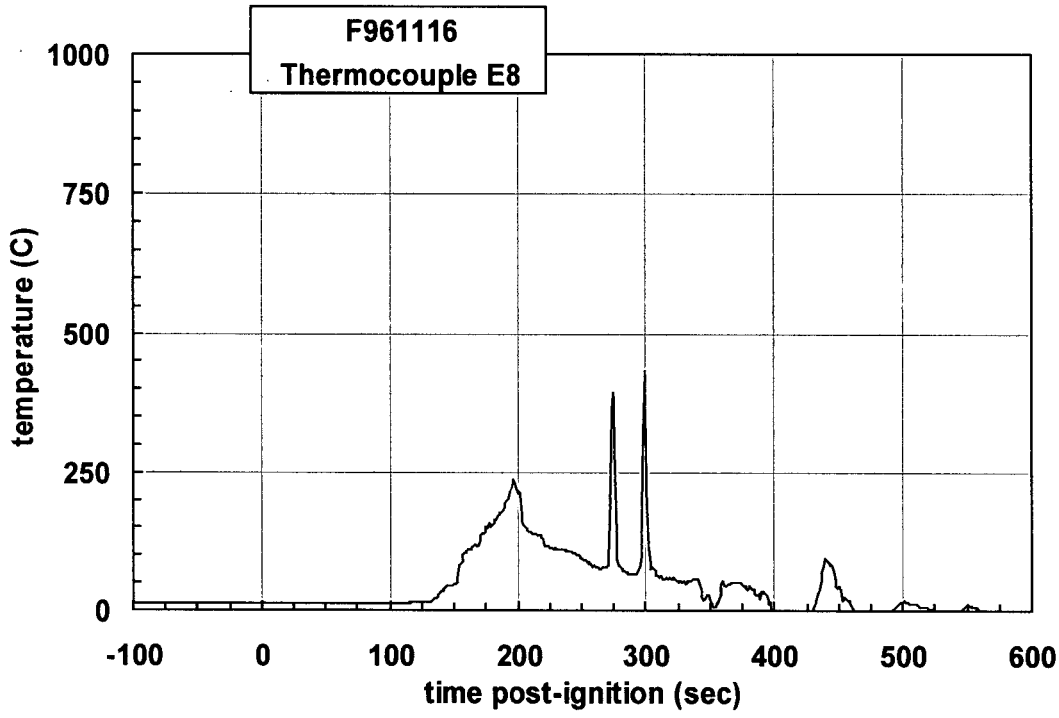


Plot C56. Fire Test F961116. Data plot from thermocouple E8.

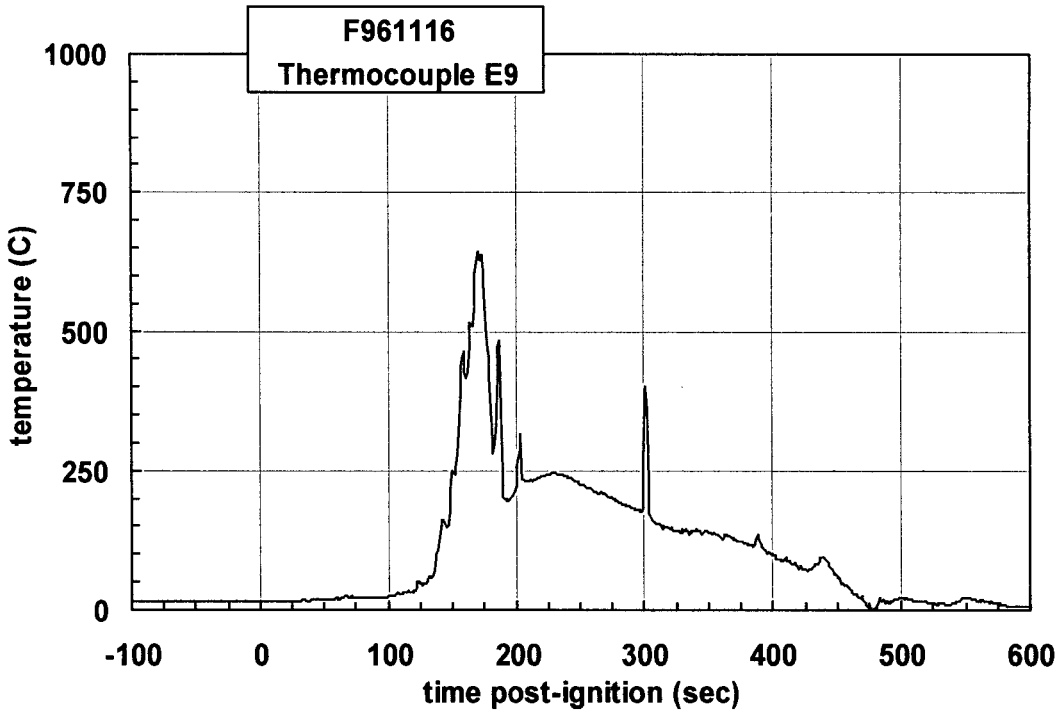


Plot C57. Fire Test F961116. Data plot from thermocouple E9.

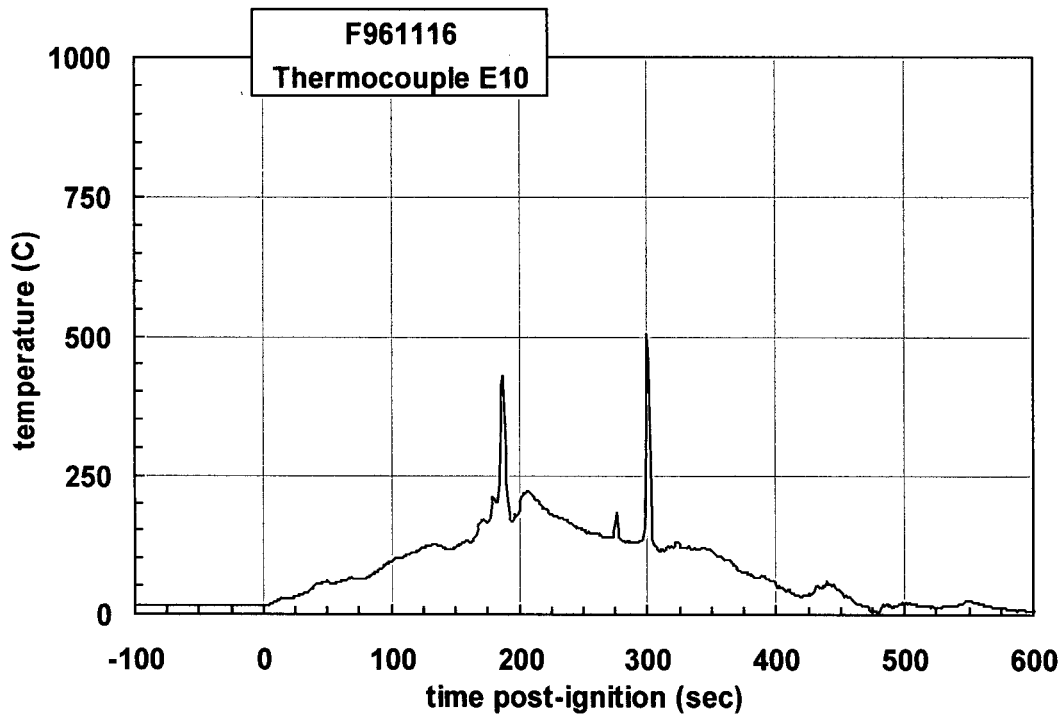


Plot C58. Fire Test F961116. Data plot from thermocouple E10.

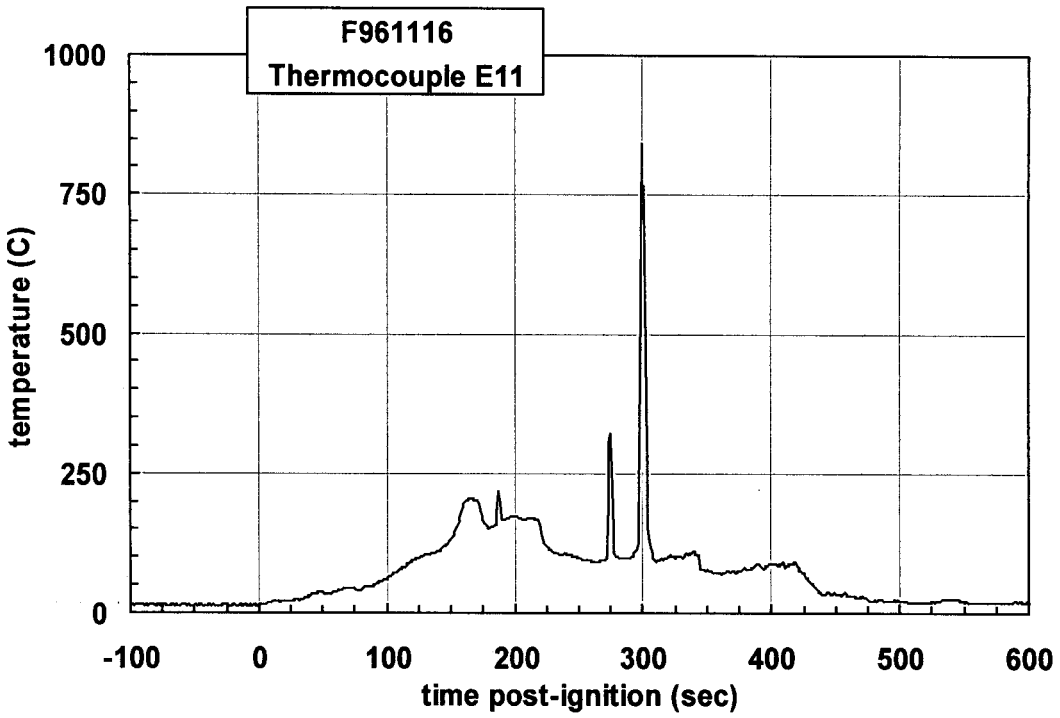


Plot C59. Fire Test F961116. Data plot from thermocouple E11.

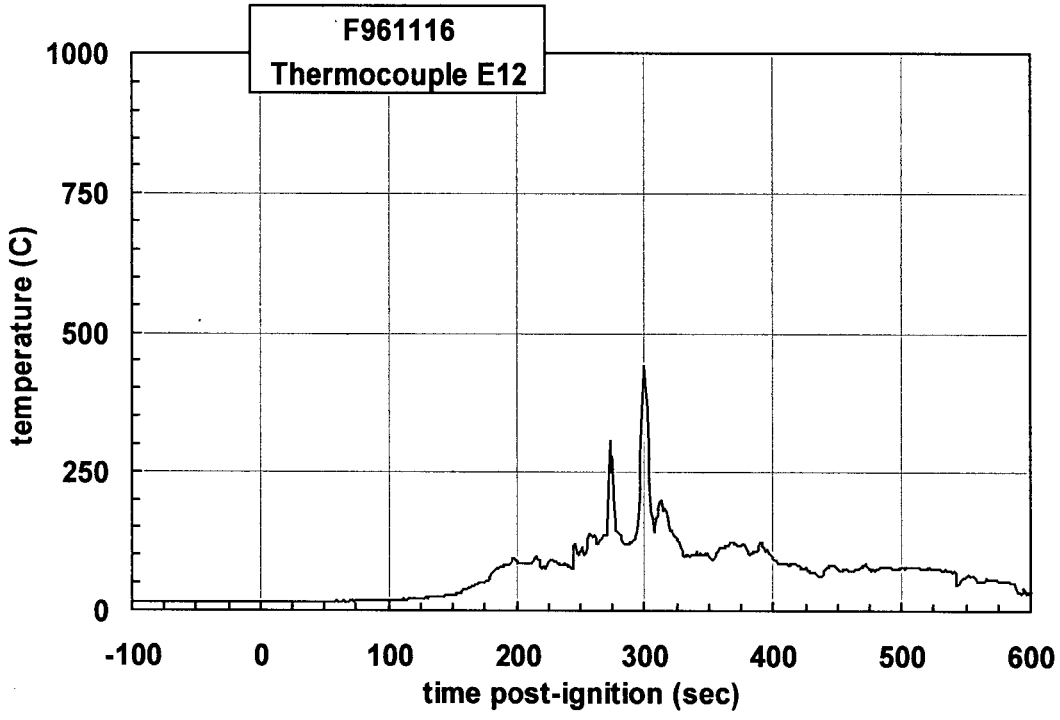


Plot C60. Fire Test F961116. Data plot from thermocouple E12.

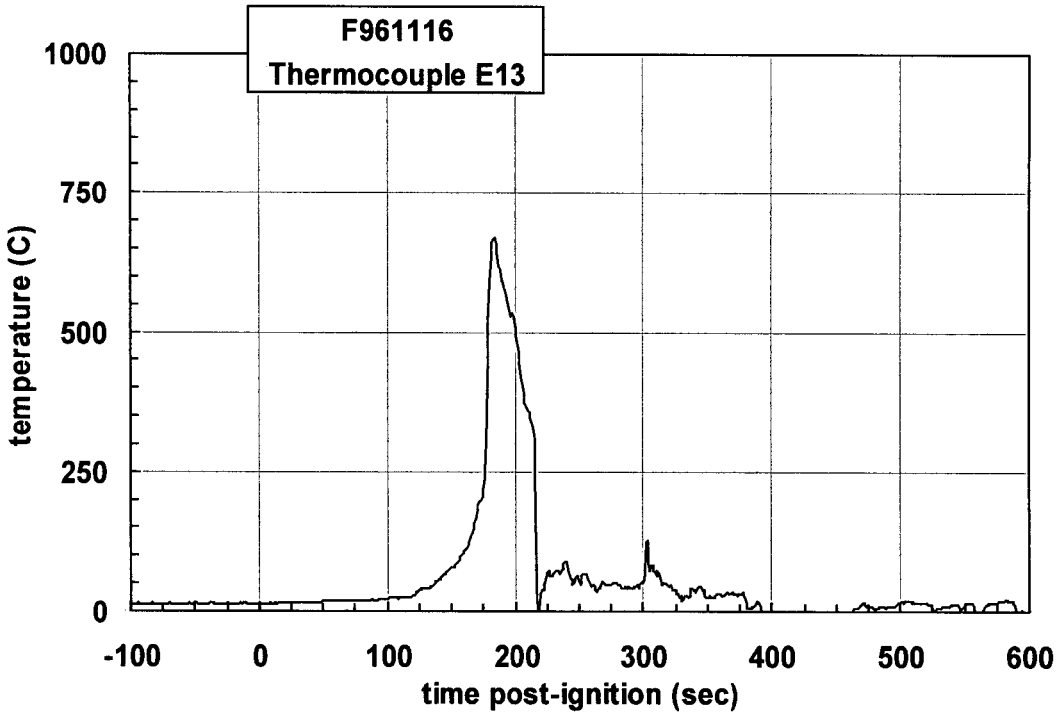


Plot C61. Fire Test F961116. Data plot from thermocouple E13.

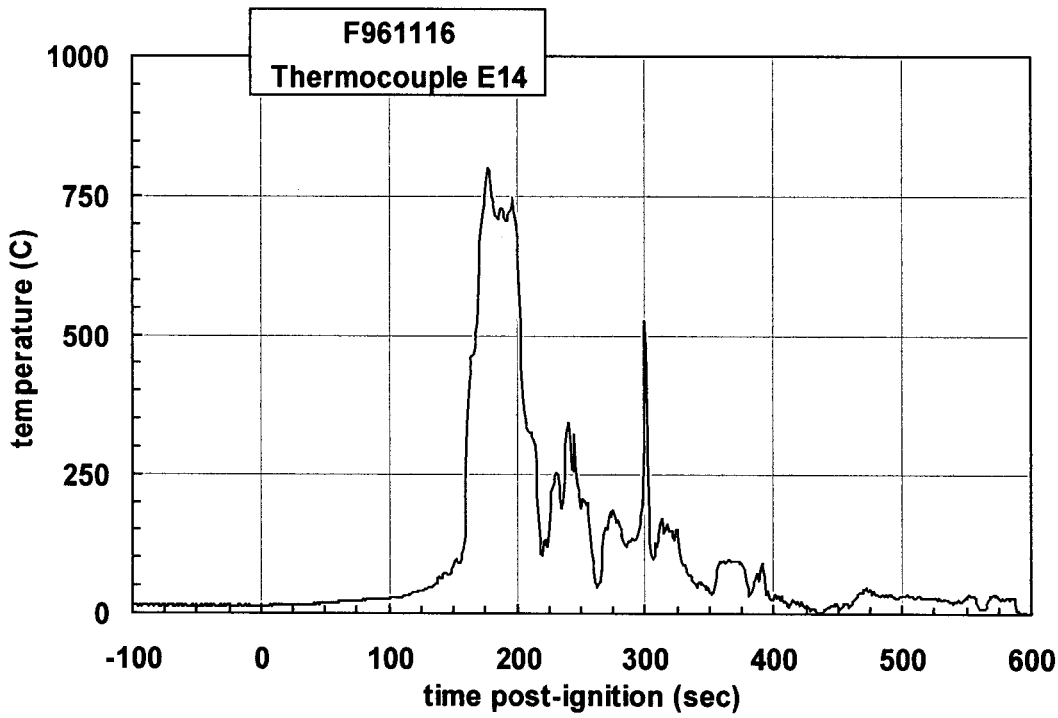


Plot C62. Fire Test F961116. Data plot from thermocouple E14.

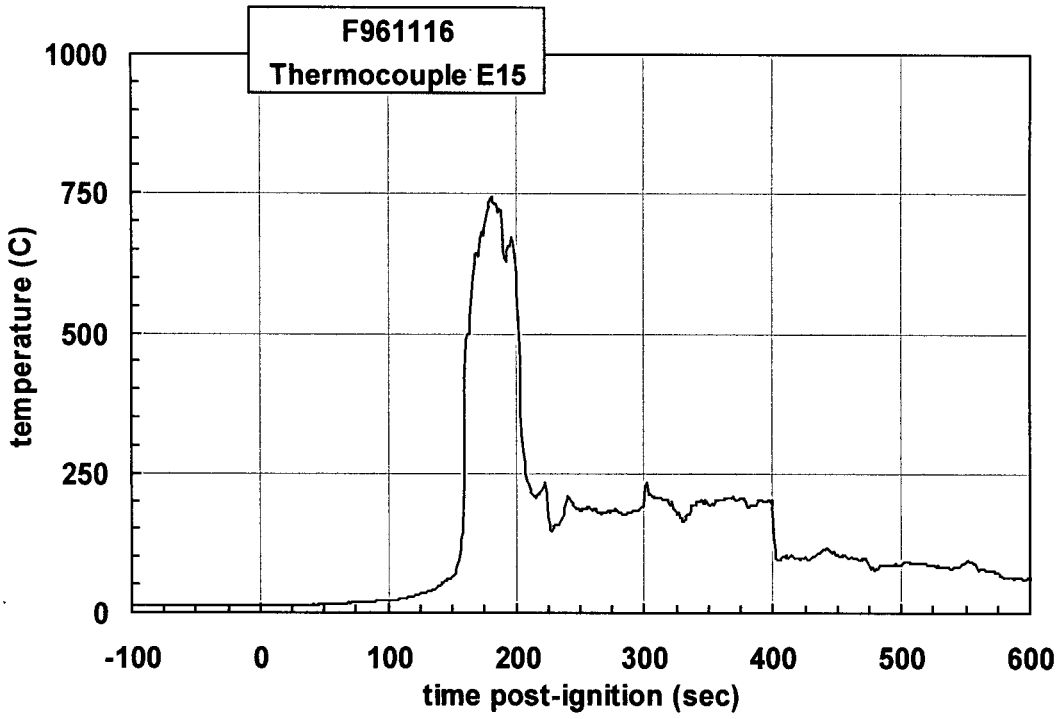


Plot C63. Fire Test F961116. Data plot from thermocouple E15.

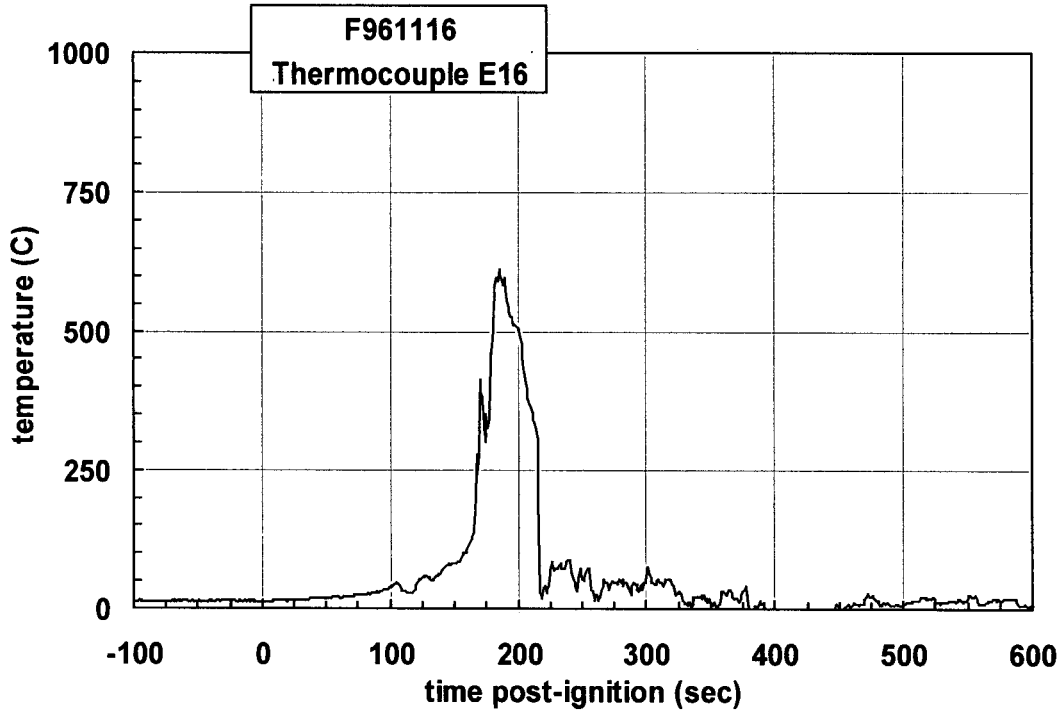


Plot C64. Fire Test F961116. Data plot from thermocouple E16.

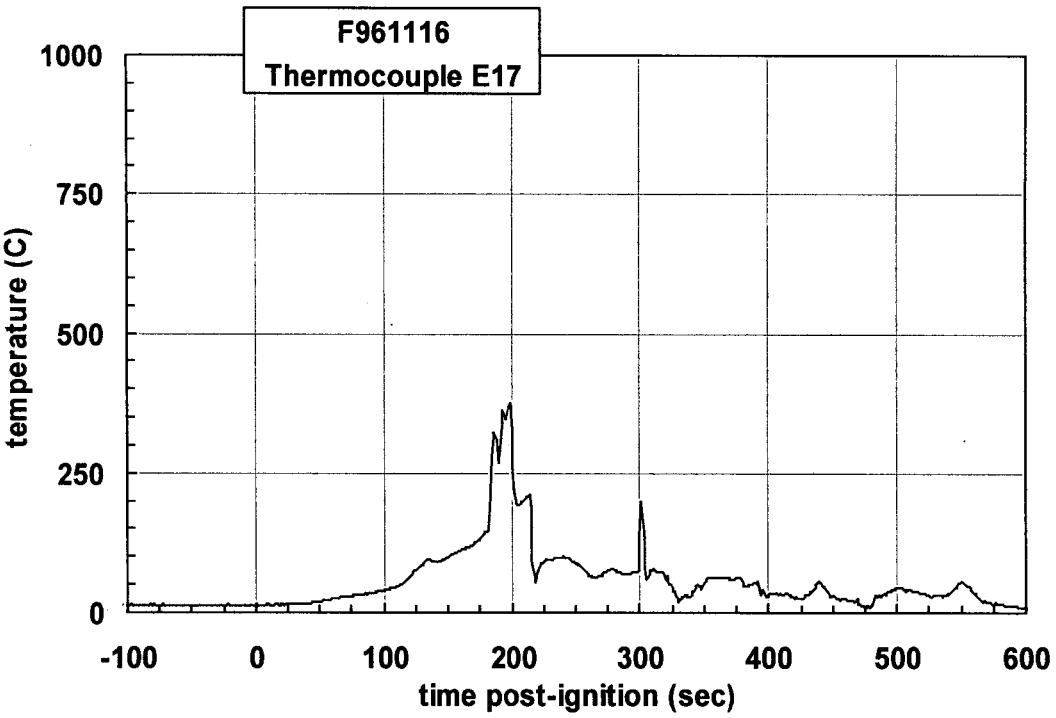


Plot C65. Fire Test F961116. Data plot from thermocouple E17.

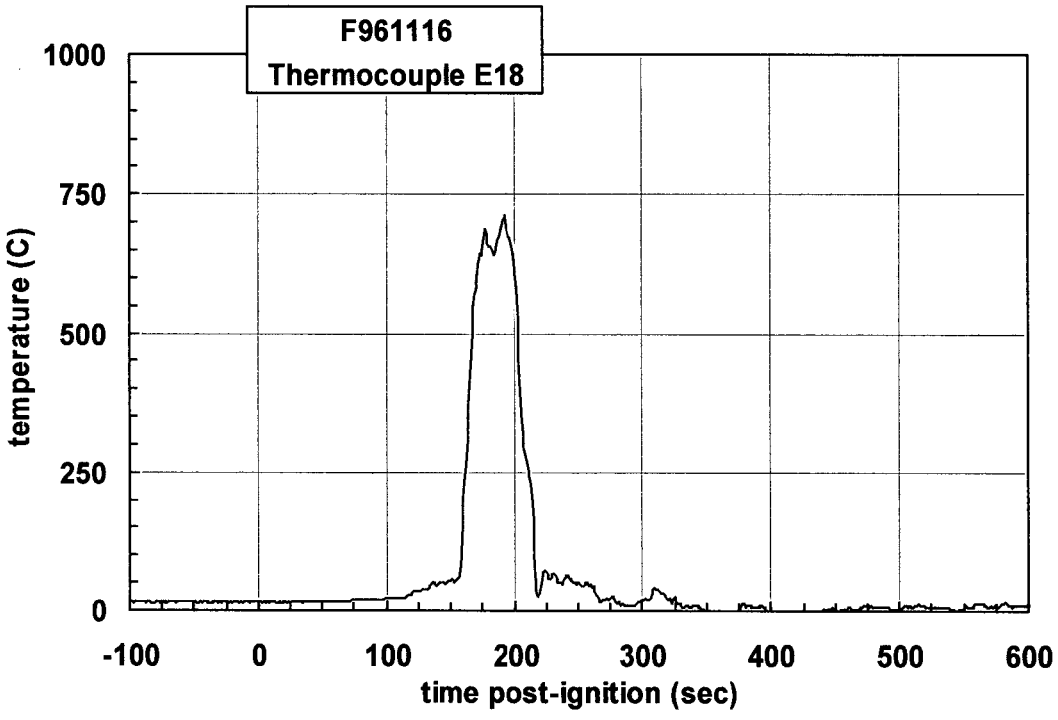


Plot C66. Fire Test F961116. Data plot from thermocouple E18.

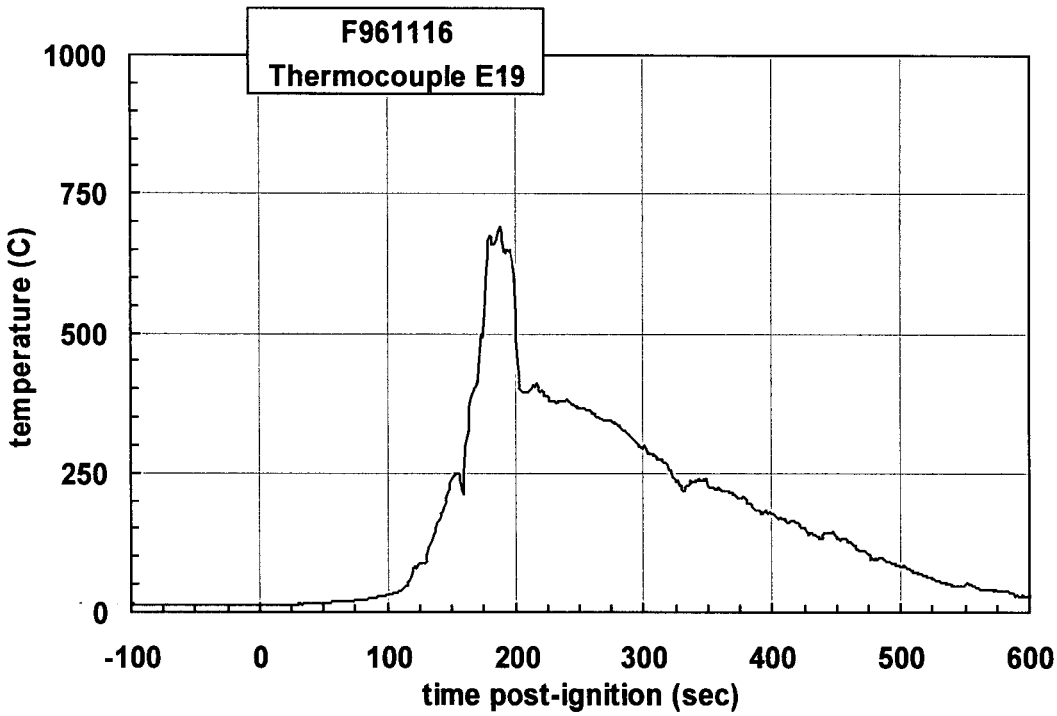


Plot C67. Fire Test F961116. Data plot from thermocouple E19.

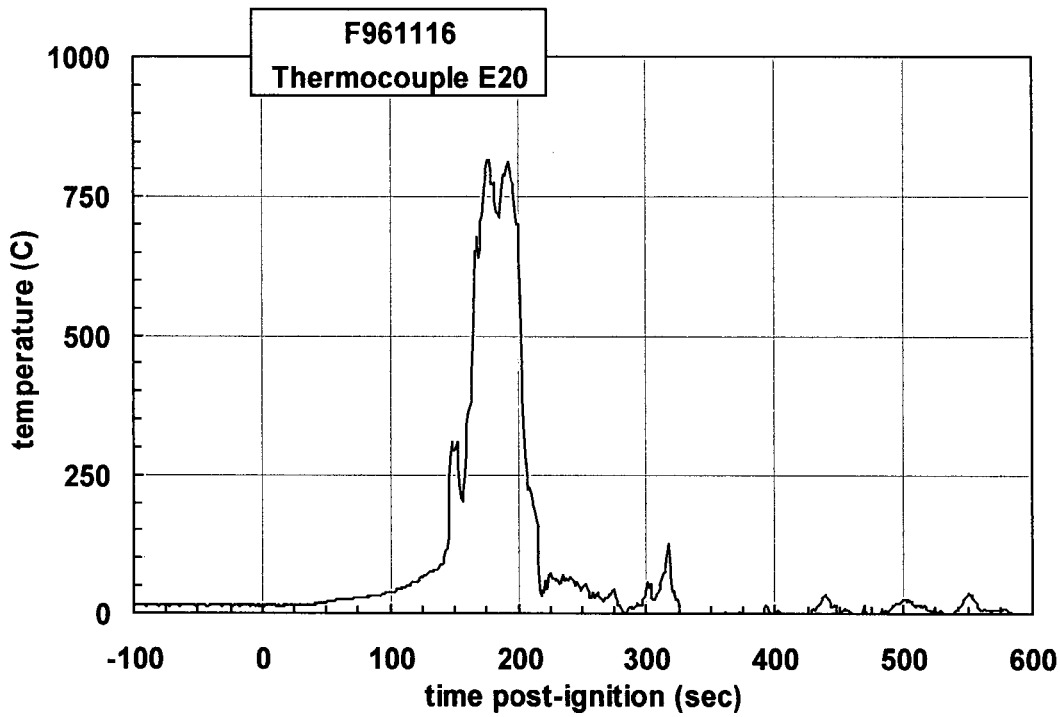


Plot C68. Fire Test F961116. Data plot from thermocouple E20.

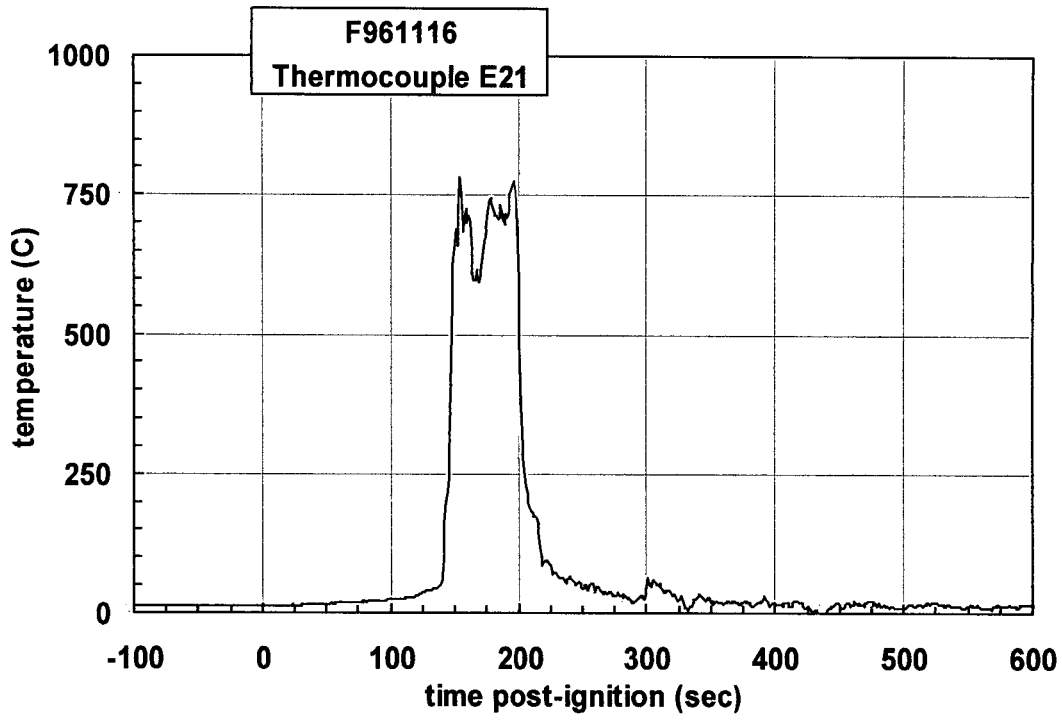


Plot C69. Fire Test F961116. Data plot from thermocouple E21.

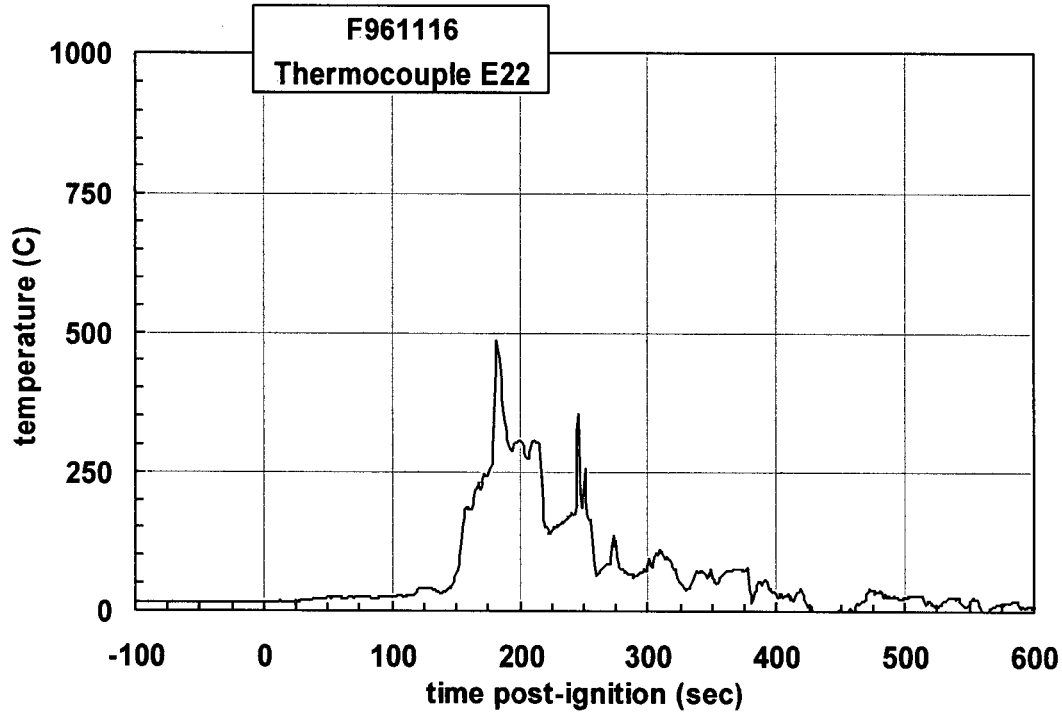


Plot C70. Fire Test F961116. Data plot from thermocouple E22.

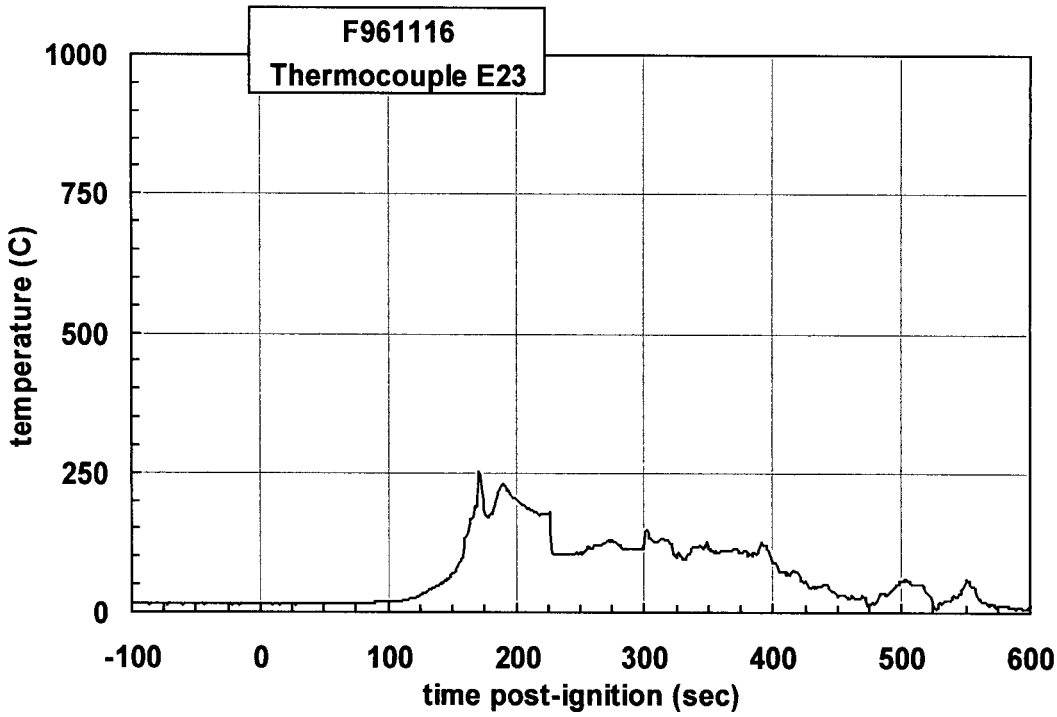


Plot C71. Fire Test F961116. Data plot from thermocouple E23.

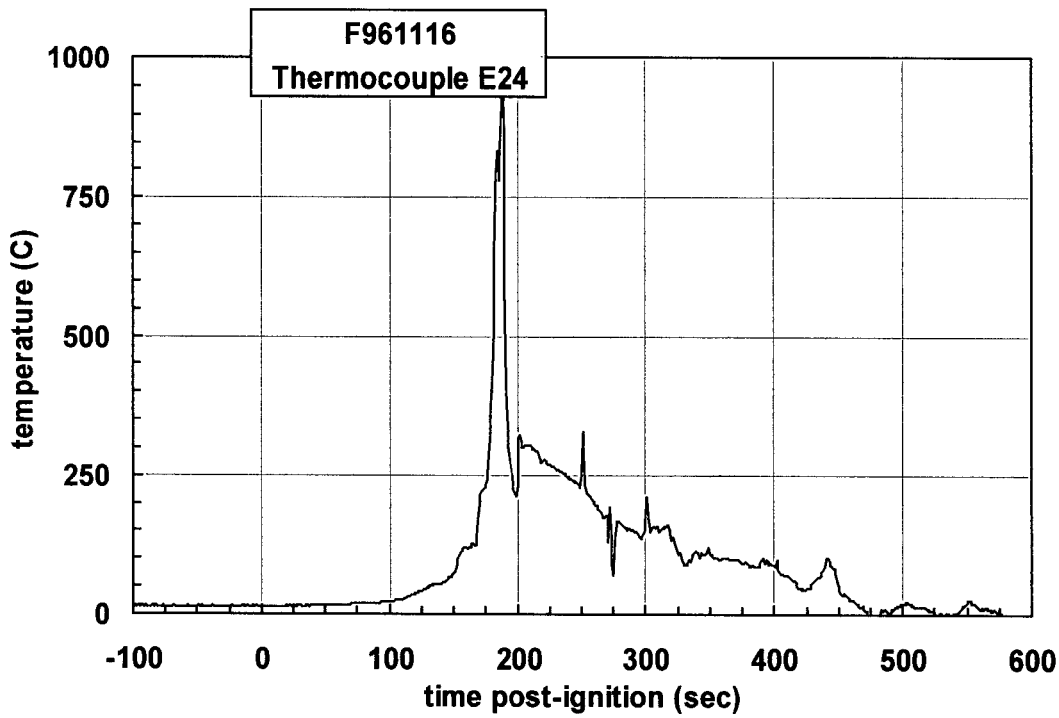


Plot C72. Fire Test F961116. Data plot from thermocouple E24.

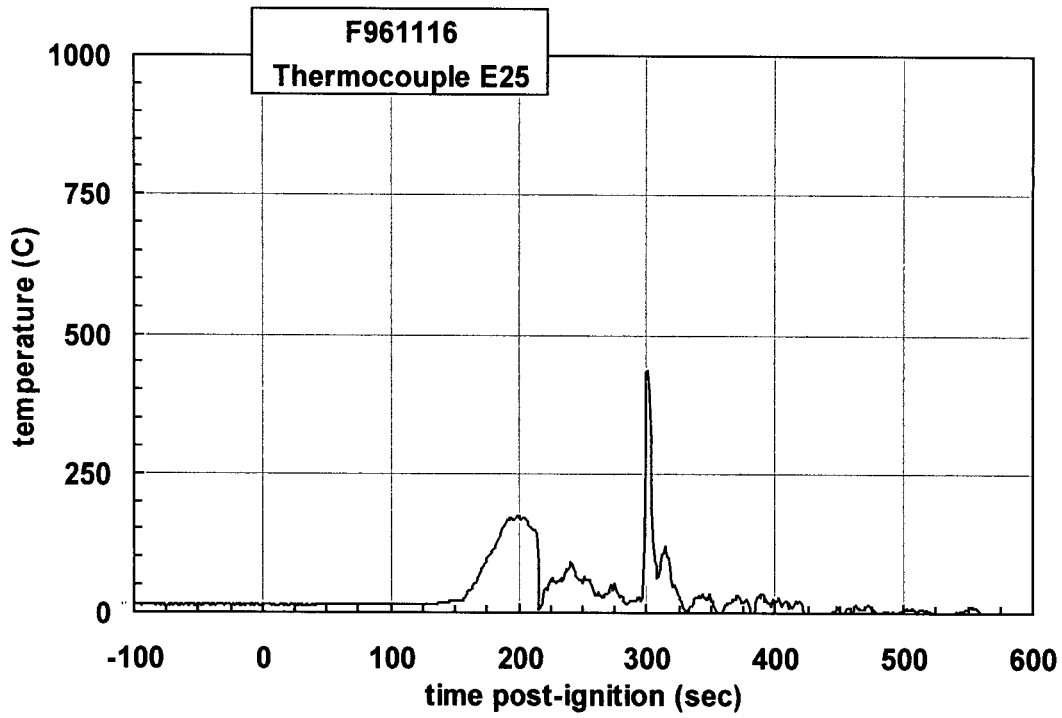


Plot C73. Fire Test F961116. Data plot from thermocouple E25.

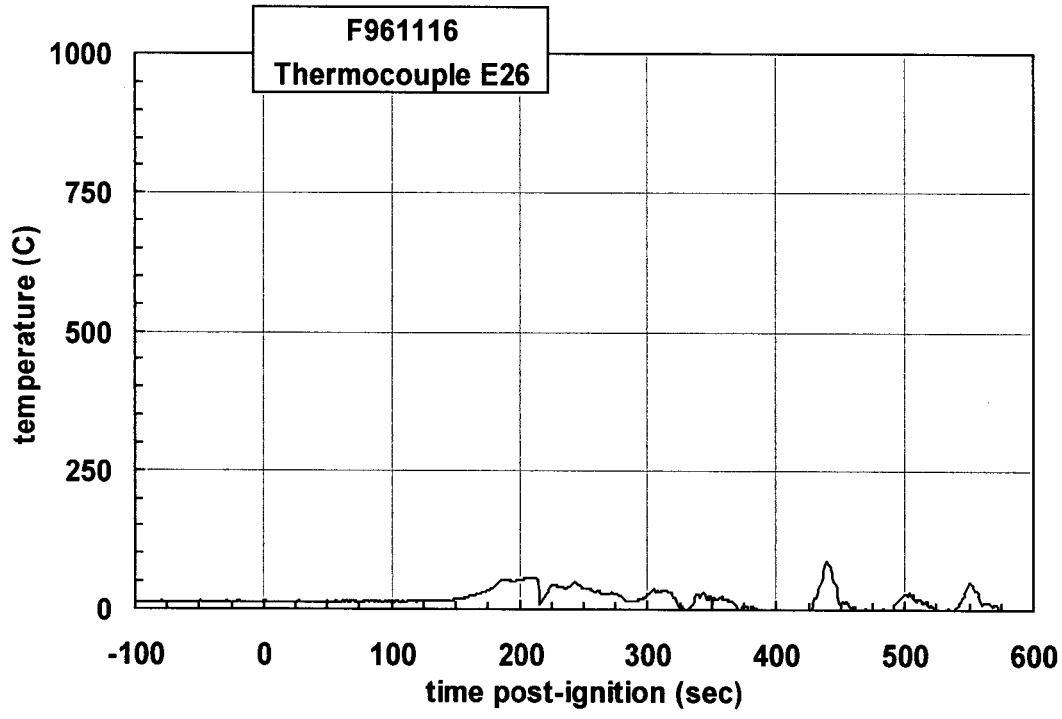


Plot C74. Fire Test F961116. Data plot from thermocouple E26.

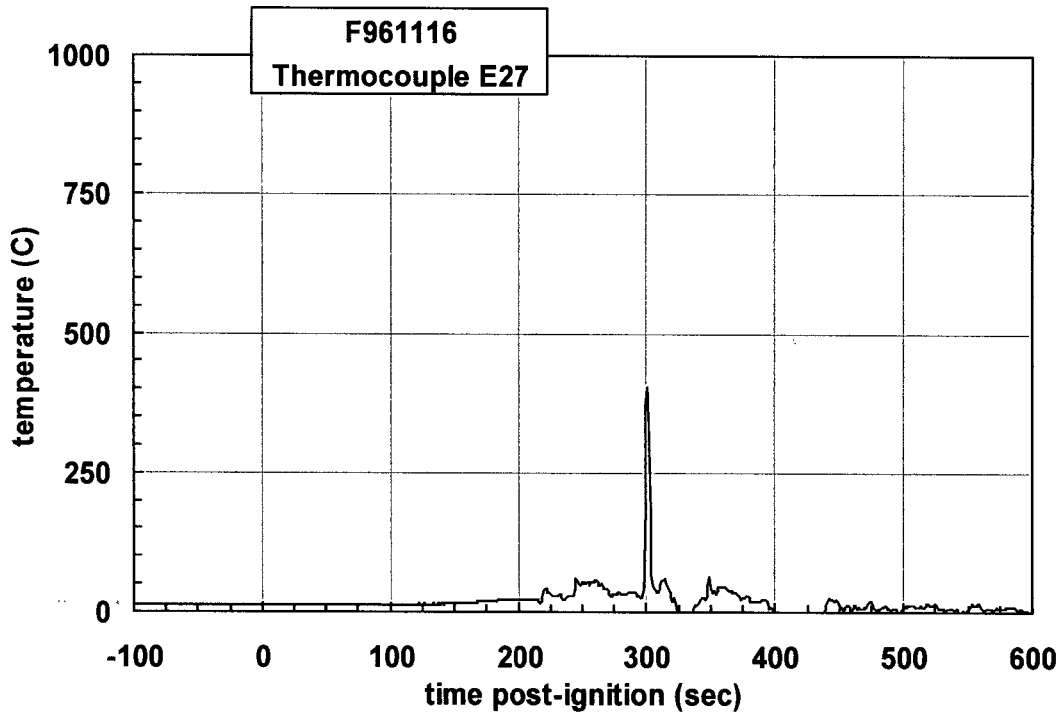


Plot C75. Fire Test F961116. Data plot from thermocouple E27.

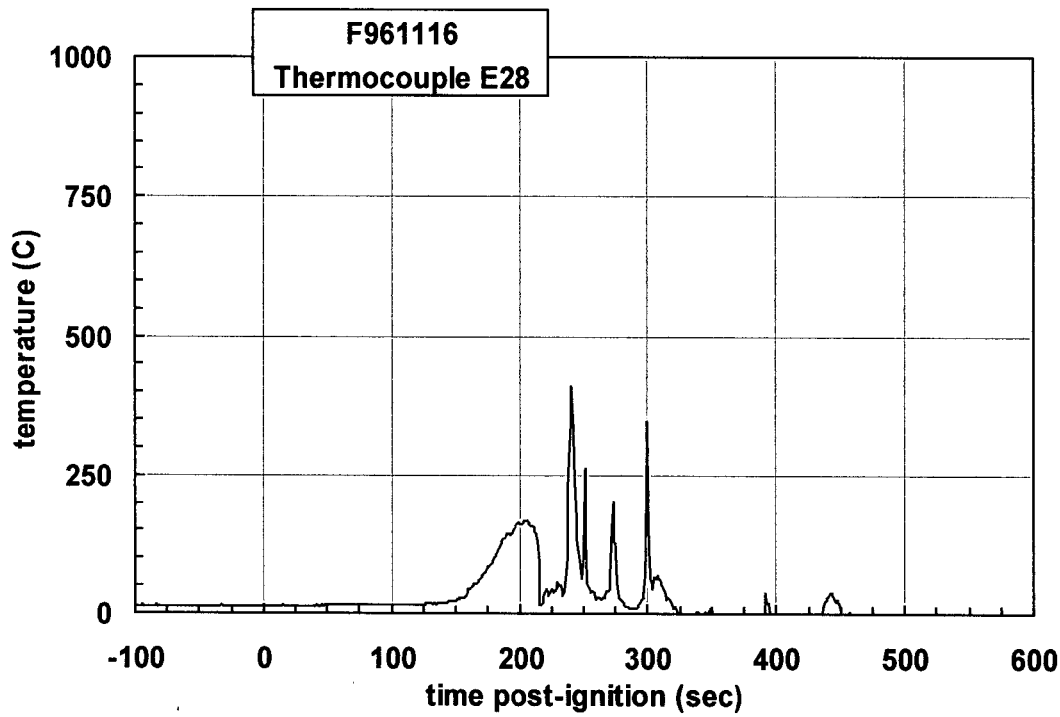


Plot C76. Fire Test F961116. Data plot from thermocouple E28.

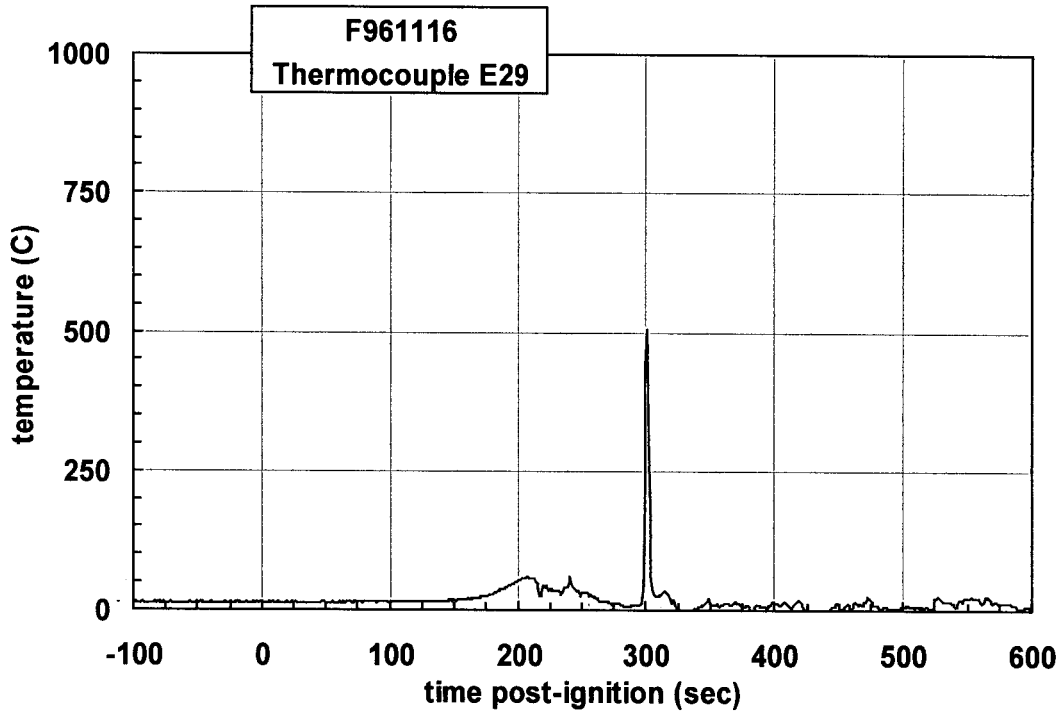


Plot C77. Fire Test F961116. Data plot from thermocouple E29.

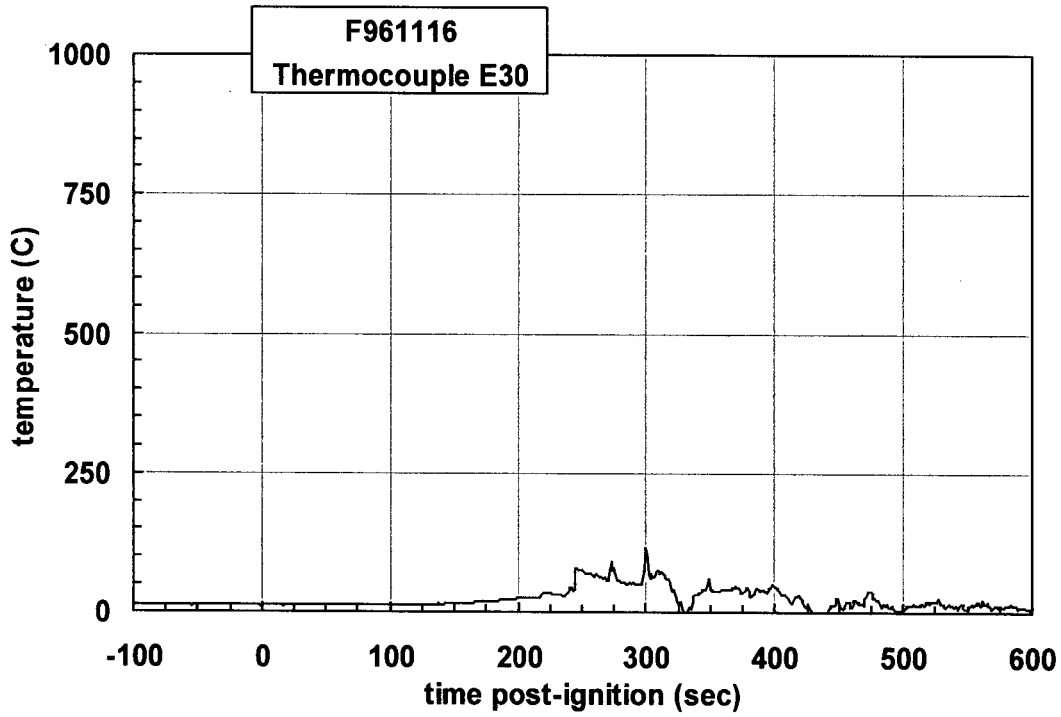


Plot C78. Fire Test F961116. Data plot from thermocouple E30.

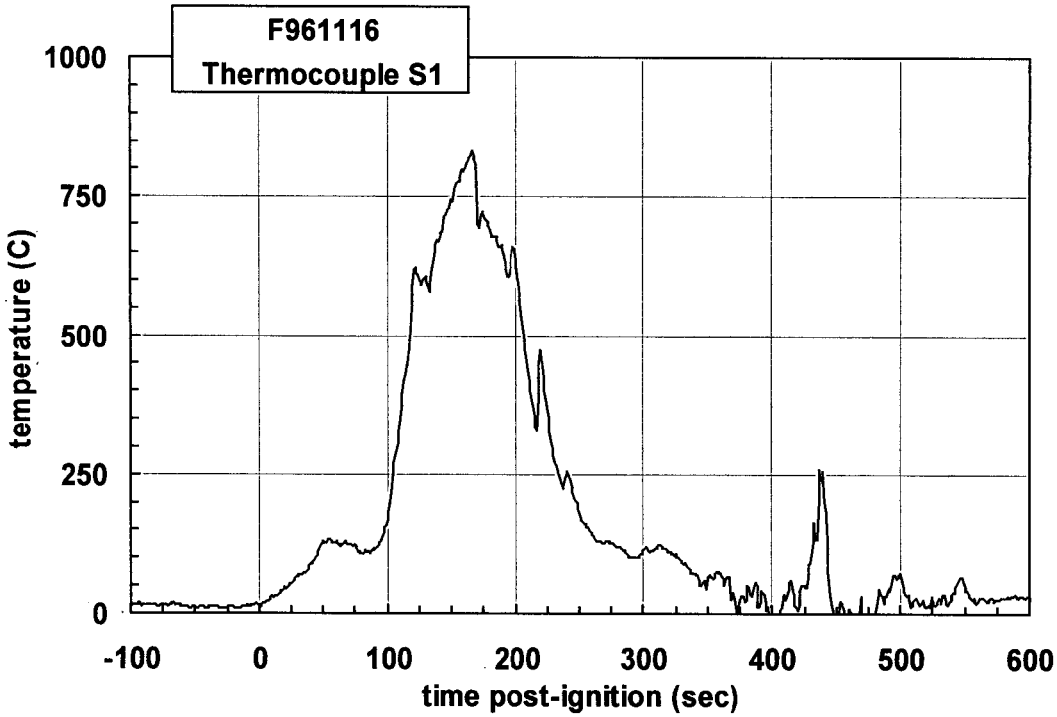


Plot 79. Fire Test F961116. Data plot from thermocouple S1.

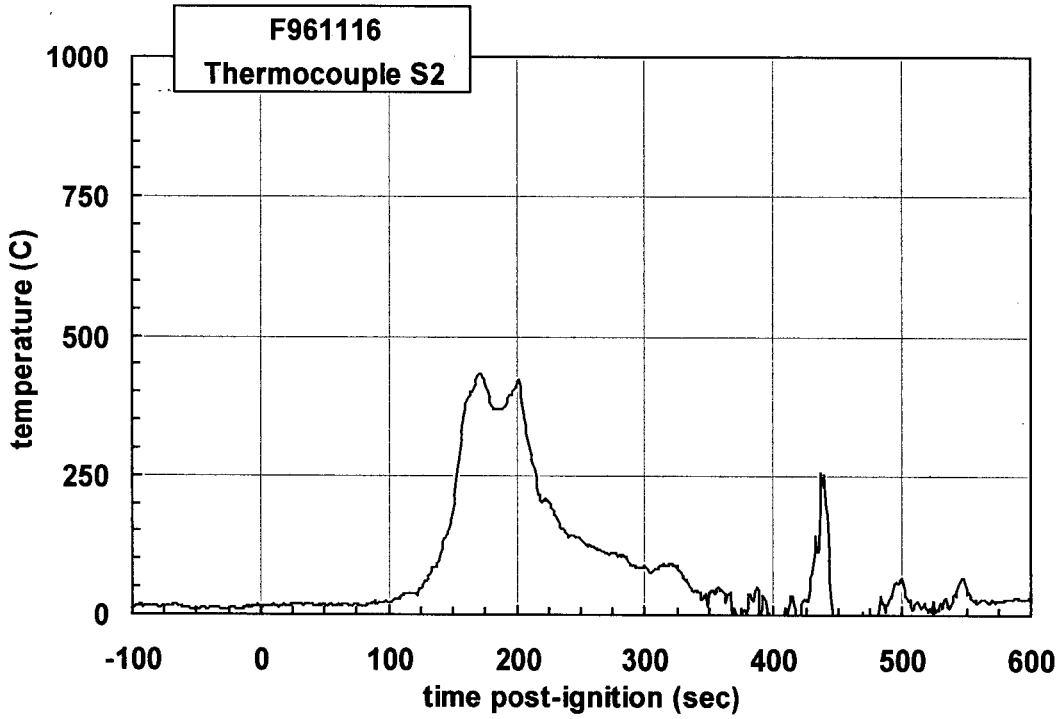


Plot C80. Fire Test F961116. Data plot from thermocouple S2.

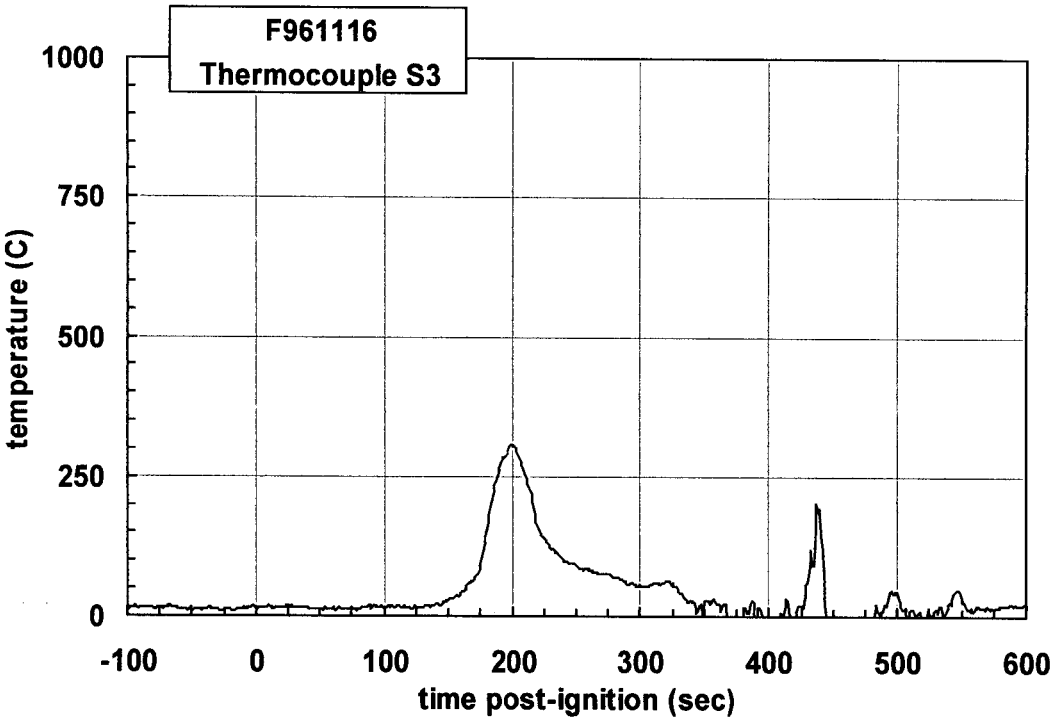


Plot C81. Fire Test F961116. Data plot from thermocouple S3.

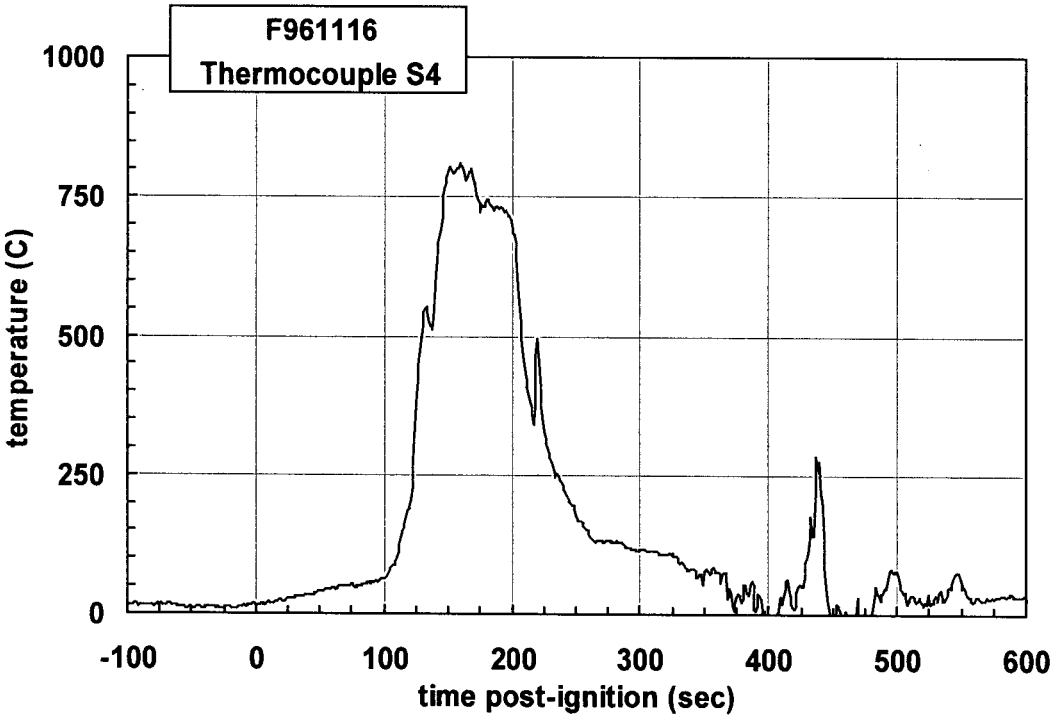


Plot C82. Fire Test F961116. Data plot from thermocouple S4.

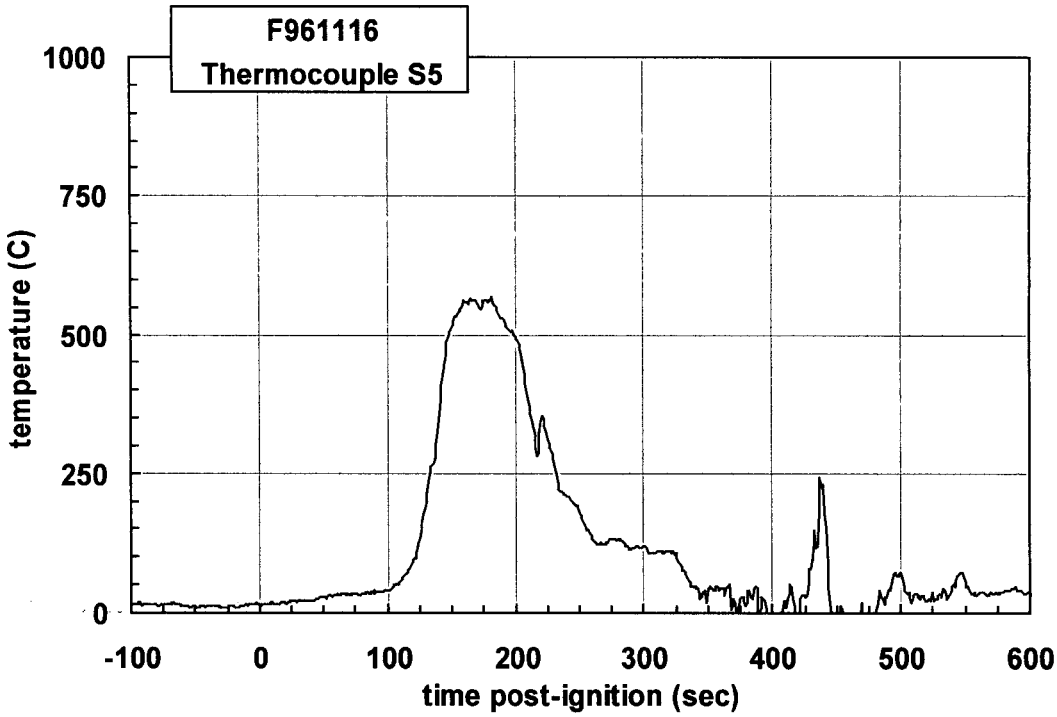


Plot C83. Fire Test F961116. Data plot from thermocouple S5.

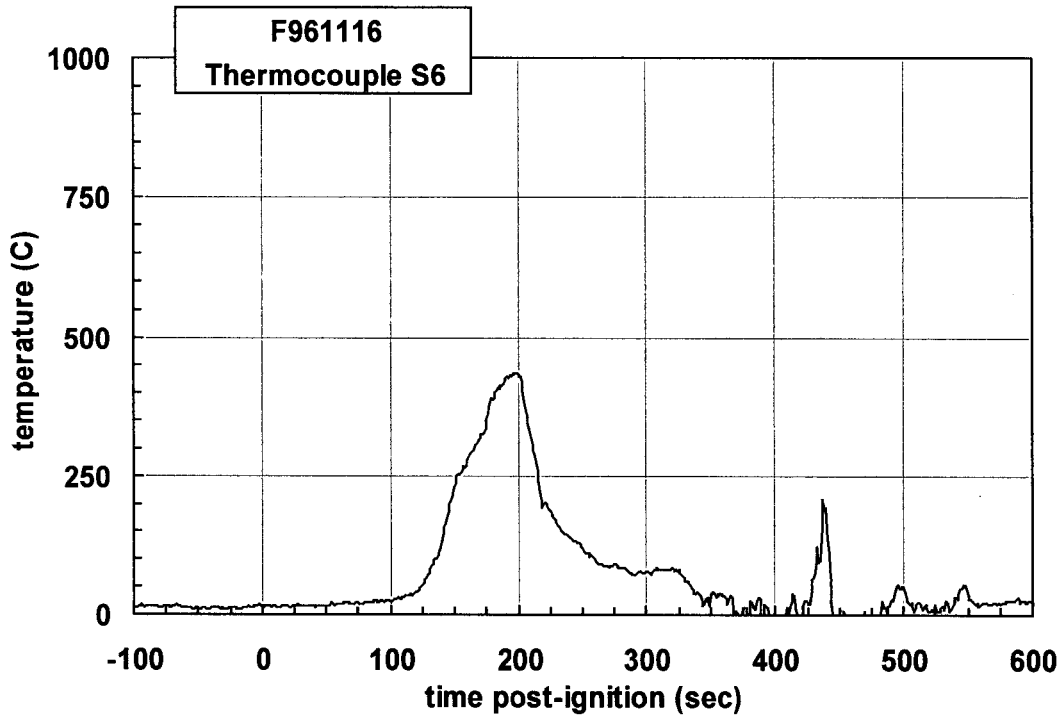


Plot C84. Fire Test F961116. Data plot from thermocouple S6.

# APPENDIX D
# ASPIRATED THERMOCOUPLE DATA

An aspirated thermocouple assembly (Medtherm Corporation) was installed in the test vehicle and used to measure air temperature at six elevations in the passenger compartment of the test vehicle during this test (Fig. D1). The aspirated thermocouple assembly was fabricated from Inconel 600 tubing. Each assembly consisted of a vertical manifold (o.d. = 0.375 in. (9.5 mm), i.d. = 0.25 in. (6.4 mm), length = 16 in. (406 mm)) with six horizontal radiation shields (o.d. = 0.25 in. (6.4 mm), i.d. = 0.19 in. (4.8 mm), length = 1.00 in. (25.4 mm)). The vertical spacing between the radiation shields along the manifold was 3 in. (75 mm). Three radial holes were drilled near the tip of each radiation shield. The holes were sized to approximately balance the airflow-rates over each thermocouple. A Type-N thermocouple inserted into each radiation shield so that the thermocouple junction was positioned approximately 0.2 in. (5.1 mm) down-stream from the inlet holes.

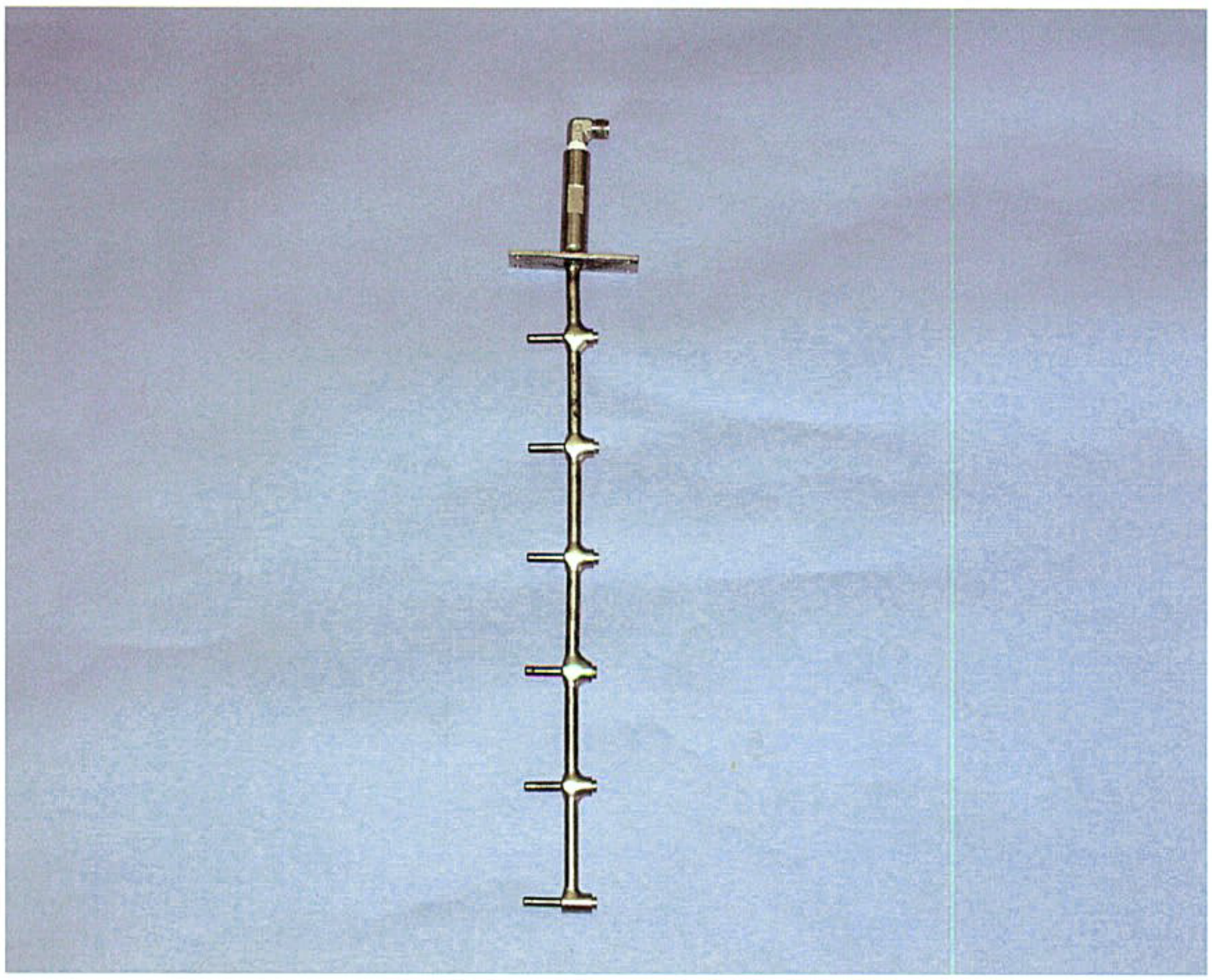

Figure D1. Fire Test F961116. Photograph of the aspirated thermocouple assembly used in the passenger compartment of the test vehicle.

The mounting flange of the aspirated thermocouple probe assembly was attached to the roof of the vehicle. The probe extended into the passenger compartment through a hole in the roof so that all 6 thermocouples were located below the headliner. The probe was vertical and located along the longitudinal mid-line of the vehicle approximately equidistant from the driver and passenger seats. The upper-most aspirated thermocouple was approximately 0.5 in. (12 mm) below the lower surface of the headliner. The manifold was connected to a rotary-vane pump with flexible copper tubing (o.d. = 0.5 in. (12 mm), length = 15 ft. (4.6 m)). The capacity of the pump was 50 L/min at atmospheric pressure. The flow rate of air into each radiation shield under these conditions was measured using a dry-gas meter. The linear velocity of the air flowing through each radiation shield was calculated from the flow rate measurements, and determined to be between 5 and 10 m/s.

The linear velocity of airflow over the thermocouple junction affects the accuracy of the air temperature measurement [D1]. The linear velocity of gas flowing through each radiation shield was sufficient to achieve a relative error of < 5% for gas temperature measurements in or close to a steady-state flame [D1]. However, the time-response of an aspirated thermocouple becomes a factor in the accuracy of the gas temperature measurement in environments where the heat release rate of the fire is changing or the flame is spreading relative to the aspirated probe. Both were the case in these tests. The time-delay in the response of the aspirated thermocouple probe used in these tests was estimated to be approximately 5 sec [D2].

Figures D2 and D3 show the approximate location of the aspirated thermocouple probe assembly in the test vehicle for this test.

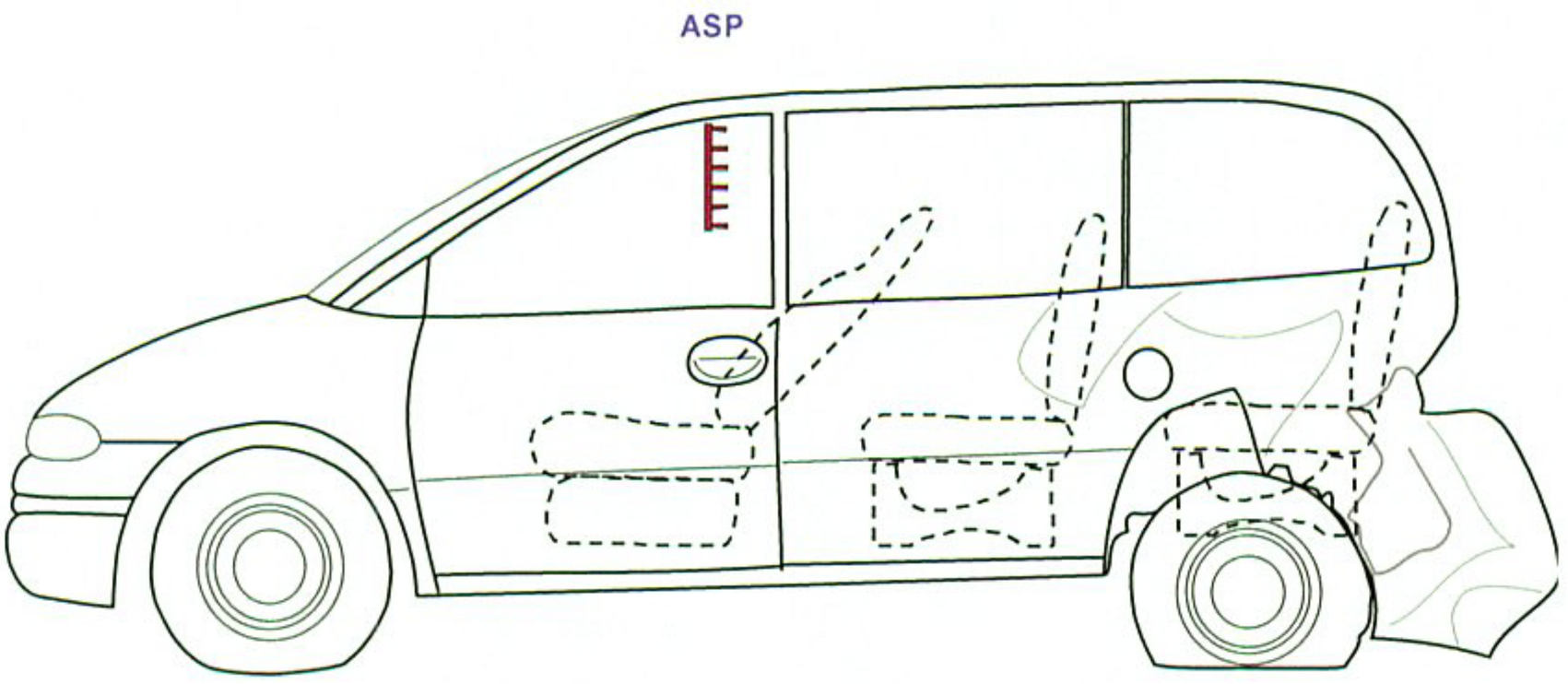


Figure D2. Fire Test F961116. Side view of the test vehicle showing the approximate location of the aspirated thermocouple probe assembly in the passenger compartment.

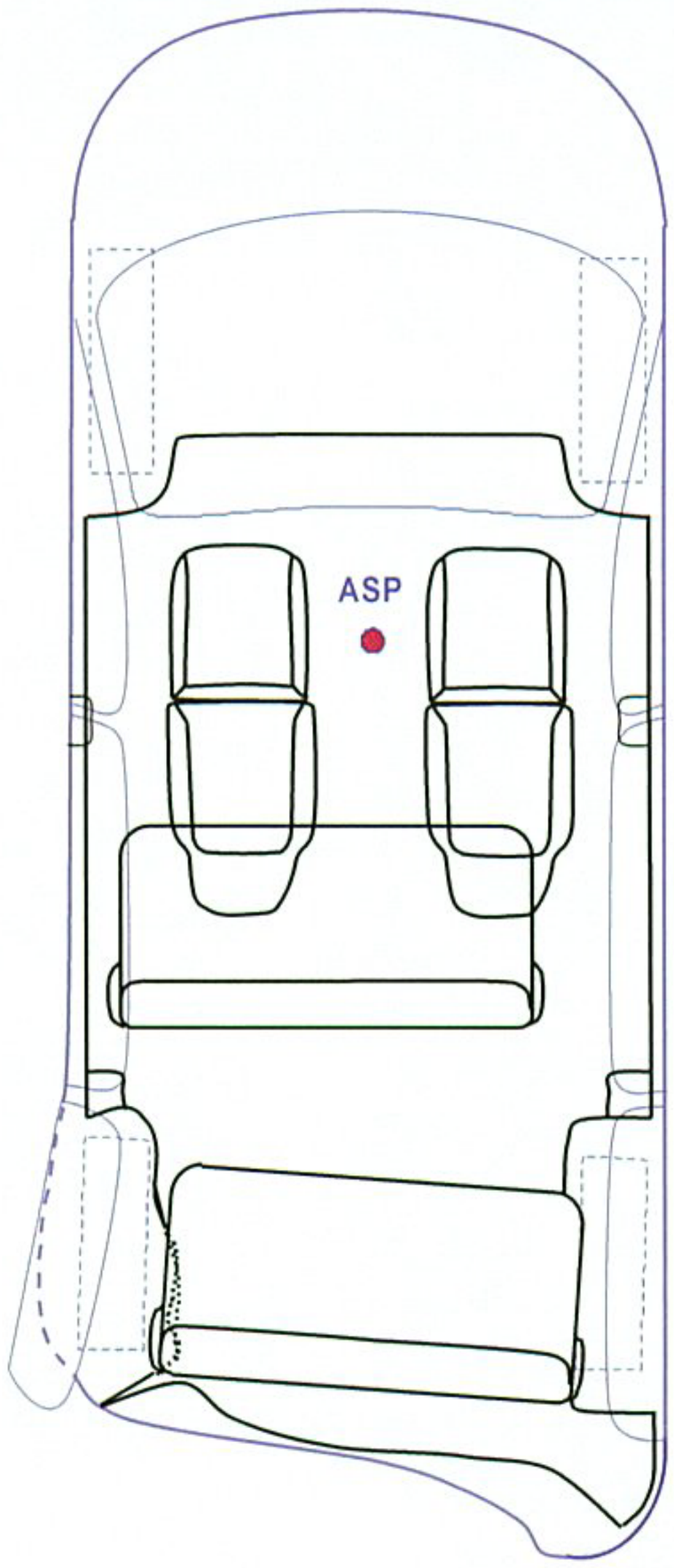


Figure D3. Fire Test F961116. Top view of the test vehicle showing the approximate location of the aspirated thermocouple probe assembly in the passenger compartment.

## REFERENCES

D1. J. S. Newman and P. A. Croce. A simple aspirated thermocouple for use in fires. *J. Fire Flamm.* **10**:326-336 (1979).

D2. N. R. Keltner and K. A. Strom. Thermal Measurement Uncertainty and Compensation. Paper in preparation.

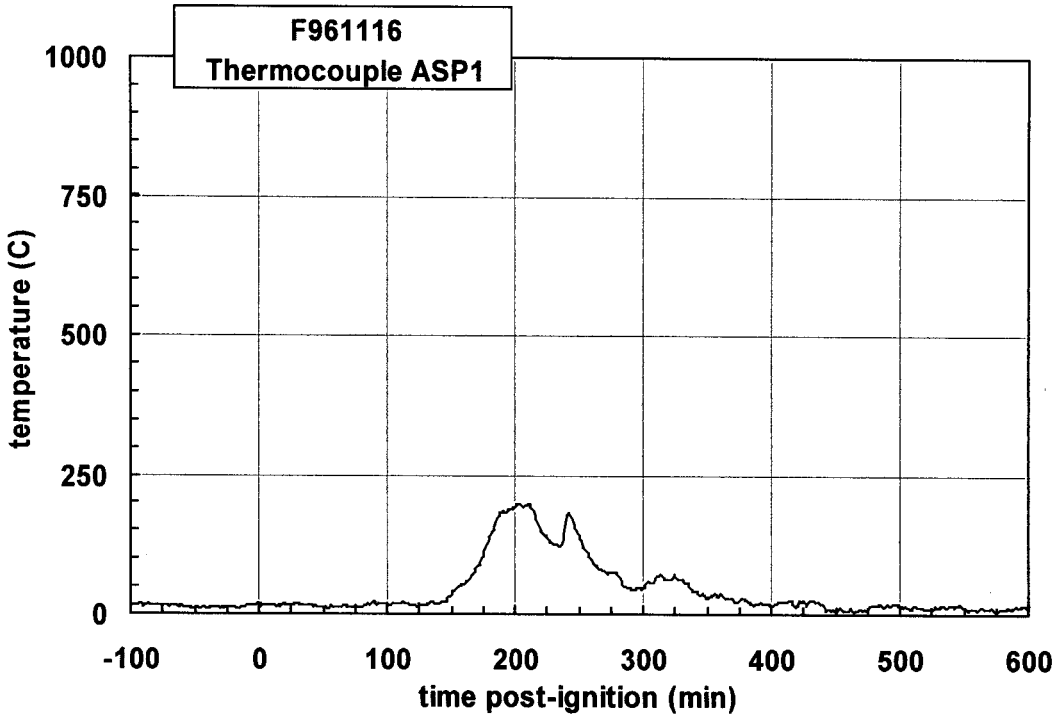


Plot C1. Fire Test F961116. Data plot from thermocouple ASP1.

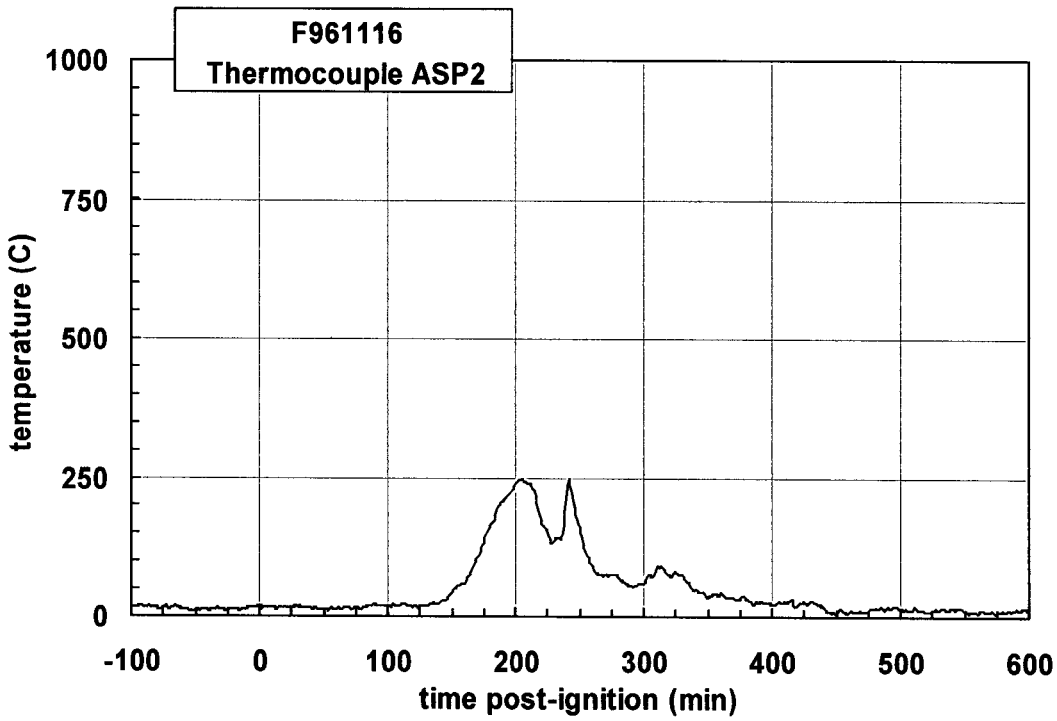


Plot C2. Fire Test F961116. Data plot from thermocouple ASP2.

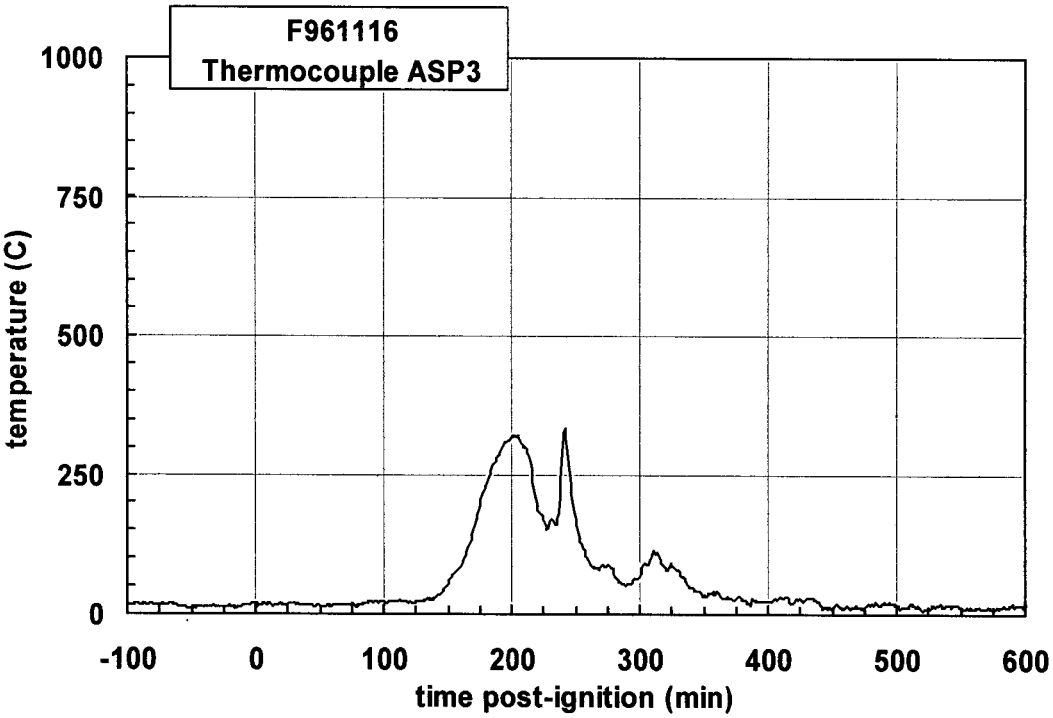


Plot C3. Fire Test F961116. Data plot from thermocouple ASP3.

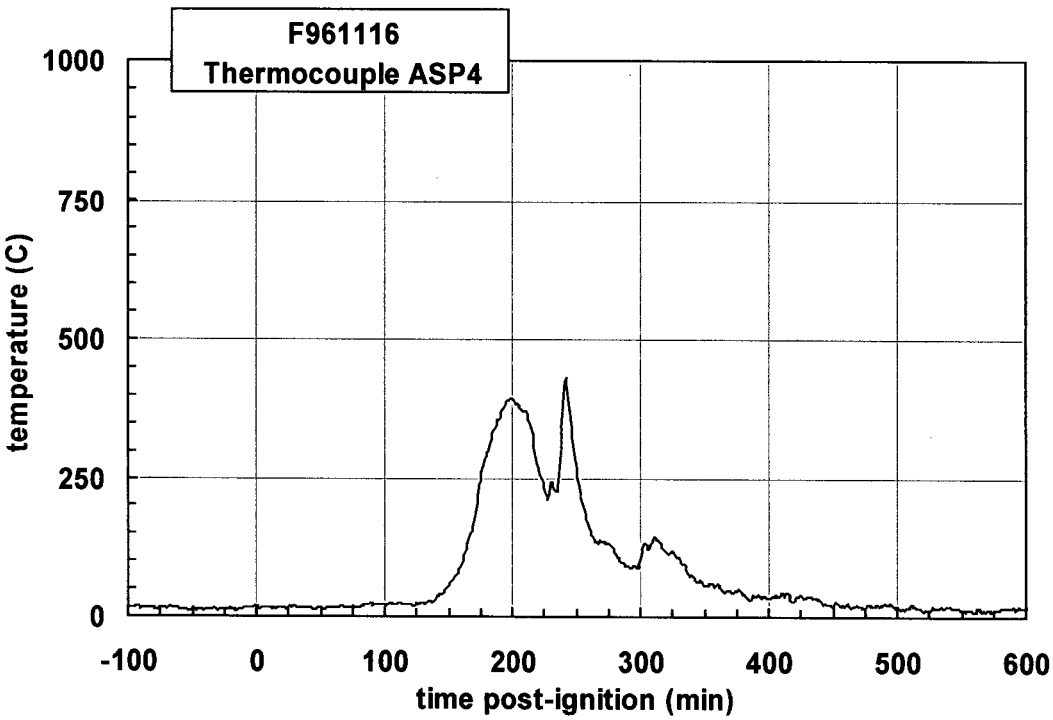


Plot C4. Fire Test F961116. Data plot from thermocouple ASP4.

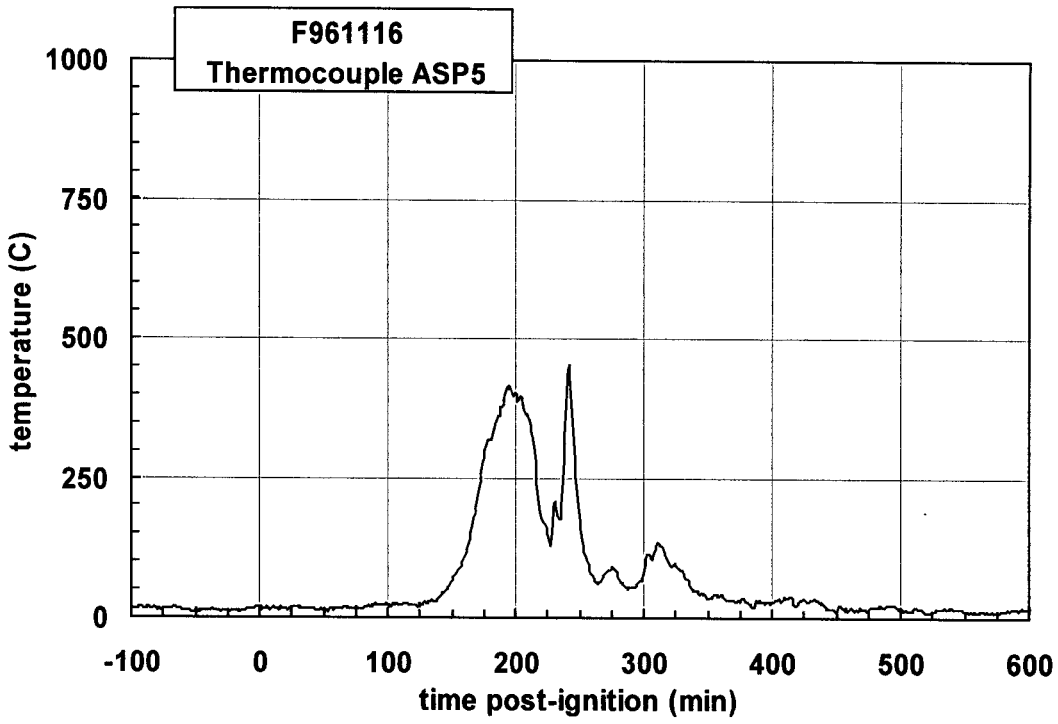


Plot C5. Fire Test F961116. Data plot from thermocouple ASP5.

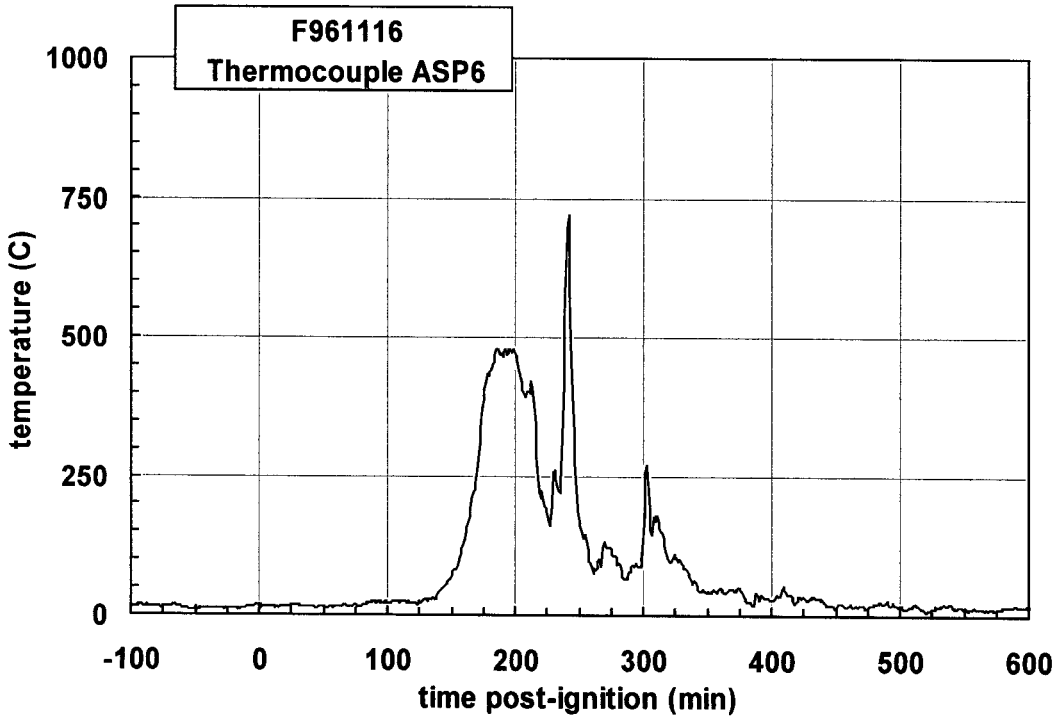


Plot C6. Fire Test F961116. Data plot from thermocouple ASP6.

# APPENDIX E
# HEAT FLUX TRANSDUCER/RADIOMETER DATA

Heat-flux transducer/radiometer assemblies (64 Series, Medtherm Corporation) were used to measure convective and radiative heat transfer to selected objects in the vehicle. Each assembly contained two Schmidt-Boelter thermopiles in a water-cooled copper body (diameter = 1 in. (25.4 mm), length = 1 in. (25.4 mm)). The faces of the heat flux transducers were coated with high-temperature optical black paint. The radiometers had permanent sapphire windows (view-angle = 150°; optical transmittance range 0.4 to 4.2 μm). Both transducers were calibrated to 100 $kW/m^2$ at a reference temperature of 25°C.

A PC-based data system was used for data acquisition from the heat flux transducers and radiometers. The PC contained a 75 MHz Pentium Processor, 16 MB RAM, an 814 MB hard disk, and a 16-bit (Model BG45-AP5CP, ACER Inc., Taiwan R. O. C.). A 100 kHz I/O board with 16 analog input channels (DaqBoard 200A, IOTech, Inc., Cleveland, OH) was installed in one of the expansion slots in the PC. An analog-input multiplex expansion card (DBK-12, IOTech, Inc., Cleveland, OH) was used for data acquisition from these transducers. The electrical shields on the signal cables were connected to the electronic chassis grounds on the analog-input expansion card. The vehicle chassis was connected to the electronic chassis ground by a large-gauge cable. The data acquisition software (DASYLab, Daten System Technik GmbH, Mönchengladbach, Germany) was configured to sample each channel at a rate of 10 Hz and store the data in 10-point block averages.

Three total Heat Flux Transducer/Radiometer Assemblies (HFT/RAD) were installed in the test vehicle. HFT/RAD 1 was installed in the rear left outer wheelhouse panel of the test vehicle (Fig. E1). HFT/RAD 2 and HFT/RAD 3 were installed in the floor pan of the test vehicle (Fig. E2). Clearance holes (diameter = 1 in.) for the transducers were drilled in the sheet metal metal. The transducer body was mounted on stand-offs so that the transducer faces were flush with the lower surface of the sheet metal and facing downward.

The data recorded from these transducers is shown in Plots E1 through E6.

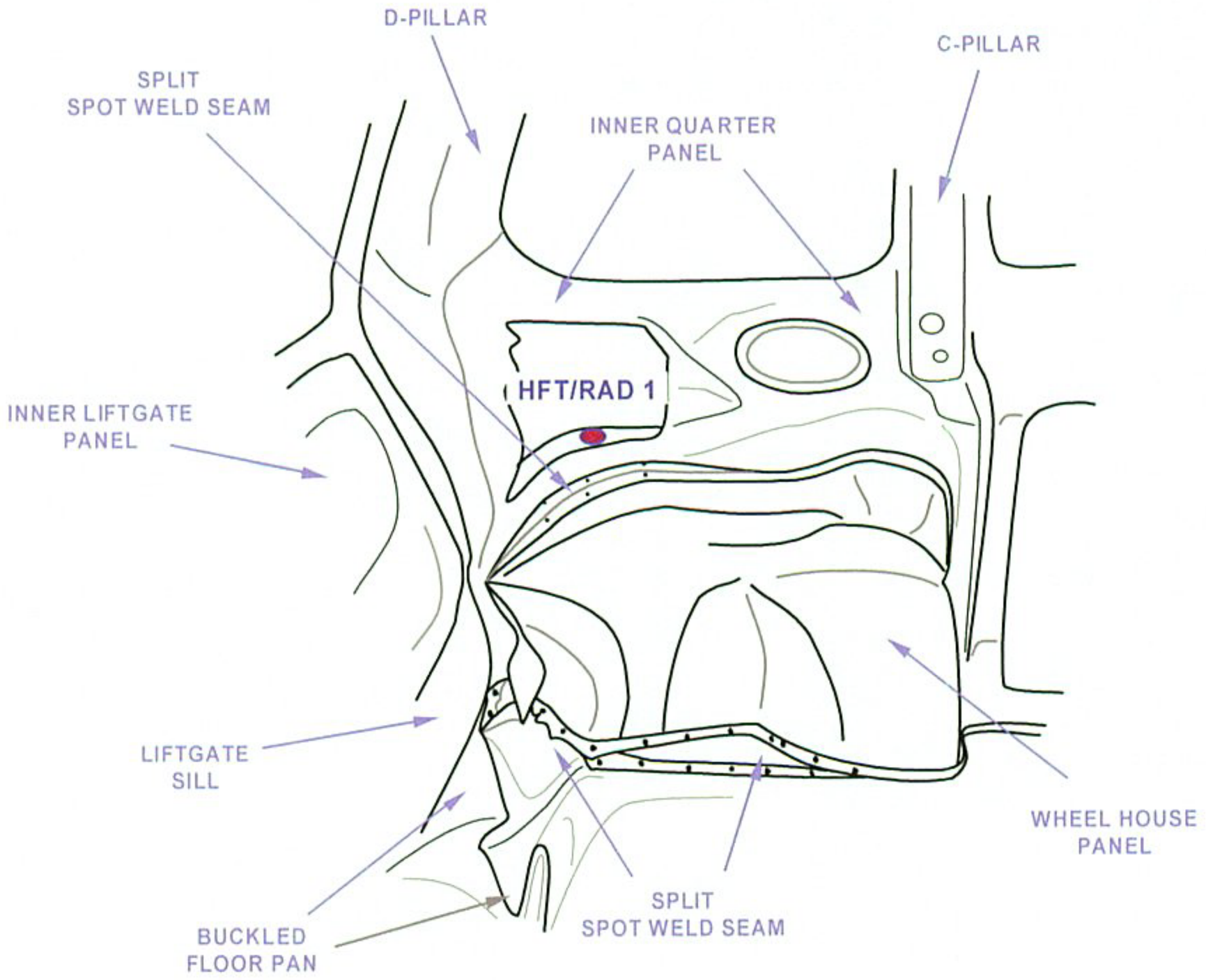


Figure E1. Fire Test F961116. View of the rear left inner quarter panel of the test vehicle showing the approximate location of HFT/RAD 1 in the rear left wheelhouse. HFT/RAD 1 extended through the wheelhouse panel that the transducer face was flush with the lower (exterior) surface of the sheet metal and oriented downward. The transducer face was directly above the rear left tire.

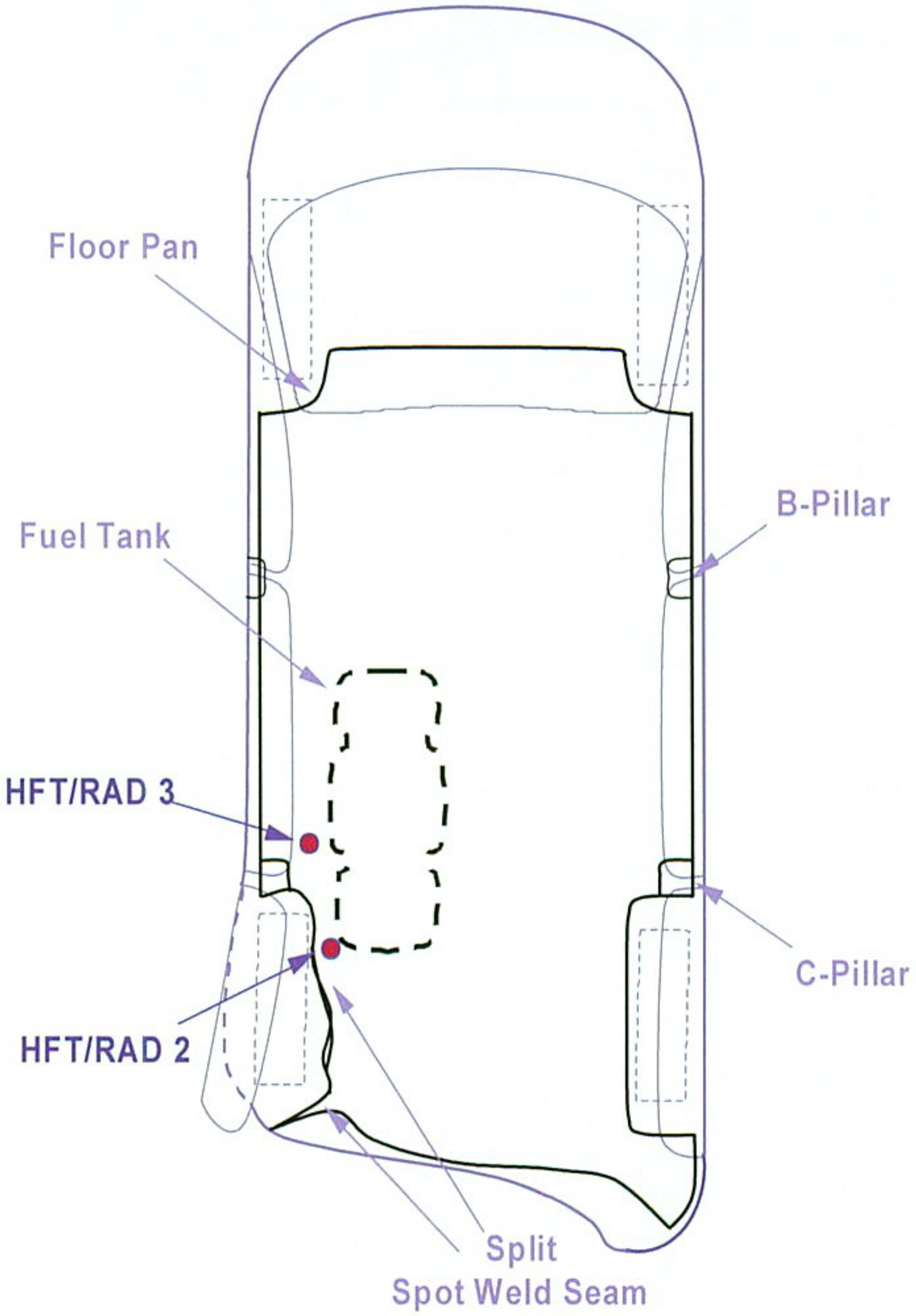


Figure E2. Fire Test F961116. Top view of the test vehicle showing the approximate locations of the HFT/RAD 2 and HFT/RAD 3 in the floor pan. HFT/RAD 2 and HFT/RAD 3 extended through the floor pan so that the transducer faces were flush with the lower surface of the sheet metal and facing downward

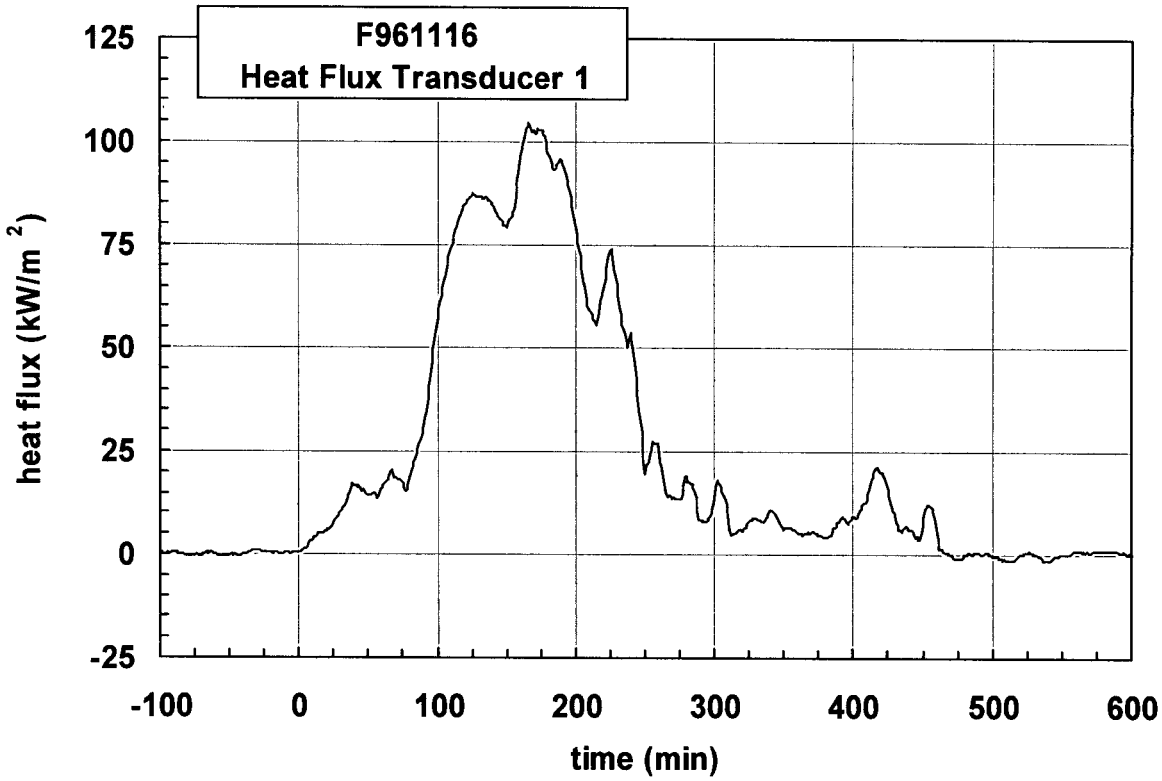


**Plot E1. Fire Test F961116. Data plot from Heat Flux Transducer 1.**

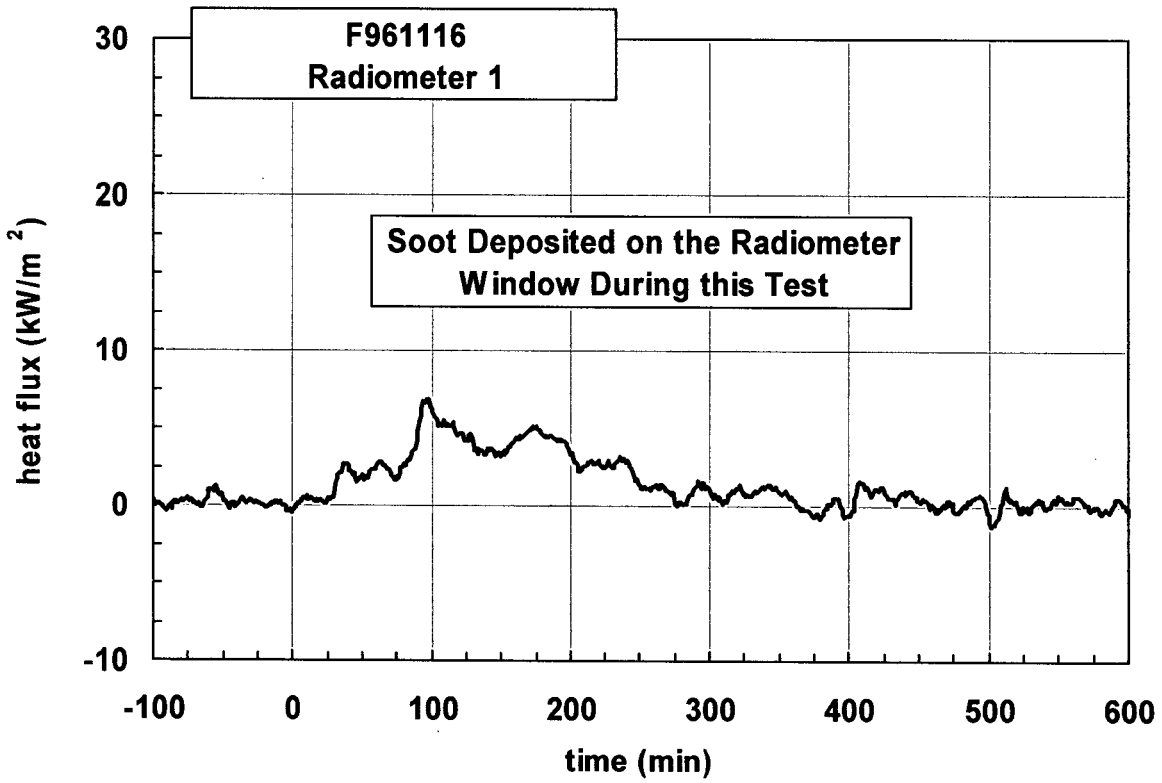


**Plot E2. Fire Test F961116. Data plot from Radiometer 1.**

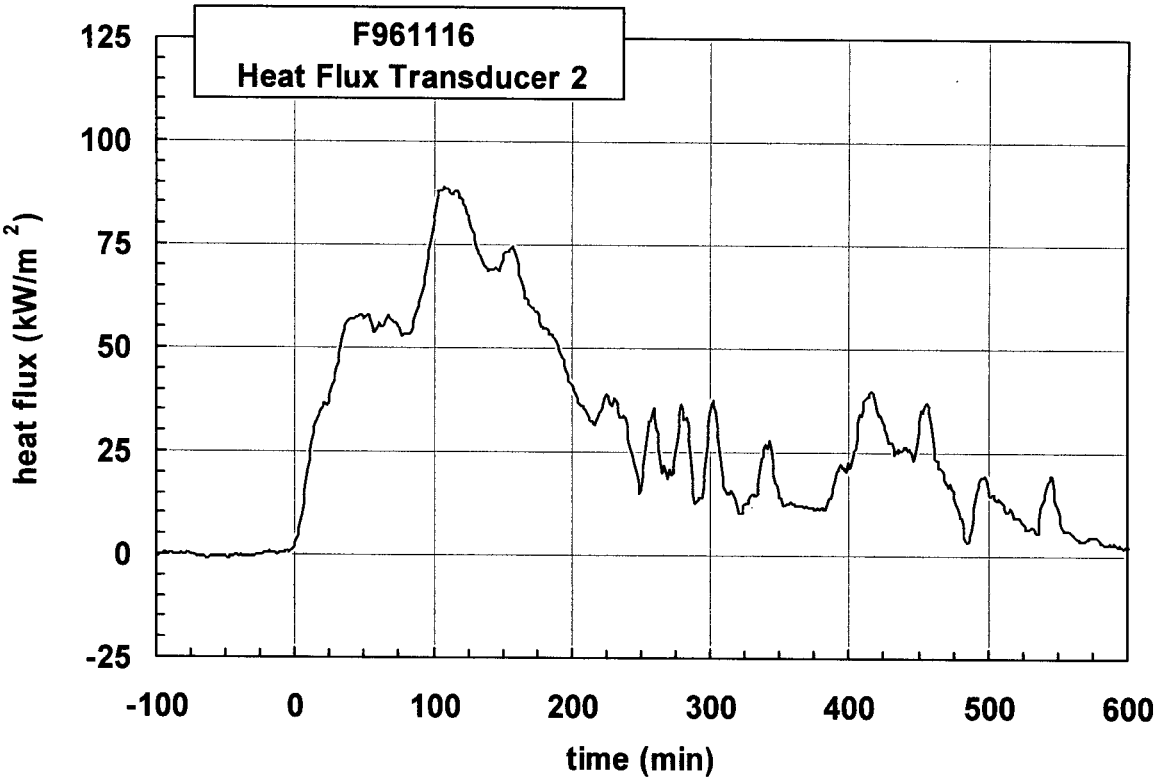


**Plot E3. Fire Test F961116. Data plot from Heat Flux Transducer 2.**

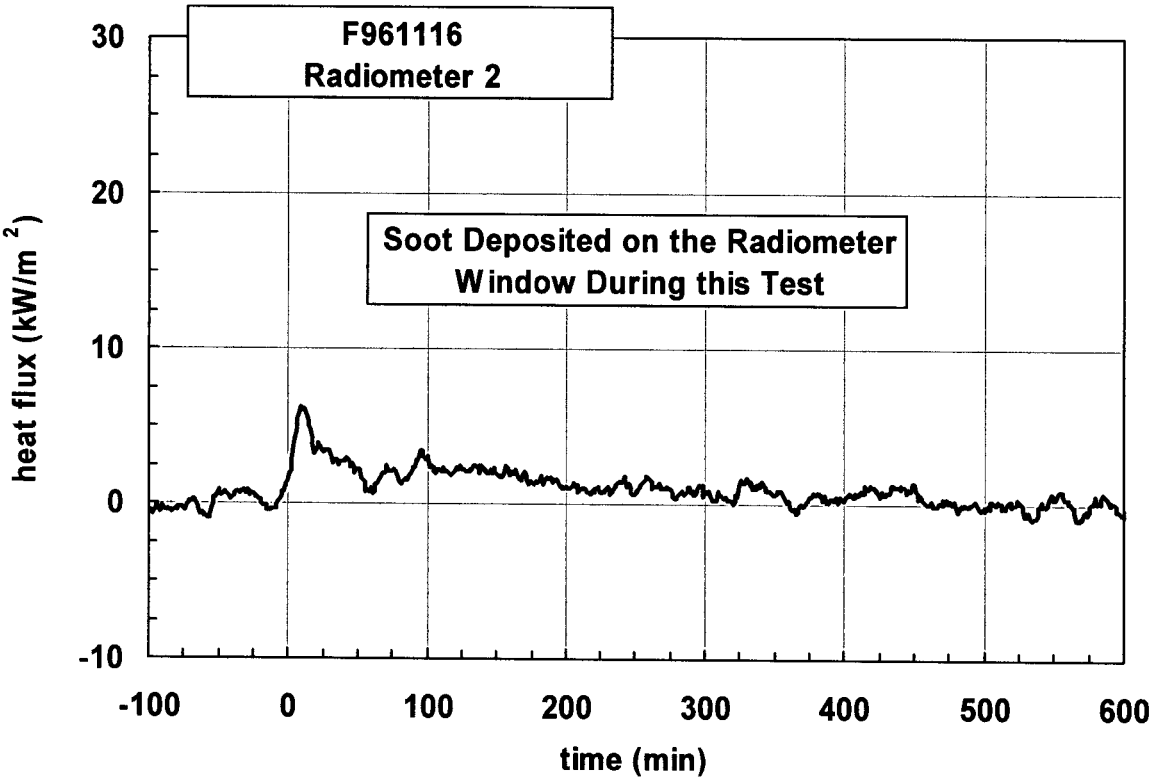


**Plot E4. Fire Test F961116. Data plot from Radiometer 2.**

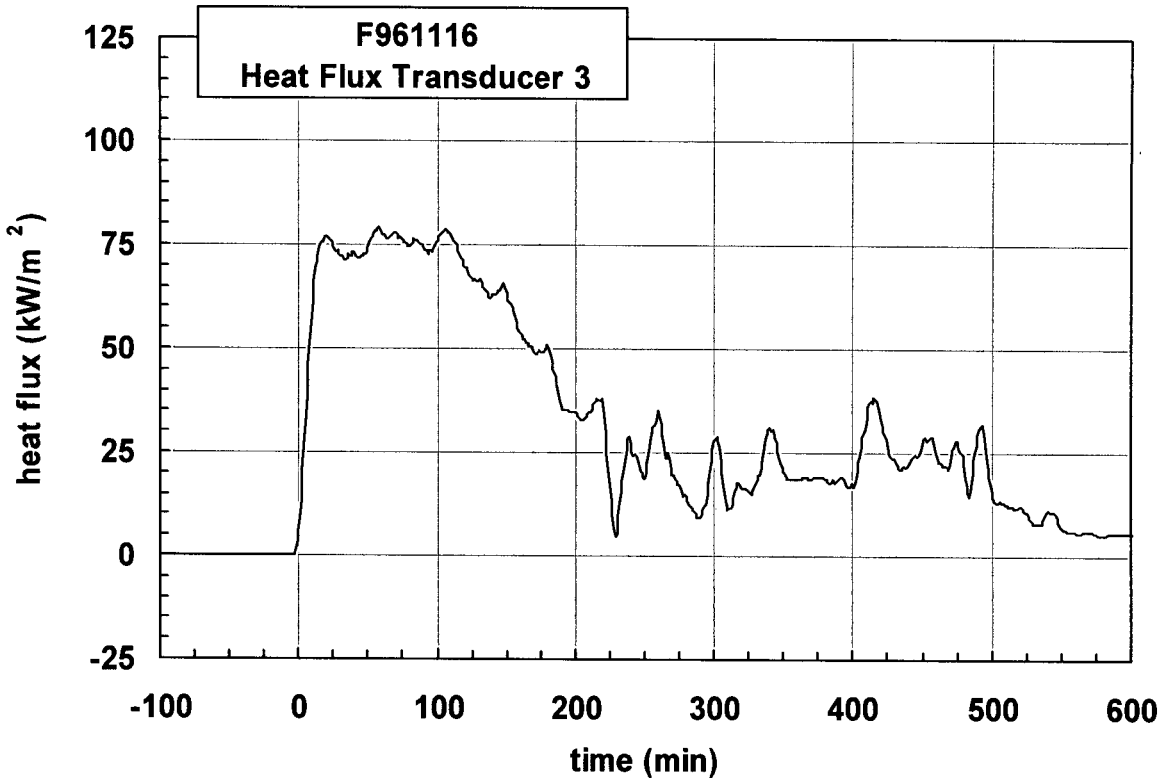


**Plot E5. Fire Test F961116. Data plot from Heat Flux Transducer 3.**
**Plot E6. Fire Test F961116. Data plot from Radiometer 3.**

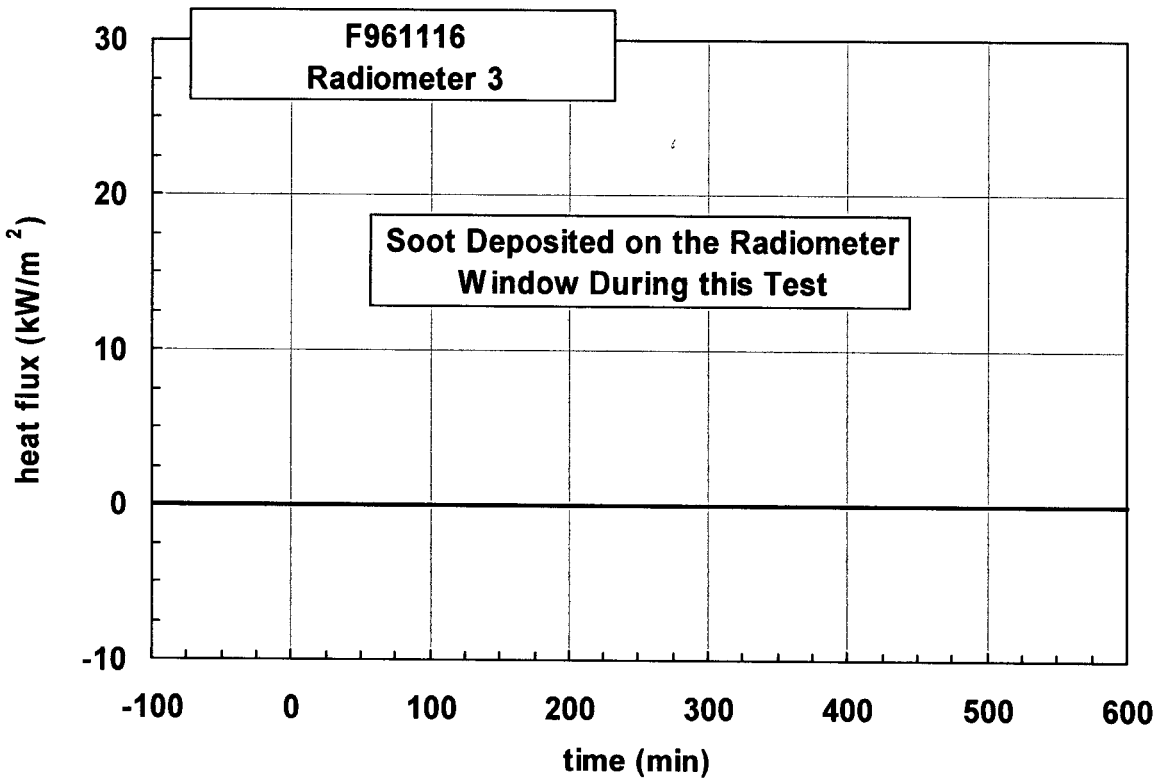

# APPENDIX F
# PRESSURE AND FLOW MEASUREMENTS

Air pressure was measured at the roof and floor in the rear of the passenger compartment of the rear of the test vehicle. Gas flow through the rear liftgate window opening (the glass was shattered during the crash test) of the test vehicle. Figures F1 and F2 show the approximate locations of the pressure tapes and the bi-directional flow probe installed in the test vehicle.

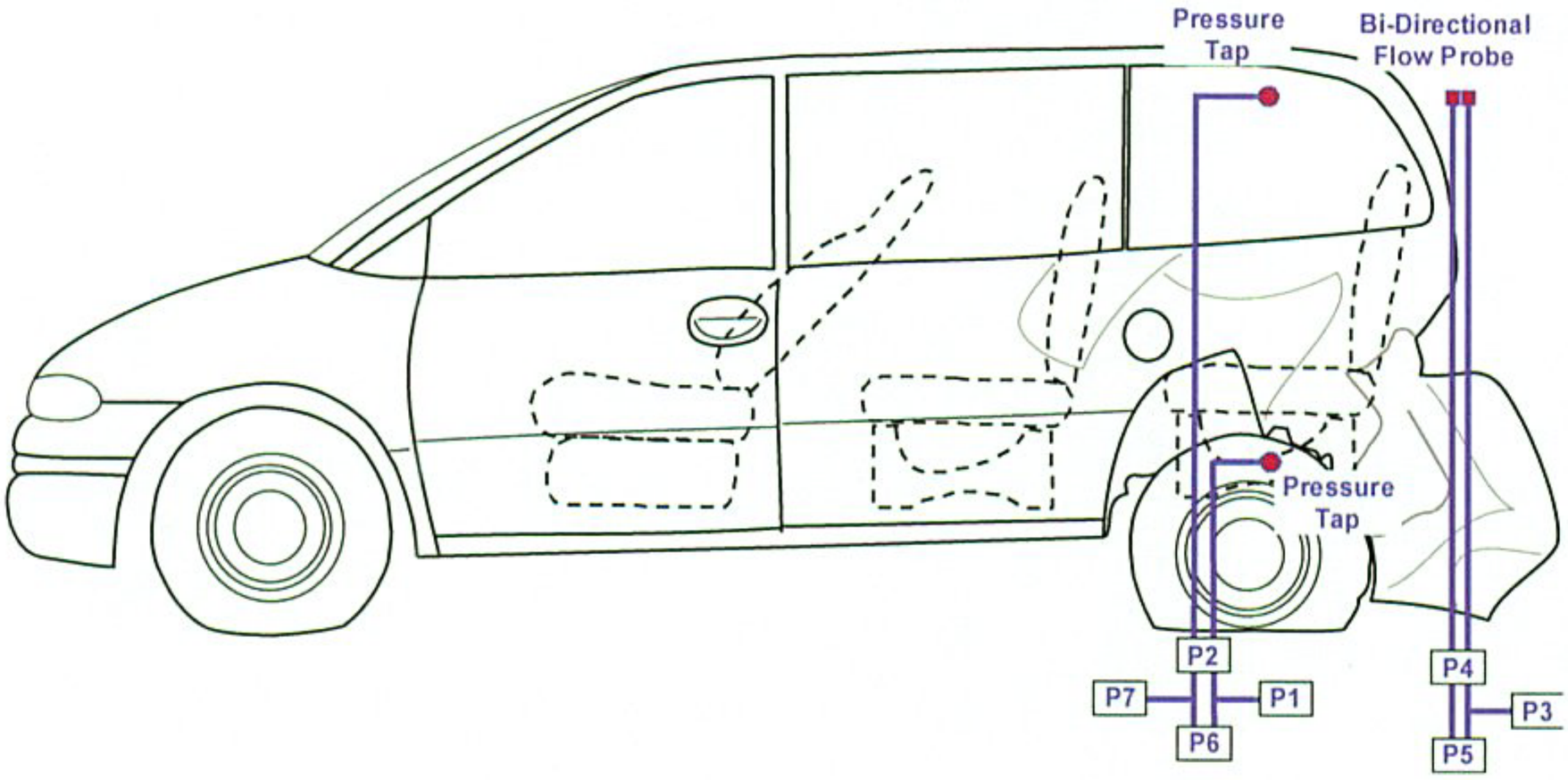


Figure F1. Fire Test F961116. Side view of test vehicle showing the approximate locations of the two pressure taps and bi-directional probe. Pressure gages P2 and P6 measured the pressure difference between the floor and roof the of the test vehicle. Pressure gauge P1 measured the pressure at the floor of the test vehcile relative to atmospheric pressure. Pressure gauge P7 measured the pressure at the roof of the test vehicle relative to atmospheric pressure. Pressure gauges P4 and P5 measured the pressure difference across the bi-directional probe. Pressure gauge P3 measured the pressure at the outside of the bi-directional probe relative to atmospheric pressure.

The pressure taps consisted of two section of stainless steel tubing (o.d. = 0.250 in.). One end of each of tubing contained a union-T fitting with compression-type couplings (Swage Union-T). The end of one section of tubing containing the union-T fitting was located just above the carpet under the center of the second bench seat. The end of the other section of tubing containing the union-T fitting was located just below the headlining above the center of the second bench seat. Each pressure tap was connected to pressure gauges (Model C-264, Setra Systems, Acton, MA) with solvent-resistant flexible tubing (Tygon Masterflex® 6049; i.d. = 0.250 in.; o.d. = 0.438 in.) as shown in Figure F1. The total length of each pressure sampling line was approximately 10 m.

Pressure gauges with two pressure ranges were used for this test: - 0.5 to 0.5 (± 0.0013) in. W.C. (-124.5 to 124.5 Pascal) and -0.1 to 0.1 (± 0.0003) in. W. C. (-24.9 to 24.9 Pascal). Both gauges were accurate to 0.25% full scale. The gages were powered with a 24 volt non-regulated power

supply (Setra Systems). The low- and high-range gages (P2 and P6, respectively) were connected in parallel to provide duplicate pressure measurement of the differential pressure across the dash panel. The low range gauge was used to maximize the sensitivity for measuring small pressure differences across the dash panel. The high range gauge was used to increase the dynamic range of the measurement in case the pressure difference across the dash panel exceeded 25 pascal. Pressure gauges P1 and P7 were high range pressure gauges used to measure static pressure at the interior- and exterior surfaces of the dash, respectively. The low-pressure inputs of P1 and P7 were left open to the atmosphere to provide a common reference pressure during the test.

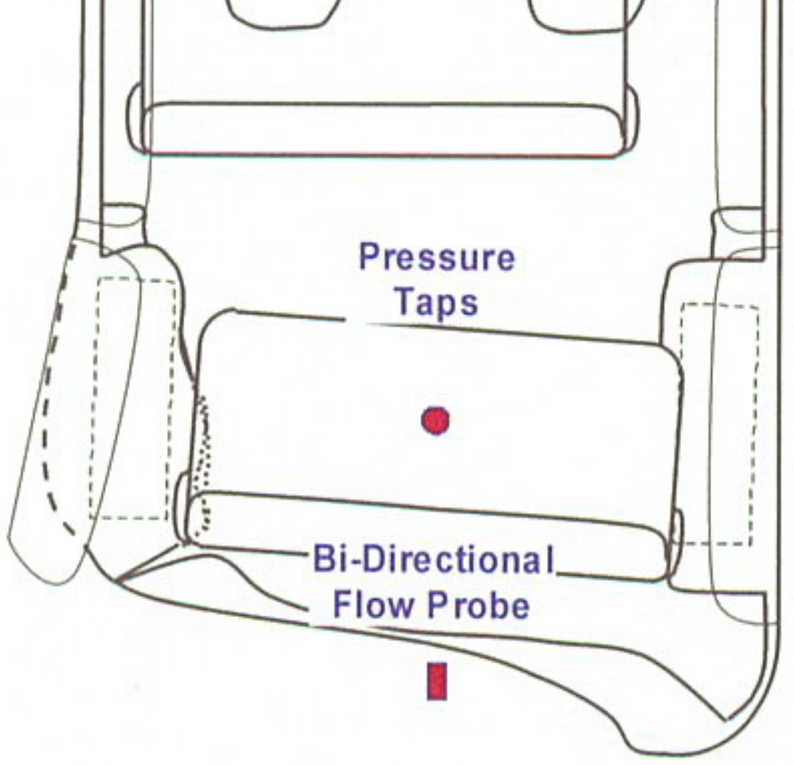


Figure F2. Fire Test F961116. Top view of test vehicle showing the approximate locations of the two pressure taps and bi-directional probe.

The bi-directional flow probe was centered horizontally opening and approximately 10 cm below the upper edge in the rear liftgate window opening. The outlets of the pressure taps in the flow probe were connected to pressure gauges with solvent-resistant resistant flexible tubing (Tygon Masterflex® 6049; i.d. = 0.250 in.; o.d. = 0.438 in.) as shown in Figures 2 and 3. The total length of tubing was approximately 10 m. Low- and high-range gages (P4 and P5, respectively) were connected in parallel to provide duplicate pressure measurements of the pressure difference across the bi-directional flow probe. Pressure Gauge P3 was a low-range gauge connected to the pressure tap on the interior side of the bi-directional flow probe. The low pressure input of this gauge was left open to atmosphere and was used to measure static pressure just inside the upper section of the window opening in the driver's door.

The velocity of gas flow through the window opening in the driver's door was calculated from the pressure difference measured across the bi-directional probe using the following relationship:

$$V = 0.070\sqrt{T\Delta p} \qquad \text{(F1)}$$

where V is the gas velocity in m/s, $T$ is the gas temperature in degrees Kelvin, and $\Delta p$ is the pressure difference in Pascals ($N/m^2$) [F1 and F2].

A PC-based data system was sued to acquire data from these transducers during this test. The signal leads from the pressure transducers were connected to a low-gain analog-input multiplex expansion card (DBK12, IOTech) interfaced to a16-bit, 100 kHz I/O board with 16 analog input channels (DaqBoard 200A, IOTech). The data acquisition software (DaqView Software version 4.10, IOTech) was configured to sample each channel at a rate of 100 Hz and store the data in 100-point block-averages.

## REFERENCERS


E1. N. R. Keltner and J. L. Moya. Defining the thermal environment in fire tests. *Fire and Materials* **14**: 133-138, 1989.

E2. B. J. McCaffrey and G. A. Heskestad. Robust bidirectional low-velocity probe for flame and fire application. *Combustion and Flame* **26**: 125-127, 1976.

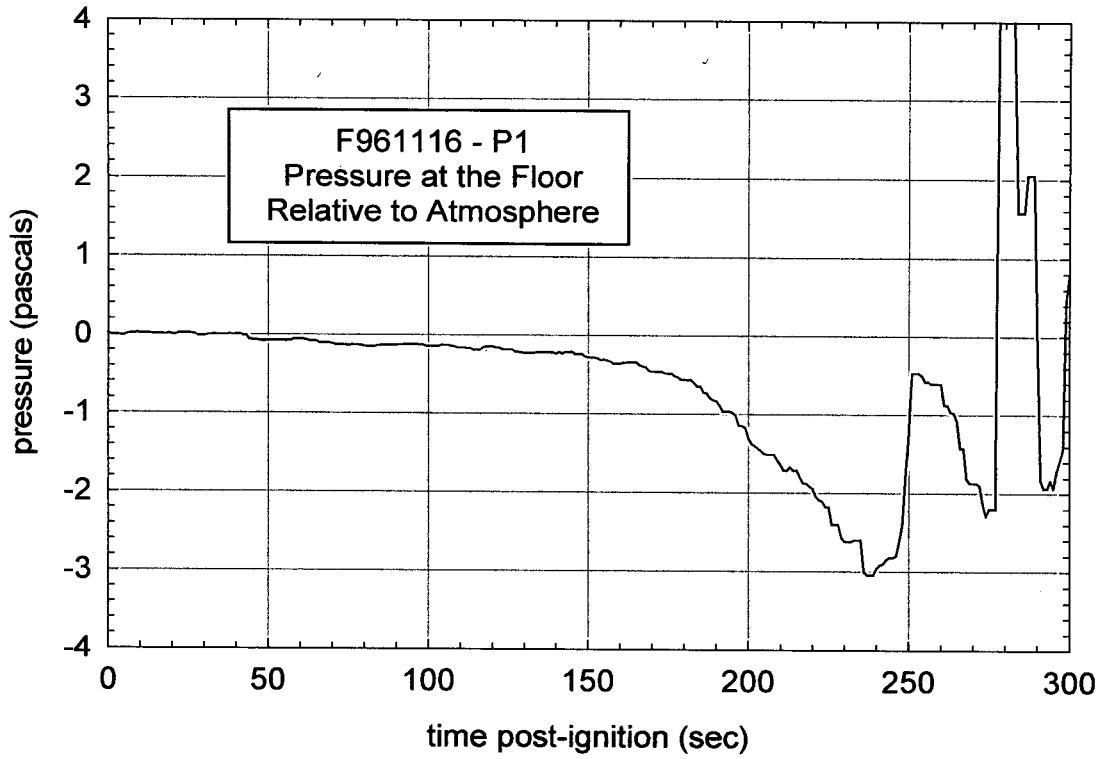


Plot F1. Fire Test F961116. Pressure relative to atmospheric pressure measured with P1.

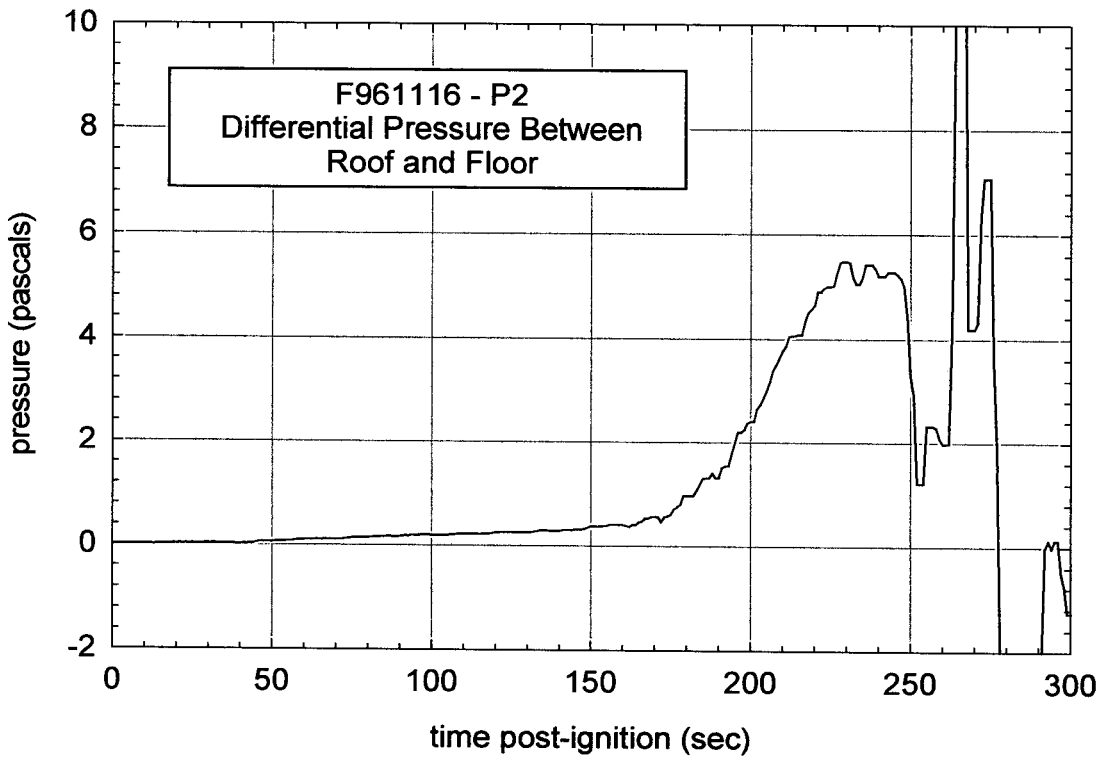


Plot F2. Fire Test F961116. Differential pressure between the headliner and floor measured with P2.

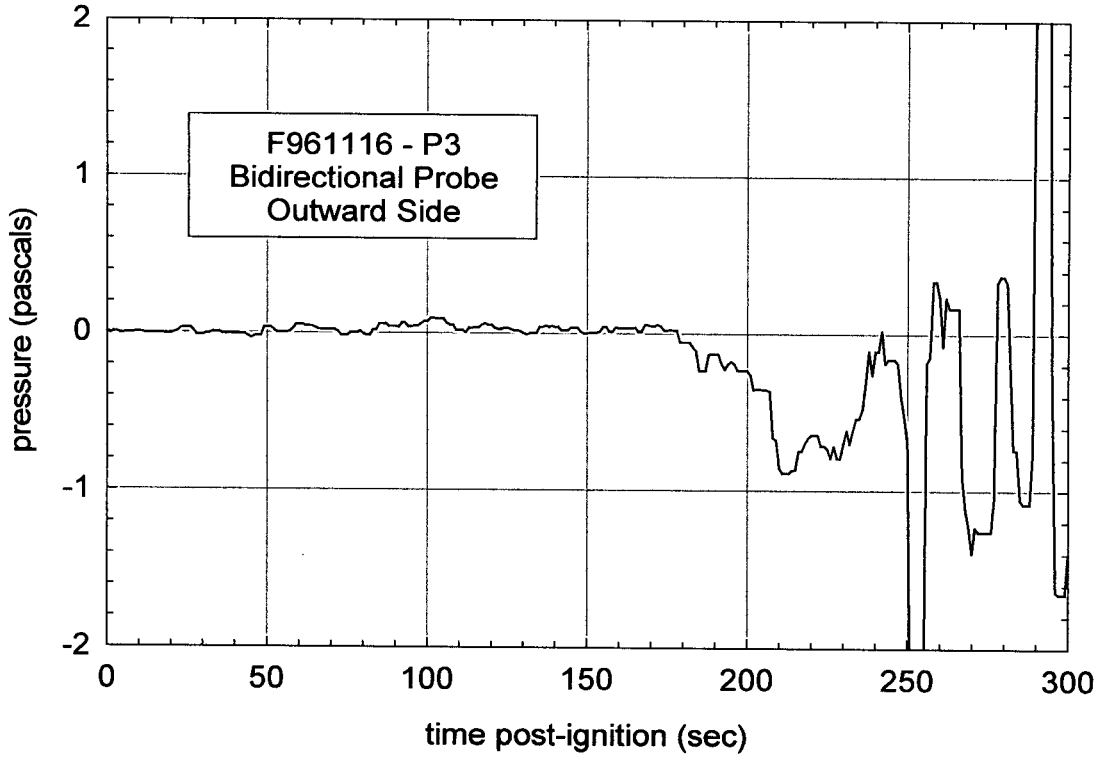


Plot F3. Fire Test F961116. Pressure relative to atmospheric pressure at the outward side of the bidirectional probe measured with P3.

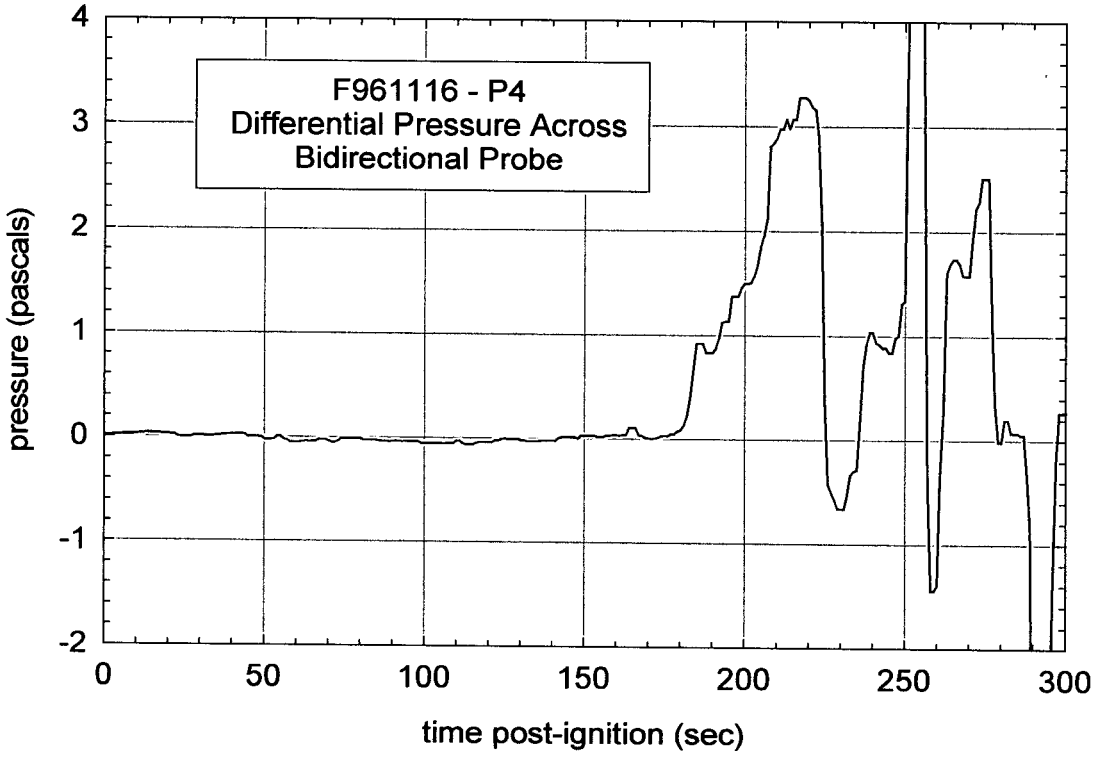


Plot F4. Fire Test F961116. Differential pressure across the bi-directional probe measured with P4.

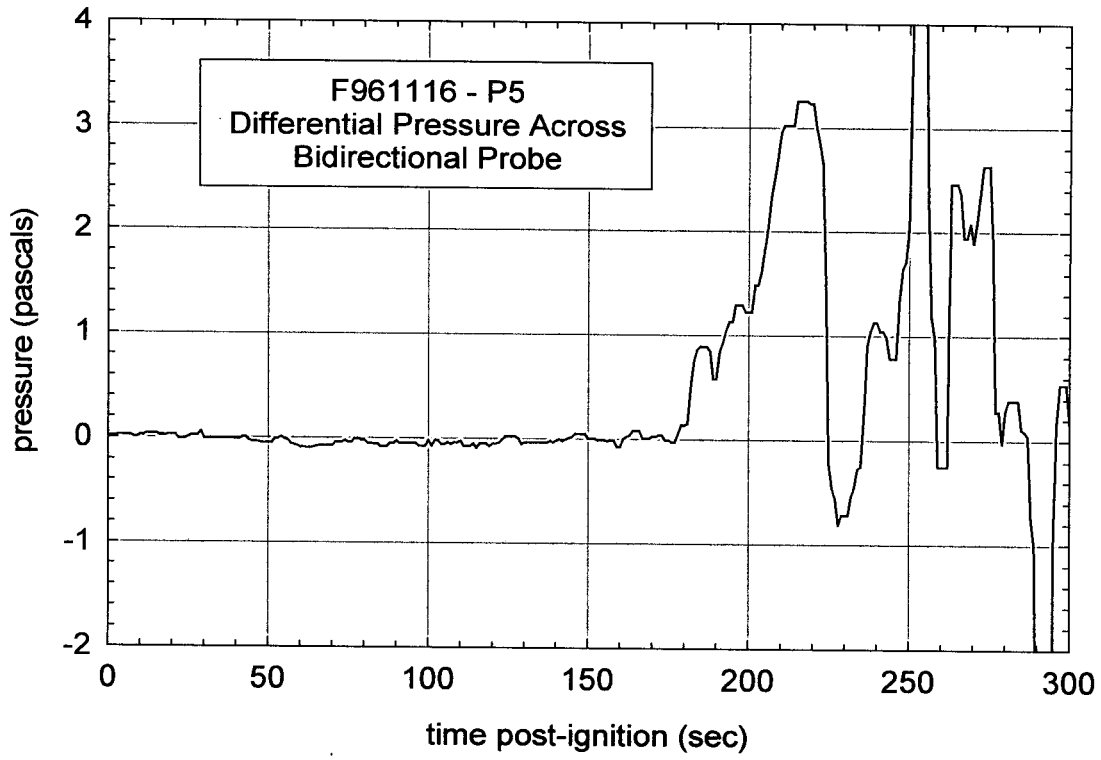


Plot F5. Fire Test F961116. Differential pressure across the bi-directional probe measured with P5.

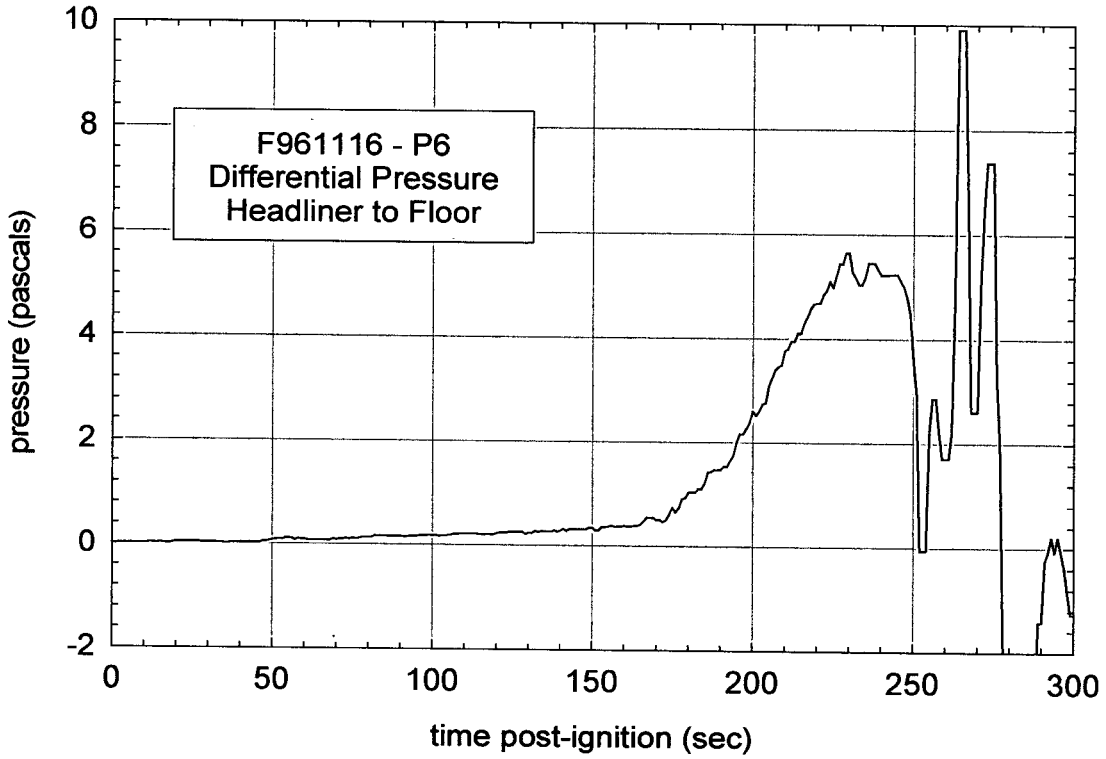


Plot E6. Fire Test F961116. Differential pressure between the headliner and floor measured with P6.

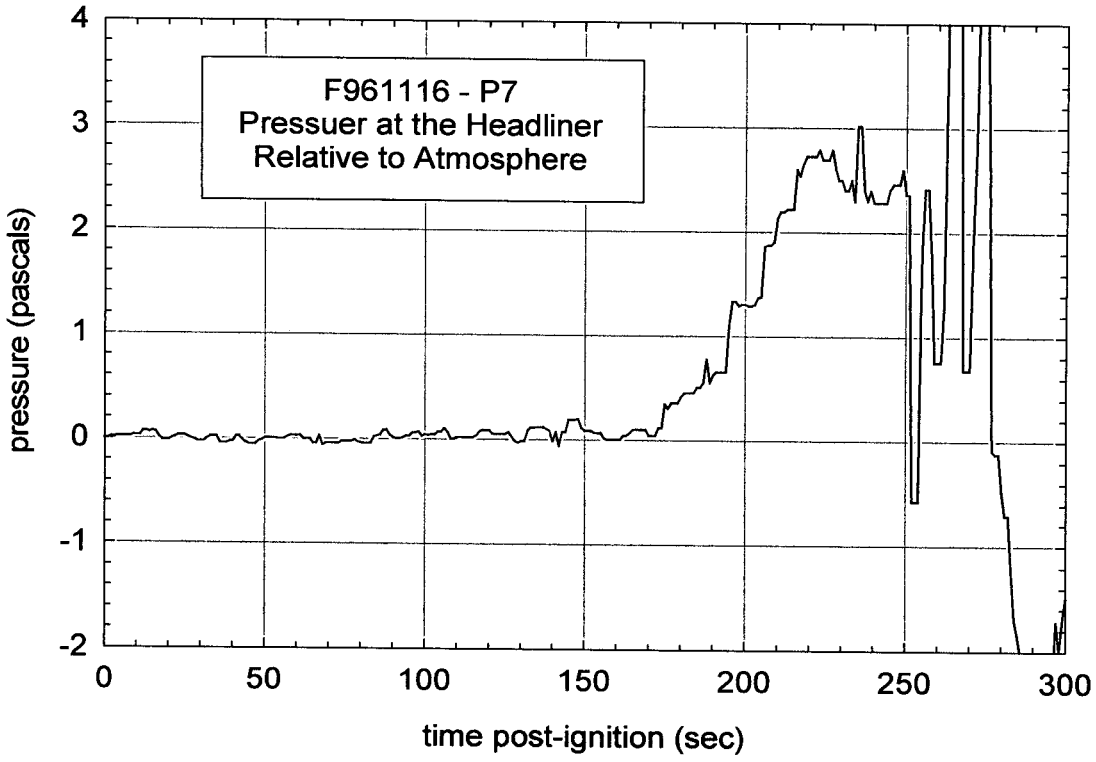


Plot E7. Fire Test F961116. Pressure relative to atmospheric pressure at the headliner measured with P7.

# APPENDIX G
# DIRECTIONAL FLAME THERMOMETER MEASUREMENTS, TIME-COMPENSATED ASPIRATED THERMOCOUPLE MEASUREMENTS, AND ESTIMATED HEAT FLUXES

Directional Flame Thermometers (DFT) (also known as slug calorimeters) were used to measure convective and radiative heat transfer [A6 and A7] to six locations in the passenger compartment. These devices were made by intrinsically welding a Type-K thermocouple (30 AWG, o.d. = 0.16 cm) to the unexposed side of a stainless steel disk (diameter = 2.54 cm; thickness = 0.06 cm). The unexposed side of the disk containing the intrinsically welded thermocouple was then insulated with 0.3 cm Fiberfrax paper (Carborundum Co., Niagara Falls, NY) and backed with another stainless steel disk. The exposed side of the DFT was coated with high temperature optical black coating with an absorptance of 0.92 from 0.5 to 20 μm (Medtherm Corp., Huntsville, AL). The thermocouple lead was enclosed in a stainless steel sheath and insulated with magnesium oxide. Refer to Figures G1 and G2 for the locations of the DFTs in the test vehicle.

Directional Flame Thermometers are passive devices that respond to both radiative and convective heating. The response-time of these devices was considerably longer than that of the water-cooled heat flux transducers described above. Radiative heat flux to the DFT was estimated from the first derivative of the temperature curve of the DFT. Convective heat flux to the DFT was estimated from the air temperature measured by the aspirated thermocouple probe. The use of the derivative in these calculations magnifies noise in the DFT-signal, therefore, an auto-recursive-moving-average (5 points) low pass filter was used to reduce electronic noise in the DFT signals. The first derivative of the filtered DFT-signal was calculated using the Lagrangian method with 5 data points. The hot wall heat flux is given by the following relationship:

$$q_h = \rho \cdot C_p \cdot \delta \cdot \frac{dT}{d\tau} \qquad \text{(G1)}$$

where q is the heat flux in $kW/m^2$; $\rho$ is the density of the metal disc in $kg/m^3$; $\delta$ is the thickness of the metal disc in m; $C_p$ is the specific heat of the metal disc in J/kg•K; and $dT/d\tau$ is the rate of temperature rise on the back disc in K/s. The heat flux was cold-wall corrected using a linearized radiation heat transfer coefficient obtained from calibration experiments.

$$q_c = \kappa_c \cdot (T_i - T_o) \qquad \text{(G2)}$$

The natural convection coefficient for cooling ($\kappa_c$) was calculated using the software "One Minute Convection", Genium Publishing Corp. to be 11 $W/[m^2 \cdot K]$. The radiative emission from the DFT is:

$$q_r = \sigma \cdot \varepsilon \cdot (T_i^2 + T_o^2) \cdot (T_i + T_o) \cdot (T_i - T_o) \qquad \text{(G3)}$$

where $\sigma$ is the Stefan-Boltzmann constant of 5.67 x $10^{-8}$ W/[$m^2$•$K^4$], $\varepsilon$ is the emissivity of the DFT surface (0.92) and temperatures are in Kelvin. The cold-wall corrected heat flux is:

$$q_t = q_h + q_r + q_c \qquad \text{(G4)}$$

where $q_h$ is the measured hot wall heat flux, $q_r$ is the correction for radiative emission and $q_c$ is the correction for convective heat loss from the DFT.

Eight directional flame thermometers (DFT) were positioned in the passenger compartment to measure heat fluxes to three occupant positions in the test vehicle during this fire test (Fig.'s G1 and G2).

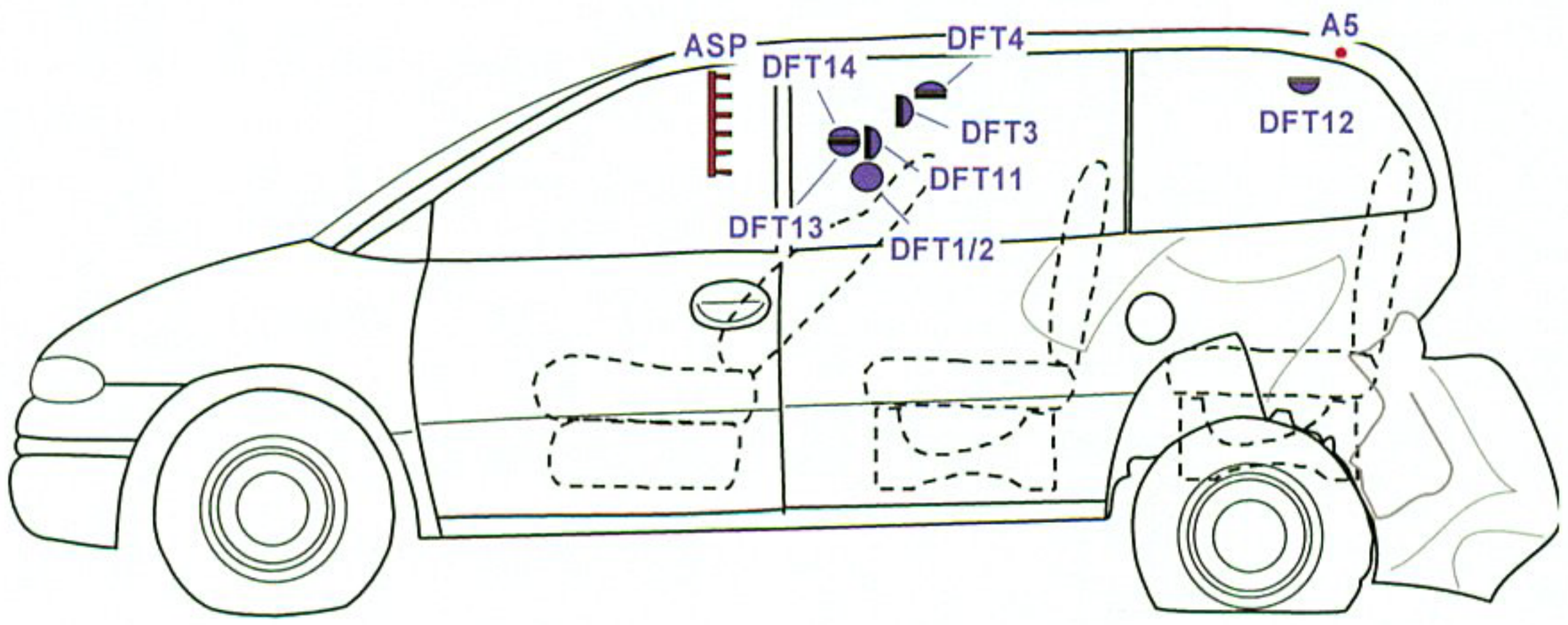


Figure G1. Fire Test F961116. Side view of the test vehicle showing the approximate locations of the DFTs in the passenger compartment. The blue surface is the heat-absorbing front of the DFT and the black surface is the insulated back of the DFT. The approximate locations of the aspirated thermocouple assembly and Thermocouple A5 are shown for reference.

DFT11, DFT13, and DFT 14 were located at approximately 35 cm above the driver's seat facing rearward, downward, and upward, respectively. DFT1, DFT2, DFT3, and DFT4 were located approximately 35 cm above the center of the first bench seat facing right, left, rearward, and upward, respectively. DFT12 was located approximately 35 cm above the center of the second bench seat facing downward.

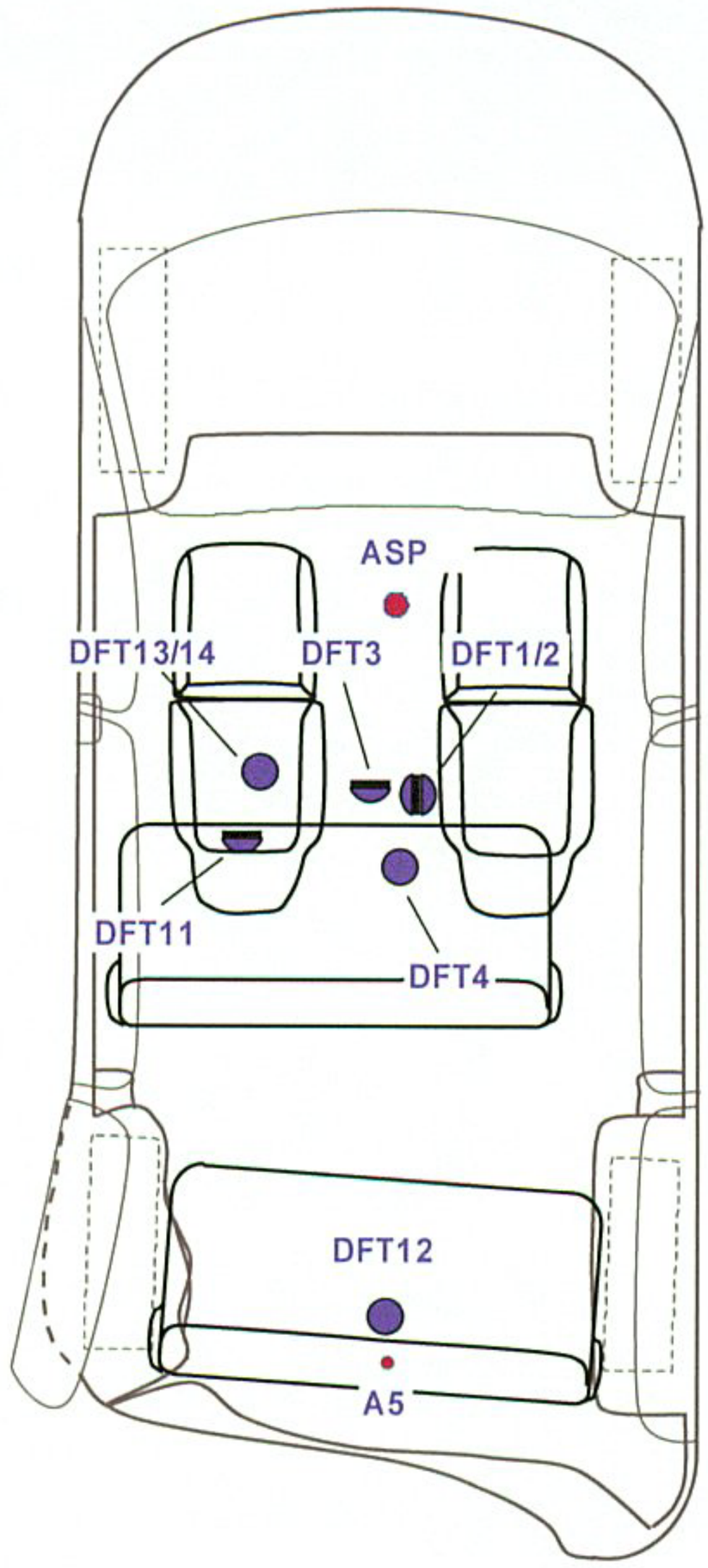


Figure G2. Fire Test F961116. Top view of the test vehicle showing the approximate locations of the DFTs in the passenger compartment. The blue surface is the heat-absorbing front of the DFT and the black surface is the insulated back of the DFT. The approximate locations of the aspirated thermocouple assembly and Thermocouple A5 are shown for reference.

A PC-based data system was sued to acquire data from these transducers during this test. The signal leads from the DFT's were connected to a thermocouple multiplex expansion card (DBK-19, IOTech) interfaced to a16-bit, 100 kHz I/O board with 16 analog input channels (DaqBoard 200A, IOTech). The data acquisition software (DaqView Software version 4.10, IOTech) was configured to sample each channel at a rate of 100 Hz and store the data in 100-point block-averages.

Plots G1, G3, G5, G7, G9, G11, G13, and G15 show the temperatures recorded by DFT1, DFT2, DFT3, DFT4, DFT11, DFT12, DFT13, and DFT14, respectively. The temperature recorded by each DFT and the air temperatures around each DFT (estimated from the temperatures recorded by the aspirated thermocouples) were used to estimate the convective and radiative heat fluxes to each DFT except DFT12. The temperature recorded by Thermocouple A5, located approximately 1 cm below the headliner above the center of the second bench seat, was used to estimate the radiative and convective heat fluxes to DFT12. The estimated convective and radiative heat fluxes to the DFTs are shown in plots G2, G4, G6, G8, G10, G14, and G16.

The temperature recorded by Thermocouple A5 may have been significantly different than the actual air temperature around DFT12. The effect of uncertainty air temperature the estimated values of the convective and radiative heat fluxes to DFT12 was investigated by varying the air temperature used in the calculation of these parameters. This series of calculations showed that the value of air temperature used in the estimation of convective and radiative heat fluxs effected the ratio of these parameters, but not the total estimated heat flux to DFT12.

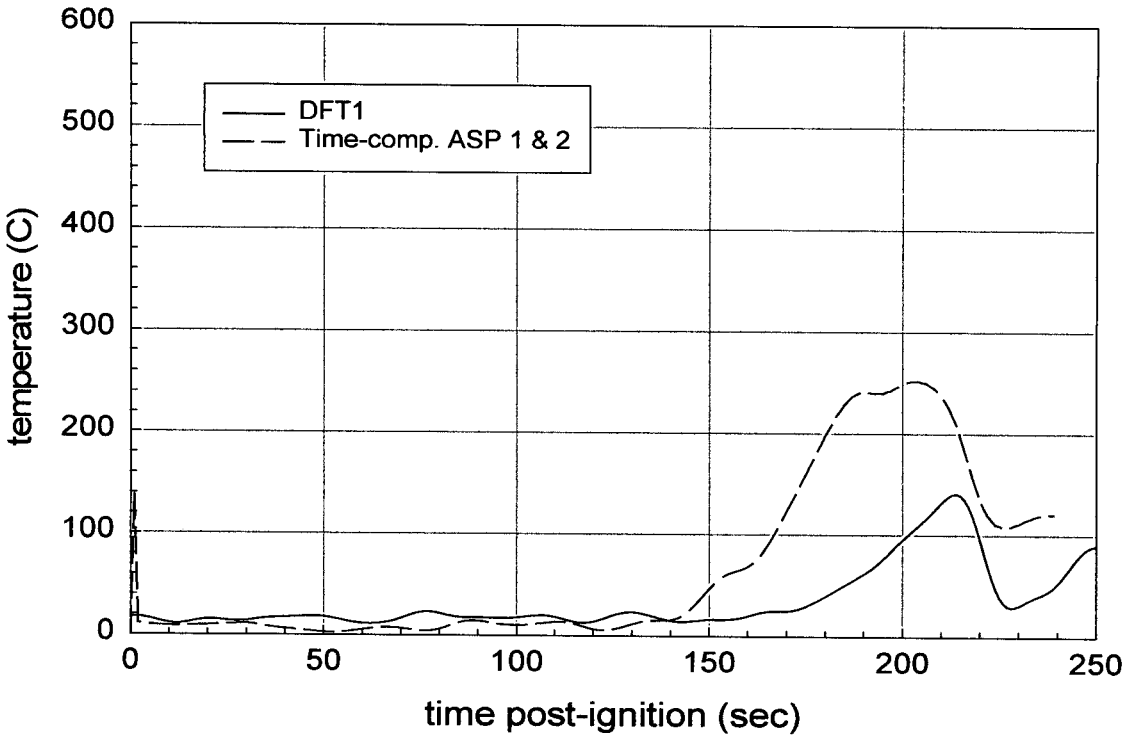


Plot G1. Fire Test F961116. Response of DFT1 and the average of the time-compensated responses of ASP1 and ASP2.

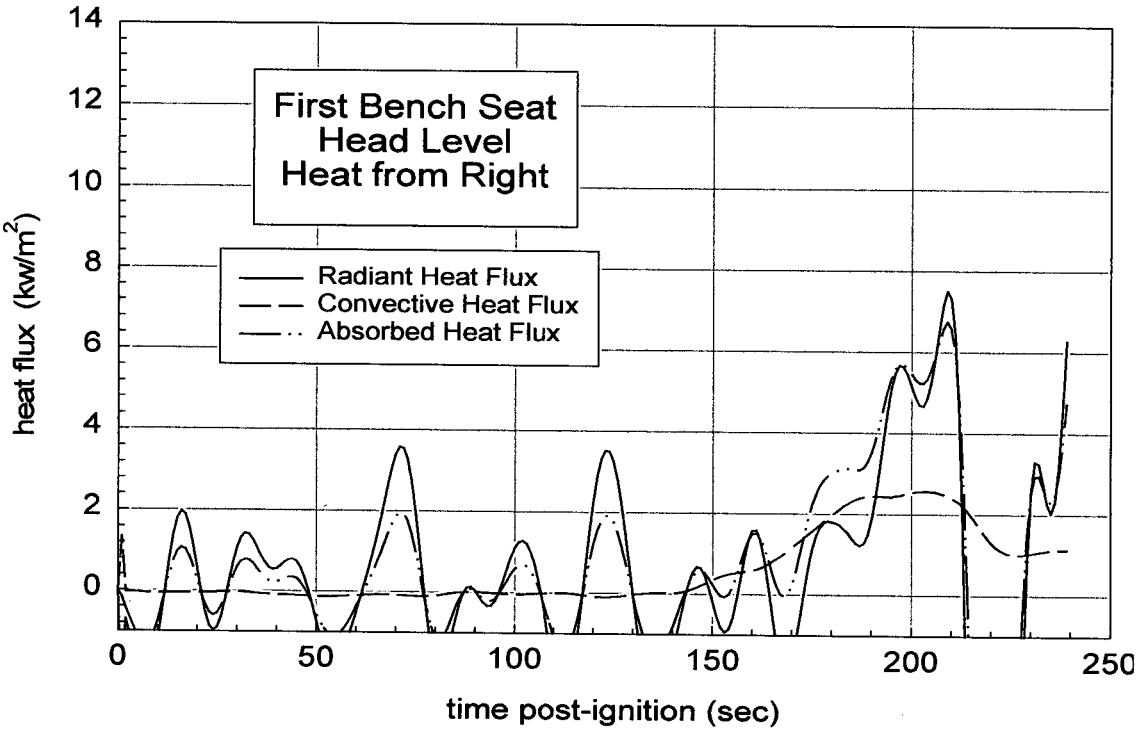


Plot G2. Fire Test F961116. Radiative, convective, and absorbed heat fluxes estimated from the response of DFT1 and the average of the time-compensated responses of ASP1 and ASP2.

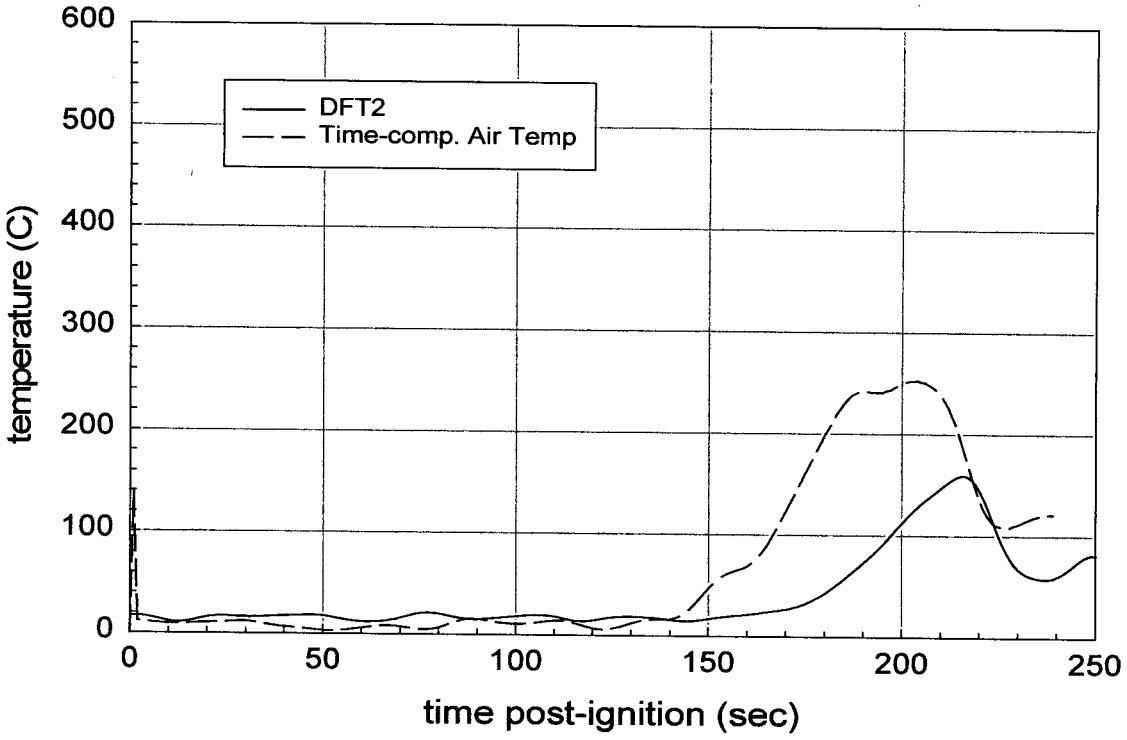


Plot G3. Fire Test F961116. Response of DFT2 and the average of the time-compensated responses of ASP1 and ASP2.

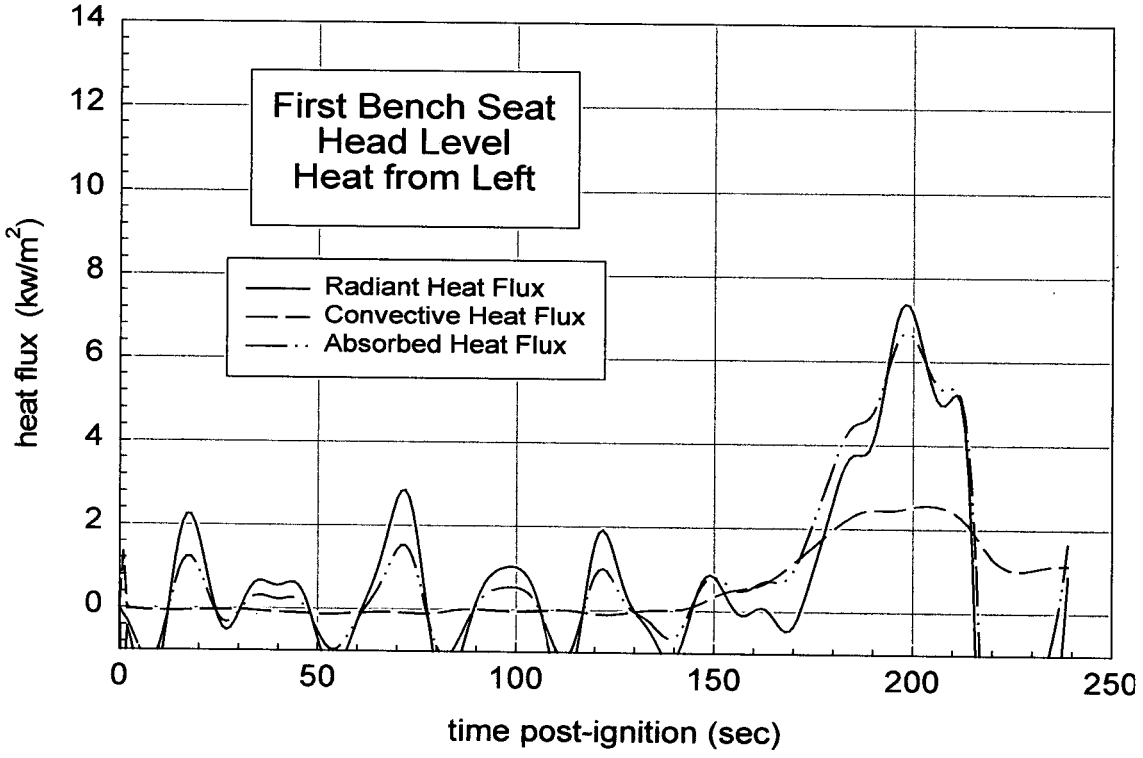


Plot G4. Fire Test F961116. Radiative, convective, and absorbed heat fluxes estimated from the response of DFT2 and the average of the time-compensated responses of ASP1 and ASP2.

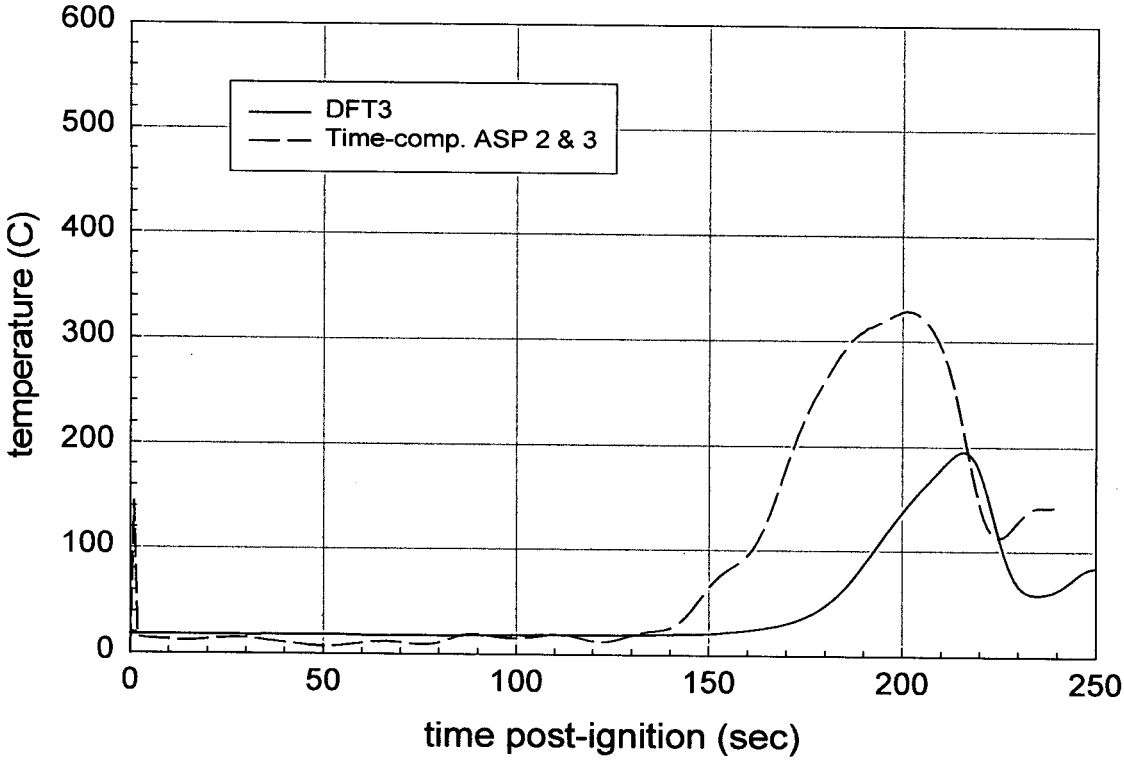


Plot G5. Fire Test F961116. Response of DFT3 and the average of the time-compensated responses of ASP2 and ASP3.

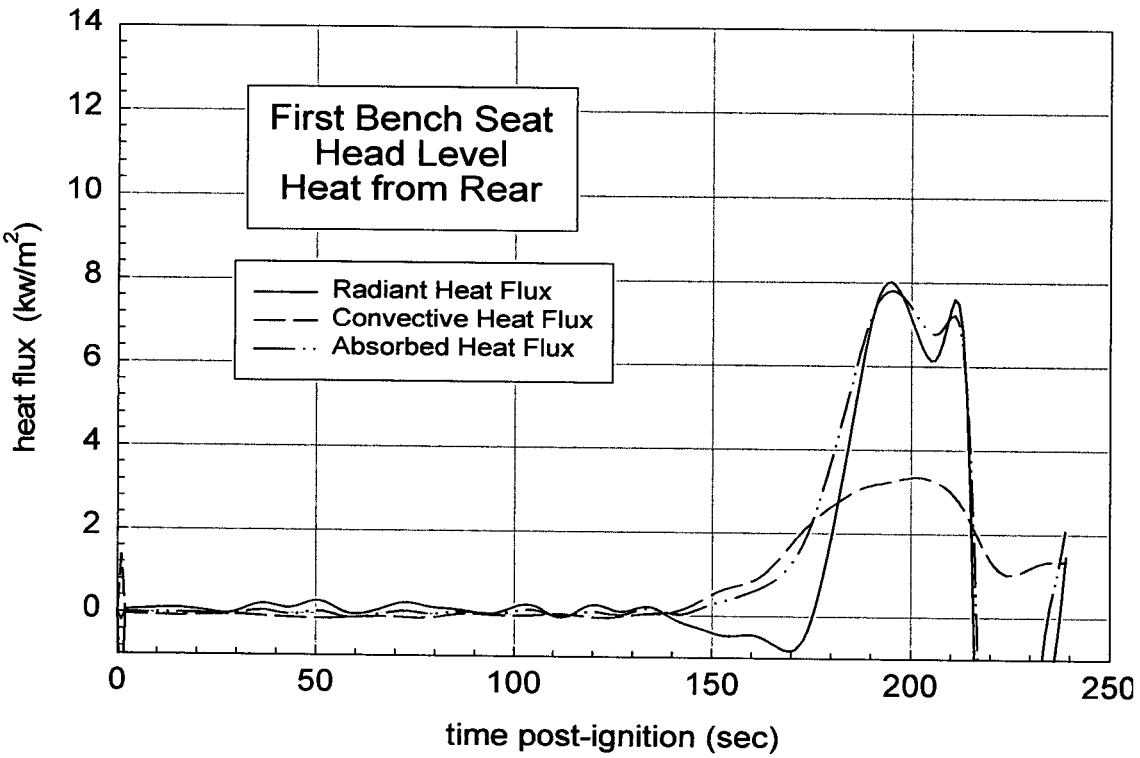


Plot G6. Fire Test F961116. Radiative, convective, and absorbed heat fluxes estimated from the response of DFT3 and the average of the time-compensated responses of ASP2 and ASP3.

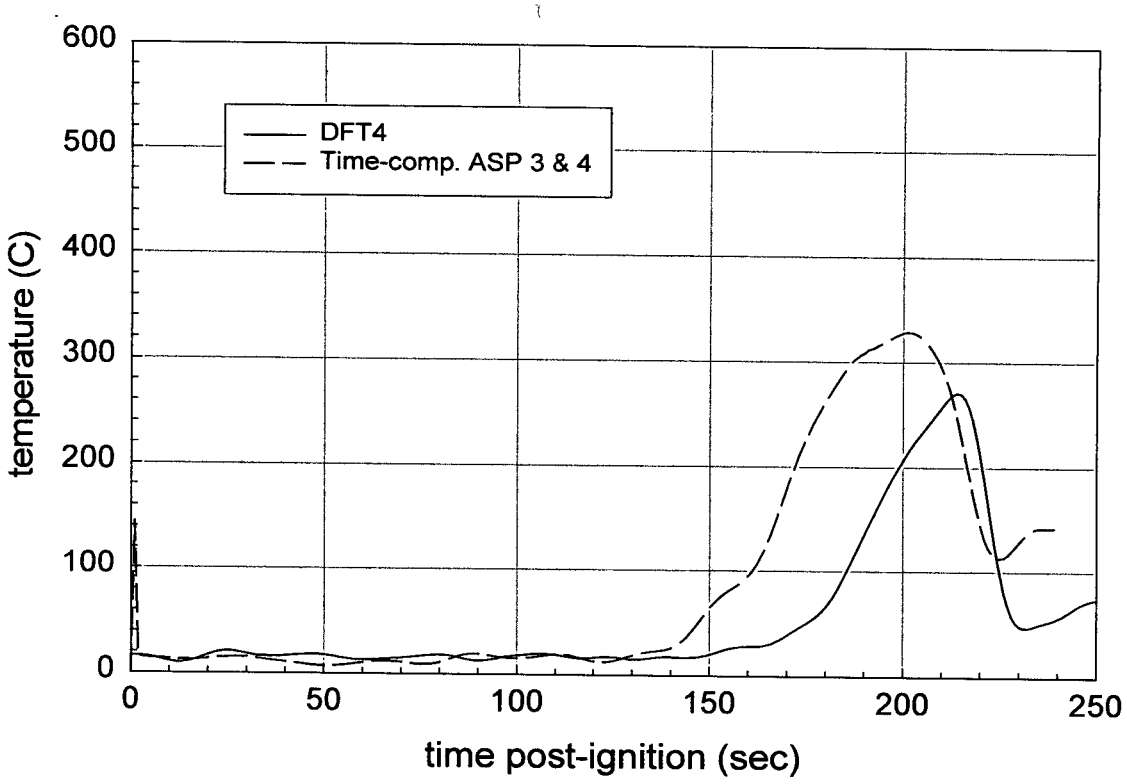


Plot G7. Fire Test F961116. Response of DFT4 and the average of the time-compensated responses of ASP3 and ASP4.

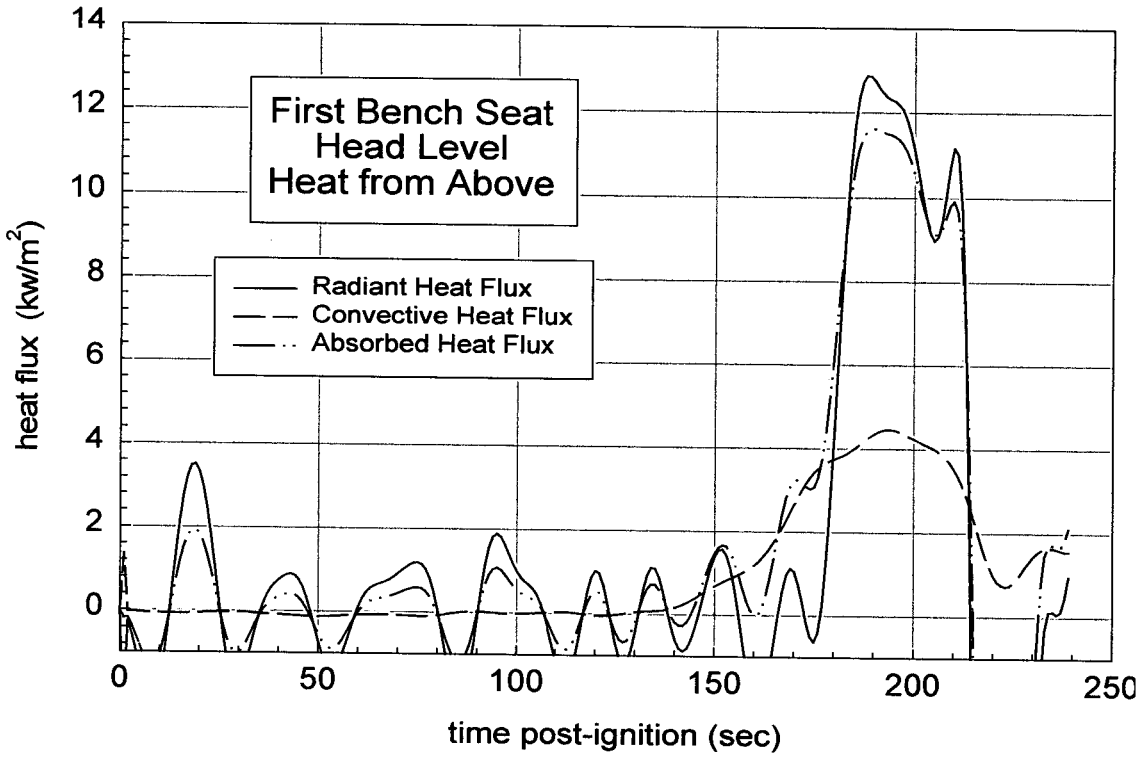


Plot G8. Fire Test F961116. Radiative, convective, and absorbed heat fluxes estimated from the response of DFT4 and the average of the time-compensated responses of ASP3 and ASP4.

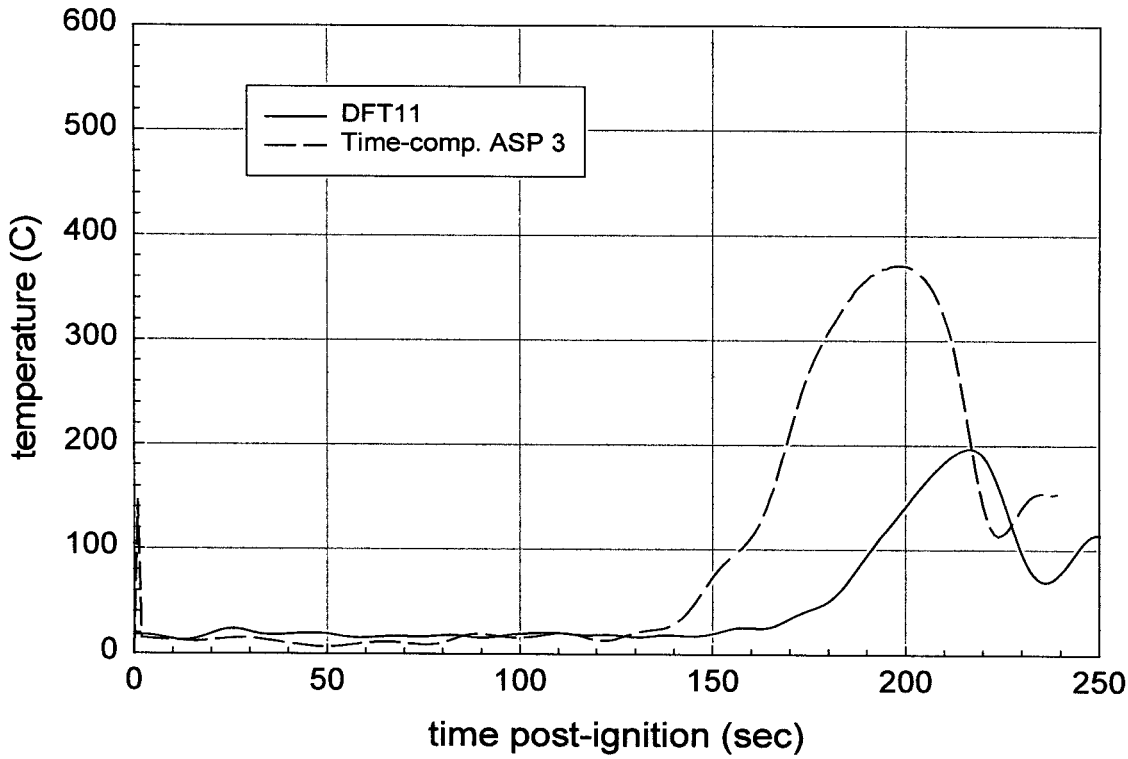


Plot G9. Fire Test F961116. Response of DFT11 and the time-compensated response of ASP3.

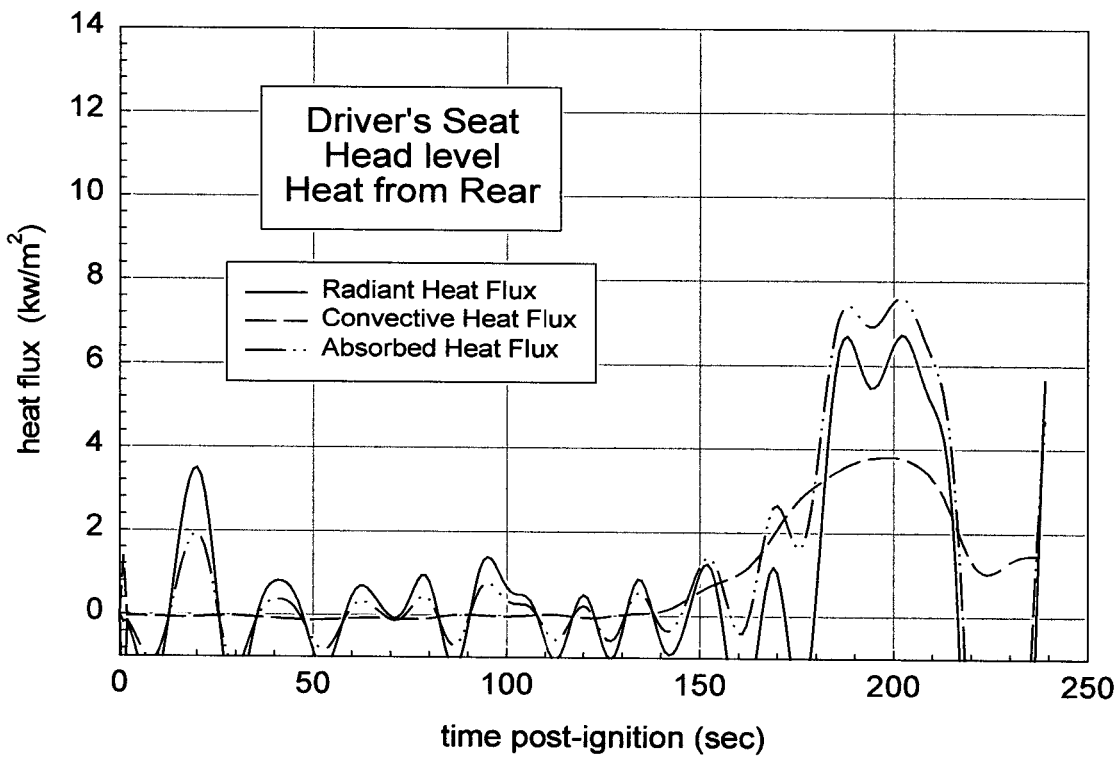


Plot G10. Fire Test F961116. Radiative, convective, and absorbed heat fluxes estimated from the response of DFT11 and the time-compensated response of ASP3.

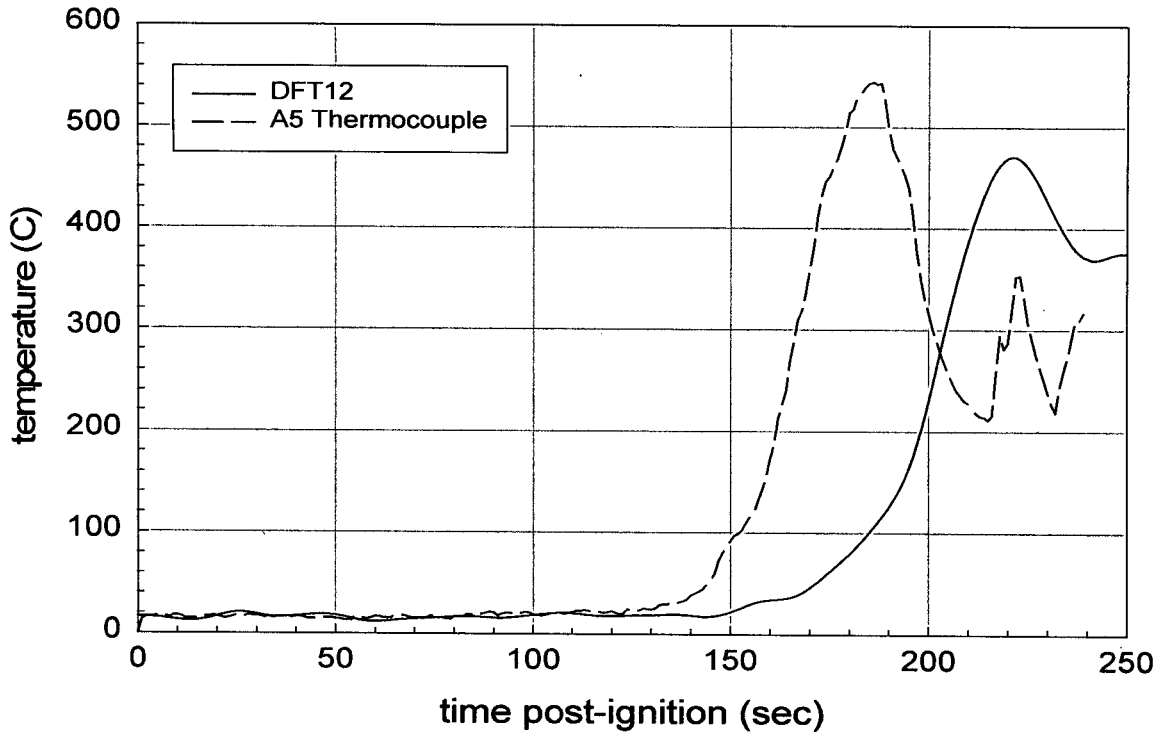


Plot G11. Fire Test F961116. Response of DFT12 and the temperature recorded by Thermocouple A5.

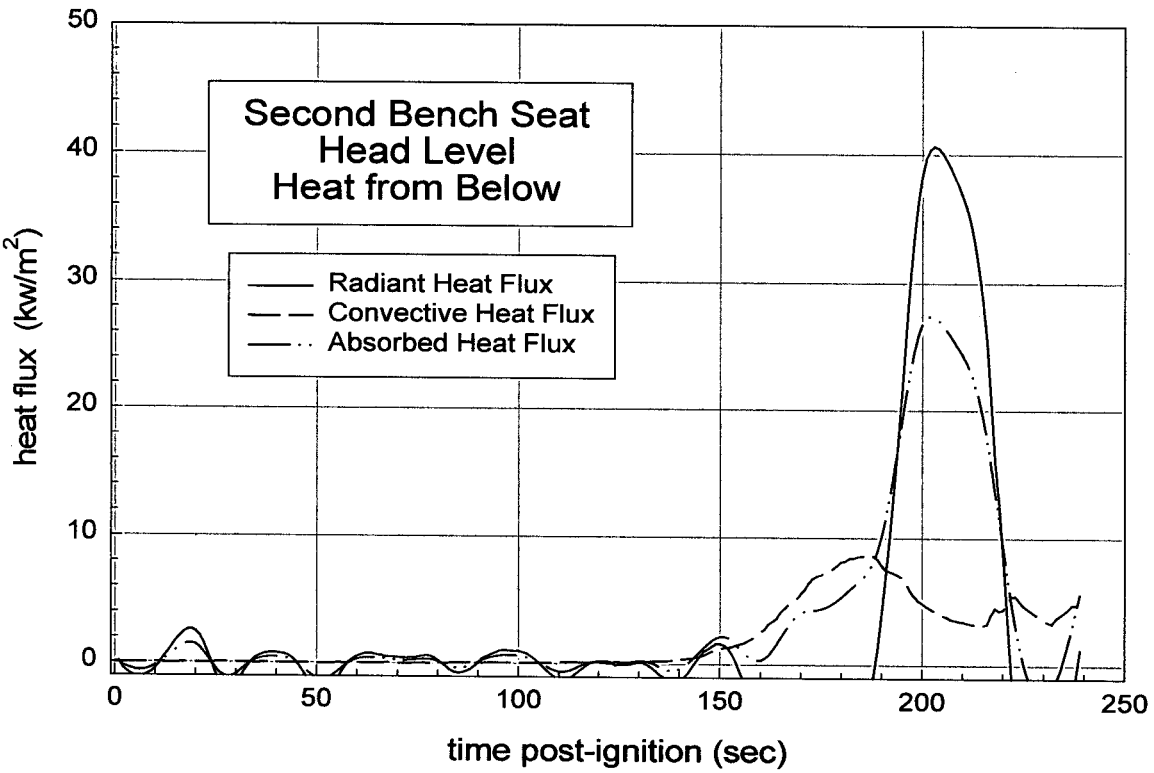


Plot G12. Fire Test F961116. Radiative, convective, and absorbed heat fluxes estimated from the response of DFT12 and the temperature recorded by Thermocouple A5.

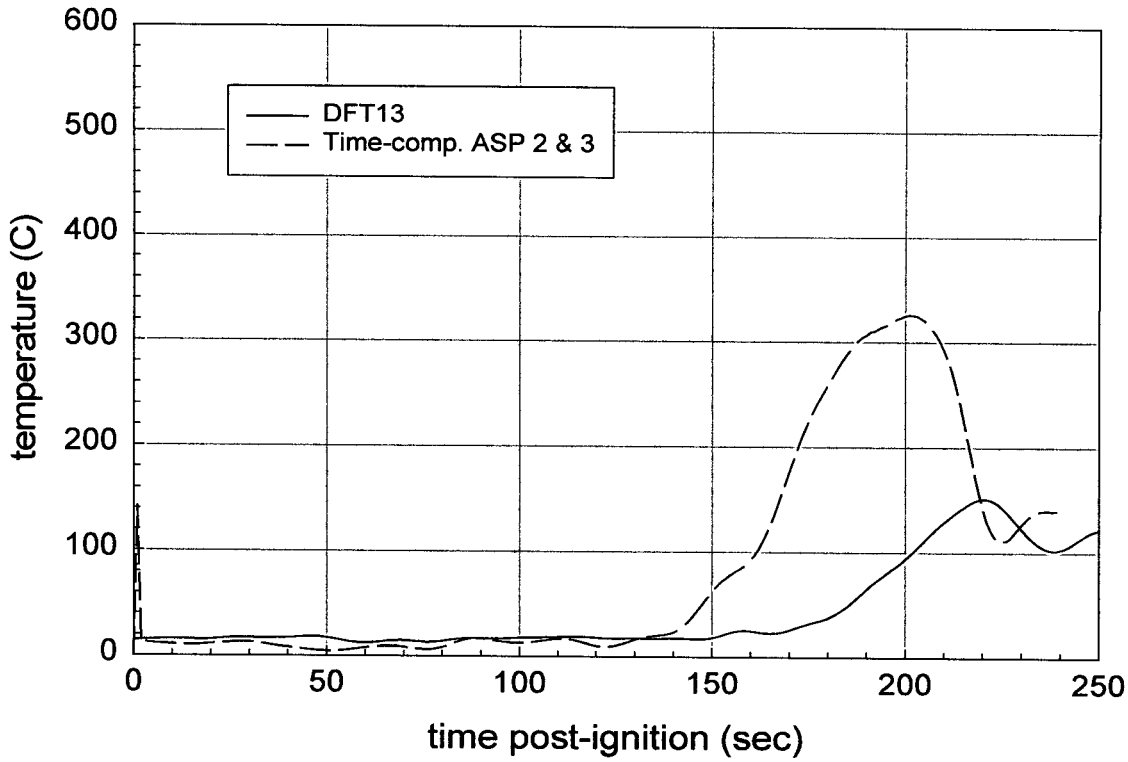


Plot G13. Fire Test F961116. Response of DFT13 and the average of the time-compensated responses of ASP2 and ASP3.

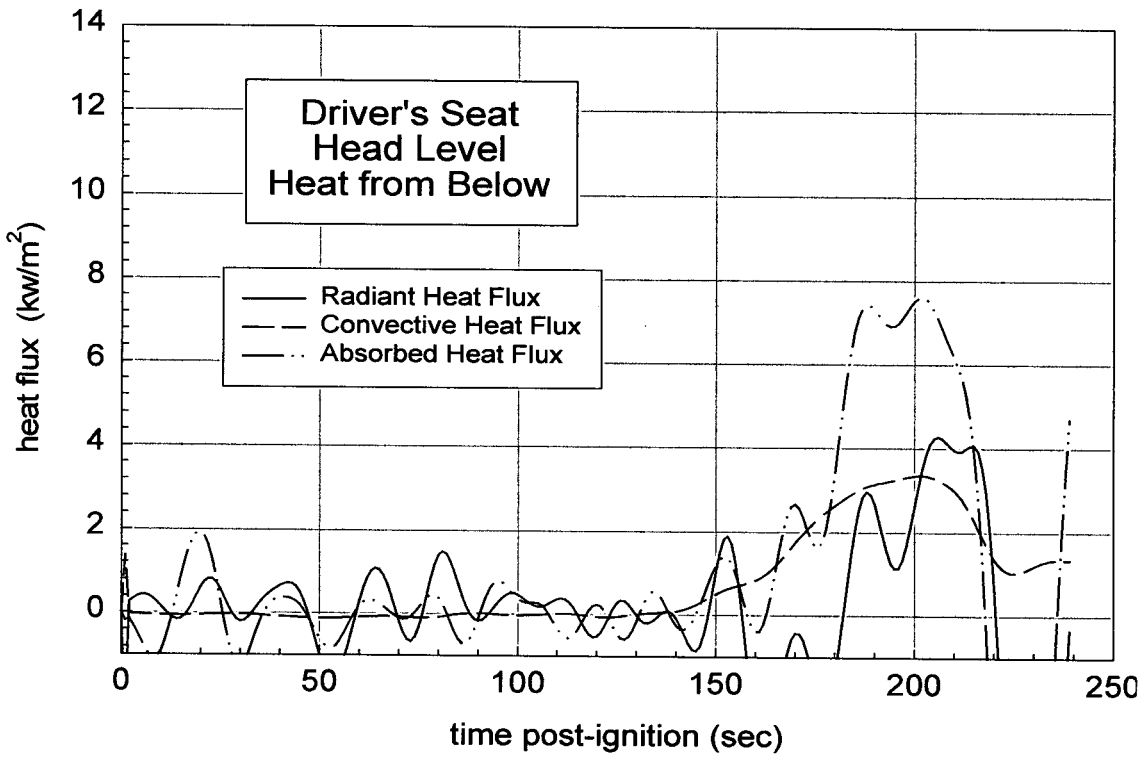


Plot G14. Fire Test F961116. Radiative, convective, and absorbed heat fluxes estimated from the response of DFT13 and the average of the time-compensated responses of ASP2 and ASP3.

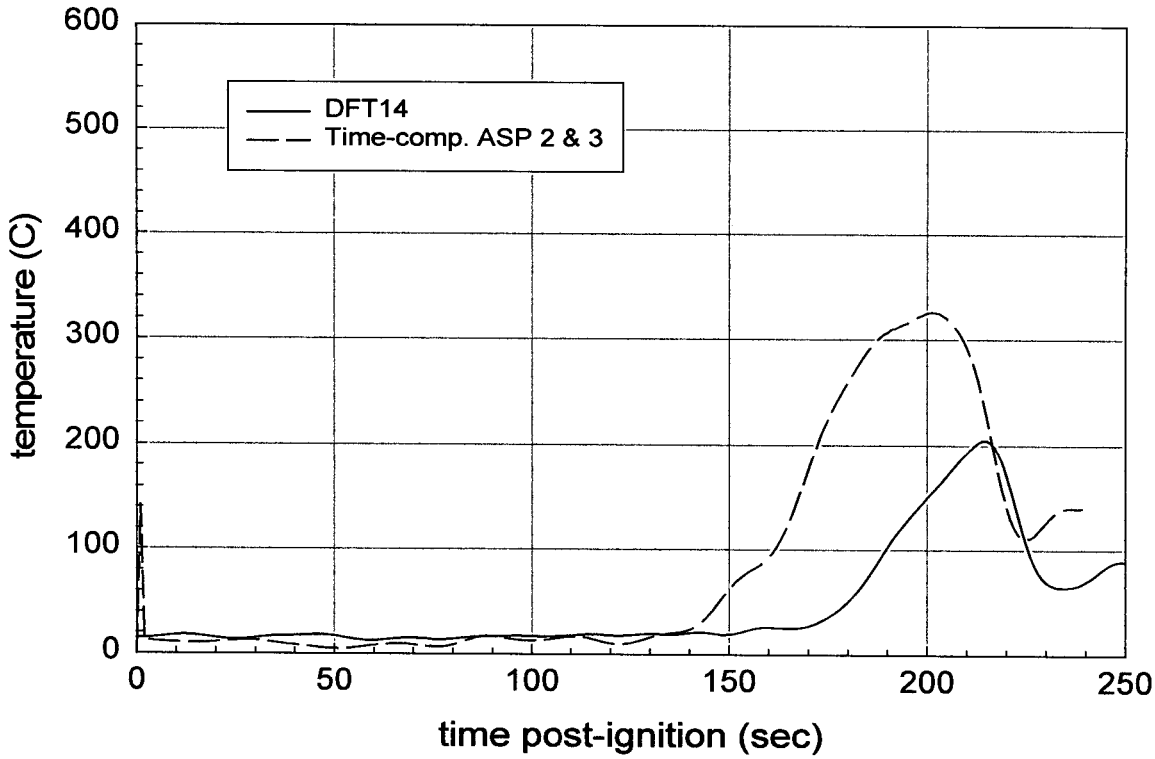


Plot G15. Fire Test F961115. Response of DFT14 and the average of the time-compensated responses of ASP2 and ASP3.

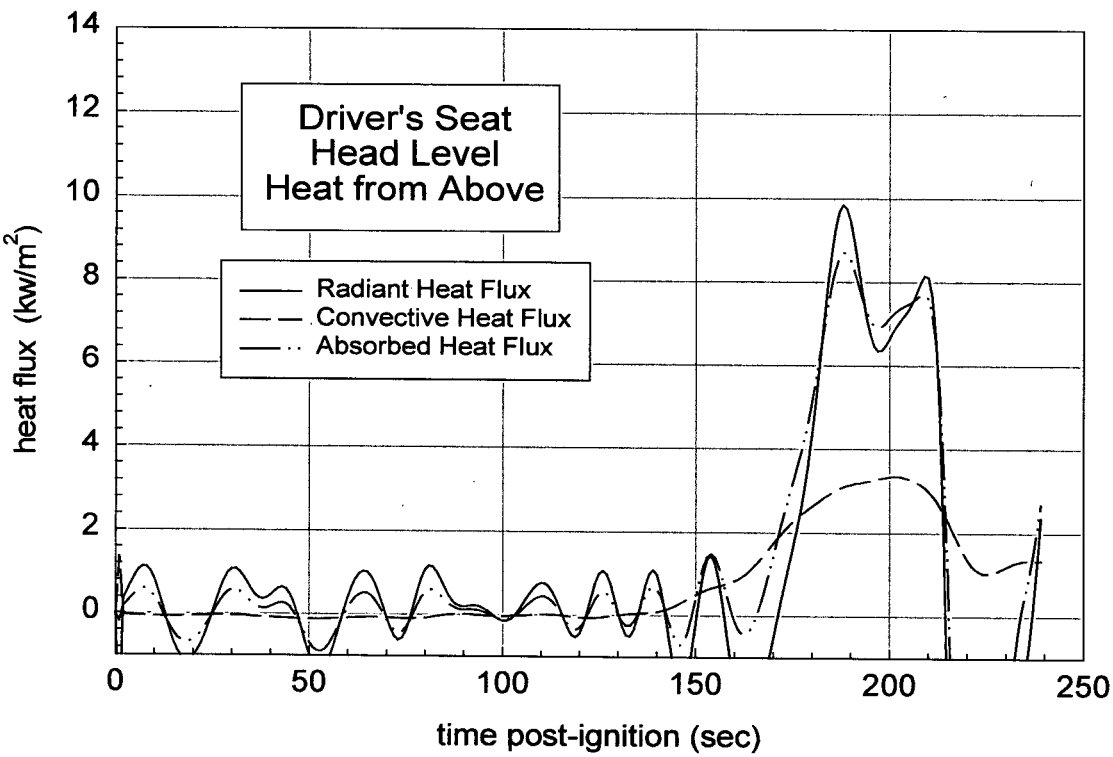


Plot G16. Fire Test F961115. Radiative, convective, and absorbed heat fluxes estimated from the response of DFT14 and the average of the time-compensated responses of ASP2 and ASP3.

# APPENDIX H
# FIRE PRODUCTS COLLECTOR DATA

The Fire Products Collector (FPC) at the Factory Mutual Test Center measured heat and combustion gases generated by the burning vehicles during these tests (Fig. H1).

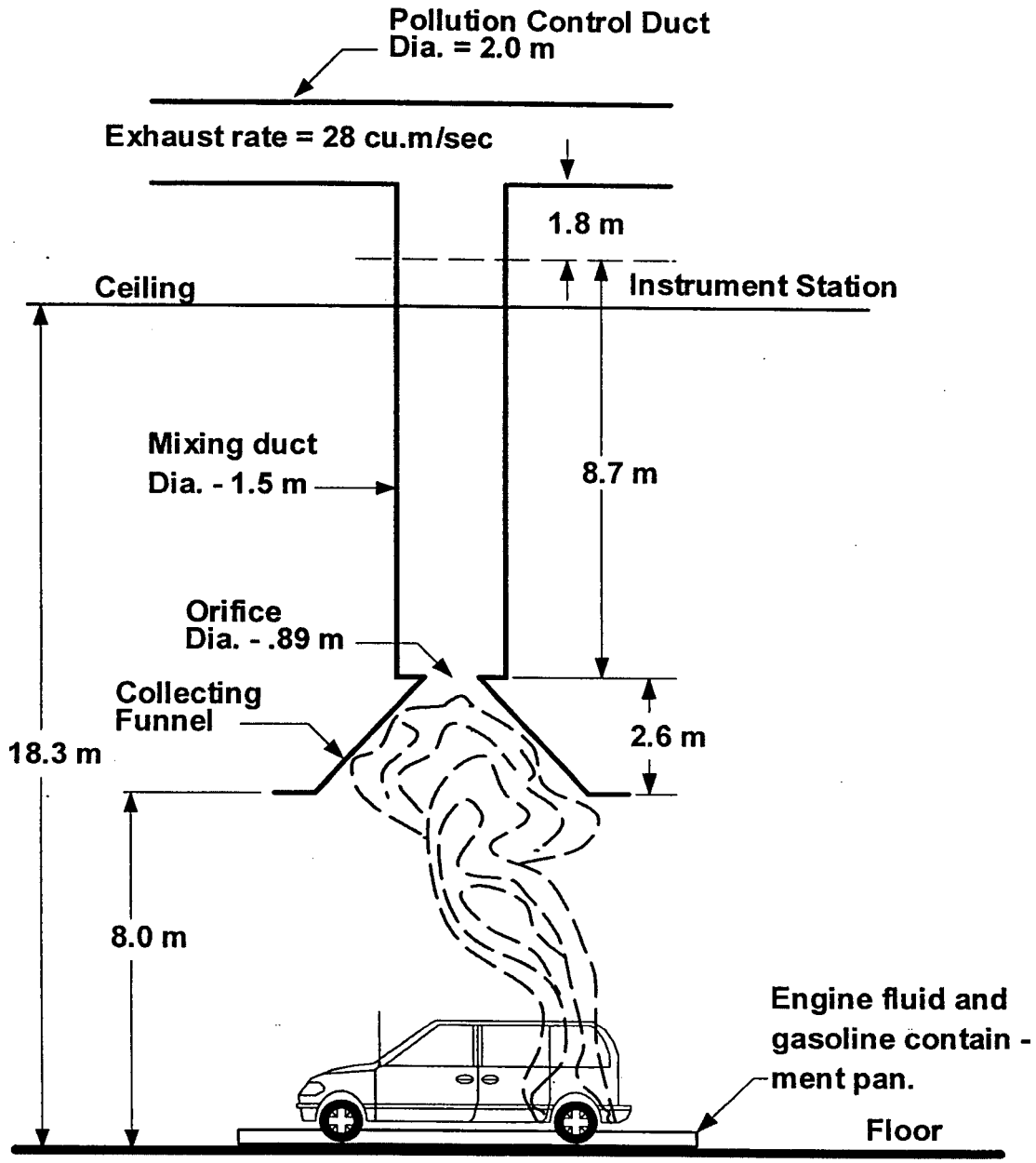


Figure H1. Fire Test F961116. Diagram of the test vehicle under the fire products collector at the Factory Mutual Test Center.

The FPC consisted of a collection funnel (diameter = 6.1 m), an orifice plate (hole = 0.9 m), and a vertical stainless steel sampling duct (diameter = 1.5 m). The sampling duct was connected to the air pollution control system of the Test Center. The blower of the air pollution control system

induces gas flow through the sampling duct. Air enters the sampling duct via the orifice plate. The temperature, linear velocity, optical transmission, and chemical composition of the entrained gas were measured in the center of the sampling duct 8.66 m (5.7 duct diameters) downstream from the orifice plate, ensuring a flat velocity profile at the sampling location. The data acquisition system consisted of a Hewlett Packard 2313B analog-to-digital conversion sub-system interfaced to a Hewlett Packard 1000 computer.

Gas temperature in the sampling duct was measured with two Type-K thermocouples (30 gage) with exposed bead-type junctions. The thermocouple leads were housed in stainless steel tubes (o.d. = 6.4 mm). Ambient air temperature in the facility was measured by five Type-K thermocouples attached to the external surface of the duct at 2.44, 5.49, 9.14, 12.8, and 15.9 m above the floor. These thermocouples were shielded from radiation from the fire.

The linear velocity of the gas entrained in the sampling duct was measured with a Pitot ring consisting of four Pitot tubes. A static pressure tap was mounted on the inside wall of the sampling duct. The pressure difference between the Pitot ring and the static wall tap was measured with an electronic manometer (Barocel Model 1173, CGS Scientific Corporation).

The particulate concentration in the entrained air was determined from the optical transmission across the duct measured at 0.4579 μm (blue), 0.6328 μm (red), and 1.06 μm (infrared). The optical path length across the duct was 1.524 m. Gas was withdrawn from the sampling duct through a stainless steel tube (o.d. = 3.9 mm) at a flow rate of $0.17 \times 10^{-3}$ $m^3/s$ for chemical analysis. The gas flowed through a particulate filter, a water condenser, and a drying agent before entering the analyzers. Carbon dioxide ($CO_2$) and carbon monoxide (CO) were measured with two dedicated non-disperse infrared analyzers (Beckman Model 864 Infrared Analyzers). Oxygen ($O_2$) was measured with a paramagnetic oxygen analyzer (Beckman Model 755 Paramagnetic Oxygen Analyzer). Total gaseous hydrocarbons were measured with a flame ionization analyzer (Beckman Model 400 Flame Ionization Analyzer).

The rate of product release was calculated using the following relationship:

$$\left(\frac{dR_j}{dt}\right) = f_j\left(\frac{dV}{dt}\right)\rho_j = f_j\left(\frac{dW}{dt}\right)\left(\frac{\rho_j}{\rho_g}\right) \qquad \text{(H1)}$$

where $d(R_j)/dt$ is the mass release rate of product j in kg/s; $f_j$ is the volume fraction of product j; dV/dt is the total volume flow rate of the gas entrained in the sampling duct in $m^3/s$; dW/dt is the

total mass flow rate of the gas entrained in the sampling duct in kg/s; $\rho_j$ is the density of product j in g/m$^3$; and $\rho_g$ is the density of the gas entrained in the concentration measurements. The rate of oxygen consumption was calculated using equation (A1), where the volume fraction of oxygen consumed was substituted for $f_j$.

The volume fraction of smoke particulate was calculated from the following relationship:

$$f_s = \frac{D\lambda \times 10^{-6}}{\Omega} \qquad \text{(H2)}$$

where $f_s$ is the volume fraction of smoke, $\lambda$ is the wavelength of the light source, $\Omega$ is the extinction coefficient of particulate (a value of 0.7 was used in these calculations), and D is the optical density at each of the three wavelengths at which measurements were made:

$$D = \frac{\ln\left(I_0 / I\right)}{L} \qquad \text{(H3)}$$

where $I_0$ is the intensity of light transmitted through clean air, I is the intensity of light transmitted through air containing smoke particulate, and L is the optical pathlength, which was equal to 1.524 m. A value of $1.1 \times 10^6$ g/m$^3$ was used for the density of smoke particulate ($\rho_j$) in equation (G1).

The convective heat release rate was calculated using the following relationship:

$$\left(\frac{dE_{conv}}{dt}\right) = \left(\frac{dW}{dt}\right) \times c_p \times \left(T_g - T_a\right) \qquad \text{(H4)}$$

where $d(E_{conv})/dt$ is the convective heat release rate in kW; dW/dt is the mass flow rate of the gas entrained in the sampling duct in kg/s; $c_p$ is the heat capacity of the gas entrained in the sampling duct at the gas temperature in kJ/(kg×K); $T_g$ is the temperature of the gas entrained in the sampling duct in K; and $T_a$ is the ambient air temperature in K.

The chemical heat release rate was calculated from the release rates of carbon dioxide and carbon monoxide as follows:

$$\left(\frac{dE_{ch}}{dt}\right) = \Delta H^{*}_{CO_2} \times \left(\frac{dR_{CO_2}}{dt}\right) + \Delta H^{*}_{CO} \times \left(\frac{dR_{CO}}{dt}\right) \qquad \text{(H5)}$$

where $d(E_{ch})/dt$ is the chemical heat release rate in kW; $\Delta H^*$ is the net heat of complete combustion per unit mass of carbon dioxide or carbon monoxide released in the fire in kJ/g; and dR/dt is the mass release rate of carbon dioxide or carbon monoxide in kg/s. Values of $\Delta H^*$ for carbon dioxide and carbon monoxide were obtained from the literature [H1 and H2].

The chemical heat release rate also was calculated from the oxygen consumption rate as follows:

$$\left(\frac{dE_{ch}}{dt}\right) = \Delta H^{*}_{O}\left(\frac{dC_O}{dt}\right) \qquad \text{(H6)}$$

where $d(E_{ch})/dt$ is the chemical heat release rate in kW; $\Delta H^*_O$ is the net heat of complete combustion per unit mass of $O_2$ consumed in kJ/g; and $d(C_O)/dt$ is the consumption rate of oxygen in kg/s. The value for $\Delta H^*_O$ was obtained from the literature [G1 and G2].

The radiative heat release rate was the difference between the chemical heat release rate and the convective heat release rate:

$$\left(\frac{dE_{rad}}{dt}\right) = \left(\frac{dE_{ch}}{dt}\right) - \left(\frac{dE_{conv}}{dt}\right) \qquad \text{(H7)}$$

where $d(E_{rad})/dt$ is the radiative heat release rate; and $d(E_{ch})/dt$ is the average chemical heat release rate calculated using equations (H5) and (H6).

Data from the fire-products collector are shown in Plots H1 through H5. The Fire Products Collector did not detect a fire plume until 10 seconds after ignition. The chemical, convective, and radiative heat release rates increased uniformly from approximately 10 seconds after ignition until the fire was extinguished (Plots H1 through H3, respectively). The maximum chemical heat rate measured during the test was approximately 1500 kW (Plot H1). The carbon monoxide and carbon dioxide release rates also increased uniformly from the time of ignition until the fire was extinguished. The maximum carbon dioxide and carbon monoxide release rates were 0.11 and 0.0.0013 kg/s, respectively (Plots H4 and H5, respectively).

## REFERENCES


H1. G. Heskestad. A Fire Products Collector for Calorimetry into the MW Range, Technical Report J.I. OC2E1.RA. Factory Mutual Research Corporation, Norwood, MA. June, 1981.

H2. Archibald Tewarson. "Generation of Heat and Chemical Compounds in Fires" Section 3/Chapter 4, SFPE Handbook of Fire Protection Engineering, 2nd Edition, 1995, pp. 3:53-124.

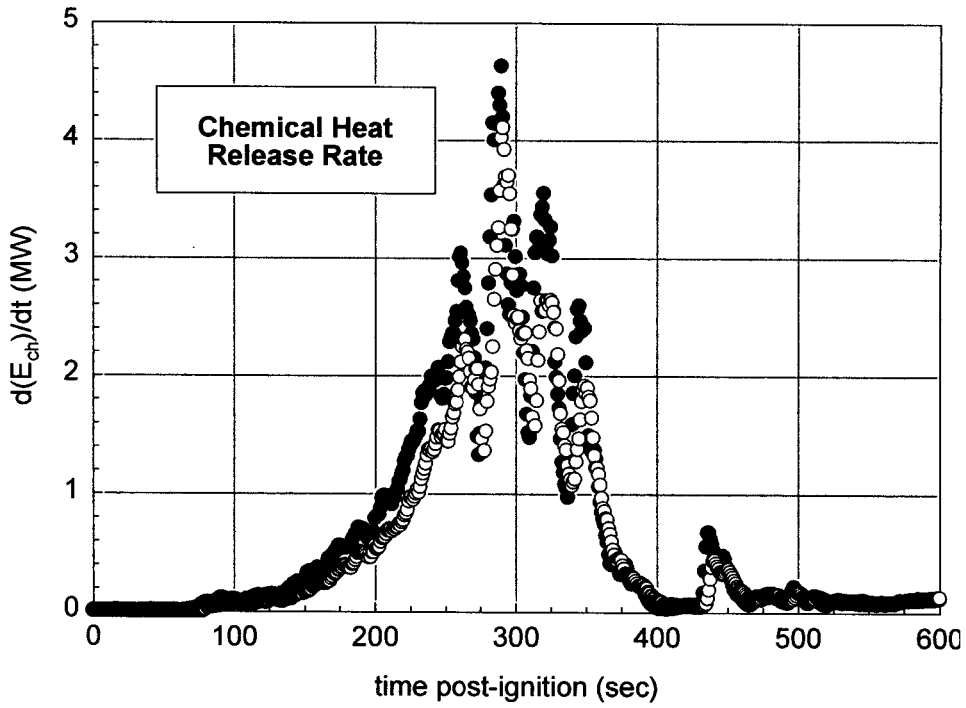


Plot H1. Fire Test F961116. Chemical heat release rate measured using the Fire Products Collector (● calculated from $CO_2$ release rate; ○ calculated from $O_2$ consumption rate).

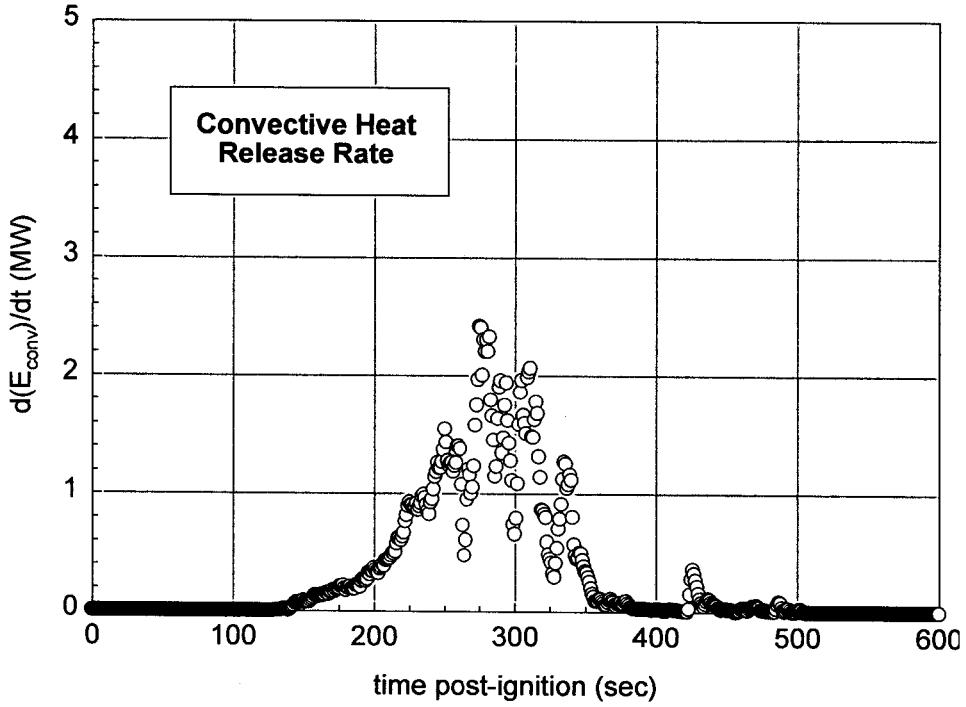


Plot H2. Fire Test F961116. Convective heat release rate measured using the Fire Products Collector

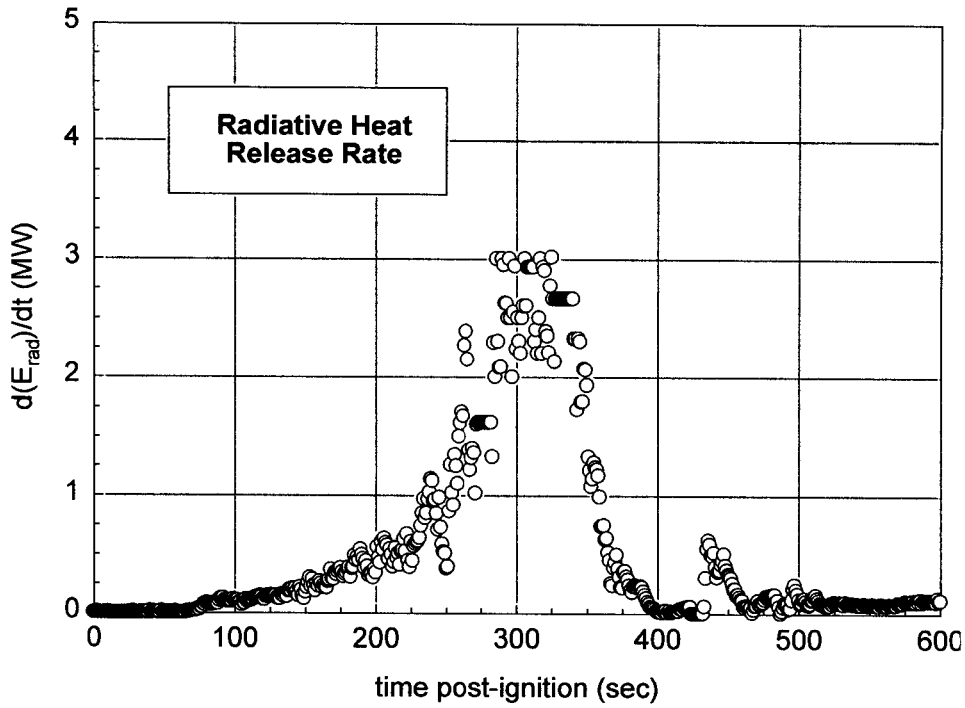


Plot H3. Fire Test F961116. Radiative heat release rate measured using the Fire Products Collector.

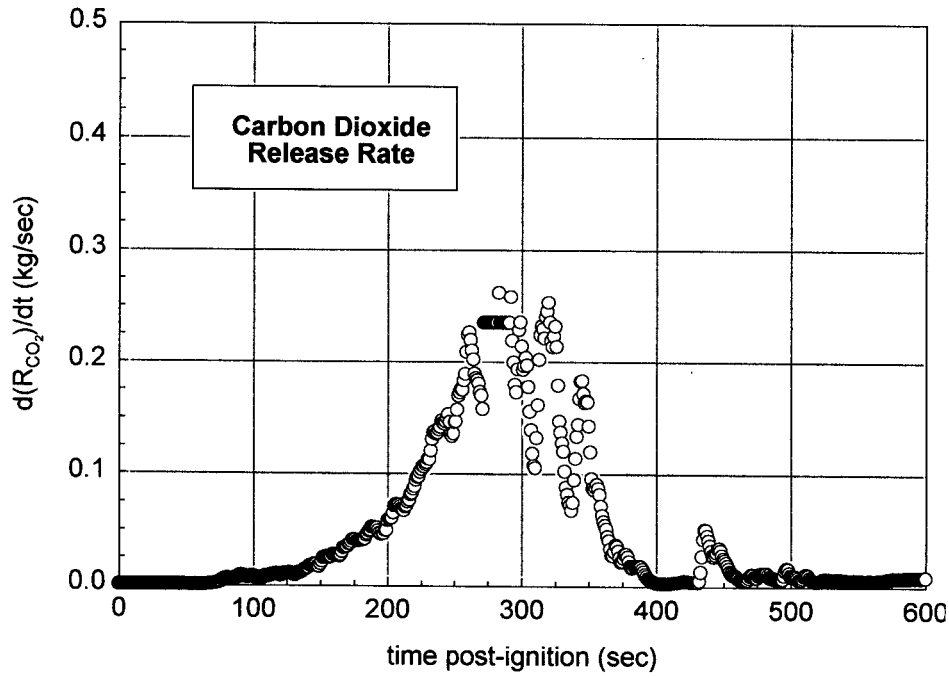


Plot H4. Fire Test F961116. Carbon dioxide release rate measured using the Fire Products Collector

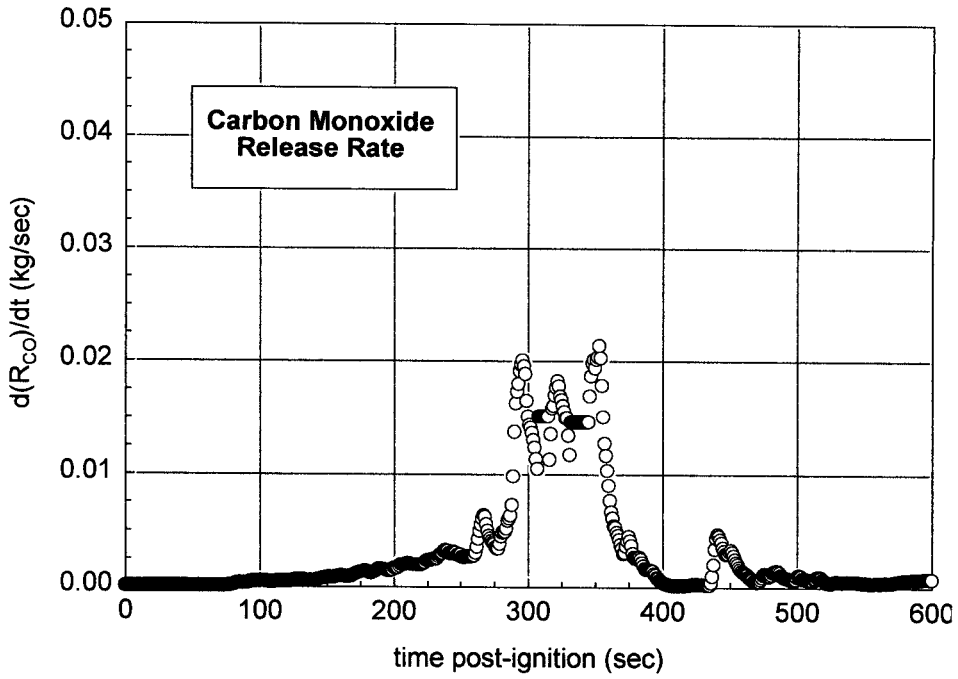


Plot H5. Fire Test F961116. Carbon monoxide release rate measured using the Fire Products Collector.

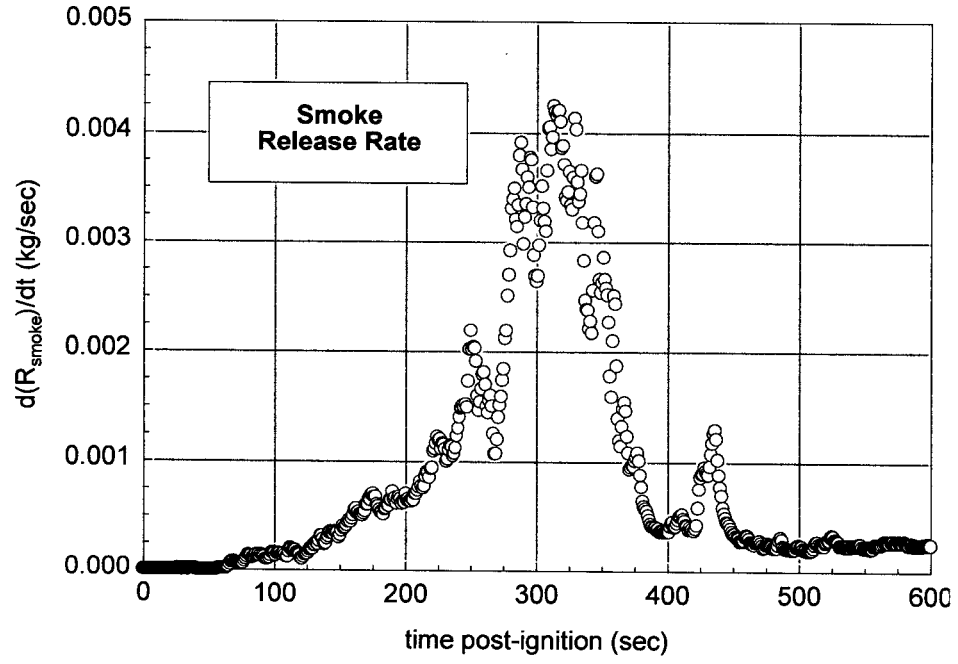


Plot H6. Fire Test F961116. Smoke release rate measured using the Fire Products Collector.

# APPENDIX I
# PASSENGER COMPARTMENT COMBUSTION GAS DATA
# FOURIER TRANSFORM INFRARED SPECTROSCOPY

Gas was withdrawn from the passenger compartment for FTIR analysis through a sampling port installed in the roof of the test vehicle. The sampling port was a stainless-steel tube (o.d. = 0.250 in., i.d. = 0.125 in., l = 20 ft) inserted through the roof along the longitudinal midline of the vehicle between the front seats. The inlet of the stainless-steel tube was approximately 25 cm below the headliner (Fig.'s I1 and I2). The tube was not heated. The outlet of the stainless-steel tube was connected to a heated Teflon® transfer-line (o.d. = 0.250 in., i.d. = 0.125 in., l = 75 ft.), which was connected to the gas cell of the FTIR spectrometer and to a sampling manifold containing five sorbent cartridges. The transfer-line was heated to 125°C during the test to prevent condensation of water and water-soluble gases (*e.g.*, HCl, HCN, NO, and $NO_2$). An in-line stainless-steel filter holder containing a quartz fiber filter (o.d. = 47 mm) was placed between the sample-tube and the transfer-line to prevent smoke particles from contaminating analytical instruments.

The FTIR spectrometer was an Model I-1000 Series FTIR Spectrometer (MIDAC Corporation, Riverside, California), with a KBr beam-splitter; a liquid nitrogen-cooled Mercury-Cadmium-Telluride detector; and gold-surfaced aluminum optics. This instrument was fitted with a stainless steel, multiple-reflectance gas cell (path length = 10 m) with zinc selenide windows. The gas cell was heated to 125°C. The optical bench was filled with clean, dry argon and hermetically sealed. The usable spectral range of this instrument was approximately 7400-700 $cm^{-1}$. Pressure in the gas cell during the fire tests was measured with a Baratron pressure gauge (MKS Instruments, Burlington, MA). The spectrometer was operated at a spectral resolution of 0.5 $cm^{-1}$.

The sampling line and gas cell were equilibrated at 125°C for at least 60 minutes before sample acquisition. A reference spectrum was acquired while the gas cell was evacuated. During the fire tests, the gas cell was purged continuously with air withdrawn from the passenger compartment at a flow rate of 7 L/min. Single-scan absorbance spectra were acquired and stored to disk at intervals of 7 second. The stored spectra were analyzed after the test using the quantitative analysis software provided by the instrument manufacturer (AutoQuant, MIDAC). This software used a Classical Least Squares algorithm to determine gas concentrations. The method developed for analysis of combustion gases was calibrated with gas standards (Scott Specialty Gases, Inc., Troy, MI). The standards were either NIST-traceable or produced by a gravimetric blending process.

The gaseous combustion products measured in the passenger compartment during this test included carbon dioxide, carbon monoxide, methane, ethylene, acetylene, hydrogen cyanide, nitric oxide, and hydrogen chloride (Plots I1 through I8). Except for carbon dioxide, which has a background concentration in air of approximately 0.05 %, the concentrations of all of these gases

were less than their respective lower limits of detection from the start of the test. Carbon dioxide, carbon monoxide, and the light hydrocarbons started to accumulate in the passenger compartment between 60 and 70 seconds post-ignition (Plots I1 through I5). Nitric oxide started to accumulate in the passenger compartment between 100 and 120 seconds post-ignition (Plot I7). Hydrogen cyanide started to accumulate in the passenger compartment between 180 and 200 seconds post-ignition (Plot I6). Hydrogen chloride (HCl) was detected in the air sampled from the passenger compartment starting at approximately 460 seconds post-ignition. The concentration of hydrogen chloride reached its maximum concentration at approximately 600 seconds post-ignition.

The Infrared spectra also contained a broad absorbance band between 2800 and 3200 $cm^{-1}$, indicating the presence of a mixture of unsaturated aliphatic hydrocarbons in the air samples from the passenger compartment. The intensity of this absorbance band generally followed the same time-course as that of methane (Plot I3). This broad band appeared to contain absorbances from ethane, propane, and butane. However, all of the gaseous species contributing to this absorbance band could not be identified or accurately quantified.

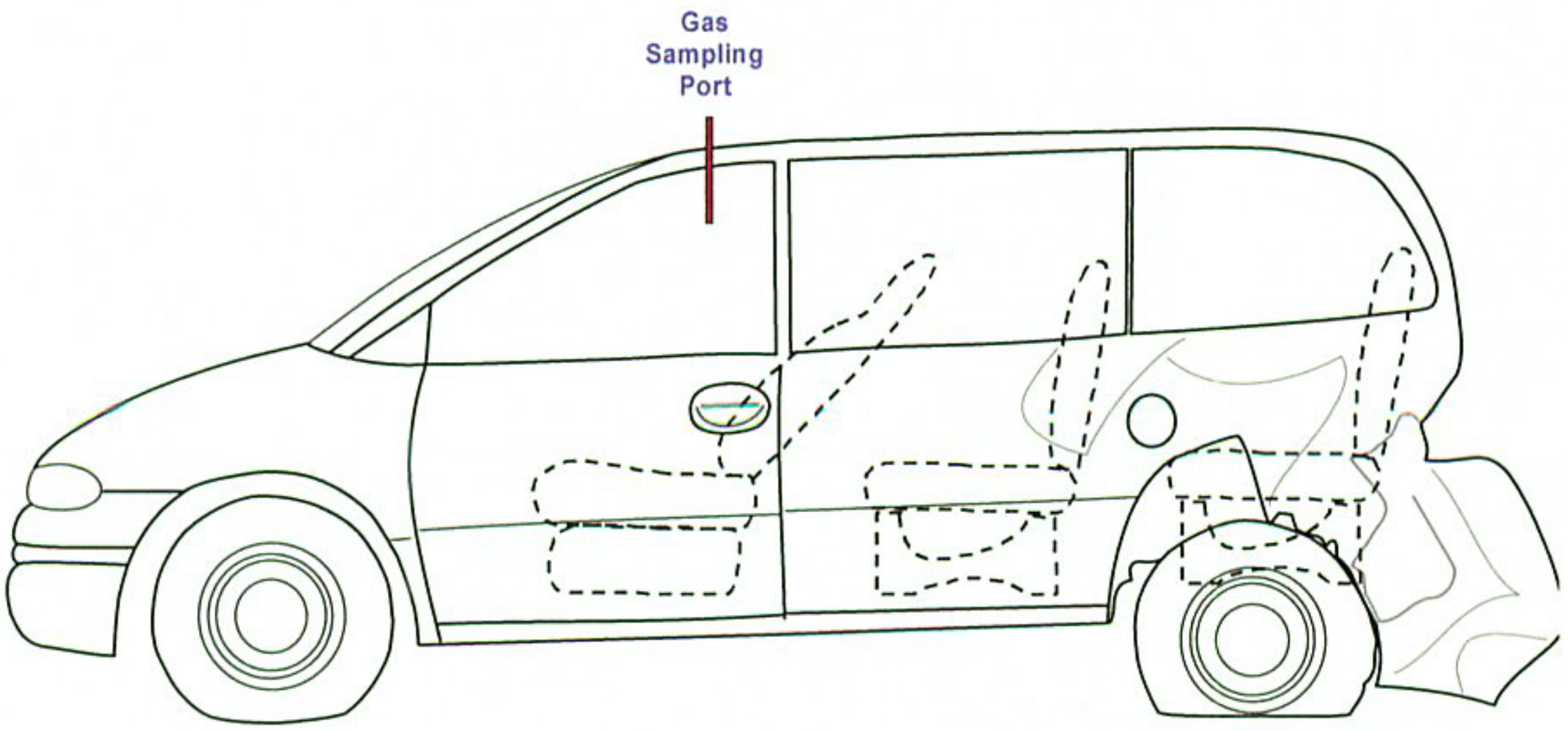


Figure I1. Fire Test F961116. Side view of the test vehicle show the approximate location of the gas sampling port in the passenger compartment.

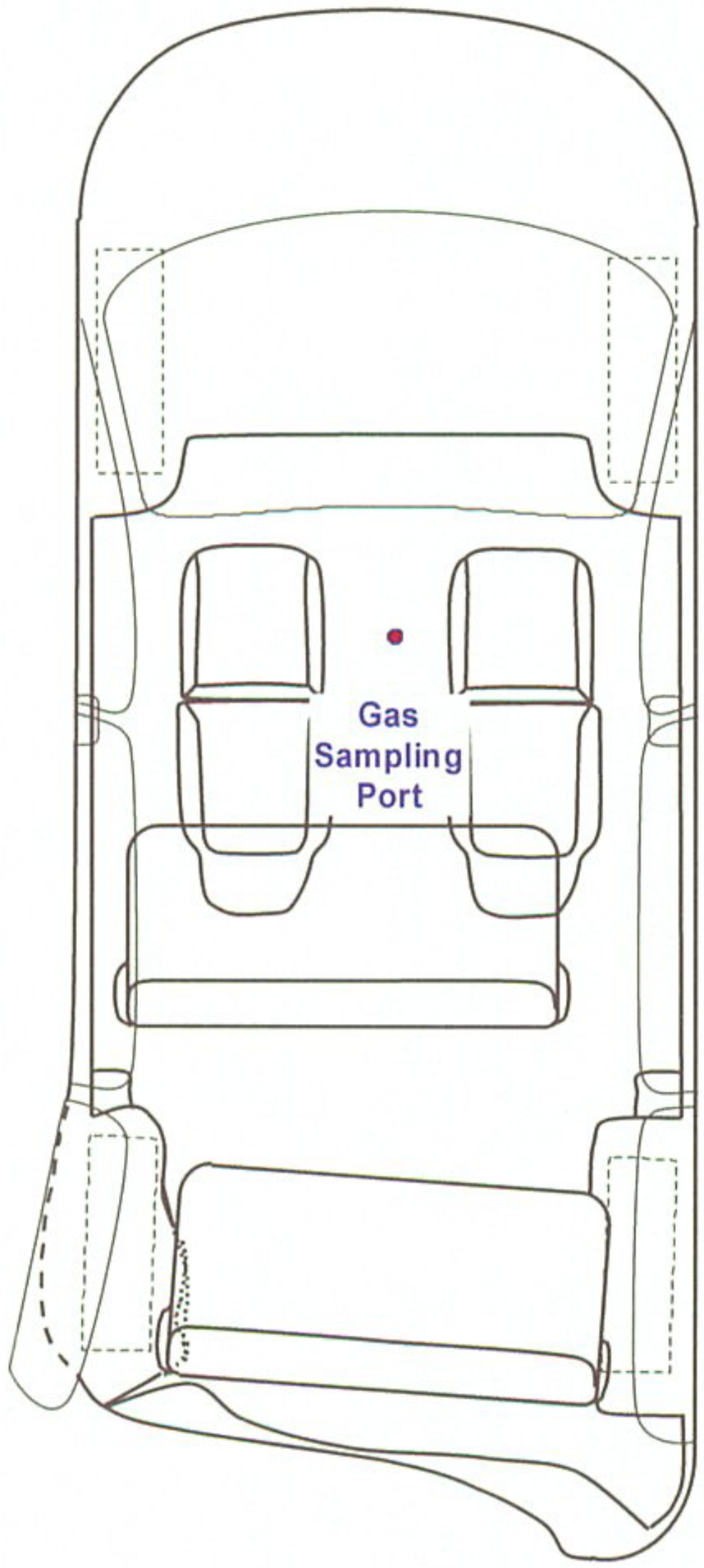


Figure I2. Fire Test F961116. Top view of the test vehicle showing the approximate location of the gas sampling port in the passenger compartment.

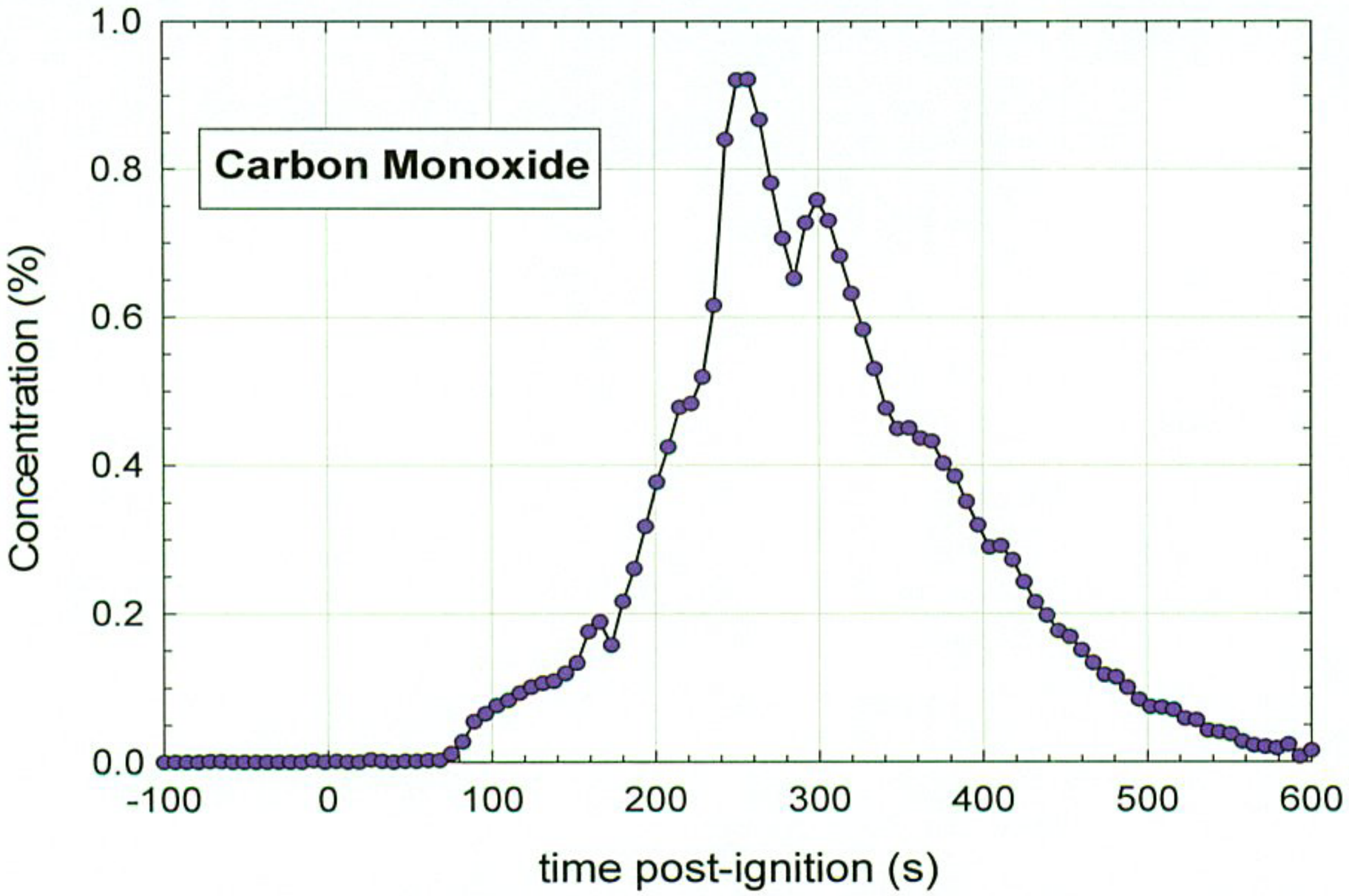


Plot I1. Fire Test F961116. Concentration of carbon monoxide (CO) in the passenger compartment measured by FTIR analysis.

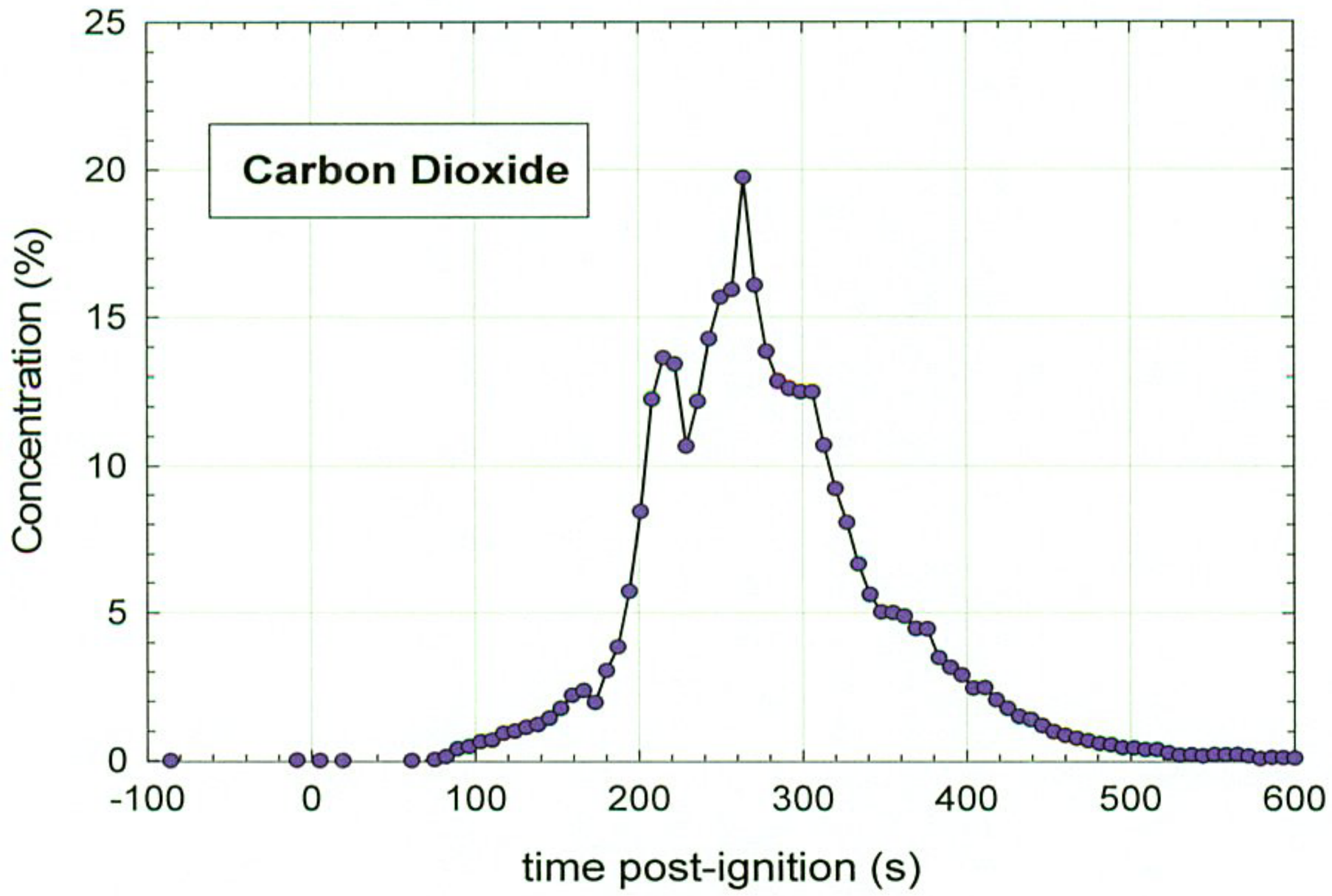


Plot I2. Fire Test F961116. Concentration of carbon dioxide ($CO_2$) in the passenger compartment measured by FTIR analysis.

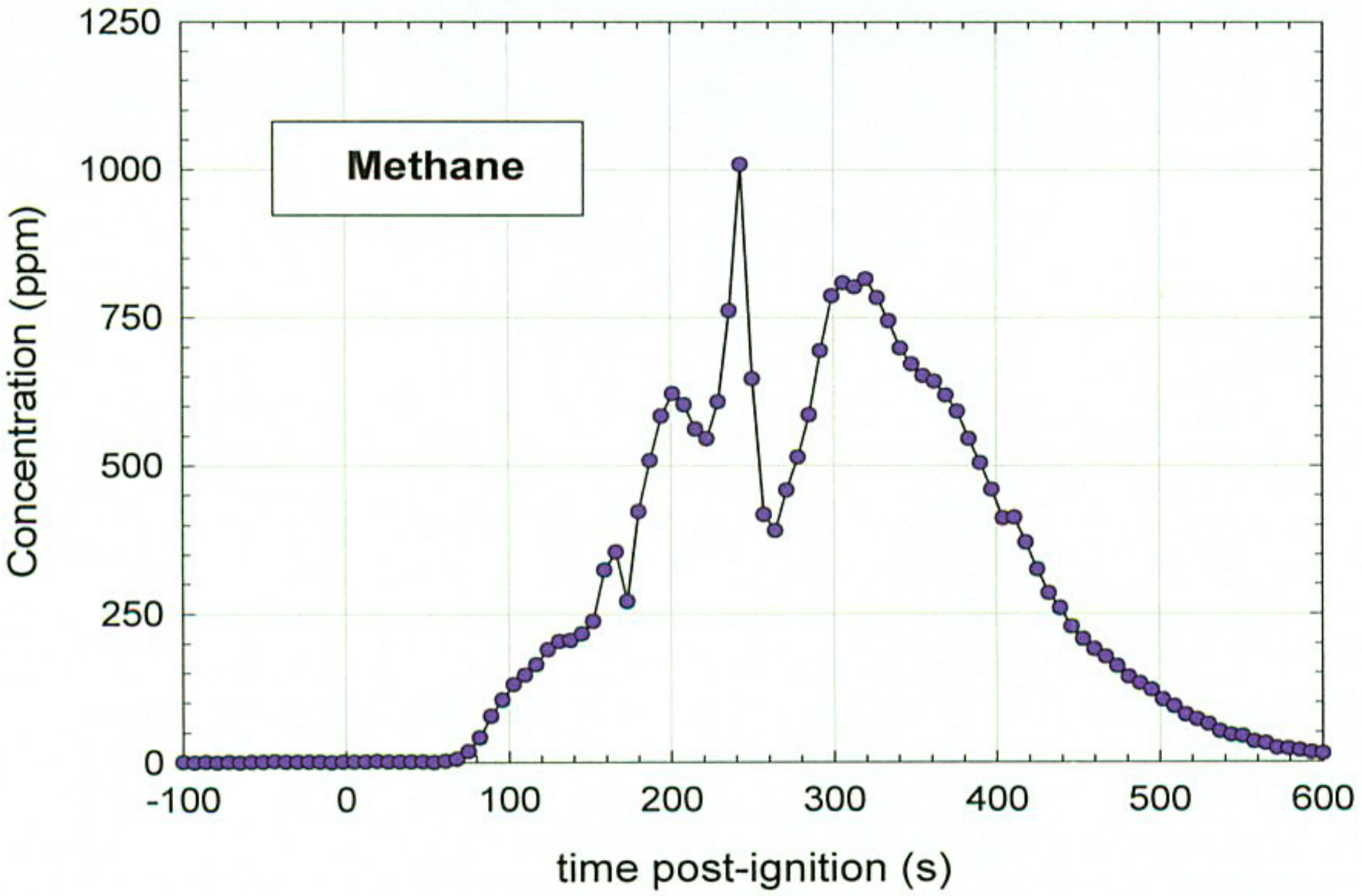


Plot I3. Fire Test F961116. Concentration of methane ($CH_4$) in the passenger compartment measured by FTIR analysis.

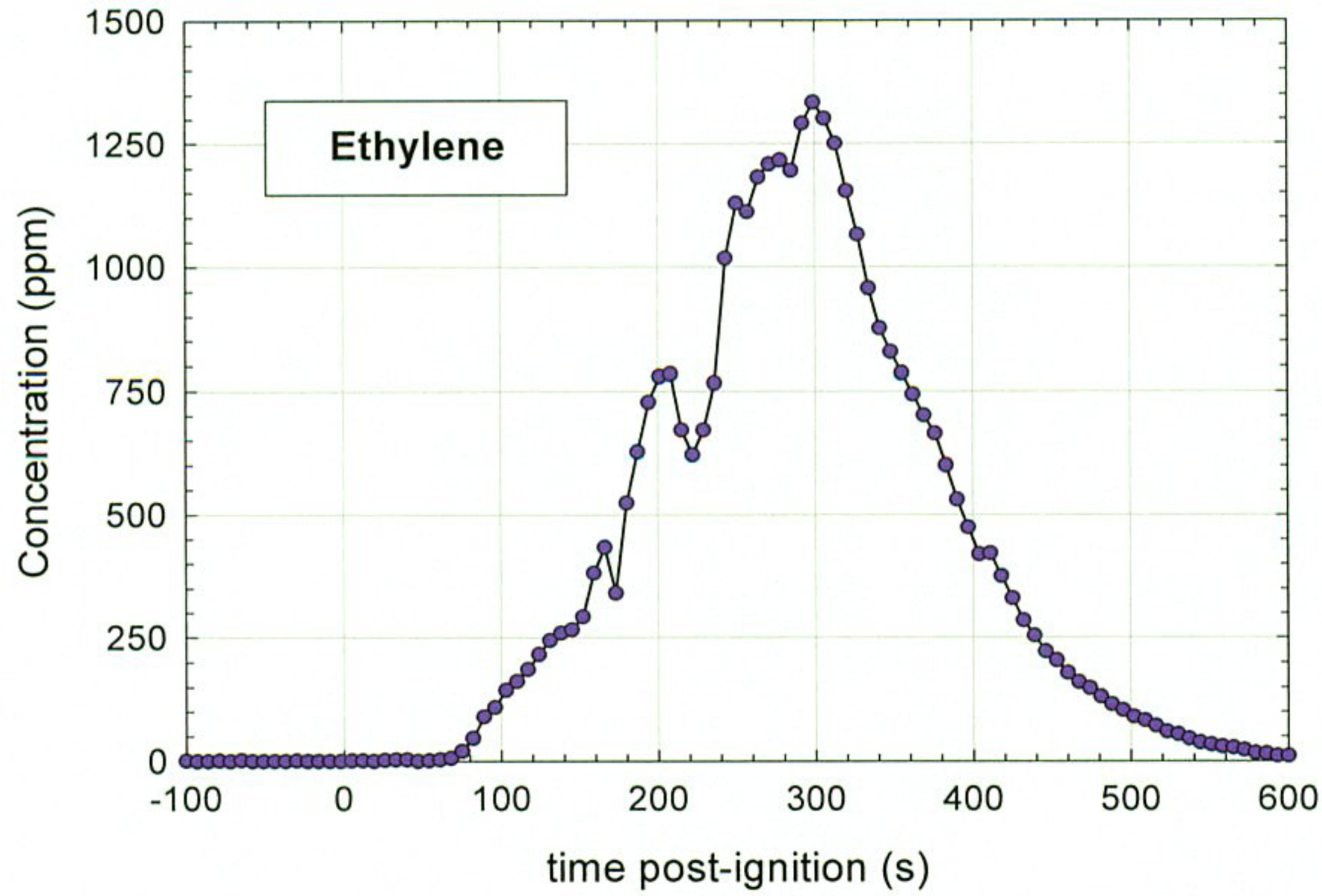


Plot I4. Fire Test F961116. Concentration of ethylene ($C_2H_4$) in the passenger compartment measured by FTIR analysis.

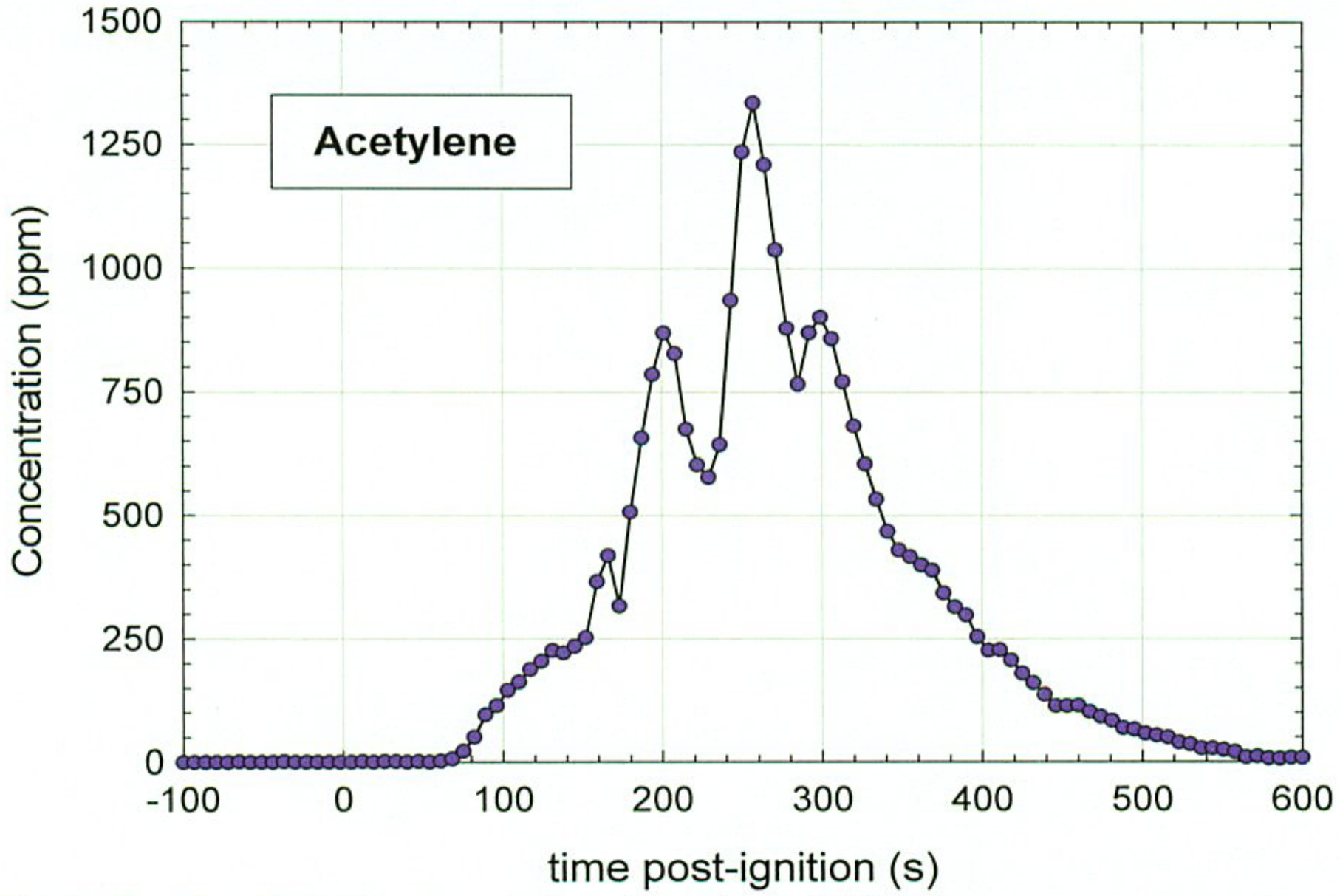


Plot I5. Fire Test F961116. Concentration of acetylene ($C_2H_2$) in the passenger compartment measured by FTIR analysis.

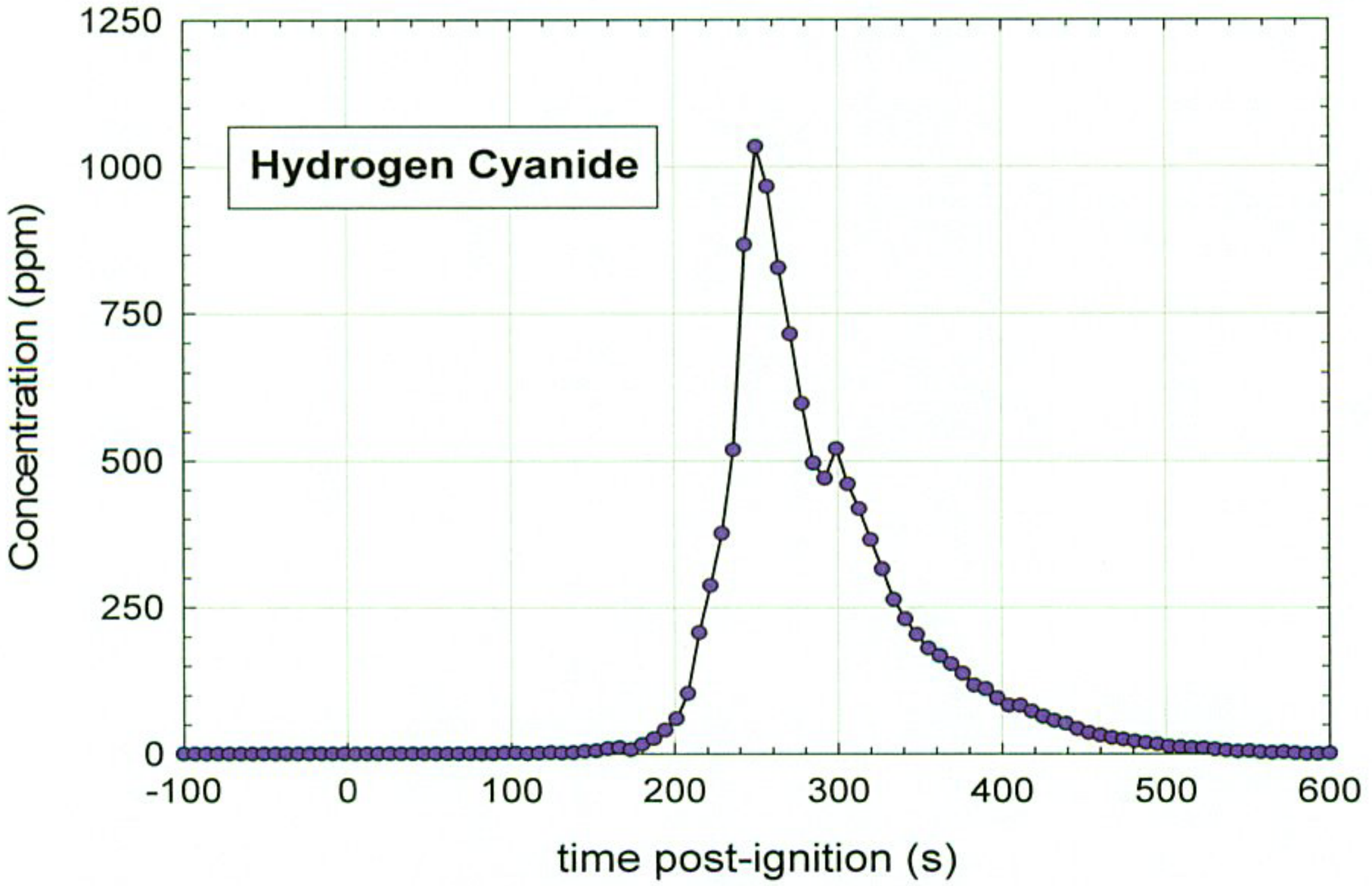


Plot I6. Fire Test F961116. Concentration of hydrogen cyanide (HCN) in the passenger compartment measured by FTIR analysis.

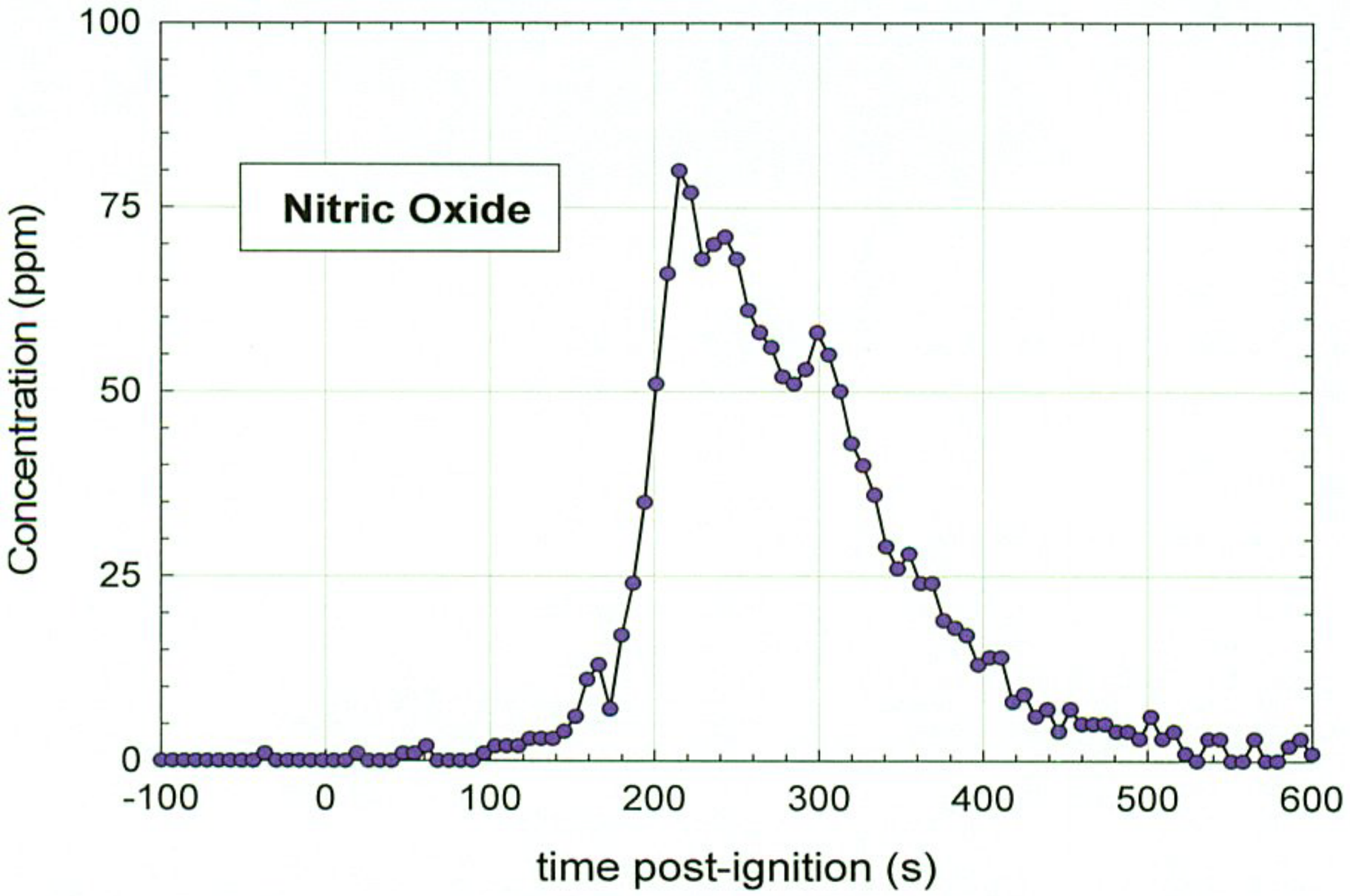


Plot I7. Fire Test F961116. Concentration of nitric oxide (NO) in the passenger compartment measured by FTIR analysis.

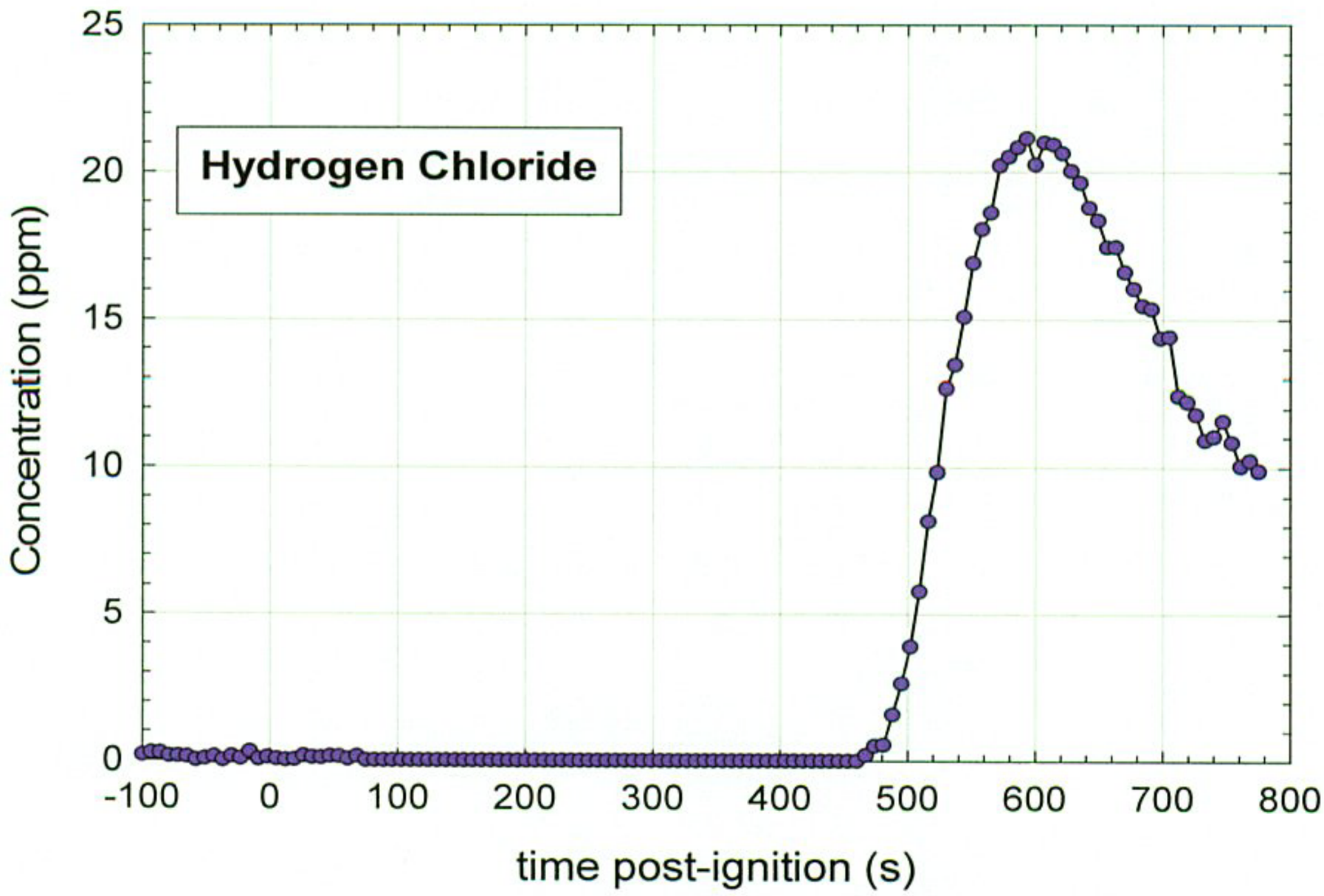


Plot I8. Fire Test F961116. Concentration of hydrogen chloride (HCl) in the passenger compartment measured by FTIR analysis.

# APPENDIX J
# PASSENGER COMPARTMENT COMBUSTION GAS DATA
# GAS CHROMATOGRAPHY/MASS SPECTROSCOPY

A manifold containing five sorbent cartridges in parallel was attached to the gas sampling line used for FTIR analysis (APPENDIX H). The cartridges were glass-lined stainless steel tubes (i.d. = 4 mm; length = 10 cm; Scientific Instrument Services, Inc, Ringoes, NJ) packed with 25 mg of Carbotrap™ C Graphitized Carbon Black (Supelco, Inc.; Bellefonte, PA) in series with 15 mg of Carbotrap™ Graphitized Carbon Black (Supelco). Airflow was directed sequentially through the sorbent cartridges by a solenoid-actuated gas-switching manifold. The sampling rate was 25 mL/min.

The sorbent cartridges were analyzed by thermal desorption/gas chromatography/mass spectrometry. Deuterated standards dissolved in deuterated methanol were added to each sorbent cartridge to monitor sample recovery. The thermal desorption analyzer was a Model TD-2 Short Path Thermal Desorption Analyzer and a Model 961 Cryo-Trap (Scientific Instrument Services). The gas chromatograph was a Model 5890A Gas Chromatograph (Hewlet Packard, Palo Alto, CA). The mass spectrometer was a Packard Model 5971 Mass Selective Detector (Hewlett Packard). The thermal desorption unit was interfaced directly to the split/splitless injector of the gas chromatograph. The injector was operated in the splitless mode with a purge flow of approximately 5 mL/min. The trapping blank was a section of deactivated fused silica capillary tubing (15 cm x 0.53 mm) attached to the head of the chromatographic column. The chromatographic column was a fused silica capillary column coated with 100% methyl silicon (HP-1 ; length = 30 m; i.d. = 0.25 mm; film thickness = 0.25 μm).

The sample was desorbed at 300°C for 10 min, and cryofocused onto the trapping blank at -80°C. The temperature of the analytical column was maintained at 0°C while the sample was desorbed. At the end of the desorption period, the temperature of the trapping blank was programmed to 300°C at a rate of approximately 15°C/sec. The column temperature was programmed from 0 to 250°C at a rate of 2.5°C/min. Mass spectra were obtained by scanning from m/z 40 to m/z 600 at a rate of 1.2 scan/s. Individual components in the gas samples were identified by performing a search of a commercial mass spectral library (Wiley 275K Mass Spectral Library). When the quality of the match to the library spectra was low, components were identified by interpretation of the mass spectra.

The mass chromatograms from GC/MS analysis of gas samples taken from the passenger compartment before (blank) and during this test are shown in Plots J1 through J6. Tables J1 through J6 contain peak identifications for these analyses. A mixture of deuterated compounds was added to each sample before analysis to monitor sample recovery and act as a retention time marker for the GC analysis.

Samples 1 and 2 (Plots J2 and Table J2, and Plot J3 and Table J3, respectively) were acquired between –30 to +173 seconds post-ignition, the period of time before flames had spread to objects in the passenger compartment. In addition to the deuterated compounds, these samples contained small amounts of a number of aliphatic and aromatic hydrocarbons not present in the blank. These hydrocarbons could be attributed to gasoline vapor.

Sample 3 (Plot J4 and Table J4) was acquired during the period of time when the second bench seat cushion, the left quarter trim panel, and the headliner ignited and were burning (between +174 to +218 seconds post-ignition). The compounds present in these samples were not appreciably different than those present in the blank.

Samples 4 and 5 (Plot J5 and Table J5, and Plot J6 and Table J6, respectively) were acquired between +219 and +326 seconds post-ignition, after fire suppression began. The compounds present in these samples were not appreciably different than those present in the blank.

The blank and Samples 1 through 5 contained peaks corresponding to a number of common polymer additives. These included: phthalate esters, *bis*(1,3-dimethylbutyl) hexanedioate, and dihexyl hexanedioate. Since these compounds were present in all samples including the blank, these compounds apparently were not present in the air sampled from the passenger compartment of the test vehicle during the test, but probably were the result of contamination of the GC/MS equipment.

The blank and Samples 1 through 5 also contained a number of cyclic dimethylsiloxanes and unidentified siloxanes. These compounds are common contaminants casued by cryo-focusing column-bleed during the sample-desorption stage of the analysis. Column-bleed is a term that describes the slow thermal decomposition of the stationary phase on the capillary gas chromatography column, which was a bonded dimethylsiloxane polymer. This process causes low-level contamination of the mobile phase with a homologous series of cyclic dimethylsiloxanes, such as hexamethyl cyclotrisiloxane, which can be seen in the mass chromatograms of the Blank and all five samples.

The deuterated internal standards produced the major peaks in each of these mass chromatograms. Even in Samples 1 and 2, which were the only two samples containing compounds attributed to gasoline vapor (compounds not present in the blank), the intensities of the peaks from these compounds were low. The concentrations of combustion gases in the passenger compartment, the sampling rate, and the acquisition interval are the variables that determined the amount of sample acquired in each sorbent tube. The sampling rate was

adjusted to approximately 25 ml/min before the start of the test. The acquisition times for each sample were determined by an operator, who was visually following flame-spread into the passenger compartment and using best-judgement when switching samples. The concentration of combustion gases in the passenger compartment generally is related to the rate of burning of interior components. Thus, the choice of sampling intervals and the concentrations of combustion gases in the passenger compartment during each interval are effected by the rate of flame spread into the passenger compartment. Fire Test F961116 was the first underbody gasoline pool fire conducted in this project. Without prior experience, it was difficult to predict the timing of flame-spread into the passenger compartment or the rate of accumulation of combustion gases in the passenger compartment for this test. The results of the GC/MS analysis of the samples acquired during this test indicate that a sampling rate of 25 mL/min is not sufficient to acquire an adequate amount of sample for GC/MS analysis during fire tests that last between 3 and 4 minutes.

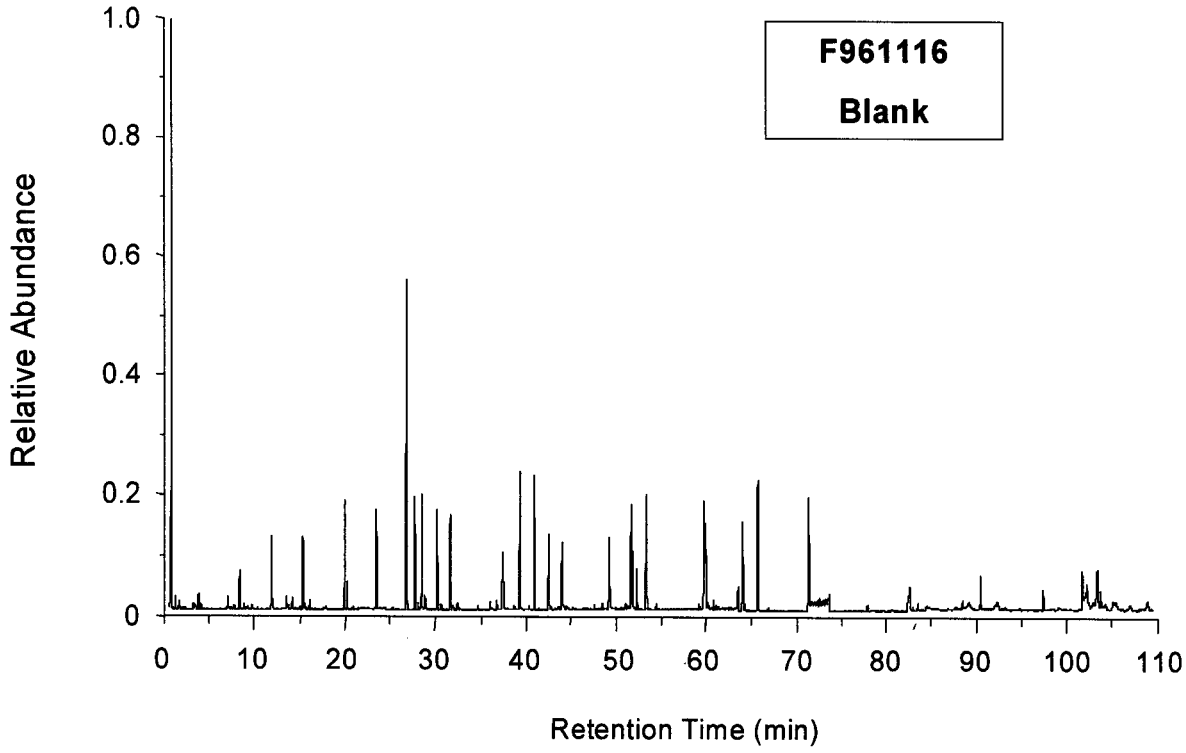


Plot J1. Fire Test F961116. Mass chromatogram from the GC/MS analysis of the blank, which was acquired before the test.

**Table J1**
**Peak Identification for Fire Test F961116 Blank**

| $t_R$ | Compound | CAS Number |
|---|---|---|
| 3.25 | carbon dioxide | 000124-38-9 |
| 6.12 | n-pentane-$d_{12}$ (IS) | 002031-90-5 |
| 10.36 | n-hexane-$d_{14}$ (IS) | 021666-38-6 |
| 13.64 | benzene-$d_6$ (IS) | 001076-43-3 |
| 13.77 | benzene | 000071-43-2 |
| 15.21 | hexane, 2-methyl | 000591-76-4 |
| 15.79 | hexane, 3-methyl | 000589-34-4 |
| 16.92 | n-heptane-$d_{16}$ (IS) | 033838-52-7 |
| 17.61 | n-heptane | 000142-82-5 |
| 21.24 | toluene-$d_8$ (IS) | 002037-26-5 |
| 21.51 | toluene | 000108-88-3 |
| 24.52 | n-octane-$d_{18}$ (IS) | 017252-77-6 |
| 27.71 | cyclotrisiloxane, hexamethyl | 000541-05-9 |
| 28.53 | benzene, ethyl-$d_{10}$ (IS) | 025837-05-2 |
| 29.25 | p-xylene-$d_{10}$ (IS) | 041051-88-1 |
| 29.56 | p-xylene | 000106-42-3 |
| 30.83 | o-xylene-$d_{10}$ (IS) | 056004-61-6 |
| 32.17 | n-nonane-$d_{20}$ (IS) | 121578-11-8 |
| 37.63 | phenol-$d_5$ (IS) | 004165-62-2 |
| 39.43 | n-decane-$d_{22}$ (IS) | 016416-29-8 |
| 40.91 | cyclotetrasiloxane, octamethyl | 000556-67-2 |
| 42.42 | p-cresol-$d_8$ (IS) | |
| 43.80 | o-cresol-$d_8$ (IS) | |
| 48.76 | 2,4-dimethyl phenol-$d_3$ (IS) | |
| 51.02 | naphthalene-$d_8$ (IS) | 001146-65-2 |
| 51.18 | naphthalene | 000091-20-3 |
| 51.60 | cyclohexasiloxane, dodecamethyl | 000541-02-6 |
| 52.60 | n-dodecane-$d_{26}$ (IS) | 121578-12-9 |
| 58.86 | n-tridecane-$d_{28}$ (IS) | 121578-12-9 |
| 58.70 | 1-methylnaphthlene-$d_{10}$ (IS) | 038072-94-5 |
| 62.11 | cyclohexasiloxane, dodecamethyl | 000540-97-6 |
| 62.59 | Biphenyl-$d_{10}$ (IS) | 001486-01-7 |
| 64.16 | n-tetradecane-$d_{30}$ (IS) | |

**Table J1, continued**
**Peak Identification for Fire Test F961116 Blank**

| $t_R$ | Compound | CAS Number |
|---|---|---|
| 69.42 | n-pentadecane-$d_{32}$ (IS) | 036340-20-2 |
| 80 to 94 | unidentified silicone polymers | n/a |
| 97.70 | hexanedioic acid, bis(1,3-dimethylbutyl) ester | 055125-22-9 |
| 98.18 | nonanedioic acid, bis(2-ethylhexyl)ester | 000103-24-2 |
| 99.28 | unidentified phthalate ester | n/a |

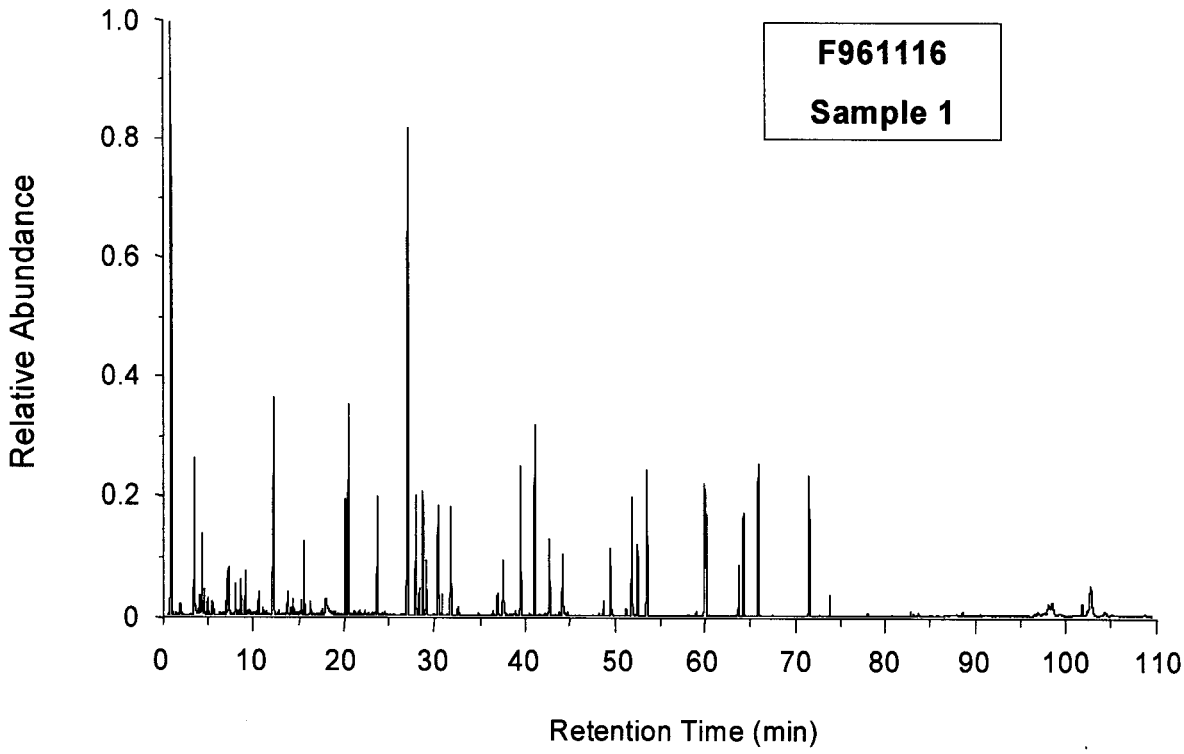


Plot J2. Fire Test F961116. Mass Chromatogram from the GC/MS analysis of Sample 1, which was acquired from -30 to +95 seconds post-ignition.

**Table J2**
**Peak Identification for Fire Test F961116 Sample 1**

| $t_R$ | Compound | CAS No. |
|---|---|---|
| 3.30 | carbon dioxide | 000057-13-6 |
| 3.77 | silane, difluorodimethyl- | 000353-66-2 |
| 4.27 | butane | 000106-97-8 |
| 5.71 | butane, 2-methyl- | 000078-78-4 |
| 6.26 | n-pentane-$d_{12}$ (IS) | 002031-90-5 |
| 6.46 | n-pentane | 000109-66-0 |
| 6.73 | 1-butene, 2-methyl- | 000563-46-2 |
| 7.16 | cyclopropane, 1,2-dimethyl- | 000930-18-7 |
| 7.57 | 1,3-cyclopendadiene | 000542-92-7 |
| 9.00 | butane, 2,3-dimethyl- | 000079-29-8 |
| 9.11 | propane, 2-methoxy, 2-methyl- | 001634-04-4 |
| 9.26 | pentane, 2-methyl- | 000107-83-5 |
| 9.97 | pentane, 3-methyl- | 000096-14-0 |
| 10.52 | n-hexane-$d_{14}$ (IS) | 21666-38-6 |
| 10.96 | n-hexane | 000110-54-3 |
| 12.37 | cyclopentane, methyl- | 000096-37-7 |
| 13.81 | benzene-$d_6$ (IS) | 001076-43-3 |
| 13.94 | benzene | 000071-43-2 |
| 13.35 | hexane, 2-methyl- | 000591-76-4 |
| 15.94 | hexane, 3-methyl- | 000589-34-4 |
| 16.80 | pentane, 2,2,4-trimethyl- | 000540-84-1 |
| 17.07 | n-heptane-$d_{16}$ (IS) | 33838-52-7 |
| 17.75 | n-hepatane | 000142-82-5 |
| 19.34 | unknown | |
| 21.39 | toluene-$d_{8\,1}$ | 002037-26-5 |
| 21.68 | toluene | 000108-88-3 |
| 24.66 | n-octane-$d_{18}$ (IS) | 017252-77-6 |
| 27.89 | cyclotrisiloxane, hexamethyl- | 000541-05-9 |
| 28.66 | benzene, ethyl-$d_{10}$ (IS) | 025837-05-2 |
| 29.03 | benzene, ethyl- | 00100-41-4 |
| 29.39 | p-xylene-$d_{10}$ (IS) | 041051-88-1 |
| 29.71 | p-xylene | 000106-42-3 |
| 29.85 | benzene, ethynyl- | 000536-74-3 |
| 30.97 | o-xylene-$d_{10}$ (IS) | 056004-61-6 |
| 31.04 | benzene-ethenyl- | 000100-42-5 |
| 31.39 | m-xylene | 00108-38-3 |
| 32.29 | n-Nonane-$d_{20}$ (IS) | 121578-11-8 |
| 37.74 | phenol-$d_5$ | 004165-62-2 |

**Table J2, continued**
**Peak Identification for Fire Test F961116 Sample 1**

| $t_R$ | Compound | CAS No. |
|---|---|---|
| 39.55 | n-Decane-$d_{22}$ (IS) | 016416-29-8 |
| 41.05 | Cyclotetrasiloxane, octamethyl- | 000556-67-2 |
| 42.53 | p-cresol-$d_8$ (IS) | 053774-23-5 |
| 53.91 | o-cresol-$d_8$ (IS) | |
| 48.88 | phenol-$d_3$, 2,4-dimethyl- | |
| 51.16 | Naphthalene-$d_8$ (IS) | 001146-65-2 |
| 51.73 | Cyclopentasiloxane, decamethyl- | 000541-02-6 |
| 52.73 | n-Dodecane-$d_{26}$ (IS) | 121578-12-9 |
| 58.69 | n-Tridecane-$d_{28}$ (IS) | 121578-12-9 |
| 58.84 | 1-Methylnaphthlene-$d_{10}$ (IS) | 038072-94-5 |
| 62.25 | Cyclohexasiloxane, docecamethyl- | 000540-97-6 |
| 62.72 | Biphenyl-$d_{10}$ (IS) | 001486-01-7 |
| 64.28 | n-Tetradecane-$d_{30}$ (IS) | |
| 69.54 | n-Pentadecane-$d_{32}$ (IS) | 036340-20-2 |
| 94.32 | unknown phthalate ester | |
| 94.75 | unknown phthalate ester | |
| 97.83 | hexanedoic acid, bis(1,3-dimethylbutyl)ester | 055125-22-99 |
| 98.67 | unknown phthalate ester | |

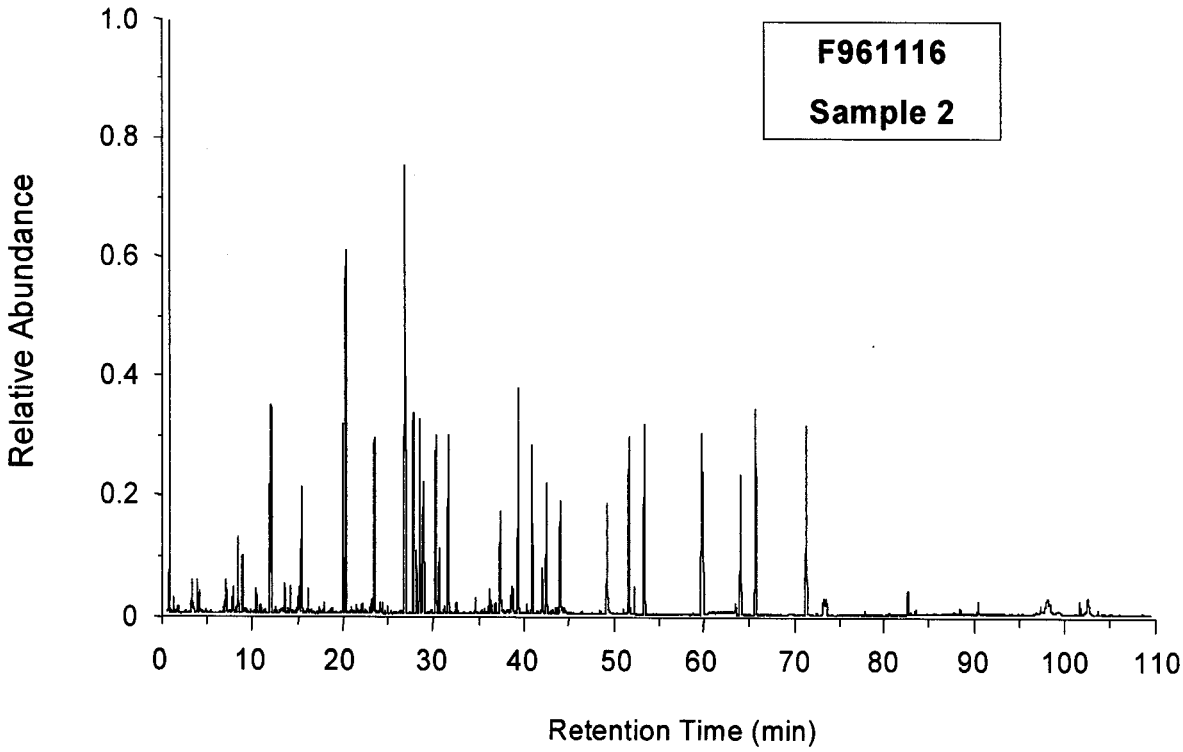


Plot J3. Fire Test F961116. Mass Chromatogram from the GC/MS analysis of Sample 2, which was acquired from +96 to +173 seconds post-ignition.

**Table J3**
**Peak Identification for Fire Test F961116 Sample 2**

| $t_R$ | Compound | CAS No. |
|---|---|---|
| 3.30 | carbon dioxide | 000057-13-6 |
| 5.59 | butane, 2-methyl | 000078-78-4 |
| 6.11 | n-bentane-$d_{12}$ (IS) | 002031-90-5 |
| 6.46 | n-pentane | 000109-66-0 |
| 9.13 | pentane, 2-methyl | 000107-83-5 |
| 9.83 | pentane, 3-methyl | 000096-14-0 |
| 10.38 | n-hexane-$d_{14}$ (IS) | 021666-38-6 |
| 10.82 | n-hexane | 000110-54-3 |
| 12.23 | cyclopentane, methyl | 000096-37-7 |
| 13.67 | benzene-$d_6$ (IS) | 001076-43-3 |
| 13.79 | benzene | 000071-43-2 |
| 15.21 | pentane, 2, 4-dimethyl | 000108-08-7 |
| 15.79 | hexane, 3-methyl | 000589-34-4 |
| 16.93 | n-heptane-$d_{16}$ (IS) | 033838-52-7 |
| 17.60 | n-hepatane | 000142-82-5 |
| 21.25 | toluene-$d_8$ (IS) | 002037-26-5 |
| 21.56 | toluene | 000108-88-3 |
| 24.52 | n-octane-$d_{18}$ (IS) | 017252-77-6 |
| 27.72 | cyclotrisiloxane, hexamethyl- | 000541-05-9 |
| 28.52 | benzene, ethyl-$d_{10}$ (IS) | 025837-05-2 |
| 28.87 | benzene, ethyl- | 000100-41-4 |
| 29.24 | p-xylene-$d_{10}$ (IS) | 041051-88-1 |
| 29.57 | p-xylene | 000106-42-3 |
| 29.70 | benzene, ethynyl- | 000536-74-3 |
| 30.84 | o-xylene-$d_{10}$ (IS) | 056004-61-6 |
| 30.92 | benzene, ethenyl- | 000100-42-5 |
| 31.24 | o-xylene | 000095-47-6 |
| 32.16 | n-nonane-$d_{20}$ (IS) | 121578-11-8 |
| 36.50 | benzene, 1-ethyl-3-methyl- | 000620-14-4 |
| 37.60 | phenol-$d_5$ | 004165-62-2 |
| 38.83 | trimethyl benzene | n/a |
| 39.42 | n-decane-$d_{22}$ (IS) | 016416-29-8 |
| 40.89 | Cyclotetrasiloxane, octamethyl- | 000556-67-2 |
| 41.92 | 1H-indene | 000095-13-6 |
| 42.38 | p-cresol-$d_8$ (IS) | |
| 43.78 | o-cresol-$d_8$ (IS) | |
| 48.73 | phenol-$d_3$, 2,4-dimethyl- | |

**Table J3, continued**
**Peak Identification for Fire Test F961116 Sample 2**

| $t_R$ | Compound | CAS No. |
|---|---|---|
| 51.01 | Naphthalene-$d_8$ (IS) | 001146-65-2 |
| 51.56 | Cyclopentasiloxane, decamethyl- | 000541-02-6 |
| 52.58 | n-Dodecane-$d_{26}$ (IS) | 121578-12-9 |
| 58.52 | n-Tridecane-$d_{28}$ (IS) | 121578-12-9 |
| 58.68 | 1-Methylnaphthlene-$d_{10}$ (IS) | 038072-94-5 |
| 62.55 | Biphenyl-$d_{10}$ (IS) | 001486-01-7 |
| 64.12 | n-Tetradecane-$d_{30}$ (IS) | |
| 69.38 | n-Pentadecane-$d_{32}$ (IS) | 036340-20-2 |
| 71.39 | unidentified siloxane | n/a |
| 79.89 | unidentified siloxane | n/a |
| 87.17 | unidentified siloxane | n/a |
| 94.34 | dioctyl phthalate | |
| 97.66 | hexanedioic acid, dihexyl ester | 000110-33-8 |
| 98.52 | unidentified phthalate ester | n/a |

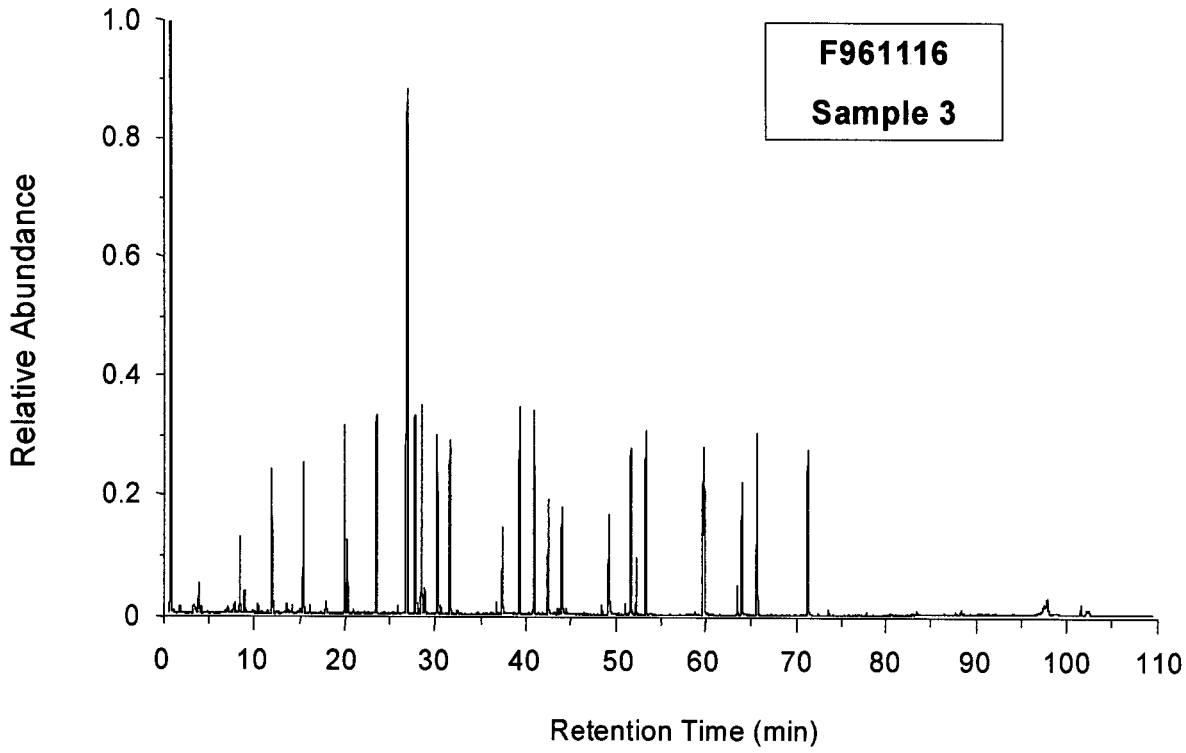


Plot J4. Fire Test F961116. Mass Chromatogram from the GC/MS analysis of Sample 3, which was acquired from +174 to +218 seconds post-ignition.

**Table J4**
**Peak Identification for Fire Test F961116 Sample 3**

| $t_R$ | Compound | CAS No. |
|---|---|---|
| 3.30 | carbon dioxide | 000057-13-6 |
| 6.07 | pentane-$d_{12}$ (IS) | 002031-90-5 |
| 10.37 | n-hexane-$d_{14}$ (IS) | 021666-38-6 |
| 10.82 | n-hexane | 000110-54-3 |
| 13.64 | benzene-$d_6$ (IS) | 001076-43-3 |
| 13.77 | benzene | 000071-43-2 |
| 16.93 | n-heptane-$d_{16}$ (IS) | 033838-52-7 |
| 21.24 | toluene-$d_8$ (IS) | 002037-26-5 |
| 21.50 | toluene | 000108-88-3 |
| 24.51 | n-octane-$d_{18}$ (IS) | 017252-77-6 |
| 27.74 | cyclotrisiloxane, hexamethyl- | 000541-05-9 |
| 28.52 | benzene, ethyl-$d_{10}$ (IS) | 025837-05-2 |
| 28.86 | benzene, ethyl- | 000100-41-4 |
| 29.24 | p-xylene-$d_{10}$ (IS) | 041051-88-1 |
| 29.53 | p-xylene | 000106-42-3 |
| 30.81 | o-xylene-$d_{10}$ (IS) | 056004-61-6 |
| 31.21 | o-xylene | 000095-47-6 |
| 32.14 | n-nonane-$d_{20}$ (IS) | 121578-11-8 |
| 37.61 | phenol-$d_5$ (IS) | 004165-62-2 |
| 39.38 | n-decane-$d_{22}$ (IS) | 016416-29-8 |
| 40.88 | cyclotetrasiloxane, octamethyl- | 000556-67-2 |
| 72.37 | p-cresol-$d_8$ (IS) | |
| 43.76 | o-cresol-$d_8$ (IS) | |
| 48.70 | 2,4-dimethyl phenol-$d_3$ (IS) | |
| 50.97 | naphthalene-$d_8$ (IS) | 001146-65-2 |
| 51.54 | cyclpentasiloxane, decamethyl | 000541-02-6 |
| 52.55 | n-dodecane-$d_{26}$ (IS) | 121578-12-9 |
| 58.50 | n-tridecane-$d_{28}$ (IS) | 121578-12-9 |
| 58.63 | 1-Methylnaphthlene-$d_{10}$ (IS) | 038072-94-5 |
| 62.02 | cyclhexasiloxane, dodecamethyl | 000540-97-6 |
| 62.50 | Biphenyl-$d_{10}$ (IS) | 001486-01-7 |
| 64.07 | n-Tetradecane-$d_{30}$ (IS) | |
| 69.33 | n-Pentadecane-$d_{32}$ (IS) | 036340-20-2 |
| 71.47 | unidentified phthalate | n/a |
| 97.62 | hexadecanoic acid, dihexyl ester | 000110-33-8 |
| 98.52 | unidentified phthalate ester | n/a |

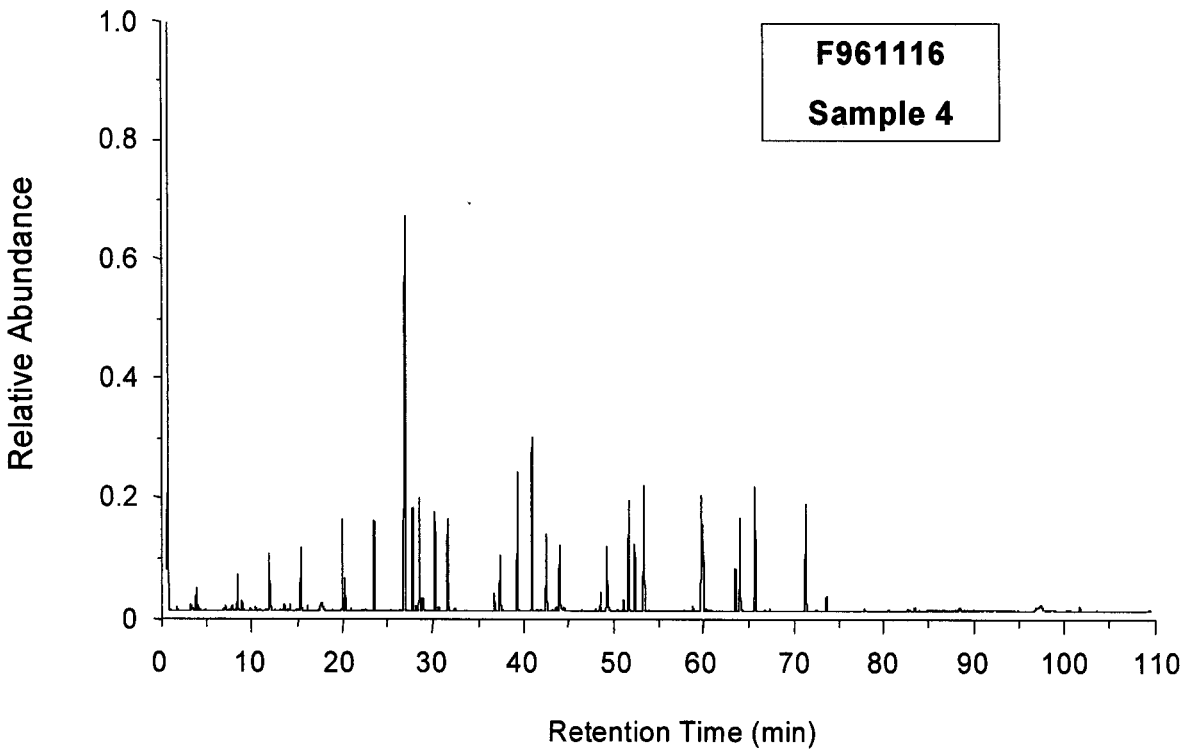


Plot J5. Fire Test F961116. Mass Chromatogram from the GC/MS analysis of Sample 4, which was acquired from +219 to +235 econds post-ignition.

**Table J5**
**Peak Identification for Fire Test F961116 Sample 4**

| $t_R$ | Compound | CAS No. |
|---|---|---|
| 3.30 | carbon dioxide | 000057-13-6 |
| 6.05 | pentane-$d_{12}$ (IS) | 002031-90-5 |
| 10.33 | n-hexane-$d_{14}$ (IS) | 021666-38-6 |
| 10.79 | n-hexane | 000110-54-3 |
| 13.61 | benzene-$d_6$ (IS) | 001076-43-3 |
| 13.75 | benzene | 000071-43-2 |
| 15.18 | hexane, 2-methyl | 000591-79-4 |
| 15.18 | hexane, 2-methyl | 000591-76-4 |
| 15.77 | hexane, 3-methyl | 000589-34-4 |
| 16.90 | n-heptane-$d_{16}$ (IS) | 033838-52-7 |
| 19.10 | unidentified | n/a |
| 21.22 | toluene-$d_8$ (IS) | 002037-26-5 |
| 21.48 | toluene | 000108-88-3 |
| 24.49 | n-octane-$d_{18}$ (IS) | 017252-77-6 |
| 27.76 | cyclotrisiloxane, hexamethyl- | 000541-05-9 |
| 28.50 | benzene, ethyl-$d_{10}$ (IS) | 025837-05-2 |
| 28.86 | benzene, ethyl- | 000100-41-4 |
| 29.22 | p-xylene-$d_{10}$ (IS) | 041051-88-1 |
| 29.53 | p-xylene | 000106-42-3 |
| 30.80 | o-xylene-$d_{10}$ (IS) | 056004-61-6 |
| 32.13 | n-nonane-$d_{20}$ (IS) | 121578-11-8 |
| 36.99 | unidentified | n/a |
| 37.59 | phenol-$d_5$ (IS) | 004165-62-2 |
| 39.39 | n-decane-$d_{22}$ (IS) | 016416-29-8 |
| 40.90 | cyclotetrasiloxane, octamethyl- | 000556-67-2 |
| 42.38 | p-cresol-$d_8$ (IS) | |
| 43.77 | o-cresol-$d_8$ (IS) | |
| 48.02 | unidentified | n/a |
| 48.73 | 2,4-dimethyl phenol-$d_3$ (IS) | |
| 51.00 | naphthalene-$d_8$ (IS) | 001146-65-2 |
| 51.60 | cyclpentasiloxane, decamethyl | 000541-02-6 |
| 52.55 | n-dodecane-$d_{26}$ (IS) | 121578-12-9 |
| 58.53 | n-tridecane-$d_{28}$ (IS) | 121578-12-9 |
| 58.69 | 1-Methylnaphthlene-$d_{10}$ (IS) | 038072-94-5 |
| 62.06 | cyclhexasiloxane, dodecamethyl | 000540-97-6 |

**Table J5, continued**
**Peak Identification for Fire Test F961116 Sample 4**

| $t_R$ | Compound | CAS No. |
|---|---|---|
| 62.54 | Biphenyl-$d_{10}$ (IS) | 001486-01-7 |
| 64.10 | n-Tetradecane-$d_{30}$ (IS) | |
| 69.35 | n-Pentadecane-$d_{32}$ (IS) | 036340-20-2 |
| 93.80 | unidentified phthalate ester | n/a |

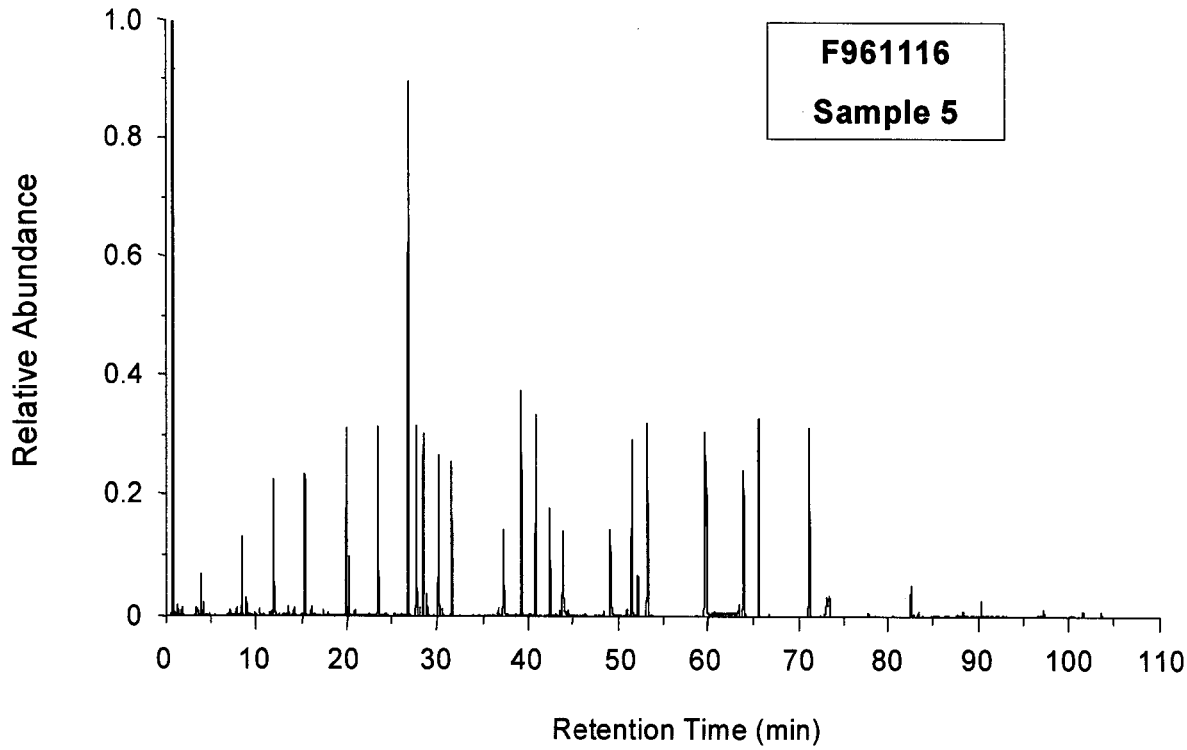


Plot J6. Fire Test F961116. Mass Chromatogram from the GC/MS analysis of Sample 5, which was acquired from +236 to +326 seconds post-ignition.

**Table J6**
**Peak Identification for Fire Test F961116 Sample 5**

| $t_R$ | Compound | CAS No. |
|---|---|---|
| 3.26 | carbon dioxide | 000057-13-6 |
| 6.07 | pentane-$d_{12}$ (IS) | 002031-90-5 |
| 10.37 | n-hexane-$d_{14}$ (IS) | 021666-38-6 |
| 10.82 | n-hexane | 000110-54-3 |
| 13.64 | benzene-$d_6$ (IS) | 001076-43-3 |
| 13.77 | benzene | 000071-43-2 |
| 16.93 | n-heptane-$d_{16}$ (IS) | 033838-52-7 |
| 21.24 | toluene-$d_8$ (IS) | 002037-26-5 |
| 21.50 | toluene | 000108-88-3 |
| 24.51 | n-octane-$d_{18}$ (IS) | 017252-77-6 |
| 27.74 | cyclotrisiloxane, hexamethyl- | 000541-05-9 |
| 28.52 | benzene, ethyl-$d_{10}$ (IS) | 025837-05-2 |
| 28.86 | benzene, ethyl- | 000100-41-4 |
| 29.24 | p-xylene-$d_{10}$ (IS) | 041051-88-1 |
| 29.53 | p-xylene | 000106-42-3 |
| 30.81 | o-xylene-$d_{10}$ (IS) | 056004-61-6 |
| 31.21 | o-xylene | 000095-47-6 |
| 32.14 | n-nonane-$d_{20}$ (IS) | 121578-11-8 |
| 37.61 | phenol-$d_5$ (IS) | 004165-62-2 |
| 39.38 | n-decane-$d_{22}$ (IS) | 016416-29-8 |
| 40.88 | cyclotetrasiloxane, octamethyl- | 000556-67-2 |
| 42.37 | p-cresol-$d_8$ (IS) | |
| 43.76 | o-cresol-$d_8$ (IS) | |
| 48.70 | 2,4-dimethyl phenol-$d_3$ (IS) | |
| 50.97 | naphthalene-$d_8$ (IS) | 001146-65-2 |
| 51.54 | cyclpentasiloxane, decamethyl | 000541-02-6 |
| 52.55 | n-dodecane-$d_{26}$ (IS) | 121578-12-9 |
| 58.50 | n-tridecane-$d_{28}$ (IS) | 121578-12-9 |
| 58.63 | 1-methylnaphthlene-$d_{10}$ (IS) | 038072-94-5 |
| 62.20 | cyclhexasiloxane, dodecamethyl | 000540-97-6 |
| 62.50 | Biphenyl-$d_{10}$ (IS) | 001486-01-7 |
| 64.07 | n-Tetradecane-$d_{30}$ (IS) | |
| 69.33 | n-Pentadecane-$d_{32}$ (IS) | 036340-20-2 |
| 71.47 | unidentified phthalate ester | n/a |
| 97.62 | hexadecadioic acid, dihexyl ester | 000110-33-8 |
| 98.52 | unidentified phthalate ester | n/a |